
# An Investigation into the Ability of a Kinetic Particle-based Solver for Study of Gas Flows in Micro-scale Structures

Thesis by

**Ferdin Sagai DON BOSCO**

University of Strathclyde,
Department of Mechanical and Aerospace Engineering
James Weir Building, 75 Montrose Street
GLASGOW, G1 1XJ
United Kingdom

ferdin-don.bosco@strath.ac.uk

# Declaration of author's rights

This thesis is the result of the author's original research. It has been composed by the author and has not been previously submitted for examination which has led to the award of a degree.



Signed: Ferdin Sagai Don Bosco

Date: 16 July 2019

# Abstract

Scientific enquiry has aligned itself, in recent times, to the understanding of the flow physics encountered in micro- and nano-scales. The prominence of this line of enquiry is due to its recurring influence in the fields of MEMS and porous media.

These flows occur in pathways whose width is comparable to the mean free path and thus, are classified as rarefied gas flows. Assuming continuum and resorting to traditional CFD techniques leads to results with severe reservations while, deterministic kinetic theory based approaches, such as DVM, implement liberal approximations such as restricting the velocity space to a limited set determined through pre-cognizance or trials. Even stochastic particle approaches, such as the DSMC, usually adept at resolving such flows, proves to be prohibitively expensive owing to the small signal-to-noise ratio necessitating a large number of samples to obtain appreciably accurate results.

The present research is aimed at recovering the inherent advantages of particle methods through the development of parallel kinetic particle-based solver founded on the low variance ideologies. The solver is validated against classical fluid dynamics problems prior to application to simple, yet practical, MEMS applications such as isothermal flow through long ducts and past infinite arrays.

The final objective of the current research is aimed at understanding and simulating the transport of unconventional gases in subterranean micro-porous networks which is of great significance in the oil and gas industry. To this end, the simulation of pore-scale flows for the entire rarefaction spectrum through idealized porous media such as Sierpinski carpets, Menger sponge etc. along with image-reconstructed porous media such as 2D Berea sandstone and 3D rock samples such as Gambier, Castlegate and Fayetteville shale are carried out and analysed.

The unique approach enables the solver to obtain novel, substantial and reliable insights at the pore level while employing appropriate averaging to predict macroscopic properties such as apparent permeability and tortuosity with a previously unprecedented computational efficiency.

# Acknowledgements

We, humans, are social beings and by that definition alone any accomplishment, Herculean or Lilliputian, is a result of a team effort. This thesis is no exception to this rule. This research is carried out in the Department of Mechanical and Aerospace engineering, James Weir Fluids Building, University of Strathclyde and I would like to acknowledge the financial support, facilities and environment extended by the university to this research.

For any aspiring researcher, the vital necessities are the guidance, freedom and trust. In this regard, I am extremely fortunate to have been under the tutelage of Prof. Yonghao Zhang. Developing a code is a trying task and I am grateful for his guidance, compassion, encouragement and above all, patience. I also acknowledge the constructive criticism and appreciation from my second supervisor Dr Mónica Oliveira which goes a long way in a venture such as this. Criticism, especially of one's research is one of the hardest things to come by and I would like to thank my research group, consisting of Dr Lei Wu, Dr Minh Tuan-Ho, Dr Peng Wang, Qingqing Gu and Lefki Germanou for their participation in our bimonthly meetings. Their discussions about their research helped me gain an overall perspective of the big picture, which is often lost when one is entangled in their web of problems.

A lab is a place of research and more often than not, the monotonicity of research can be a demotivating factor. Thankfully, this has not been the case in my venture. I would like to thank my fellow researchers and friends; Dr. Faidon Kyriakou , Iasonas Zekos for the numerous discussions; Dr. Paolo Capobianchi and Dr. Nikos Ioannou for always having a word of advice; Dr. Andreia Silva for being a steadfast friend and a stationary target; Dr. Thomas Burel for being that *poteau* I needed; To Dr. Daniel Espinoza for motivating me to roll the dice; To Jack Hanson, my American IT guy and to my numerous friends outside the workplace for reminding me its okay to loosen up.

My family has always been my greatest bastion and without the collective sacrifice, encouragement, and presence, I doubt my ability to have seen this task across the finish line. Thank you!

This has been an important chapter in my life filled with triumphs and trials, proving to be the most singular challenge of my life and there are so many others that I would like to extend my sincere gratitude towards, unfortunately, in Pierre de Fermat's immortal words, *"...this margin is too narrow to contain."*

# Scientific contributions

## With peer review

### International conferences

#### Presentation

- 2017 InterPore Investigation into the Applicability and Feasibility of Low Variance Kinetic Particle Based Solver For Study of Shale Gas Flows in Micro-Porous Structures

### National conference

#### Presentation

- 2016 29th Scottish fluid mechanics meeting Investigation into the Applicability and Feasibility of LV-DSMC-BGK Based Solver For Study of Shale Gas Flows in Micro-Porous Structures.
- 2016 Multi-scale Fluid Dynamics Conference Low Variance DSMC for the Study of Shale Gas Transport in Micro–porous Media

# Contents

# List of Figures

# List of Tables

# Abbreviations

**AR** Argon gas

**BBGKY** Bogoliubov-Born-Green-Kirkwood and Yvon

**BGK** Bhatnagar-Gross-Krook

**CFD** Computational Fluid Dynamic

**CLL** Cercignani-Lampis-Lord model

**$CO_2$** Carbon dioxide

**CPU** Central Processing Unit

**DNS** Direct Numerical Simulation

**DSBGK** Direct Simulation Bhatnagar-Gross-Krook

**DSMC** Direct Simulation Monte-Carlo

**DUGKS** Discrete Unified Gas Kinetic Scheme

**DVBE** Discrete Velocity Boltzmann Equation

**DVM** Discrete Velocity Method

**EMA** Effective Medium Approximation

**EOR** Enhanced Oil Recovery

**FDM** Finite Difference Method

**FEM** Finite Element Method

**FORTRAN** FORmula TRANSlation

**FVM** Finite Volume Method

**VHS** Generalized Hard Sphere

**VHS** Generalized Soft Sphere

**HS** Hard Sphere

**KOH** Potassium Hydroxide

**LBM** Lattice Boltzmann Method

**LGA** Lattice Gas Automata

**LGCA** Lattice Gas Cellular Automata

**LHS** Left hand side

**MC** Monte Carlo

**MD** Molecular Dynamics

**MEMS** Micro-Electro-Mechanical-System

**MPI** Message Passing Interface

**MRT** Multiple Relaxation Time

**NS** Navier-Stokes

**OpenFOAM** Open-source Field Operation And Manipulation

**PA** Pore Activity

**PC** Percolation Carpet

**PDE** Partial Differential Equation

**PEGASUS** Pore-scale Environ Gas Analyser and Solver Utilizing Stochastic

**PPC** Particle Per Cell

**REV** Representative Elementary Volume

**RHS** Right hand side

**RMF** Reduced Mass Flow rate

**SAS** Sum And Substance

**SC** Sierpinski Carpet

**SEM** Spectral Element Method

**SI** Surface Interactivity

**SOTA** State Of The Art

**STM** Scanning Tunnelling Microscopy

**UGKS** Unified Gas Kinetic Scheme

**VHS** Variable Hard Sphere

**VHS** Variable Soft Sphere

## Nomenclature

$\alpha$ Maxwell accommodation parameter

$\lambda$ Mean free path

$\tau$ Tortuosity

$\tau_r$ Relaxation time

$G_p$ Reduced mass flow rate

$k_a$ Permeability

$Kn$ Knudsen number

$L_0$ Reference length

$Ma$ Mach number

$Po$ Poiseuille Number

$Pr$ Prandtl number

$Re$ Reynolds number

$t_{coll}$ Instantaneous collision time

$t_{mct}$ Mean collision time

# Chapter 1

# Introduction

*"If I had a world of my own, everything would be nonsense. Nothing would be what it is because everything would be what it isn't. And contra-wise, what it is it wouldn't be, and what it wouldn't be, it would. You see?"*

*-Alice, Alice in Wonderland by L. Carrol*

## 1.1 The need of the hour

The past century has witnessed a growth in the technological prowess of the human race, the likes of which has neither been seen nor foreseen. In a relatively short period of time, our standard of living has improved significantly owing to rigorous scientific investigations, meticulous engineering practices, and wide-spread dissemination of technical knowledge. Outlook towards the future is at its optimistic zenith and we are keen on undertaking even more ambitious projects. Attempts to understand the curiosities of the universe are under-way, even at this very instant, be it via the satellites peering into the vast infinity of space in their orbits around our planet [1] or through the particles accelerating close to the speed of light in the long tunnels of the Large Hadron Collider ensconced within the bowels of the Earth [2].

We live in a crucial, albeit, golden era in our history where our actions will dictate and influence the course of our immediate and distant future more prominently than ever before. This is both a promising and daunting prospect. 'Promising'; because as disciples of science, our principal motivation has always been to understand the mysteries of the universe and the current social and technological climate is highly conducive, with the assistance of modern technology significantly enhancing scientific efforts. 'Daunting'; because we are in a position where progress must be achieved responsibly and sustainably which proves to be a formidable challenge, especially, in the ever-changing landscape of our economically–driven incremental ambitions. Mutual reliance of the scientific sphere on the economic sphere and vice-versa is a demanding juggling act that is difficult to maintain in the best of times. The price of not striking this balance is felt tangibly through a severe scarcity of basic resources or adverse and

potentially irreversible deterioration of our ecosystems [3]. The recent plight of Cape Town in South Africa serves as a stark reminder to the tangibility of the threat posed by unmonitored progress [4].

One way towards sustainable progress is through optimization of our existing technology and developing new ones that levy a minimal strain on our, already overstretched, resources. Another promising ideology is the exploration and exploitation of new and alternate resource repositories which has had an encouraging effect in the amelioration of the resource scarcity. These objectives are synonymous with the rise in popularity of miniaturization as prominently seen by the establishment of Microtechnology [5]. The success achieved by this field has encouraged other industries to appreciate the importance of the small-scale physics arising from miniaturization and are finding innovative means to incorporate these ideologies into their applications; foremost among these is the porous media industry which includes flow of gases through industrially manufactured apparatus such as sand-filled drying towers and also naturally occurring micro-porous structures such as sandstones and shale rock structures. These applications require an intricate understanding of the mechanics at small-scale environments, specifically, mechanisms relating to the transport of mass, momentum and energy through fluid flows.

The transference of technological interest into the physics of small-scale gaseous flows has created a demand for the establishment of the fundamental science that was, thus far, underdeveloped. The popular theories, mathematical models and methods developed for continuum and high-speed rarefied fluid dynamics are rendered moot since these flows defy the well-established principles considered canon in macroscopic fluid dynamics. The shortcomings of the current tools further emphasize the need for an alternate method; one more attuned to the physics of small-scale flows while at the same time being computationally cost-efficient. Rising to this challenge, the development of a new stochastic kinetic particle scheme relying on variance reduction principles applied to the Boltzmann equation is undertaken with the resulting parallel solver employed to effectively and efficiently study and characterize flows at these scales.

The present chapter aims to establish the premise for the research carried out in this thesis. To this end, substantiation of the importance and role of micro-flows in the industrial sphere is furnished in the next section by exploring some of the major industries reliant on the understanding of such flows. Examples have been chosen specifically to highlight the significance of small-scale gaseous flows and the need for closer scrutiny. Attention is drawn to the reason behind the non-conformance of small-scale flow physics to the established axioms and the issues facing the state-of-the-art methods. The central theme of the method espoused in this thesis is then presented along with a brief discussion of the means by which the method is more suitable to the application to the problem at hand. A plan of action is devised to identify, isolate and investigate the complex environments encountered in an industrial, research and geological setting. The final section of this chapter defines the thesis structure.

## 1.2 Significance of small-scale flows

Within each of the fields mentioned previously, an industry and sector that is most likely to benefit from these studies is recognized and discussed in this section.

### 1.2.1 The field of micro/nanotechnology

One of the brilliant achievements in the past half a century that has taken center-stage is miniaturization. At its core, the principle of miniaturization is to replicate the results produced by large-scale machines through the use of minute machinery. The saving in material and cost of operation obtainable through such an initiative is self-evident when one considers the scale of the size reduction.

Though these devices revolutionized the modern industries, the idea itself is not revolutionary. In fact, the advantage of such fabrications was appreciated even before their existence as is evident from the immortal lecture titled "There's plenty of Room at the Bottom" delivered by Dr. Richard Feynman at a meeting of the American Physical Society as far back as 1959 [6]. Feynman was interested in exploring, manipulating and controlling the systems at a small scale. He explored ideas that bordered on science fiction at that time such as, the possibility of writing the entire 24 volumes of the Encyclopaedia Britannica on the head of a pin along with ways to read it and the creation of microscopic robots to conduct surgery. The potential challenges that could be encountered while attempting to work at such scales were also brought to light in this lecture. At the end of the lecture, Feynman put forth two challenges, namely, the creation of a tiny motor and the writing of a page of information on a surface that is $1/25000^{th}$ the original size. As of today both these challenges have been completed [7,8].

Thus, the foray of technology into the miniaturization was a forgone conclusion and since then many significant strides have been made in the fabrication and application of such small scale devices. This has laid the foundation for the Micro-Electro-Mechanical-Systems(MEMS) or Micro-Systems-Technology(MST) or Micro-Machined-Devices(MMD) industry.

#### 1.2.1.1 The MEMS industry with a focus on the microfluidics sector

MEMS can be defined as a class of miniature devices and systems fabricated by micromachining processes. The critical dimensions of these devices are in the range of 1000 $\mu$m to 1 nm. Typically, MEMS uses electronics to interface between its functional domain and the electrical circuitry for signal processing and recording. However, the term has become generic with applications devoid of mechanical functions such as electro-chemical sensors included in the family of MEMS devices. The industry is a booming one with new applications expected to lead to a 17.5 % growth in value between 2018 and 2023 [9].

The attraction with MEMS is evident due to factors such as small size, light-weight,

low power consumption, high functionality and ease of production. Apart from these obvious advantages, one of the two alluring aspects of MEMS is its ability to create synergy between previously unrelated fields while simultaneously delivering innovative and unique products to address the needs of the new field. A clear example of this is the advances in the field of biotechnology where MEMS has delivered products such as micro-machined Scanning Tunnelling Microscopes (STM), biochips for detection of hazardous chemical and biological agents to name but a few.

The second allure of MEMS is the ability to sense and actuate on a micro-scale producing macroscopic results either independently or in conjunction with other devices. Demonstration of this ability was presented by the results of an experiment in which micro-flaps placed at the leading edge of an aerofoil have been able to steer the aircraft through micro-actuation of the flaps alone [10].

Typically, a MEMS device consists of mechanical, chemical, electronic and electrical components designed to measure and modify the behaviour of the domain under its influence called the functional domain. One of the most widely encountered functional domain is that of microfluidics. MEMS devices associated with microfluidics are designed to exert precise control and manipulation; either through physical, biological and/or chemical means; of fluids that are contained in the functional domain. The physical control and manipulation can be active through the use of micro-pumps and micro-valves or passive utilizing obstacle arrays, adsorbent films or complicated flow pathways. It is a multi-disciplinary field playing pivotal roles in engineering, physics, chemistry, biotechnology, etc. Applications such as micro-needles of the order of 300 $\mu$m for drug delivery, blood tests, etc. and gas characterization through vapour phase gas chromatography are some of the many examples within the scope of microfluidic MEMS devices.

### 1.2.2 Fields utilizing porous media

Porous media finds application in many branches such as geomechanics, soil mechanics, acoustics, etc. Engineering fields of petroleum, construction, material science, etc. are likewise benefited by advances in this field. While most applications such as packed sand beds, metallic foams inherently accommodate a flow network, naturally occurring porous structures of geological origins such as shale and sandstones may not be forthcoming. In such cases, artificial flow networks are introduced through fractures.

A clear example of such actions is the Shale Gas revolution in the oil and natural gas industry and has played a significant role is the delaying of the global energy crisis. The revolution focusses on the increase in the oil and natural gas productivity of wells by augmenting the output with resources trapped within the porous shale rock networks of size in the order of micro- and nanometers. The revolution has also caused an increased interest in porous media structures with a rise of new potential applications such as $CO_2$ sequestration and in combustion technology revolving around fuel cells.

#### 1.2.2.1 Oil and gas industry with an emphasis on the shale gas sector

The oil and natural gas industry can trace its origin back by more than 2000 years to ancient China [11, 12] where, historical evidence reveals, the first oil wells were drilled. Ever since that archaic attempt, the world's fascination with these non-renewable sources of energy has intensified.

In order to appreciate the industry, it is essential to have a clear view regarding the anatomy of an oil and natural gas reservoir. The formation of these hydrocarbon fossil fuels is through the process of decomposition of organic matter under high pressures over a large period of time spanning hundreds of years. The organic matter is seldom large creatures, but rather microbes that are deposited by the ancient rivers along their banks and beds along with slit. Over time the slit hardens into rocks such as shale and the trapped organic matter decay in an oxygen deficit atmosphere. Constant shifts in the tectonic plates and microearthquakes cause these individual reservoirs to fracture thereby forming pathways for the hydrocarbons to flow and occupy the largest available free volume resulting in the underground reservoir encased in impermeable rocks. The operation principle of wells is to tap into these reserves by drilling. It has been a well-known fact that the hydrocarbons accumulated in such an underground reserve are only a fraction of that available and a majority of the resources still lies entombed within the shale rock formations. This is depicted in figure 1.1a below.

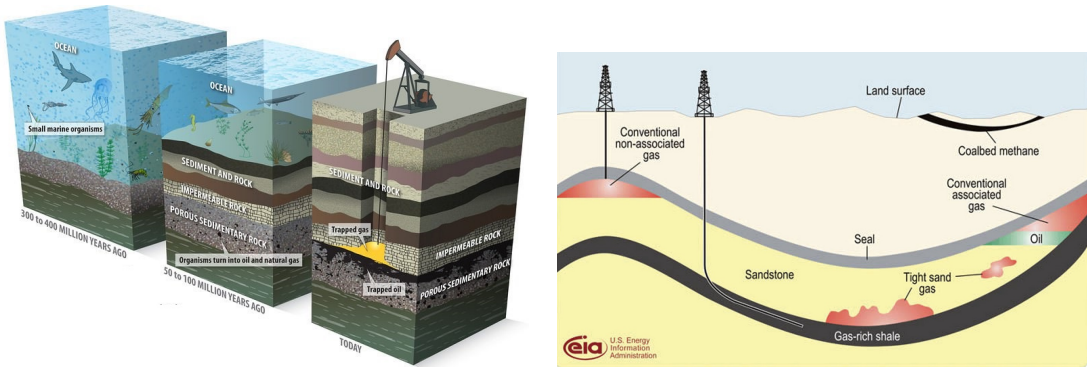


(a) Formation of reservoirs (Source: [13]). (b) Types of wells (Source: [14]).

Figure 1.1: Oil-gas reservoir formation and exploration techniques.

Although a typical well contains vast quantities, the growing demand for these fuels has placed severe stress on these resources and the potential of a crisis was imminent owing to their limited availability and inaccessibility of the trapped resources. Such a crisis was the focus a decade ago leading to a world-wide situation of panic emphasizing our dependence on these resources. However, the crisis was averted for the present time owing to a large role played by the shale gas revolution.

The shale gas sector is predicated on the attempts to access and exploit the trapped resources through artificial manipulations, such as fracturing, of the resource-bearing rock formations. This process pioneered by Farris and Clark was coined as "Hydraulic

Fracturing" or "Fracking" [15] and has come a long way since its crude inception by Preston Barmore in 1857 [16] through game-changing contributions such as the inclusion of proppants, surfactants and, critically, the ability drill horizontal [17]. A testament of this technique's popularity is seen by noting that the number of horizontal wells (shown in fig.1.1b) under construction has increased from 9% in the late 1990s to 50% in 2010 [18].

Part of the appeal with shale gas is the fact that it is a cleaner source of energy compared to coal meaning that the combustion of shale gas produces less $CO_2$ than coal. Moreover, an added benefit of extracting shale gas is that it provides an effective solution for the control of $CO_2$. The premise of $CO_2$ sequestration is the capture and storage of pressurized $CO_2$ in reliable locations such as depleted oil and gas reservoirs [19, 20]. The injection of $CO_2$ into the reservoir's pore networks have also been used to recover the residual oil from the pore space and is called $CO_2$ enhanced oil recovery. The Sleipner project [21] in the North Sea by a Norwegian Oil company in 1996 is deemed as the first international example of sequestration.

In spite of the benefits of the Shale gas industry, recent times have seen opposition to the method owing to the possible negative impact on the environment [22]. Hydraulic fracturing is a resource-intensive method that requires a large amount of water as part of the operating cost. Although the water pumped into the pore network is recovered, the number of dissolved substances render it highly toxic and necessitate the infrastructure for its treatment and disposal [23]. Other than this difficulty, there have been instances where the water flows through underground networks to the water tables and pollutes the groundwater. The potential destabilization of the surface structure due to underground fracking is also of major concern in many communities.

The fallout of these concerns has resulted in the imposition of severe restrictions and outright bans on fracking by many governments [24]. Further heightening the unrest is the number of films such as Gasland, Gasland II, Promised land, etc. which claim to exposit the dangers of fracking [25–27]. While it is clear that shale gases are not a permanent solution, the energy scarcity of modern times along with the promise of a temporary amelioration of the global crisis that shale gases offer has caused many governments to reconsider their position [28] and in some cases rescind their decision [29]. Anxiety about possible seepage of $CO_2$ into populated regions or eruptions of the underground $CO_2$ reservoirs due to geothermal heating have been expressed and the technique is regarded with some degree of suspicion [30].

The final lasting solution is obviously in the rise and establishment of clean and renewable sources of energy. Although the current state of these industries is improving, with examples like Burlington, Vermont in the USA becoming the first city to be completely powered by renewable sources [31], the field is still embryonic with the task of supplying the basic needs of a highly populated industrial city several decades away.

Although the present situation looks bleak with a looming threat of an energy crisis; cautious fracking bolstered by full and complete information with regards to the rock

structures and flow characteristics obtained via a meticulous and unbiased scientific investigation into the physics involved and the effect of industrial processes is likely to assuage the public unrest. Though a temporary solution, we can take solace in the words of Sheikh Zaki Yamani, the former oil minister of Saudi Arabia who famously proclaimed, [32]

"The Stone Age did not end for lack of stone, and the Oil Age will end long before the world runs out of oil."

## 1.3 Challenges posed by small-scale flows

The interest in small-scale flows is not new per se, but up until now, empirical relations based on experimental results provided a sufficient approximation of the flow behaviour. This fostered the growth of macroscopic flow theory based on near-canonical assumptions such as the continuum hypothesis. The greater degree of scientific focus on macroscopic continuum flows is justifiable since it affects the working of day-to-day activities more prominently than an isolated microscopic phenomenon. However, with the advancement of MEMS and other small scale flows, the luxury of neglecting such physics is lost.

### 1.3.1 Source of complications

The efforts of the scientific community have been directed at understanding and establishing the fundamental science behind these class of flows. The task is, however, a challenging one owing to the fact that these flows have certain unique characteristics that have resulted in the observation of peculiar phenomena such as the Thermomolecular Pressure Difference effect [33] and presence of a Knudsen minimum [34].

The first unique characteristic is that the flows are often low-signal flows. In gas dynamics, gaseous molecules are in a state of constant motion with velocities which are a function of the temperature. Literature refers to these velocities as peculiar velocity, thermal velocity or random velocity. This is true even in equilibrium conditions. A gradient in-state properties across such gas will cause gas molecules to move in a direction of the gradient, thereby enticing a flow velocity. Borrowing from the signal processing parlance, this enticed flow velocity is termed as a "signal" and the random velocities possessed by the molecules are termed as the "noise".

If the gradient is large, the associated flow velocity (signal) is larger than the thermal velocity (noise) and an average will be dominated by the signal. However, if the gradient is small, the associated flow velocity is smaller than the corresponding noise and detection of such a signal through averaging is only possible by using a larger sample size which is an expensive process. Such flows are said to have a low signal-to-noise ratio and are termed as low-signal flows. If the signal is velocity, as in the illustration above, then the term low-speed flows is used whereas if the signal is thermal in nature

then the term low-temperature variation flows is more appropriate.

Secondly, despite the low speeds, these flow occurs in structures where the characteristic flow paths are comparable to the mean free path of the gas and thus, the flow is classified as rarefied gas flows. The situation is especially exacerbated in the case of porous media wherein, various regions exhibit different degrees of rarefactions that co-exist. This leads to the need of a multi-scale approach.

Finally, the difficulty arises because the scales we are accustomed to have measurable inertial and surface effects with inertial effects usually dominating the surface effects. However, in the micro-flows under consideration, the surface effects dominate the inertial effects. Porous media are characterized by an inordinate amount of surfaces and the effect of the surfaces is greatly influential in the flow behaviour.

Expressed in terms of dimensionless similarity parameters, these flows are low Mach number, low Reynolds number, and high Knudsen number multi-scale flows.

### 1.3.2 Shortcomings of the currently popular methods

The prospect of dealing with such flows is a novel one. The rarefaction of the gases implies that the continuum assumption is no longer reliable and thus, the mathematical modeling based on continuum assumptions such as the Euler, Navier-Stokes-Fourier system of equations are expected to deliver inaccurate estimations.

The solution of the Boltzmann equation is complex and solutions have only been obtained for the most fundamental cases. A porous media environ offers a much more complex flow field and the direct numerical solution of the Boltzmann equation is not a viable option. Deterministic mesoscopic methods of solving the Boltzmann equation such as Lattice Boltzmann Method (LBM) [35] and Discrete Velocity Method (DVM) [36] rely on the discretization of the velocity space and have achieved a moderate degree of success. Though it is within the ability of stochastic mesoscopic methods such as Direct Simulation Monte Carlo (DSMC) [37], the associated computational cost due to a large number of samples required renders the method unusable.

Although the DSMC method has insurmountable issues, the methods also offer advantages that cannot be matched by any other treatment. Some of the advantages such as the ability to incorporate a complex geometry, natural treatment of the advection operator, probabilistic handling of the collision operator and the ease of a parallel implementation have justified the attempts to develop new methods that are particle-based and akin to DSMC. To this end, one of the successful modifications to the DSMC routine is the IP-DSMC (Information Preservation-DSMC) that was proposed by Fan [38]. The method is particularly designed to tackle the problems of low-speed flows and has achieved a moderate degree of success. The method, however, suffers from certain disadvantages, such as the associated need to store additional information regarding particles, that make it a poor option. Variance-reduced particle methods [39–41] are promising, but have remained in the stage of a technical demonstration and have not

been tested against real-world applications.

Fundamental microscopic approaches such as Molecular Dynamics (MD) [42] based approach require a lot of information in order to replicate a system accurately. Moreover, the computational cost of such methods is prohibitive even for simple cases owing to the large number of molecules along with their reliance on statistical sampling. Situations such as those involving multiple surface interactions and intermolecular collisions are beyond the capability of the current MD solvers.

## 1.4 Scope of the thesis

The scope of this thesis can be concisely stated as two sequential tasks. The first of these tasks is the design, development, and validation of a stochastic particle-based solver relying on variance reduction principles applied to the Boltzmann equation with appropriate added features enabling it to study a wide class of small-scale low-signal rarefied gas flows.

The second task is rooted in the realization that such flows are typical occurrences in the fields of MEMS-microfluidics and porous media and these fields provide the current solver with a plethora of interesting flow scenarios worthy of scientific scrutiny. Thus, this task entails the setting up of a flow scenario, running simulations with a wide range of varying parameters and analysis of results obtained.

Recently, the idea of controlling the statistical uncertainty by incorporation of variance reduction techniques has been presented [39, 43, 44]. Through the treatment of a variance reduced form of the Boltzmann collision operator, it is possible to construct a particle-based stochastic method that is capable of replicating the advantages enjoyed by the stochastic particle methods while also efficiently handling low-speed complex structure environments.

In the present research, the principle of variance reduction is used to devise a method of interpreting a system governed by the Boltzmann-BGK equation, as a system of signed particles that represent the deviation from a local equilibrium state. The various processes involved in the evolution of the system such as particle advection, boundary interactions, and collision are appropriately designed.

The in-house solver is developed using the FORTRAN 90 language with parallel implementation through the Message Passing Interface (MPI) framework. The validation of the solver is done through comparisons with canonical benchmark cases.

The method and the solver are uniquely suited to the present studies owing to several reasons. Firstly, the large number of surfaces, which are essentially an inconvenience for most solutions methods, are a means of retaining solver stability in the current implementation (provided the studies are isothermal). Secondly, the focus on the deviation from equilibrium allows the capture of the signal while excluding the noise which is dominant in low signal flows encountered here. Thirdly, the particulate nature combined with the source-sink view of the collision process allows the effect of

rarefaction to influence the collision part alone. Also, the local cell-confined nature of the collisions makes it possible to take into account the local rarefaction and thus, capture multi-scale effects. Moreover, the implementation of the boundary conditions is straight forward. The physical nature of the simulation removes any necessities of mathematical conditions of stability and consistency. Finally, the particulate nature along with the omission of any particle cancellation scheme eliminates any need for discrete velocities. The solver thus operates on the continuous phase space with particles capable of possessing all probable velocity.

The importance of the microfluidic-MEMS and porous and fractured media has been expounded in the above sections. It is vital to devise a proper plan to study each of these applications in a wholesome manner. Thus, the studies in this thesis are relegated to one of the two branches of study.

The first branch is aimed at components ubiquitous in the MEMS-microfluidics field such as flows through ducts of a long and short nature, flow through networks and flow around arrays of objects. These applications can be generically classified as flows through 2-phase ordered media.

The second branch deals with porous media. The complex structure of micro-scale porous media has led to the rise of many idealizations oft used in the literature. The advent of digital imaging and computer-assisted reconstruction has opened the avenue to procure and conduct studies on the actual internal structure of porous media. Accordingly, both these avenues are part of the present investigation and can be generally classified as flows through 2-phase disordered media.

## 1.5 Structure of the thesis

In the **Present Chapter**, the foundations of the research are laid through the exposition of the role that small-scale flows play in a variety of applications. The need for the method developed as part of this research is highlighted along with the studies needed to perform a judicious, yet impartial evaluation of the method and solver's capability to reconcile such unique flows.

**Chapter 2** is a presentation of the theoretical principles used for the development of various governing equations that are often employed to describe the flows at these scales. The description and resources available for popular numerical methods for the study of the rarefied gas flows are discussed along with reasons for the non-candidacy of these methods. Through this discussion, the need for the current solver development is underlined. Other introductory formalisms relating to flow classification, porous media and formulation are also established as part of this chapter. The formulation consisting of the chosen governing equation and the non-dimensional quantities used in the current development are elaborated.

**Chapter 3** highlights the principal details of the idea utilized in the method that is advocated in this thesis. Previous research contributions and resources are also pre-

sented and explained. The processes essential to simulate the various flow physics likely to be experienced while solving small scale flows are enumerated and their treatment under the current variance reduced formulation is elaborated. Their implementation into the developed solver is described. The various processes followed by this solver is outlined along with a demonstration of its remarkable features. The consequent chapters focus on the utilization of the solver to various applications.

**Chapter 4** concentrates on proving the efficacy of the current solver through the investigation of various classical flow problems. The benchmark cases that are usually used to study the validity of a solver are an important part of any solver development process and are done here in accordance. The secondary ambition of the chapter is to demonstrate, through simulation of appropriately designed toy problems, the salient features of the solver that were highlighted in the previous chapter. The verification of these features will bolster the confidence in handling complex structures further on in this thesis.

**Chapter 5** deals with flows belonging to the first branch of studies, namely those often encountered in MEMS devices. The effect of the rarefaction and the surface properties are of immense relevance at these scales and thus, the flow's behavioural changes with respect to these quantities is the focus of the studies conducted in this chapter. Various flow domain geometries that find application in numerous industrial practices are included in the scope of these studies.

**Chapter 6** is a dedicated attempt to study the second branch, namely porous media, consisting of geometrically generated realistic facsimiles such as fractals, randomly placed objects, etc. while also including image-based reconstructions such as the Berea sandstone. The solver‘s efficient extension to the 3D level is also explored through the simulation of 3D image-based reconstruction of real samples including Bead pack, Sand pack, Castlegate, Gambier and shale rock samples.

**Chapter 7** is a discussion the computational effort demanded by the presently implemented method/solver specially in the context of 3D porous media with highly complex internal structures. The chapter further addresses the effect of the various choice of simulation parameters on the accuracy and computational expense which are two important metric by which modern solvers are evaluated.

**Chapter 8** aspires to consolidate the contribution of the various chapters and studies in order to establish the ability of the method/solver. The solver's pros, cons, and place in the hierarchy of other state-of-the-art solvers are discussed with the possible future scopes and improvements.

# Chapter 2

# Theoretical Background

*"Science, my boy, is made up of mistakes, but they are mistakes which it is useful to make because they lead little by little to the truth."*

*— Professor Lidenbrock, Journey to the Center of the Earth by Jules Verne*

## 2.1 Chapter overview

The aim of this chapter is to establish a detailed foundation through discussions of the governing equation systems evolution, popular methods based on these systems with an emphasis on their ill-suited nature for the task at hand, familiarization with the lexicon prevalent in the fields of rarefied gas dynamics and porous media and presentation of the formulation and nomenclature favoured in this research. The objectives of this chapter are ambitious at best and, though the scope is large, an attempt has been made to cover the ground in a brief yet concise manner.

## 2.2 State of the art

### 2.2.1 Governing equations

It has been long established that fluid, like all matter, consists of small particles called atoms (and molecules) and that the observed macroscopic phenomena are a direct result of the dynamics of these fundamental particles. At present, two major schools of thought are popular in describing the behaviour of particles. These are 'classical mechanics'; whose foundations are rooted in the three physical laws of motion put forth by Newton in his celebrated work titled 'Philosophiæ Naturalis Principia Mathematica' published in 1687 [45] and 'quantum mechanics' whose foundations are based on the uncertainty principle and contributions by Planck, Bose, Einstein, etc. [46].

Classical mechanics assumes that the particles are point masses that occupy no physical volume which is reasonable when the size of the particles is small in comparison with the distance separating them as is very often the case when dealing with fluids and

is more prominent in gases. These laws in conjunction with the axiomatic conservation laws for mass, momentum, and energy define the framework under which the particles of matter can be defined and studied. Direct mathematical formulation of these laws and axioms was investigated by many analytical mechanists such as Euler, Newton, Hamilton, and Lagrange. For an $N(\sim O(10^{23}))$ particle system, the conservation of energy can be expressed as a Hamiltonian, $H$, given by,

$$H = \frac{1}{2m}\sum_{i=1}^{N}\overrightarrow{p_i}^2 + \sum_{i=1}^{N}V(\overrightarrow{r_i}) + \sum_{i<j}U(\overrightarrow{r_i} - \overrightarrow{r_j}), \tag{2.1}$$

where, $\overrightarrow{p_i}$ is the momentum vector of the $i^{th}$ particle, $\overrightarrow{r_i}, \overrightarrow{r_j}$ is the position vectors of the $i^{th}$ and $j^{th}$ particle respectively, and $m$ is the mass of a single particle. The 3 terms on the $RHS$ represent the kinetic energy of the system, the effect of an external force on the system in terms of a potential field $(V)$ and the internal force field of the system through a two-particle interaction potential$(U)$.

The statistical evaluation of this system has been encouraged by the realization that the dynamics of a group of molecules, rather than a single molecule, dictates the macroscopic observations. The shift of the focus into a statistical description requires the introduction of some associated concepts.

Firstly, the phase space is the combination of the physical space denoted by $\overrightarrow{r} = \overrightarrow{r}(x, y, z)$ and momentum space given by $\overrightarrow{p} = \overrightarrow{p}(m\overrightarrow{u}, m\overrightarrow{v}, m\overrightarrow{w}) = m\overrightarrow{c}$. Thus, to locate a single particle in phase space, 6 co-ordinates are needed. Every particle is confined to the phase space whose elementary volume is $dV_p$. Secondly, the variable $f(\overrightarrow{r}, \overrightarrow{p}, t)$ is known as the probability density function over the $2N$ dimensional phase space. For a given phase space volume, the probability density $f(\overrightarrow{r}, \overrightarrow{p}, t)$ signifies the likelihood of finding a particle in an infinitesimally small physical volume $\overrightarrow{dr}$ centred around $\overrightarrow{r}$ and in an infinitesimally small momentum space volume $\overrightarrow{dp}$ around $\overrightarrow{p}$ at an instant of time $t$. Being a probability distribution, the value of $f(\overrightarrow{r}, \overrightarrow{p}, t)$ is meaningful only when expressed over a volume; it cannot be specified at a specific point.

The probability density function exhibits some interesting properties. For one, it can be normalized since all the particles are located in the phase space, thus,

$$\int_{phase\ space} f(r, p, t)dV_p = 1; \qquad dV_p = \prod_{i=1}^{N} d^3r_i d^3p_i. \tag{2.2}$$

Another important property is the adherence to the continuity equation which is manifested through the local conservation of the probability distribution function. This indicates that the decrease in probability in one region means that the particle has left that region and has moved into another region whose probability has thus, increased

as a consequence. Mathematically,

$$\frac{Df}{Dt} = \frac{\partial f}{\partial t} + \sum_{i=1}^{N} \left( \frac{\partial (f \overrightarrow{r_i})}{\partial \overrightarrow{r_i}} + \frac{\partial (f \overrightarrow{p_i})}{\partial \overrightarrow{p_i}} \right) = 0. \tag{2.3}$$

The use of Hamiltonian equations and Poisson bracket notation (i.e. $\{H, f\}$) results in the Liouville equation stated in a concise form as,

$$\frac{\partial f}{\partial t} = \{H, f\}; \qquad \{H, f\} = \frac{\partial f}{\partial \overrightarrow{p_i}} \cdot \frac{\partial H}{\partial \overrightarrow{r_i}} - \frac{\partial f}{\partial \overrightarrow{r_i}} \cdot \frac{\partial H}{\partial \overrightarrow{p_i}}. \tag{2.4}$$

It is worth taking a pause here to understand the implications of the above equation. Firstly, we have moved from the deterministic description into a probabilistic one which is by no means simpler than the former. Secondly, the Liouville equation is a representation of the Liouville theorem which states that the phase space can change its shape but not its volume under Hamiltonian evolution. This means that given an initial system, the particles can spread out and occupy more physical space but will have a smaller velocity space or the particles can compress to occupy less physical space but then, will have a larger velocity space. In other words, a spread system will have a nearly uniform velocity whereas a compressed system will have a more random spread of velocities.

The probabilistic description is still complex since we are now dealing with a function with $\sim O(10^{23})$ variables. Further simplification is only possible through the relaxation of the high dimensionality of the probability density, $f$. For a distribution function whose dimensionality is relaxed up to $n$ particles, the system of equation can be expressed by a $n(< N)$ particle Liouville equation and a correction term to account for the remaining terms. Thus,

$$\left( \frac{\partial f_n}{\partial t} \right) = \{H_n, f_n\} + \sum_{i=n+1}^{N} \int \frac{\partial U(\overrightarrow{r_i} - \overrightarrow{r_{n+1}})}{\partial \overrightarrow{r_i}} \cdot \frac{\partial f_{n+1}}{\partial p_i} d^3 r_{n+1} d^3 p_{n+1}, \tag{2.5}$$

where, the effective $n$-body Hamiltonian includes the external force and interactions between the n particles, i.e.,

$$\{H_n, f_n\} = \sum_{i=1}^{N} \left( \frac{\overrightarrow{p_i^2}}{2m} + V(\overrightarrow{r_i}) \right) + \sum_{i<j \leq n} U(\overrightarrow{r} - \overrightarrow{r_j}). \tag{2.6}$$

Thus, for $n = 1$,

$$\left( \frac{\partial}{\partial t} + \frac{\overrightarrow{p_1}}{m} \cdot \frac{\partial}{\partial \overrightarrow{r_1}} \right) f_1 = \int \frac{\partial U(\overrightarrow{r_1} - \overrightarrow{r_2})}{\partial \overrightarrow{r_1}} \cdot \frac{\partial f_2}{\partial \overrightarrow{p_1}} d^3 r_2 d^3 p_2. \tag{2.7}$$

A closer look will reveal that the evolution of $f_1$ depends on the evolution of $f_2$ which in turn depends on the evolution of $f_3$ and so on resulting in a set of, potentially

$N$ coupled equations known as the Bogoliubov, Born, Green, Kirkwood and Yvon (BBGKY) hierarchy of equations. The solution of the hierarchy in its entirety is an impossible task and even the truncation to a specific order is fraught with difficulties as it is an open system of equations. Identifying, specifying and implementing closure equations is a complex task. The approximation of how deep we must go into the hierarchy to describe a phenomenon of interest is subjective.

One resolution to break this correlated nature of the equation is through the establishment of a relation between the two-particle distribution function and the single particle distribution function expressed as,

$$f_2(\overrightarrow{r}, \overrightarrow{r}, \overrightarrow{p}, \overrightarrow{p_2}) = f_1(\overrightarrow{r}, \overrightarrow{p}) f_1(\overrightarrow{r}, \overrightarrow{p_2}). \tag{2.8}$$

This is called the molecular chaos introduced by Maxwell in 1867 [47] and used by Ludwig Boltzmann [48] in which event it is the renowned 'Stosszhalanstaz' assumption. The assumption states that the velocities of the molecules participating in a collision are uncorrelated *before* and *after* the collision. In other words, the particles move through phase space completely oblivious to the existence of other particles until they collide with them and forget about them immediately after a collision. Thus, the awareness of other particles exists for a time period during which the collision process lasts, i.e. $t_{coll}$.

In the arguments used to justify the molecular chaos assumption, the terms 'before' and 'after' are used quite nonchalantly and this is not as innocuous as it seems, principally because the usage of these terms implies the passage of time. The arrow of time signifies irreversibility and Boltzmann utilizes this property of his equation to put forward the H theorem and prove that entropy of a system inevitably increases. The molecular chaos assumption has been widely viewed as a paradox because the starting point of the derivation was a completely reversible Hamiltonian system of equations whereas, the endpoint is an irreversible equation, not by adding an external element like friction, but by simply assuming uncorrelated particles. The resolution of this paradox put forth by Loschmidt [49] who stated that the particles are not truly uncorrelated after a collision and the assertion that they are is the reason for the irreversibility.

In spite of the paradox and its subsequent resolution, the molecular chaos is by no means a non-physical assumption. It is possible for two particles to be uncorrelated before the collision and then correlate during the collision if these particles then travel for a time $t_{mct}$ (mean collision time) which is much longer than the collision time $t_{coll}$. The particles can lose their correlation during this time and their next collision may be with a completely different particle. Thus, the particles can also be uncorrelated after a collision as per the molecular chaos assumption if,

$$t_{mct} \gg t_{coll}. \tag{2.9}$$

Based on this assumption (eq.2.8), the collision term can be recast as,

$$\frac{\partial f_1}{\partial t} = \{H_1, f_1\} \tag{2.10}$$
$$+ \int \omega(\overrightarrow{p_1}^*, \overrightarrow{p_2}^* \mid \overrightarrow{p}, \overrightarrow{p_2}) \left[f_1(\overrightarrow{r}, \overrightarrow{p_1}^*) f_1(\overrightarrow{r}, \overrightarrow{p_2}^*) - f_1(\overrightarrow{r}, \overrightarrow{p}) f_1(\overrightarrow{r}, \overrightarrow{p_2})\right] d^3p_2 d^3p_1^* d^3p_2^*.$$

This is the Boltzmann equation with scattering function $\omega$ representing the effect of the potential $U$ and $^*$ indicating post collision values. At its core, the Boltzmann equation is a conservation equation for the number density of the gas molecules. Any further simplification is only possible if the nature of the scattering function $\omega$ is known. For a generic potential applied to spherical particles, the scattering function can be simplified through the definition of the differential collision cross section. This approach has lead to the development of many collision models such as the Hard Sphere (HS) [37], Variable Hard Sphere (VHS) [50], Variable Soft Sphere (VSS) [51], Generalized Hard Sphere (GHS) [52] and Generalized Soft Sphere (GSS) [53]. Consider the simplest case of the HS collision model which leads to,

$$\frac{\partial f_1}{\partial t} + \overrightarrow{c} \cdot \frac{\partial f_1}{\partial \overrightarrow{r}} + \overrightarrow{F} \cdot \frac{\partial f_1}{\partial \overrightarrow{c}} = \int \left[f_1(\overrightarrow{r}, \overrightarrow{c}^*) f_1(\overrightarrow{r}, \overrightarrow{c_2}^*) - f_1(\overrightarrow{r}, \overrightarrow{c}) f_1(\overrightarrow{r}, \overrightarrow{c_2})\right] \tag{2.11}$$
$$\left|\overrightarrow{c} - \overrightarrow{c_2}\right| \sigma_d d\Omega d^3 c_2.$$

The first term on the $LHS$ is the change of the molecular number density in a given phase space over a small period of time. The second term on the $LHS$ is the change in the molecular number density due to the move out of the physical space caused by the velocity. The third term of the $LHS$ is the change in the molecular number density due to the move out of the velocity space due to an applied force. The $RHS$ represents the change in the molecular number density due to the inter-molecular collisions. The term accounts for particles exiting a velocity space via collision and particle entering the velocity space via inverse collision.

In their paper in 1954, Bhatnagar [54] put forth a simple model that shifted the focus from attempting to obtain an exact solution to obtaining an approximate solution that would retain and reflect the key qualitative behaviour of the exact solution, thus, promising an insight into the inherent gas dynamics of the described system. A similar mathematical simplification was proposed by Welander [55] contemporaneously. The proposed BGK-W model is expressed as,

$$\frac{\partial f}{\partial t} + c_i \cdot \frac{\partial f}{\partial r_i} + F_i \cdot \frac{\partial f}{\partial c_i} = \frac{f^{eq} - f}{\tau_r} \tag{2.12}$$

The BGK model is the simplest relaxation time ($\tau_r$) approximation model and is extremely powerful owing to the fact that it captures the essence of the collision operator. The collision operator is the process by which a disturbed system returns to equilibrium. This process is modelled as a swarm of molecules moving towards

their equilibrium via relaxation. This is statistically sound reasoning and is physically justifiable as seen by the high-quality results produced by its use.

Although hailed as a mathematical simplification over the original collision operator, the BGK term has a higher degree of non-linearity. It is still more tractable than the triple integral of the Boltzmann equation.

A main cause of concern is the use of a single relaxation parameter $\tau_r$, making it possible to either conserve momentum or energy but not both simultaneously. This is highlighted by showing that the Prandtl number for a monoatomic gas is unity instead of the expected value of $\frac{2}{3}$. Attempts to correct this discrepancy have been made. Popularly, the idea of using multiple relaxation time has been proposed. Other extensions to the single relaxation time approximation have culminated in the development of the BGK-S [56] and ES-BGK model [57]. However, what these models gain in accuracy is lost in simplicity.

The equilibrium solution of the Boltzmann equation is the Maxwell-Boltzmann distribution function. In order to verify this, we reiterate that for equilibrium condition, $f$ must be constant with respect to $t$, $\overrightarrow{r}$ and $\overrightarrow{c}$. This condition is met only if the collision integral is zero implying,

$$f^{eq}(\overrightarrow{r}, \overrightarrow{p_1}^*) f_1^{eq}(\overrightarrow{r}, \overrightarrow{p_2}^*) = f^{eq}(\overrightarrow{r}, \overrightarrow{p_1}) f_1^{eq}(\overrightarrow{r}, \overrightarrow{p_2}). \tag{2.13}$$

This is known as the detailed balance equation. Taking logarithm on both sides, we get,

$$log(f^{eq}(\overrightarrow{r}, \overrightarrow{p_1}^*)) + log(f_1^{eq}(\overrightarrow{r}, \overrightarrow{p_2}^*)) = log(f^{eq}(\overrightarrow{r}, \overrightarrow{p_1})) + log(f_1^{eq}(\overrightarrow{r}, \overrightarrow{p_2})). \tag{2.14}$$

It is clear that the sum of must be conserved before and after collision. We know that the conserved quantities are mass, momentum and energy. It follows that for $log(f)$ to be conserved, it must be a function of mass, momentum and energy.

Therefore,

$$f^{eq} = \frac{N}{V} \left( \frac{\beta}{2\pi m} \right)^{\frac{3}{2}} e^{\frac{-\beta(\overrightarrow{c} - \overrightarrow{u}^b)^2}{2}}, \tag{2.15}$$

which is the Maxwell—Boltzmann distribution $f_{mb}$ with a stream velocity $\overrightarrow{u}^b$ if we relate $\beta$ to the inverse temperature.

Local distributions are functions of the position and the streaming term does not vanish. However, note that even for local distributions, the collision integrals vanish. This is because of the spatial independence of the collision operator arising from the local nature of the collision and its short time period.

The microscopic world is one of constant change. Even in an equilibrium state, the particles are constantly in motion and participating in collisions which moves them out of the equilibrium state. However, the excited particles relax to the original equilibrium state at time scales associated with the microscopic scale. Macroscopic observation is

based on the average measure of the behaviour of the microscopic states. A change that relaxes in a microscopic time scales does not register in the average and thus, to a macroscopic observer, the state remains in equilibrium.

However, a significant microscopic disturbance that relaxes over a macroscopic time scale will be detected and represented by the macroscopic average and these macroscopic averaged properties will slowly converge towards equilibrium. The properties commonly scrutinized at the macroscopic scale are the hydrodynamic properties of density, velocity, and temperature principally because they are associated with the macroscopic conservation laws of mass, momentum, and energy.

The Boltzmann transport equation is one of the important results that can be derived from the Boltzmann equation and is pivotal in connecting the microscopic considerations evaluated thus far to the macroscopic perspective. Consider an arbitrary variable $Q$ such that $Q = Q(\overrightarrow{r}, \overrightarrow{c})$. In order to find the transport characteristics of $Q$, we multiply the Boltzmann equation (eq.2.11) by $Q$ and integrate over the whole velocity space. This results in

$$\int Q(\overrightarrow{r}, \overrightarrow{c}) \left( \frac{\partial f_1}{\partial t} + \overrightarrow{c} \cdot \frac{\partial f_1}{\partial \overrightarrow{r}} + \overrightarrow{F} \cdot \frac{\partial f_1}{\partial \overrightarrow{c}} \right) d^3c = \int \int \int Q(\overrightarrow{r}, \overrightarrow{c})(f_1^* f_2^* - f_1 f_2) \left| \overrightarrow{c_2} - \overrightarrow{c_1} \right| \sigma d\Omega d^3c_1 d^3c. \tag{2.16}$$

If $Q$ is a conserved quantity then the $LHS$ must not lead to any change in the value of $Q$ and the process must only be one of transport. Thus,

$$\int Q(\overrightarrow{r}, \overrightarrow{c}) \left( \frac{\partial f_1}{\partial t} + \overrightarrow{c} \cdot \frac{\partial f_1}{\partial \overrightarrow{r}} + \overrightarrow{F} \frac{\partial f_1}{\partial \overrightarrow{c}} \right) d^3c = 0. \tag{2.17}$$

This naturally implies that,

$$\int \int \int Q(\overrightarrow{r}, \overrightarrow{c})(f_1^* f_2^* - f_1 f_2) \left| \overrightarrow{c} - \overrightarrow{c_1} \right| \sigma d\Omega d^3c_1 d^3c = 0. \tag{2.18}$$

This means that the variable $Q$ can be chosen such that it does not change with collision and is thus a collisional invariant.

An average can be defined as,

$$\langle Q \rangle = \frac{\int Q(\overrightarrow{r}, \overrightarrow{c}) f(\overrightarrow{r}, \overrightarrow{c}, t) d^3c}{\int f(\overrightarrow{r}, \overrightarrow{c}, t) d^3c}. \tag{2.19}$$

Under this definition of an average, the starting point of this derivation is the averaged form of the Boltzmann transport equation expressed as,

$$\frac{\partial \langle nQ \rangle}{\partial t} + \frac{\partial \left\langle nQ \overrightarrow{c} \right\rangle}{\partial r} - n \left\langle \overrightarrow{c} \cdot \frac{\partial Q}{\partial r} \right\rangle - n \left\langle \overrightarrow{F} \cdot \frac{\partial Q}{\partial \overrightarrow{c}} \right\rangle = 0. \tag{2.20}$$

Here, the property $Q$ is an arbitrary function that is a collision invariant and can

take on the values of $Q = \left\{1, m\overrightarrow{c}, \frac{1}{2}m(\overrightarrow{c} - \overrightarrow{u}^b)^2\right\}$. Each of these values are considered separately and it is seen that the resulting outcomes are the conservation of mass, momentum and energy respectively.

1. Mass Conservation ($Q = 1$) :

   Using this relation in eq.2.20, we get,

$$\frac{\partial \rho}{\partial t} + \frac{\partial \rho \overrightarrow{u}^b}{\partial \overrightarrow{r}} = 0; \qquad \rho = m\left\langle n(\overrightarrow{r}, t)\right\rangle; \qquad \overrightarrow{u}^b = \left\langle \overrightarrow{c} \right\rangle, \tag{2.21}$$

   with the zeroth and first moment of $f$ defined as,

$$n(\overrightarrow{r}, \overrightarrow{c}) = \int f(\overrightarrow{r}, \overrightarrow{v}, t) d^3v \tag{2.22}$$

   and

$$\overrightarrow{u}^b = \left\langle \overrightarrow{c} \right\rangle = \int \overrightarrow{c} f(\overrightarrow{r}, \overrightarrow{c}, t) d^3c. \tag{2.23}$$

2. Momentum Conservation ($Q = m\overrightarrow{c}$) :

   Using this relation in eq.2.20, we get,

$$\left(\frac{\partial}{\partial t} + u_j^b \frac{\partial}{\partial r_j}\right) \rho u_i = \frac{\rho}{m} F_i - \frac{\partial P_{ij}}{\partial r_j}. \tag{2.24}$$

   Here, the term $\rho\overrightarrow{u_i}$ is the momentum and the conservation of the momentum is ensured by satisfying the above equation. However, the equation involves the term $P_{ij}$ that is the second moment of $f$ defined as,

$$\begin{aligned} P_{ij} = P_{ji} &= \rho \left\langle \left(\overrightarrow{c_i} - \overrightarrow{u_i}^b\right)\left(\overrightarrow{c_j} - \overrightarrow{u_j}^b\right) \right\rangle \\ &= \int \left(\overrightarrow{c_i} - \overrightarrow{u_i}^b\right)\left(\overrightarrow{c_j} - \overrightarrow{u_j}^b\right) f(\overrightarrow{r}, \overrightarrow{c}, t) d^3v. \end{aligned} \tag{2.25}$$

   This term is analogous to the macroscopic pressure and is defined by thermodynamics as,

$$P_{ij} = nk_BT\delta_{ij}, \tag{2.26}$$

   where, $\delta_{ij}$ is Kronecker delta function with $\delta_{ij} = 1$ if $i = j$, else $\delta_{ij} = 0$.

3. Energy Conservation ($Q = \frac{1}{2}m(\overrightarrow{c} - \overrightarrow{u}^b)^2$) :

   Using this relation in eq.2.20, we get,

$$\rho\left(\frac{\partial}{\partial t} + u_i \frac{\partial}{\partial r_i}\right) k_BT + \frac{2}{3}\frac{\partial q_i}{\partial r_i} + \frac{2}{3} m\Pi_{ij} P_{ij} = 0. \tag{2.27}$$

We now define the strain rate tensor $\Pi_{ij}$ as,

$$\Pi_{ij} = \frac{1}{2}\left(\frac{\partial u_i}{\partial r_j} + \frac{\partial \overrightarrow{u_j}^b}{\partial r_i}\right) = \rho\left\langle\left(\overrightarrow{c_i} - \overrightarrow{u_i}^b\right)\left(\overrightarrow{c_j} - \overrightarrow{u_j}^b\right)\right\rangle$$
$$= \int\left(\overrightarrow{c_i} - \overrightarrow{u_i}^b\right)\left(\overrightarrow{c_j} - \overrightarrow{u_j}^b\right) f(\overrightarrow{r}, \overrightarrow{c}, t) d^3v.$$

This equation demonstrates the conservation of energy. As with the previous conservation laws, the term $q_i$ is unknown that makes the equation open and unsolvable.

$$q_i = \frac{1}{2} m\rho\left\langle (c_i - u_i^b)(\overrightarrow{c} - \overrightarrow{u}^b)^2\right\rangle = \int (c_i - u_i^b)(\overrightarrow{c} - \overrightarrow{u}^b)^2 f(\overrightarrow{r}, \overrightarrow{c}, t) d^3c. \quad (2.28)$$

To close this system of equations, the terms $n, \overrightarrow{u}, P_{ij}, \Pi_{ij}, q_i$ have to be determined which requires the knowledge of $f$, the evolution of which is governed by the Boltzmann equation. The solution of the Boltzmann equation is immensely difficult owing to the scope of the collision integral.

The principal idea involves the expansion of the distribution function using appropriate expression and then, isolating the important terms while neglecting the unimportant ones with the intention of simplifying the system. Expansions such as Grad's [58] have been used to develop a system of equations with moments of the distribution function. Accordingly, the distribution function is expressed as a series using Hermite polynomials in three independent variables as,

$$f = f_0\left(a^{(0)}H^{(0)} + a_1^{(1)}H_1^{(1)} + ...\frac{1}{N!}a_{1...N}^{(N)}H_{1...N}^{(N)} + ...\right), \quad (2.29)$$

where, $a^{(i)}$ are the co-efficients of the expansion and $H^{(i)}$ are the Hermite polynomials.

For cases close to equilibrium, the critical idea is to restrict the expansion to the $1^{st}$ order leading to the Chapman-Enskog expansion which expands the single-particle distribution function around the equilibrium distribution function with perturbation $k$ using the Taylor series. Thus,

$$f = f_0(1 + k\varphi_1 + k^2\varphi_2 + ..), \quad (2.30)$$

where, $\varphi_n$ is the $n^{th}$ derivative of the distribution function $f$.

Retention of higher orders of $k$ functions leads to a progressively higher scale of hydrodynamic equations known as the extended hydrodynamics equations such as Burnett and super-Burnett equations. More information about these can be found in literature [59, 60]. The discussion of these equations, while interesting, is beyond the scope of this thesis.

Brevity has been implied in the writing of this review of the kinetic theory and part of the reason is the belief that there is no reason to reinvent the wheel. The references

provided [61,62] are an immense cache of knowledge and serves to fill in the gaps created by excluding algebraic procedures. The evolution of the governing equations can be adequately represented by the flowchart shown in fig.2.1.

### 2.2.2 Numerical methods

The Hamiltonian description is the most fundamental description of a system of particles and is related to Newton's $2^{nd}$ equation of motion. The principle of a Molecular Dynamics (MD) simulation is the integration of the equations of motion of N particle system to determine the dynamical trajectory, namely,

$$m_i \frac{\partial^2 r_i}{\partial t^2} = F_i = -\frac{U(r_1, r_2, ...r_N)}{r_i}. \tag{2.31}$$

The primary facets of the method are the determination of the initial system of molecules, the definition of the force term $F_i$ and the integration of the equation. The set of initial conditions is in the form of positions and velocities. For a disordered system, the positions can be generated randomly whereas, the velocity of each particle is assigned randomly from a Maxwellian distribution centred on the desired temperature and then they are adjusted in order to initialize (set to zero) the angular momentum and the center of mass velocity of the total system. A good model to represent the forces acting between particles either from electronic structure calculations or from using empirical force fields is then necessary. Often, the most basic of these potentials namely, the Lennard-Jones potential is considered. The development of complex intramolecular potentials is a difficult scientific process and is an active field of research. It is possible to obtain analytical expressions for some types of forces as demonstrated in Allen and Tildesley [63].

The resulting system of $N$ coupled second-order non-linear differential equations cannot be solved exactly and recourse to numerical integration advanced over small time steps is taken. Apart from the simplest Taylor expansion, many efficient, stable and reasonably accurate algorithms such as Verlet, velocity Verlet, and leapfrog have been proposed. Predictor corrector type methods for integration have also seen development in this field. An extensive discussion of the merits and demerits of the various algorithms is given in Berendsen [64]. Depending on the nature of the simulation the temperature and pressure are can be held constant using thermostats [65] and barostats [66].

The incorporation of MD into the field of simulations was a foregone conclusion with studies in the condensed matter going as far back as the 1950s with research conducted by Metropolis [67] and Alder and Wainwright [68]. The rise in due to the advent of digital computers, because the very essence of molecular dynamics is performing heavy computations involving simple operations repeated a large number of times. There is a vast number of good software to perform MD simulations available in the public domain. Some general, reliable and popular programs worth mentioning are DL_POLY [69],

NAMD [70], LAMMPS [71], Gromacs [72], GULP [73], CHARMM [74], AMBER [75] to name a few. Visualization of the simulation configurations or trajectories include VMD [76], gOpenMol [77] among others.

Molecular dynamics is a promising method owing to its roots being in the fundamental and unassailable first principles. However, the method is inapplicable to the present study subject owing to a number of its unavoidable pitfalls. One of these is the computational cost associated with the high-pressure environments in gas reservoirs affecting the choice of the time step. The choice is a tricky one because a very small one, while accurate, will lead to large computational times whereas, a large time step will cause fluctuations in the conserved quantities. Furthermore, as mentioned in Allen [78], no matter how accurate the integrator algorithm, a large-duration MD simulation will be subject to Lyapunov instability which essentially states that an error in the trajectories grows exponentially. This implies that the surface effects need to be predicted accurately which is impossible since the interaction potential between the rocks and gas molecules is not an established science and speculation will only lead to less dependable results. Finally, although MD is deterministic in its treatment of system evolution, the microscopic nature of the method requires the procurement of macroscopic results through statistical sampling thereby inevitably victimizing it to statistical noise.

The Boltzmann equation represents the dynamics of a complex system whose analytical solution is difficult to obtain except for the most trivial of cases, but even these instances are subject to simplifying assumptions. The difficulties faced with obtaining analytical solutions paved the way to the development of numerical solutions. Numerical simulation method ideologies bifurcate further into either deterministic or stochastic methods.

Among the deterministic classification, the most popular method is the discrete ordinate method or Discrete Velocity Method (DVM) introduced by Broadwell [36]. The principle behind DVM is the discretization of physical space into nodes and the infinite velocity space into a few chosen velocity values allowing the Boltzmann equation to be replaced by a set of non-linear hyperbolic differential equations. The number of equations in this set depends on the number of discrete velocities $N_v$ and the collision term involves a double summation over the velocity points [79, 80]. The Boltzmann-BGK equation without an external force can be written as,

$$\frac{\partial f(c_i)}{\partial t} + c_i \cdot \frac{\partial f(c_i)}{\partial r} = \nu(f_{eq}(c_i) - f(c_i)); \qquad f(c_i) = f(r, c_i, t); \quad i = 1, ..., N_v. \tag{2.32}$$

This equation is often referred to in the literature as the Discrete Velocity Boltzmann Equation (DVBE). Traditional DVM methodology would employ numerical quadrature rules to integrate the moments of the distribution function approximately to yield macroscopic variables. However, the simplicity and utility afforded by the DVBE have led to the development of a large class of methods that fall within the category of DVM

methods. Schemes such as Finite Volume Method (FVM) [81] or Finite Difference Method (FDM) [81] are often employed as exhibited by Yang [82]. Specifically, the use of the FVM to discretize the DVBE is the principal ideology behind the Unified Gas Kinetic Scheme (UGKS) [83, 84] and the Discrete Unified Gas Kinetic Scheme (DUGKS) [85, 86]. In the UGKS, the flux of distribution function is computed by applying the local integral solution of the DVBE, while in the DUGKS, this flux is calculated by using the characteristic solution of the equation. In addition, in the UGKS, the conservative variables at the cell center are computed by marching the macroscopic governing equations in time.

Historically, the Lattice Boltzmann Method (LBM) is a tamer implementation of the extremely over-optimistic Lattice Gas Cellular Automata (LGCA) [87,88] although LBM can be derived independently from the Boltzmann equation in the limit of low Mach numbers. LBM's dependence on the discrete velocities often results in it being considered as a special form of the DVM [89]. Conceptually, the LBM is referred to as a pseudo-particle approach allowing the implementation of the time integration of the Boltzmann equation as a sequence of particle streaming along with lattice connections and collision processes at lattice nodes. LBM is intended to seek a minimal set of velocities and discrete distribution function in the particle velocity space rather than directly use the complete Maxwellian distribution function. The set of discrete velocities and the corresponding equilibrium distribution functions definitions determine the LBM model. For high-order LBM models obtained by using high-order Hermite expansion to the Maxwellian distribution function, discrete velocities are chosen through the application of the Gauss-Hermite quadrature.

The common concern for all methods employing a discrete set of velocities is the appropriate choice of the number of discrete velocities and spatial discretization. High rarefaction demands a large number of discrete velocities to accurately represent the rarefaction effects whereas, near-continuum systems are more demanding of the spatial discretization. Either way, DVM methods are forced to contend with the simultaneous solution of a large number of equations. While the increase in modern computational power has nourished the growth of many efficient DVM schemes [90], the number of discrete velocities cannot be changed once set forcing either usage of a superfluous set of discrete velocities or a means of determining the required number of discrete velocities *a priori*. This issue is exacerbated in the multi-scale flows of porous media. In addition to this, LBM's lattice boundedness relegates the method to continuum flows. Recent times have witnessed the extension of the method to rarefied flows. Off-lattice implementations have been investigated although, in their quest for an extension, they usher in interpolation methods and their associated host of issues. The low-speed nature of the current flows of interest requires LBM models to choose the Gauss-Hermite quadrature carefully as it directly affects the methods ability to capture the non-equilibrium effect in low-speed flows [91].

The Direct Simulation BGK (DSBGK) [92–94] in many ways is an alleviation of the

lattice bound-nature of the LBM. The DSBGK method seems to be a combination of the LBM and particle-based approach [95]. The central idea of the DSBGK is to track down the evolution of $f$ along enormous molecular trajectories at constant velocities which are selected randomly when simulated molecules are generated or reflected at the boundaries. The DSBGK has demonstrated capabilities of simulating pore-scale Shale gas flows [96, 97] and is a potential field of research.

The hydrodynamic systems are strong contenders with their vast store of literature, arsenal of solvers and research to extend their viability to higher rarefaction regimes through the extension of the slip boundary conditions to higher orders or the use of beyond Navier-Stokes hydrodynamics systems such as the Burnett and super-Burnett equations. However, these attempts have met with considerable stability issues and the extension of the slip conditions is suspicious owing to the ambiguity in the determination of the slip coefficient. At present, it is unlikely for such methods to ever be successfully employed in the low-speed rarefied environs of porous media.

Attempts at obtaining the solution to the Boltzmann equation through stochastic means have also flourished. The first successful method for direct numerical solution of the Boltzmann equation was introduced in a series of papers by Nordsieck and Hicks [98]. They dealt with one-dimensional steady flow problems and noted that though a conventional analytical integration of the five-dimensional integral would be expensive, the use of statistical sampling to mimic the realistic statistical collision phenomena would be immensely practical. This paved the way for the direct simulation Monte Carlo (DSMC) which is the brainchild of the late Prof. Bird [37] and, since its inception in 1967, has enjoyed widespread popularity and has established itself as a prevalent method in high speed rarefied gas flows ubiquitous in space exploration applications. The method derives its strength from the physical simulation of the Boltzmann equation by employing a set of representative particles to emulate the physical effects. Its particulate nature allows a natural treatment of the advection while the stochastic nature allows probabilistic treatment of collision in the entire velocity space. The method satisfies the convergence condition by demonstrating a solution that approaches and agrees with the Boltzmann equation solution in the limit of an infinite number of particles as presented by Wagner [99].

Standard DSMC employs a few assumptions and non-violable conditions for obtaining accurate results. A key assumption is the ability to represent a distribution function by a set of simulated particles,

$$f(x,c) = mN_{eff} \sum_{i=1}^{N} \delta^3 (x - x_i)\, \delta^3 (c - c_i)\,, \tag{2.33}$$

where, each particle represents $N_{eff}$ number of physical particles and $\delta$ is Kronecker delta.

Each of the simulated particles is assigned a velocity drawn from the distribution

function and is distributed in a randomly selected position in physical space. Enforcing collision between neighbours is a critical component of DSMC and is ensured by discretization of the physical domain into cells in accordance with the condition,

$$\Delta x < \frac{\lambda}{3}, \tag{2.34}$$

where, $\lambda$ is the mean free path and $\Delta x$ is the cell dimension.

The second assumption is based on the fact that DSMC is an explicit time marching method and the time step chosen allows the splitting of the Boltzmann transport equation into two decoupled operations, namely, advection and collision which coincide with the processes depicted on the $LHS$ and $RHS$ of the Boltzmann transport equation as shown,

$$\frac{\partial f}{\partial t} + c \cdot \frac{\partial f}{\partial x} + F \cdot \frac{\partial f}{\partial c} = 0; \qquad \left(\frac{\partial f}{\partial t}\right)_{coll} = 0. \tag{2.35}$$

The above operator splitting is valid only if the time step satisfies the condition,

$$t_{coll} << \Delta t < t_{mct}. \tag{2.36}$$

The procedure for DSMC is through the definition of an initial state that is adequately represented by distributing particles in the domain with drawing velocities from a chosen distribution function through efficient methods like Box-Muller (refer Appendix C of Bird, 1994 [37] for illustration in the present context). The time integration is implemented by repeating the advection and collision processes. Sufficient samples are generated to obtain macroscopic properties with the least statistical uncertainty. The 5 major steps are enumerated below accompanied by a brief description.

1. The collisionless advection step:

   It is reasonable to assume that the particles can move without interacting with any other particle as long as the gas is dilute and the time step condition is satisfied. In the absence of an external force, the process is simply an update of the particle's position as,

   $$x_i\left(t + \Delta t\right) = x_i\left(t\right) + c_i\left(t\right)\Delta t. \tag{2.37}$$

2. Boundary interaction:

   This process is an integral part of the advection process outlined previously. It deals with situations where particles encounter either domain boundaries or obstacle surfaces. The effect is often the reintroduction of the particles into the domain with modified velocity or internal energy. The nature of the modification depends on the gas-surface interaction model, the simplest of which is the fully specular or fully diffusive models [100].

3. Indexing:

   This is a process that precedes the collision process and essentially locates and assigns each simulated particle to a spatial cell. The particle's position, and consequently the spatial cell, is changed in the previous two processes creating the need for this update process. The proper linking of particles with their cells is needed to ensure the proper selection of a collision pair in the collision step.

4. Collision step:

   The collision step integrates $\frac{df}{dt}_{coll}$ term is each cell in a probabilistic manner by selecting a valid collision pair and performing collision based on an acceptance-rejection rule. In order to adequately capture the effects of collision, sufficient particles must exist within the collision cell. Research has revealed that the optimum number is in the anywhere between of 15 to 20 particles with a minimum of 10 ( [101], [37]). The number of collisions that must be performed is not known in the Time Counter scheme [102] that was initially introduced. The currently prevalent No-Time-Counter scheme [103], however, has this knowledge *a priori*.

5. Property evaluation:

   DSMC is reliant on averaging the generated samples in order to produce the macroscopic hydrodynamic variables of interest. The sampling volume must contain sufficient particles to ensure a steady, reliable average. Often times, the collision cells themselves are utilized as sampling cells although it is possible to define a separate sampling cell structure for the same domain. The hydrodynamic properties are evaluate as shown below,

$$\rho = \frac{mN_{eff}}{\Delta V} N_{cell}, \tag{2.38}$$

$$\rho u = \frac{mN_{eff}}{\Delta V} \sum_{i \in N_{cell}} c_i, \tag{2.39}$$

$$P + \rho uu = \frac{mN_{eff}}{\Delta V} \sum_{i \in N_{cell}} c_i c_i, \tag{2.40}$$

$$\rho \left(3RT + u^2\right) = \frac{mN_{eff}}{\Delta V} \sum_{i \in N_{cell}} c_i^2, \tag{2.41}$$

$$2\left(q + P \cdot u\right) + \rho \left(3RT + u^2\right) u = \frac{mN_{eff}}{\Delta V} \sum_{i \in N_{cell}} c_i c_i^2. \tag{2.42}$$

The rapid evolution of the DSMC through the implementation of new models for gas-surface interaction such as Maxwell accommodation model and the Cercignani-Lampis-Lord model [104–106], collision models and speed up through parallel implementation stand as a testament to its popularity. The method's innate ability to capture

non-equilibrium phenomena like shocks, expansion fans and the like justifies its wide usage. DS1V, DS2V, and DS3V are the original DSMC programs written by the late Prof. G.A. Bird [107,108]. dsmcFoam [109] is a DSMC solver for 2D and 3D flows that is developed as part of the open-source CFD package OpenFOAM. MONACO [110] is a solver developed by Boyd at the University of Michigan, Ann Harbor. PI-DSMC [111] is a commercial software package for 2D and 3D flows. SMILE [112] is a general-purpose 2D/3D parallel DSMC software system developed since 1998 by the Computational Aerodynamics Laboratory at the Khristianovich Institute of Theoretical and Applied Mechanics, Siberian division of the Russian Academy of Sciences. DAC [113] is a general-purpose DSMC code developed by NASA at the Johnson Space and Langley Research Centers. MGDS [114] is a fully 3D DSMC solver incorporating three-level adaptive mesh refinement and a cut cell algorithm developed by Schwartzentruber's group at the University of Minnesota. Stochastic PArallel Rarefied-gas Time-accurate Analyzer (SPARTA) [115] is a parallel implementation of DSMC in 2D and 3D enviroments developed and tested under the auspices of Sandia National Laboratories, USA and available to the public through their website [116]. Molflow [117] is a 3D DSMC simulator currently developed at CERN for the simulation of free molecular flow systems. SACRED is a solver developed by NFS labs at IITK by the author under the guidance of Kumar [118].

The method is not without its limitations. While the method excels in regions of high non-equilibrium, it suffers when the system's deviation from equilibrium is small i.e. near-equilibrium flows. DSMC is a stochastic method and relies heavily on the ability to obtain a sufficient number of representative samples to divine the macroscopic properties. While sufficiently attainable in high-speed rarefied flows, this task is the bane of DSMC in the low-speed rarefied flows. The low signal-to-noise nature of the flows of interest forces the need of an inordinate number of samples and leads to an expensive computation.

Attempts to extend the method to low speed rarefied flows have been made with varying degrees of success. Fan [38] developed a variant of DSMC known as the Information Preservation DSMC abbreviated as IP-DSMC. Improvements were effected on IP-DSMC by Sun [119] and Cai [120]. The foundational idea is based on the recognition that in low signal flows, the mean velocity of colliding particles is more significant than the thermal velocity. Thus, a particle is not only aware of its thermal velocity, but also its mean velocity. A collision alters the mean velocity by assigning it as the mass average of its pre-collision value. Although successful for simple problems, its extension to practical applications is hampered by the complexity of storing additional information regarding each of its particles. Its success, though limited, has highlighted the potential utility acquired by treating the deviation from equilibrium separately enabling DSMC to resolve low signal flows. The fallacy of using the terms "inlet" and "outlet" in DSMC simulations of low-speed flows encouraged the inclusion of implicit boundary conditions as demonstrated by studies by Nance [121], White [122] etc.

The idea of capturing the deviation from equilibrium by modification of the simulated particle weight is a notion that has found great support. Accordingly, Chun [123] developed a method where particles representing the equilibrium move and interact alongside particles that represent the deviation a.k.a ghost particles. This method is termed as Low Mach number DSMC abbreviated as LM-DSMC.

The overwhelming success of DSMC is attributable to the ease of implementation, natural treatment of the advection operator, versatility in including various models, the viability of massive parallel implementation and ability to handle complex flow through complicated geometry. The method's elegance is further underlined when considering DSMC achieves all this without resorting to any form of velocity space discretization. Instead DSMC and methods akin to DSMC resort to approximate integration of the Boltzmann equation through Monte Carlo (MC) integration. The MC integration is stochastic and is a victim to statistical errors encouraging the use of variance reduction techniques. DSMC, for example, uses the Importance Sampling (IS) method of variance reduction. Other methods such as control variate, antithetic sampling, etc. exist.

One recent solution is the implementation of additional variance reduction techniques in tandem with the importance of sampling utilized in DSMC. Such ideologies have been presented in a large number of recent literature [39–41, 43, 44, 124–132] and have been found to be of great utility especially in the near continuum flows. This is the ideology adopted in the current work and will be explored in detail in the pertinent chapter (3).

The central idea of DSMC and any method akin to DSMC is the integration of a function by Monte Carlo methods. The standard MC integration of a function $y(r)$ over a region $R$ can be performed by approximating,

$$\int_R y(r)dr = V_R \langle y \rangle \approx \frac{V_R}{N} \sum_{i=1}^{N} y(r_i), \tag{2.43}$$

where, $N$ is the number of samples, $V_R$ is the volume of region $R$, $r_i$ is a randomly chosen candidate.

The value of $r_i$ is chosen from a uniform probability distribution function. The statistical nature of the MC integration leads to uncertainties in the result which can be stated as,

$$\sigma_y = V_R \sqrt{\frac{\langle y^2 \rangle - \langle y \rangle^2}{N}}. \tag{2.44}$$

The uncertainty is an undesirable feature of the MC integration and steps are often taken to reduce it. A simple technique, evident from eq.2.44, is the increase in the number of sample points, $N$. Though effective, this method leads to an increase in the computational cost as more $r_i$ needs to be drawn from the uniform distribution function over $R$.

Also evident from the eq.2.44 is the idea of decreasing the numerator, i.e $\sqrt{\langle y^2 \rangle - \langle y \rangle^2}$

which is the variance and techniques associated with this are called the variance reduction techniques. Many such techniques have been introduced in literature and a detailed description of these can be found in various resources. In the present context, two such methods are of great relevance and will be discussed below. First, the importance sampling technique is introduced followed by the control variate technique.

In the **importance sampling** technique, the idea is to focus and draw samples from regions which are more significant. To this end, the selection of $r_i$ is not done based on a uniform distribution function, but rather a non-uniform distribution function. This is achieved by defining a normalized probability $p$ over the region $R$ and selecting sample points $r_i$ based on his probability. The mathematical form is shown below,

$$\int_R y(r)dr \approx \frac{V_R}{N} \sum_{i=1}^{N} \frac{y(r_i)}{p(r_i)} \sum_{i=1}^{N} p(r_i). \tag{2.45}$$

If we choose it as,

$$\sum_{i=1}^{N} p(r_i) = \frac{1}{V_R}. \tag{2.46}$$

Then the equation simplifies to,

$$\int_R y(r)dr \approx \frac{1}{N} \sum_{i=1}^{N} \frac{y(r_i)}{p(r_i)}. \tag{2.47}$$

The corresponding statistical uncertainty is given by,

$$\sigma_y = V_R \sqrt{\frac{\left\langle \frac{y}{p}^2 \right\rangle - \left\langle \frac{y}{p} \right\rangle^2}{N}}. \tag{2.48}$$

The improvement in the statistical certainty depends on the non-uniform probability distribution $p$. An improvement over the standard MC method is seen only if,

$$\left\langle \frac{y}{p}^2 \right\rangle - \left\langle \frac{y}{p} \right\rangle^2 < \left\langle y^2 \right\rangle - \langle y \rangle^2 . \tag{2.49}$$

It is also important that $p$ be a distribution function from which samples can be generated quickly and efficiently. Another variance reduction technique outlined here is the **control variate** method. In this method, the function to be integrated can be rewritten as a sum of two integrals where one part is analytically obtainable and the other is solved through a MC integration. The process in mathematical form is,

$$\int_R y(r)dr = \int_R z(r)dr + \int_R \big[y(r) - z(r)\big]\, dr. \tag{2.50}$$

The method's efficiency depends on the existence of a function $z$ that can be analytically computed while also ensuring that samples can be drawn from the remaining function,

$\big[y(r) - z(r)\big]$, with ease. The choice of $z$ should also be such that the value of the remaining function is small since if it is large, then any improvement obtained from this method may be negated.

It is possible to apply multiple variance reduction techniques to the same MC integration problem. A formulation that combines the **importance sampling and control variate** techniques can be expressed as,

$$\int_R y(r)dr = \int_R z(r)dr + \frac{V_R}{N}\sum_{i=1}^{N}\frac{\big[y(r_i) - z(r_i)\big]}{p(r_i)}; \tag{2.51}$$

$$\sigma_y = V_R\sqrt{\frac{\left\langle \frac{y-z}{p}^2 \right\rangle - \left\langle \frac{y-z}{p} \right\rangle^2}{N}}. \tag{2.52}$$

A pictorial synopsis of the above monograph is presented in the fig.2.1.

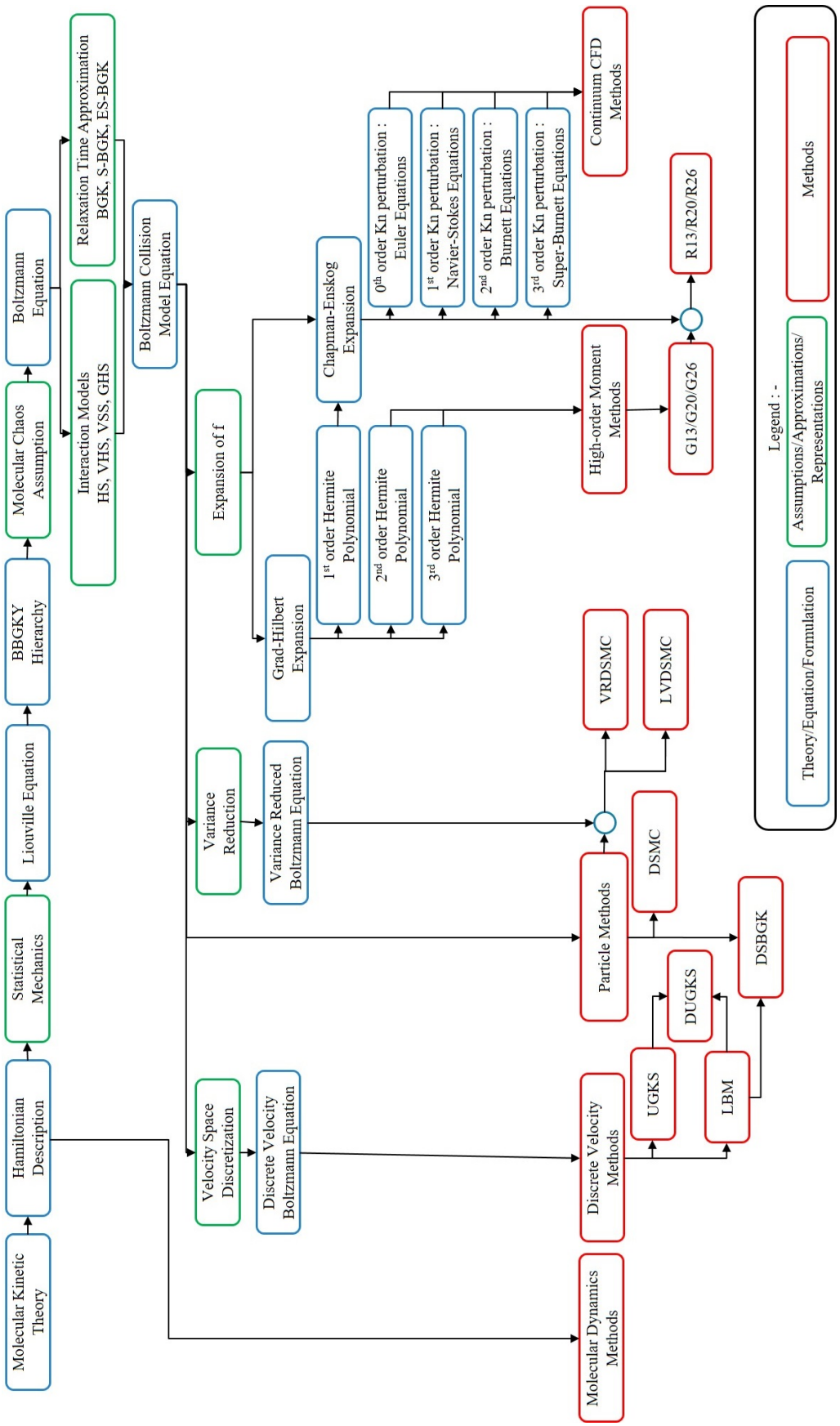


Figure 2.1: Flowchart depicting the evolution of the various systems of governing equation and associated numerical methods.

## 2.3 Introductory formalisms

The terms and concepts frequently used in this thesis are introduced in the following section.

### 2.3.1 Similarity parameters

In the following section, the aim is to characterize the flow likely to be encountered in the micro-scale media. To do so, three well-known similarity parameters are defined.

Firstly, the **Reynolds number** which is a ratio that signifies the relative importance of the inertial and viscous force. A low value of Reynolds number is encountered for low-speed viscous flows while high Reynolds number is associated with high-velocity, low-viscosity flows. At the macroscopic scale, the effect of inertial force is more prominent than the viscous forces; however, the converse is true at microscopic scales. This can be attributed to the fact that the velocity of transport at the microscopic scales is small and, in combination with, the prevalence of wall influence leads to low Reynolds numbers implying laminar flows.

Secondly, the **Mach number** is a dimensionless quantity that describes the local speed of the flow with respect to the speed of sound in that medium. Based on the Mach number, the flows are classified into subsonic, transonic, supersonic and hypersonic flows. Each of these regimes is accompanied by the unique behaviour of the flow and its thermodynamic properties. In the case of micro-scale flows, the velocity is very low and consequently, the Mach number is small. The flows are not subjected to the complicated aero-thermodynamics associated with high-speed flows. The low speeds are the reason for the classification of these flows as low-signal flows.

Finally, the degree of rarefaction of gas is characterized by the **Knudsen number**. It is more commonly defined as the ratio of the mean free path of the gas under the flow conditions to the characteristic length of the flow although an alternate gradient-based definition is also prevalent in literature [37]. The higher the degree of rarefaction, the higher the value of Knudsen number. Another parameter frequently utilized in the rarefied gas dynamics research is the rarefaction parameter often denoted by $\delta$ and is the inverse of the Knudsen number. Mathematically,

$$Re = \frac{\rho \langle u \rangle L_0}{\mu}; \qquad Ma = \frac{u}{a}; \qquad Kn = \frac{1}{\delta} = \frac{\lambda}{L_0}, \tag{2.53}$$

where, $\mu$ is the dynamic viscosity and $L_0$ is the reference length.

Unlike $Re$ and $Ma$, micro-scale flows are capable of exhibiting a wide range of Knudsen numbers. More specifically, porous media are capable of exhibiting multiple regions of different Knudsen numbers in the same scenario. This warrants a closer description as to the effects of the Knudsen number variation.

The Knudsen number-based classification of the flow regimes was first proposed by Schaaf in 1961 [133]. Consequent classifications by Moghaddam [134], Zhang [135]

and Beskok [136] have legitimized this taxonomy of flow regimes. According to this, the gaseous flow regime can be divided into four regimes with each exhibiting unique physical characteristics.

Firstly, the continuum regime is said to exist if the Knudsen number is small. Although, it is believed that the range is $Kn < 10^{-2}$, the breakdown in the thermodynamic equilibrium leads to the suggestion that the range should be $Kn < 10^{-3}$ [137]. In this regime, the continuum hypothesis is valid and the Navier-Stokes set of equations is widely accepted as the governing equation. The walls are treated by the conventional no-slip boundary conditions and the main mechanism of transport is through bulk diffusion.

The second regime extends from $10^{-2} < Kn < 10^{-1}$ and is commonly known as the slip flow regime. In this regime, the effect of the walls on the flow adjacent to it is pronounced and a region of non-equilibrium is observed. This results in velocity at the wall rendering the no-slip boundary condition invalid. Although the Navier-Stokes set of equations remains as the governing equation, its solution can only be regarded as an inner solution for the bulk flow [138,139] and the effect of the walls must be considered as a correction to this solution. This is done through the use of slip models, the most common of which is the first-order slip boundary condition proposed by Maxwell and is sufficient in the slip regime [140].

The transition regime is the third classification and extends from $10^{-1} < Kn < 10$. This is a complex region wherein the transport is dominated by bulk diffusion and surface transport. In the lower reaches of this range, the continuum based Navier-Stokes equation can still be used albeit with second-order boundary conditions. The extension to higher-order boundary conditions is possible, but suspect because the Navier-Stokes equation is first-order accurate in Knudsen number. Higher-order governing equations such as the Burnett and super Burnett equation is applicable to simple flows only. Such approaches are valid up until $Kn < 0.2$. As the $Kn$ increases, the rarefaction effects are more dominant in this regime leading to a breakdown of the continuum hypothesis thereby invalidating the Navier-Stokes set of equations. The governing equation in this regime is the Boltzmann equation the solution of which is extremely complex.

Finally, the fourth regime is flow, wherein $Kn > 10$ and is often referred to as the free-molecular flows. The intermolecular collisions are negligible as compared with the collisions between the gas molecules and wall surfaces. [136,141].

Essentially, the Knudsen can be viewed as a number that characterizes the relative number of intermolecular and molecule wall collision. To this end, a molecule can be redirected either through an intermolecular collision or a molecule wall collision. In the extremes of $Kn$, one of the phenomena dominate. In transition, both these phenomena play an important role and contribute to the overall diffusion. The possibility of co-existence of all the regimes in a porous media calls for a multi-scale analysis increasing the associated challenge.

### 2.3.2 Concepts in porous media

The characterization of porous media is principally based on microscopic factors such as its pore structure, connectivity, and surface area. The field has developed its lexicon with defined parameters to account for these microscopic details.

Principal among these parameters is the **porosity** ($\phi$) which is defined as the volume of pore space to the total volume of a porous media sample. It is a parameter that attempts to signify the fraction of the media that can participate in a flow. However, the realization that pore spaces need not be occupied by a fluid and those occupied could be completely encapsulated by solid phase and thus, unable to influence the flow, has led to the definition of effective porosity or apparent porosity ($\phi_{eff}$). This is defined as the ratio of the volume of pore space participating in the flow to the bulk volume. The porosity is expected to vary between 0 and 1 with 0 signifying occupation by solid phase alone and vice versa. The variation of the effective porosity lies between 0 and the porosity. The mathematical expressions for the above terms are,

$$\phi = \frac{V_f}{V_t}; \quad 0 < \phi < 1 \tag{2.54}$$

and

$$\phi_{eff} = \frac{V_f^{eff}}{V_t}; \quad 0 < \phi_{eff} < \phi, \tag{2.55}$$

where, $V_f$ is the volume of the pore space, $V_t$ is the total or bulk volume and $V_f^{eff}$ is the volume of the pore space accessible to a flow. Diffusion of the fluid through the porous media is a great figure-of-merit for the analysis of porous media and is quantified by the **permeability**. The term was first introduced into literature by Henry Darcy in relation to his hydrological studies pertaining to the supply of water to the fountains in the French city of Dijon in 1856 [142]. Through his studies, Darcy was able to establish a relation between the volume flow rate and the applied pressure gradient and area of flow expressed as,

$$Q \propto \frac{A\left(\Delta P - \rho g z\right)}{L}, \tag{2.56}$$

where, $Q$ is the volume flow rate, $A$ is the cross sectional area of flow, $\Delta P$ is the pressure difference and $\rho g z$ is the pressure of the fluid at a depth of $z$ due to itself.

Subsequent research, such as those by Muskat in 1937 [143], indicated that the flow rate is inversely proportional to the fluid viscosity and thus, the equation is modified to the well known form known as Darcy's law,

$$Q \propto \frac{A\left(\Delta P - \rho g z\right)}{\mu L} = k\frac{A\left(\Delta P - \rho g z\right)}{\mu L}. \tag{2.57}$$

The constant of proportionality $k$ was termed as the permeability and it was assumed to be a representation of the physical aspects of the porous media.

The mathematical similarity of the expression with other phenomenological trans-

port laws such as Ohm's law of electrical resistance, Fick's law of mass diffusion and Fourier's law of heat conduction is evident. In the case of Darcy's law, the flow is driven by the difference in the total energy between two states.

Further studies challenged initially assumed properties of permeability. For one, although the flow is driven in a specific direction by the pressure gradient, flows in other directions can also occur simultaneously. This is especially true for porous media. Under this understanding, permeability is a tensor and is capable of being non-isotropic expressed as,

$$\mathbf{k} = \begin{bmatrix} k_{xx} & k_{xy} & k_{xz} \\ k_{yx} & k_{yy} & k_{yz} \\ k_{zx} & k_{zy} & k_{zz} \end{bmatrix}, \tag{2.58}$$

where,

$$q_x = \frac{-k_{xx}}{\mu}\frac{\partial P}{\partial x}; \quad q_y = \frac{-k_{xy}}{\mu}\frac{\partial P}{\partial x}; \quad q_z = \frac{-k_{xz}}{\mu}\frac{\partial P}{\partial x}, \tag{2.59}$$

$$q_x = \frac{-k_{yx}}{\mu}\frac{\partial P}{\partial y}; \quad q_y = \frac{-k_{yy}}{\mu}\frac{\partial P}{\partial y}; \quad q_z = \frac{-k_{yz}}{\mu}\frac{\partial P}{\partial y}, \tag{2.60}$$

and

$$q_x = \frac{-k_{zx}}{\mu}\frac{\partial P}{\partial z}; \quad q_y = \frac{-k_{zy}}{\mu}\frac{\partial P}{\partial z}; \quad q_z = \frac{-k_{zz}}{\mu}\frac{\partial P}{\partial z}, \tag{2.61}$$

where, $q_i = \frac{Q_i}{A_{jk}}$ is the volume flux.

However, studies such as those by Ghanbarian in 2017 [144] and Guibert in 2015 [145] has demonstrated that the off-diagonal elements are significantly lower than the diagonal elements and are often neglected to transform the permeability into a diagonal matrix, with anisotropy exhibited by $k_{xx} \neq k_{yy} \neq k_{zz}$.

The determination of permeability is of utmost interest in the oil and natural gas industry where it is measured in Darcy units related to the SI system as 1 $darcy = 0.987X10^{-12}m^2$. Although Darcy law finds widespread application in the oil and natural gas industry, its reliability drops remarkably for gas flows. This is because Darcy law was initially developed for liquids and the extension to gases is valid only under the assumption of continuum theory and creeping (viscous, laminar) flows where it is essentially a macroscopic solution of the Stokes equation which neglects the effect of non-linear inertial terms.

In gaseous flow through porous media, the flow undergoes rapid acceleration as it enters a tight porespace and deceleration as it enters a larger porespace. These changes in flow rate causes inertia to become relevant. The inclusion of the non-linearity leads to non-Darcy equations that incorporate inertial effects such as those put forth by

Dupuit [146] and Forchheimer [147] expressed as,

$$\frac{dP}{dx} = \frac{-\mu}{k} q_x - \frac{\rho}{k_{iner}} {q_x}^2. \tag{2.62}$$

where, $k_{iner}$ is the inertial permeability.

Furthermore, gaseous flows in porous media that are rarefied owing to the size of the pore space leading to the gas slippage effect. The rarefaction effects were initially treated as a correction term in the Darcy law. Experimental and numerical results were used to determine phenomenological constants which are then used in empirical formulae based on modification and extensions of the Darcy law to predict the characteristics of the flow. One of the most popular corrections to the Darcy law for rarefied gases was put forth by Klinkenberg in 1941 [148] based on the discrepancies observed in experimental results conducted by them and Muskat in 1937 [143]. As per this correction, the gas permeability($k_g$) (often referred to as apparent permeability($k_a$)) is greater than the liquid permeability($k_l$) (often referred to as the intrinsic permeability($k_\infty$)) by a factor as shown below,

$$k_g (or\ k_a) = k_l (or\ k_\infty) \left(1 + \frac{b}{\overline{p}}\right). \tag{2.63}$$

Alternatively,

$$k_a = k_\infty \left(1 + b' Kn\right), \tag{2.64}$$

where, $b'$ is the equivalent slip factor.

The parameter $b$ is termed as the Klinkenberg constant and is a term that is indicative of the gas slippage effect that causes the discrepancy. Although assumed constant for a long time, recent research by Wu in 2017 [149] has demonstrated that the parameter is capable of variation.

Although a large number of studies have established the viability of the Klinkenberg correction model to study porous media of low permeability containing rarefied gas flows, the truth of is that the model is a linear phenomenological extension and is reliable in a narrow corridor of rarefaction, namely the initial onset of slip. At, higher degrees of rarefactions the apparent permeability varies as a higher order of $Kn$ [150]. Second-order apparent permeability correlation that aims to capture the non-linear relationship between the apparent and intrinsic permeability have been proposed such as those by Tang [151] (eq.2.65). The expression can be written as,

$$k_a = k_\infty \left(a + bKn + cKn^2\right), \tag{2.65}$$

where, $a$, $b$ and $c$ are correlation coefficients.

These models also have their range of applicability and are prone to fail for some porous media configuration. Moreover, a notable demerit of such approaches arises from the dependence of phenomenological constants on experimental results that possess

non-existent prediction capability making it essential to conduct experimental studies for each case specifically.

The correlation between porosity and permeability has been a topic of much interest and considerable work has been carried out to establish accurate models for this relationship. One of the popular models is the Kozeny relation proposed in 1927 [152]. The model is based on the treatment of flow through porous media as Poiseuille flows through a bundle of capillaries that is a popular modelling technique prevalent in porous media studies.

$$k = c_0 \frac{\phi^3}{S^2}, \tag{2.66}$$

where, $c_0$ is the Kozeny constant. $S$ is the specific surface area

The notability of the equation is not in its success to accurately capture the relationship for capillary models of porous media but in its failure to do so in the case of actual complicated porous media [153]. The generalization of the relation was proposed by Carman and is based on the observation that streamlines in complex media are seldom straight and follow tortuous pathways around a solid grain. This leads to the introduction of the concept of **tortuosity** that describes the average elongation of the flow pathway with respect to the free flow. This lead to the, now well-renowned, Carman-Kozeny relation [154] expressed as,

$$k = c_0 \frac{\phi^3}{S^2 \tau^2}; \qquad \tau = \frac{\langle l \rangle}{L} \geq 1 \tag{2.67}$$

where, $c_0 = \frac{1}{\beta}$ is the Kozeny constant $\beta$ is the shape factor.

The determination of tortuosity ($\tau$) is by far one of the most difficult and ambiguous topics of porous media largely due to the contextual nature of its definition. Based on the application, a given porous media can be characterized by geometrical, hydraulic, electrical, diffusional, thermal and acoustic tortuosity. Even a clear mathematical consensus of the definition is unavailable with various literature [154–156] defining it as,

$$\tau = \frac{L_e}{L}; \qquad \tau = \left(\frac{L_e}{L}\right)^2; \qquad \tau = \frac{L}{L_e}; \qquad \tau = \left(\frac{L}{L_e}\right)^2 \quad . \tag{2.68}$$

Modern times has seen the increase in the capabilities of numerical methods leading the computation of tortuosity away from geometric methods such as Bo-ming [157] to those that can be linked to the fluid velocity field. This is not a novel idea, with Carman [155], Koponen [158, 159] and others alluding to such formulations. However, recent contributions have seen that such determination methods are more fundamental. Results by Matkya [160, 161], Duda [162], Nabovati [163] have encouraged the definition of tortuosity as,

$$\tau = \frac{\Sigma u_{mag}}{\Sigma u_x} = \frac{\langle u_{mag} \rangle}{\langle u_x \rangle}. \tag{2.69}$$

Even under the assumption that the tortuosity is defined as eq.2.69, issues arise

regarding the determination of the numerator. The numerator is, by definition, the average path of the fluid particles through porous media. Debates regarding the type of average have been raised with Bear [155] adopting a geometrical average whereas researchers like Clennell [154] opting for a kinematic average.

The result of either approach is to propose a correlation between tortuosity and porosity. Many such correlation have been proposed in literature by researchers like Koponen [158, 159], Nabovati [163], Comiti [164] each with their own fitting parameter making them valid for certain cases; [165] for sandy, [166] for clay.

Transport properties in porous media are influenced by tortuosity almost as much as by permeability. Initially, both these terms were assumed to be geometric properties, However, the flow of rarefied gases through porous media has exhibited that the properties are dependent on the rarefaction of the gases too. Consequently, the determination of the highlighted quantities is of principal interest in the studies conducted as part of this thesis.

There are a number of caveats which concern the validity of the assessment results obtained from the correlations.

The popularity of the usage of correlations especially in the field of porous media is largely attributable to the volume-averaged models that a majority of the numerical methods rely on. Such models (REV and EMA) consist of a large degree of approximations. The ideal scenario would be numerical methods that are capable of simulating the flow physics at the pore-scale level. However such numerical methods are computationally expensive.

Though the correlations are based on approximations, they provide a qualitative understanding of the trends that can be expected in porous media. For example, based on the Carman-Kozeny equation (2.67), the porous media is conducive to flow (i.e. exhibits high permeability) when the porosity is high, tortuosity is low, and exposed surface area is minimal. Based on the Klinkenberg equation (2.64), the permeability is expected to increase with rarefaction whereas, the tortuosity is expected to decrease. The decrease in tortuosity will be indicated by the curvature of the streamlines. Highly tortuous flows will exhibit lower permeability.

However, correlation models for the estimation of permeability and tortuosity are proposed principally due to the inability of volume-averaged model to capture the dynamics at the pore-scale. Such simulations require sophisticated computational methods and efficient solvers which is the ambition of the current work.

## 2.4 Formulation in this research

In the current section, the paradigm under which this research operates is described. The considerations with regards to the governing equations, assumptions involved and formulations are elaborated herein.

### 2.4.1 Governing equation and gas-surface interaction model

The Boltzmann-BGK model equation is chosen to be the governing equation for the present study. This choice is based on the qualitative advantages offered by the method such as the intuitive evolution of the collision term which essentially conveys that the local distribution approaches the equilibrium distribution by the mechanism of collision. The choice has relegated the study to isothermal conditions due to the model's inability to simultaneously simulate viscous and thermal transport (evidenced by unity Prandtl number), but for the present cases, the temperature variation can be deemed to be negligible. Accordingly,

$$\frac{\partial f}{\partial t} + c \cdot \frac{\partial f}{\partial r} + F \cdot \frac{\partial f}{\partial c} = \frac{f^{eq} - f}{\tau_r}, \tag{2.70}$$

where,

$$f^{eq} = n\pi^{-\frac{3}{2}} c_0^{-3} exp\left[-\frac{\|c-u\|^2}{c_0^2}\right], \quad c_0 = c_{mp(0)} = \sqrt{\frac{2K_bT_0}{m}}; \tag{2.71}$$

and $K_b = 1.380649X10^{-23}J/K$. [167]

The gas-surface interaction model employed in this work is the simple Maxwell accommodation coefficient model. This choice over the Cercignani-Lampis-Lord (CLL) model [105, 106, 168] is justified by realizing that the CLL model is principally attuned to the dynamics of gases in high-vacuum where the incomplete accommodation is dominant. In the current flow of interest, the use of CLL model is inappropriate and besides, in the case of actual rock samples, the determination of a single accommodation coefficient is difficult let alone the two employed by the monoatomic CLL model. A popular method frequently used in LBM is the bounce-back boundary condition which is found to be valid in the continuum and near continuum regime. According to this interaction, the particle's reflected path is the same as it's incident path resulting in reflection being a retrace. In the present work, the bounce-back reflection model is implemented but rarely applied.

The simple Maxwell model allows the variation of the accommodation coefficient $\alpha$ between 0 to 1 which can be assumed as an indicator of a smooth, polished surface and a rough surface respectively with intermediate values describing the degree of surface roughness. Molecules interacting with the polished surface are reflected in a specular manner with an angle of reflection equal to the angle of incidence. On the other hand, the interaction with a rough surface is resolved through a diffuse surface reflection wherein, the angle of reflection is determined randomly and the velocity of the reflected particles are randomly drawn from the distribution of the wall. Under the consideration of the diffuse reflection as a rough wall, the understanding is that the particle in entrapped in the roughness and suffers multiple reflections prior to escaping. The multiple interactions result in the complete accommodation of the particle with the wall condition.

From an implementation perspective, a particle interacting with a surface with $\alpha$ is tested against $r$ and is reflected either in a specular manner if $\alpha < r$ or diffusively if $\alpha > r$, where $r$ is a random number $[0, 1]$.

### 2.4.2 Establishing dimensionless quantities and nomenclature

Non-dimensional or dimensionless terms are based on the cardinal rule that two systems of measurement should not be used in the language of sophisticated science. Existence of such systems can cause confusion and lead to extensive damage as evidenced by the incident involving NASA's climate orbiter on $23^{rd}$ September 1999 [169]. By definition, non-dimensionalization is the partial or complete removal of units from an equation involving physical quantities by the suitable substitution of variables. The technique can simplify and parametrize problems. The process is more relevant if the measured quantities do not vary from their reference unit by a large value.

Such a case is a feature of low signal-to-noise ratio flows, wherein the deviation from a defined equilibrium state is small. Contrary to this, flows exhibiting high signal-to-noise ratios such as hypersonic flows stand to be advantaged by the use of dimensional quantities [102]. This is observed in literature through DSMC studies, the results of which are seldom reported in dimensionless quantities. The non-dimensional parameters in the present work are represented by a caret ($\hat{}$) or are marked with a subscript $_{ND}$ denoting non-dimensional.

Mesoscopic methods such as the present one are concerned with the evolution of the distribution function in the phase space. Thus, the first task is the non-dimensionalization of the phase space. Accordingly, the physical coordinates of the phase space are made dimensionless by defining a length $L_0$ termed as the characteristic length of the flow domain. Thus,

$$x_{ND} = \hat{x} = \frac{x}{L_0}; \qquad y_{ND} = \hat{y} = \frac{y}{L_0}; \qquad z_{ND} = \hat{z} = \frac{z}{L_0}. \tag{2.72}$$

The velocity space is non-dimensionalized with respect to the most probable speed of the molecules occupying the phase space. This velocity is represented by $c_0$ (or $c_{mp}$ or $v_{mp}$) and is a function of the temperature and type of gas. Accordingly,

$$u_{ND} = \hat{u} = \frac{u}{c_0}; \qquad v_{ND} = \hat{v} = \frac{v}{c_0}; \qquad w_{ND} = \hat{w} = \frac{w}{c_0}. \tag{2.73}$$

The non-dimensionalization of time follows based of the parameters $c_0$ and $L_0$ as,

$$t_{ND} = \hat{t} = \frac{L_0 t}{c_0}. \tag{2.74}$$

Following the phase space, the hydrodynamic state variables namely, density $\rho$, temperature $T$ and pressure $P$ are non-dimensionalized with respect to a reference state defined by a reference number density $n_0$, temperature $T_0$ and pressure $P_0$. For a

flow consisting of a single species of gas the relation between the number density and density is given by,

$$\rho = mn, \tag{2.75}$$

where, $m$ is the mass of the gas in $kg$.

Thus,

$$n_{ND} = \hat{n} = \frac{n}{n_0}; \quad T_{ND} = \hat{T} = \frac{T}{T_0}; \quad P_{ND} = \hat{P} = \frac{P}{P_0}. \tag{2.76}$$

Additionally, the dependence of most probable velocity $c_{mp}$ and temperature $T$ lead to an alternate non-dimensionalization of temperature, namely,

$$c_{ND} = \hat{c} = \frac{c_{mp}}{c_{mp(0)}} = \frac{\sqrt{T}}{\sqrt{T_0}} = \sqrt{T_{ND}} \tag{2.77}$$

or

$$\hat{c} = \sqrt{\hat{T}}. \tag{2.78}$$

Moreover, the gas used in the current research is assumed ideal leading to the equation of state given by,

$$P = \rho RT = mnRT, \tag{2.79}$$

where, $R = \frac{K_B}{m}$ is the Regnault constant. The non-dimensionalization for pressure can be expressed as,

$$P_{ND} = \frac{P}{P_0} = \frac{mnRT}{mn_0RT_0} = \frac{nT}{n_0T_0} = n_{ND}T_{ND} \tag{2.80}$$

or

$$\hat{P} = \hat{n}\hat{T} \tag{2.81}$$

Using the present non-dimensionalization parameters, the dimensionless form of the distribution function is given by,

$$f_{ND} = \hat{f} = \frac{c_0^3}{n_0} f. \tag{2.82}$$

Applying this to the Boltzmann-BGK equation (eq.2.70) can be written as,

$$\begin{aligned}
LHS \;\; Term\; 1 &: \frac{\partial f}{\partial t} = \frac{\partial \hat{f}}{\partial \hat{t}} \frac{n_0}{L_0 c_0^2}; \\
LHS \;\; Term\; 2 &: c \cdot \frac{\partial f}{\partial x} = \hat{c} \frac{\partial \hat{f}}{\partial \hat{x}} \frac{n_0}{L_0 c_0^2}; \\
LHS \;\; Term\; 3 &: F \cdot \frac{\partial f}{\partial c} = \hat{F} \frac{\partial \hat{f}}{\partial \hat{c}} \frac{n_0}{L_0 c_0^2} \\
RHS \;\; &: \frac{f^{eq} - f}{\tau_r} = \frac{n_0}{\tau_0 c_0^3} \frac{\hat{f^{eq}} - \hat{f}}{\hat{\tau_r}}.
\end{aligned} \tag{2.83}$$

Thus,

$$kn\left(\frac{\partial \hat{f}}{\partial \hat{t}}+\hat{c}\cdot\frac{\partial \hat{f}}{\partial \hat{x}}+\hat{F}\cdot\frac{\partial \hat{f}}{\partial \hat{c}}\right)=\frac{\hat{f^{eq}}-\hat{f}}{\hat{\tau_r}}. \tag{2.84}$$

From the non-dimensional procedure, we obtain $kn$ as,

$$kn=\frac{c_0\tau_0}{L_0}. \tag{2.85}$$

Introducing $\bar{c}=\sqrt{\frac{8K_bT}{\pi m}}$ as the mean molecular speed, the equation for $kn$ then becomes,

$$kn=\left(\frac{c_0}{\bar{c}}\right)\frac{\tau_0\bar{c}}{L_0}=\frac{\sqrt{\pi}}{2}\frac{\lambda}{L_0}=\frac{\sqrt{\pi}}{2}Kn, \tag{2.86}$$

where, $\tau_0\bar{c}=\lambda$ and $Kn$ is the Knudsen number.

We can make a few qualitative statements about $kn$ from the above equation. The parameter $kn$ is proportional to the ratio of the relaxation time and the flow characteristic time. It is also proportional to the ratio of the mean free path and the characteristic scale of the flow i.e. the Knudsen number. Both these parameters suggest that for a low degree of rarefaction the value of $kn$ will be small and higher rarefaction will increase the value of $kn$. In low $kn$ cases, the effect of the streaming operator ($LHS$ of eq.2.84) is diminished and the flow is collision dominated. On the other hand, high $kn$ values will tend to make the collision operator ($RHS$ of eq.2.84) insignificant thereby establishing a ballistic dominated flows with an extreme case of free molecular flows. The degree of rarefaction of the flow is often represented by the scaled rarefaction parameter that is related to the Knudsen number as,

$$\delta_{scaled}=\frac{2}{\sqrt{\pi}}\frac{1}{Kn}. \tag{2.87}$$

The final section to end the discussion of non-dimensional formulation is to define the dimensionless computed quantities of interest in the present study. The first class of the computed quantities relates to the fluxes such as mass flow rate and heat flux.

The mass flow rate is obtained from the law of conservation of mass and is given in the integral form as,

$$\dot{m}=\int\int \rho u dA=\int\int mnu dA. \tag{2.88}$$

Using the non-dimensional formulation defined previously in addition to $L_0^2$ to make the cross sectional area dimensionless,

$$\dot{m}=\dot{m}_{ND}\ n_0c_0L_0^2. \tag{2.89}$$

Using the relation $P_0=\frac{1}{2}mn_0c_0^2$,

$$\dot{m}=\dot{m}_{ND}\ \frac{2P_0}{c_0}L_0^2. \tag{2.90}$$

Rearranging terms,

$$2\dot{m}_{ND} = \dot{m}\frac{c_0}{P_0 L_0^2}. \tag{2.91}$$

Literature commonly refers to mass flow rate as reduced mass flow rate that is defined in the current context as,

$$G_p = 2\dot{m}_{ND} = 2\int\int n_{ND} u_{ND} dA_{ND}. \tag{2.92}$$

The second class of the computed quantities relates to the porous media figure-of-merit, namely, permeability, porosity, and tortuosity. While the latter two are dimensionless by definition, permeability carries a dimension of $[L]^2$. The non-dimensional apparent permeability is computed and can be related to other non-dimensional parameters as,

$$\hat{k_a} = \frac{k_a}{L_0^2} = KnG_p. \tag{2.93}$$

The friction characteristics are characterized by the Reynolds product or the Poiseuille number defined as,

$$Po = \frac{8\tau_w D_h}{\mu_0 u_{\bar{N}D}}. \tag{2.94}$$

Additionally, for flows under a small and constant pressure or temperature gradient along a direction (say, $z$), the non-dimensional form of the gradient can be expressed as,

$$\xi_p = \frac{D_h}{P_0}\frac{\mathrm{d}P}{\mathrm{d}z}; |\xi_p| << 1. \tag{2.95}$$

A simplified expression for the Poiseuille number for the long micro duct was obtained from kinetic considerations [170] and is used in the related study which is expressed as,

$$Po = \frac{\delta_{scaled}}{u_{\bar{N}D}}. \tag{2.96}$$

The flow domain commonly chosen in most of these studies is a rectangular parallelepiped essentially featuring 6 boundaries. These boundaries can be assigned a condition as appropriate. The domain boundary conditions in a particular study is conveyed through an exploded dice view as demonstrated in fig.2.2.

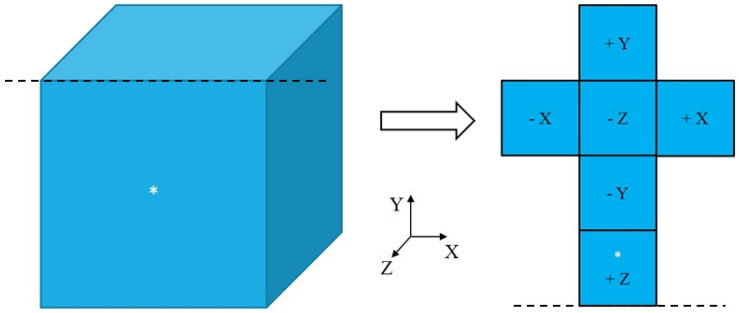


Figure 2.2: Protocol for the specification of domain boundary conditions adopted in the present work.

The results are often small values and are scaled by an appropriate value for efficient comparison and visualization. Furthermore, the contour plot of a hydrodynamic property for various Knudsen numbers are often presented together. This juxtaposition is more amenable to comprehension if each of the cases is normalized with respect to its local maximum value. For example, we represent the velocity magnitude $|V|$ by the Local Maximum Normalized Scaled Speed ($LMNS\ Speed$) defined as,

$$LMNS\ Speed = \frac{|V|}{|V|_{Max}}; V = \sqrt{u_{ND}^2 + v_{ND}^2 + w_{ND}^2}. \tag{2.97}$$

The comparison of two results, say $V1$ and $V2$ is expressed by a their percentage difference which is calculated as,

$$Percentage\ Difference = \frac{|V1 - V2|}{0.5 * (V1 + V2)} * 100 \tag{2.98}$$

## 2.5 Chapter summary

Through this chapter, the background theory regarding the principles of the mathematical governing equations and their evolution through assumptions and approximations was discussed in addition to a review of the numerical methods associated with some of the popular governing equations. The need for a new method tailored to small-scale rarefied flows in porous media was emphasized through the shortcoming of the currently popular numerical methods demonstrating that they are ill-suited for the current problem. The prevalent terminology in the fields of fluid mechanics and porous media was then revisited and an understanding of the current standard was established.

Through this examination, it was possible to identify the appropriate governing equation, surface model and parameters of interest for the present research endeavour. Additionally, the framework in which the current method and solver are required to function is established and aids in the design and development described in the next chapter.

# Chapter 3

# Method and Solver Development

*"They say no plan survives first contact with implementation. I'd have to agree."*

*— Mark Watney, in The Martian by Andy Weir.*

## 3.1 Chapter overview

In the present chapter, the method espoused in this thesis is elaborated along with means for its numerical implementation. Its realization is presented in the form of a solver developed for the sole purpose of studies conducted in the present research. The various processes and features of the solver are also explored in this brief.

## 3.2 Introduction

The method advocated in the current research is best appreciated when contrasted against the DSMC method. The key idea behind DSMC is the representation of the initial equilibrium state of the system by a set of simulated particles that evolve in time through advection, surface interaction and collision to eventually reach the final state (steady state if the problem is not transient) of the system. This is achieved by advection of (moving) all particles and performing all probable collisions between the particles in a small spatial region demarcated by a cell. The cases where DSMC is typically employed is characterized by high degrees of non-equilibrium where most of the simulated collisions play a crucial role in the system's evolution. However, in low-signal flows, only a small fraction of the intermolecular collisions are effective in the evolution of the system while the majority of the collisions have a net-zero effect. DSMC possesses no mechanism for recognizing the effect of a collision beforehand and thus proceeds with the simulation of these non-effective collisions as well as the effective ones. If it were possible to make such a distinction, then the computational effort could be redirected on the interactions that cause a shift in the system and a large degree of computational saving could be garnered. This is the principal premise of variance reduction techniques.

## 3.3 Literature review

An ideal solution to the issues faced by DSMC would be the development of a method that retains the key ingredients of the DSMC method such as simplicity and efficiency stemming from the stochastic treatment of the collision operator through importance sampling while improving the performance for low-signal flows. Such an approach was investigated in 1994 by Tan [171] for high speed flows. In this research, the collison operator of the Boltzmann equation was evaluated through a Monte Carlo sampling procedure *a la* DSMC with a notable distiction of using a discrete velocity set. High-speed flows were also investigated by Cheremisin [172] where the idea of solving only for the deviation from equilibrium was studied as a method for removing the stiffness in explicit time integration of deterministic discrete velocity approximations of the Boltzmann equation. However, the investigation did not yield significant benefits for two reasons. Firstly, the deviation from the equilibrium at high speeds is very large and no significant computational saving is expected. Secondly, the approach was deterministic. The paper, however, inspired researchers to pursue the idea of simulating only the deviation from equilibrium in the case of low-speed flows, where the deviation is small. Concentrating computational effort to the deviated part alone was expected to yield significant computational savings. Such an approach taxonomically falls under the variance reduced techniques.

In their first-ever paper on the subject, Baker [173] introduced a method for a more efficient calculation of the collision integral based on the hard-sphere collision model. The novelty of this research lies in the fact that prior to this, the handling of the deviational collision operator via an importance sampling framework was not investigated. The treatment of the collision operator in such a fashion is justified since this is the most expensive operation in the equation. In this paper, the formulation for the collision integral is presented, the role of importance sampling is elaborated and parallels with DSMC is drawn. The numerical implementation of the idea follows the DSMC ideology of splitting the Boltzmann equation into a collisionless advection and a homogeneous collision operation. The discrete velocity framework is put in place and the integration of the advection and collision operation is carried out by a first-order finite volume discretization and a first-order Euler step respectively although the possibility of extension to more comprehensive integration techniques exists. This formulation is then validated by solving the unsteady Couette flow and pressure-driven flow with a fully diffusive Maxwell reflection treatment for the walls. The more significant finding is that the statistical uncertainty remains constant even as the signal-to-noise ratio is decreased, unlike the DSMC method where the uncertainty increases with a decrease in signal strength unless the number of samples is increased significantly thereby drastically increasing the computational cost, sometimes to a crippling degree.

The extension of the idea to particle-based methods was executed by Baker in 2006 [124]. The method presented keeps the basic idea of particle methods, namely,

the developed collisionless advection and collision between particles. The change arises from the way the particles are drawn. In particle methods, the particles are drawn from the distribution function whereas, in the current method, the distribution function is represented as a combination of underlying Maxwell-Boltzmann distribution and deviation. The particles are drawn from the latter and a system of positive and negative particles representing the deviation from equilibrium is obtained. The paper presents the rules for a non-linear collision between hard spheres. The efficiency of the method comes from the collisions that don't need to be processed, namely, those between the Maxwell-Boltzmann particles since their net effect is zero. The issue with this method is the unrestricted growth in the number of deviational particles, which calls for a rigorous particle cancellation scheme. The inherent particle cancellation through interaction with boundaries proved ineffectual if the number of boundaries was small or the Knudsen number was large thereby limiting boundary interactions. The stability of the method demanded the implementation of particle cancellation routines that suffered from ambiguous conditions for implementation. Moreover, most particle cancellation methods required the use of discrete velocity which effectively increases the execution complexity while also undercutting the gains and advantages enjoyed by the DSMC. Further details are available in Baker's thesis [39].

The allure of particle methods is practical and historical. Specifically, the success of DSMC is a strong motivation that has encouraged the development of variants of the method to cater to the low-speed flows. The change is, more often than not, implemented through the modification of the particle weights. An example of this approach is the contemporary and independent efforts by Chun in 2005 [123] describing a particle-based method to solve small velocity flows. In their method, the distribution function is represented by real particles drawn from the equilibrium distribution and ghost particles which represent the deviation from equilibrium as weights. The method closely resembles the DSMC approach except that the interactions between particles result in the creation of additional particles. In this method, the number of particles was maintained by implementing schemes for splitting and combining particles if the weight exceeded a certain number. The publication reveals the procedure including diffuse reflection, intermolecular collisions and body force implementations.

It is evident that a particle representation either through positive or negative particles or through weighted particles suffers from an unbounded increase in the number of particles representing deviation principally due to the interpretation and implementation of the collision routine.

This problem was overcome by treating the collision algorithm differently as a source-sink term. This is the principle behind LVDSMC methods proposed by Homelle in 2007 [125]. Further details was published in 2007 [126]. In LVDSMC, the key idea is recognizing the function of the collision term can be interpreted as a phenomenon intent on driving the system towards equilibrium. Thus, the collision term is executed by shifting the underlying equilibrium Maxwell distribution and generating deviational

particles for the representation of the deviation that cannot be absorbed as a shift into the underlying Maxwellian distribution. The introduction of spatially varying Maxwellian distribution gives rise to the occasion where neighbouring cells have different equilibrium states. This discontinuity in the equilibrium across cells in resolved by generating particles at the boundary between cells. While the adoption of such an interpretation eliminates the need for particle cancellation, the process of drawing particles from the collision kernels along with the inhomogeneous advection limit the applicability of the method to simple cases. Further details are available in Homolle's thesis [43].

The method, thus far, has been only used for the hard-sphere model and the extension to a generic specified potential along with an in-depth study of the method from a mathematical standpoint was presented in a detailed work by Wagner in 2008 [174]. In this elaborate brief, Wagner presents various algorithms for the collision implementation for generic potentials and also discusses the source-sink interpretation of the collision algorithm. The extension of the LVDSMC method to pressure-driven flows was presented by Allshouse in 2009 [175] wherein, the pressure gradient was implemented as either a shift in the underlying equilibrium or by generating deviational particles. The linearized formulation is used to make the problem one dimensional.

The interpretation of the collision as an approach to equilibrium and decrease in the deviational particles is aligned with the principles behind the relaxation time approximation, thus, the natural extension of the LVDSMC method to the BGK collision model was put forth by Hadjiconstantinou in 2009 [40]. The publication describes the procedure for updates and the creation of the deviational particles. The acceptance-rejection sampling is used by this method is replaced by Radtke in their 2009 paper [41] which advocates the ratio-of-uniforms method to efficiently sample the difference in distribution to generate particles. Furthermore, the symmetrized version of the algorithm exhibiting a second-order convergence in time is presented in this work. The research is validated for pressure-driven flows through an infinite channel and for the heat flux between two plated at different temperatures. The method was utilized to study the small-scale heat transfer applications by Hadjicontatinou in 2010 [127]. The discrepancies of the BGK model i.e. the prediction of a unity Prandtl number encouraged the extension of the LVDSMC algorithm to collision models of engineering importance. Accordingly, the Variable Hard Sphere model was incorporated into the LVDSMC method by Radtke in 2011 [130].

One of the key issues with the LVDSMC method is that the conservation of mass, momentum, and energy are only done on average (owing to the source-sink interpretation of the collision term), unlike DSMC where conservation is ensured for every collision event. The conservation of mass which was difficult to maintain due to statistical errors that causes the number of positive and negative particles to vary resulting in a mass residual. This was addressed in this publication through the inclusion mass conservation routines which monitor the residual and regenerates generated particles at

each step to minimize the residual. Further details are available in Radtke's thesis [44]. Another way of resolving this issue was also proposed by Li in 2010 [176] wherein, the residual was monitored through the introduction of a separate class of particles termed as auxiliary particles.

Further applications and details regarding the application are presented in 2012 by Radtke [177]. These include the study of the second-order temperature jump using the BGK and Hard Sphere model of the LVDSMC method. The ability of the method to simulate the multi-scale effects without any approximations is promising and is highlighted by Radtke in 2013 through the study of a Knudsen compressor [131].

The extension of the method to study Phonon transport was also demonstrated in 2011 by Péraud [129]. A particle method based on the importance weights of the particles was presented in 2011 by Al Mohassen [128]. Replacement of the BGK collision operator by the McCormack kinetic model was investigated in 2012 by Szalmas [132] thereby enabling the simulation of a binary gas system.

## 3.4 Principle ideology

The method developed in this thesis is a loose adaptation of the LVDSMC-BGK [44] which is a low variance method that is well suited for handling situations where the deviation from equilibrium is small as is the case for small-scale, low-speed flows encountered in porous media. The principal idea is very similar in spirit to the control variate method. The problem i.e. evolution of $f$ in the domain is separated into a part that is analytically solvable and a part that requires an alternate method, thus, the distribution function can be expressed as,

$$f = f_{eq} + f_d, \tag{3.1}$$

where $f_{eq}$ is the equilibrium distribution function that is analytically solvable and $f_d$ is the deviation from this equilibrium state.

The equilibrium could be defined to be either a global constant equilibrium of a spatially varying local equilibrium. Either way, the solution of the $f_{eq}$ is done analytically and thus, the function representing $f_{eq}$ should be analytically solvable making the Maxwell-Boltzmann distribution an ideal candidate. Thus,

$$f_{eq} = f_{mb} = \frac{mn_{mb}}{c_{mb}^3 \pi^{\frac{3}{2}}} exp\left(-\frac{\|c - u_{mb}\|^2}{c_{mb}^2}\right), \tag{3.2}$$

with $m$ as the molecular mass and $f(n_{mb}, u_{mb}, c_{mb})$ being functions of $x$ and $c$ for local equilibrium, $f_{loc0}$, at a time $t$ OR $f(n_{mb}, u_{mb}, c_{mb})$ being functions of $c$ alone for global equilibrium, $f_0$, at a time $t$.

It has been established [44] that the spatially variable equilibrium is considerably more efficient and requires increasingly fewer samples than simulations based on global

equilibrium especially in the vicinity of the continuum limit. However, the efficiency is lost when multiple spatial dimensions are considered and since such multi-spatial dimensional cases are the focus in this current research, the global equilibrium $f_0$ is adopted.

$f_d$ is the deviation from an equilibrium distribution function and is most certainly not a probability distribution function as is evident from the fact that it is neither positive everywhere in phase space nor is it necessarily normalized or continuous. This makes an analytical evaluation of $f_d$ impossible and the integration of $f_d$ is done through particle representation instead. However, the fact that the sign of $f_d$ can vary depending on $f$ and $f_{eq}$ leads to the generated particles possessing either a positive or negative sign. A positive particle indicates that the $f$ is greater than $f_{eq}$ in that phase space element while a negative particle dictates that the $f$ is lesser than $f_{eq}$ in that phase space element. This stipulates that if an equal number of positive and negative particle occupies the same phase space element, then the net change to the distribution function is zero. In such an event, these oppositely signed particles are considered to have cancelled each other and is implemented by removing the particles from consideration. The particle representation of $f_d$ is shown in eq.3.3. The DSMC equivalent is also reiterated to draw parallels.

$$DSMC :: \quad f(c) = mN_{eff} \sum_{i=1}^{N} \delta^3(x - x_i)\delta^3(c - c_i). \tag{3.3}$$

$$LVDSMC :: \quad f_d(c) = mW_{eff} \sum_{i=1}^{N} s_i\delta^3(x - x_i)\delta^3(c - c_i). \tag{3.4}$$

Here, $s_i$ represents the sign of the particle and $N_{eff}$ represents the number of physical particles per simulated particle. $W_{eff}$ represents the number of physical particles per simulated particle in addition to the unit deviation represented by the particle. The idea is further emphasized through fig. 3.1.

Under this distribution function decomposition (eq.3.1), and considering a global equilibrium, the governing equation in the absence of external forces can be recast as shown in eq.3.5. The principal idea is the evolution of the deviational part of the distribution function $f_d$ through the dynamics of signed particles where, $f^{loc}$ is the instantaneous local equilibrium distribution. Thus,

$$\left[\frac{\partial f_d(c)}{\partial t} + c \cdot \frac{\partial f_d(c)}{\partial x}\right] = \frac{1}{\tau}\left[f^{loc}(c) - f_0(c)\right] - \frac{1}{\tau}f_d(c). \tag{3.5}$$

The method emulates the DSMC's idea of splitting the collision and advection operator. The operator splitting is valid provided that the chosen time step $\Delta t$ satisfies the condition $\Delta t < t_{mct}$. Thus, the evolution of the system of signed deviation particles in a single time step $\Delta t$ is governed by,

$$Advection\ Operator :: \left[\frac{\partial f_d(c)}{\partial t} + c \cdot \frac{\partial f_d(c)}{\partial x}\right] \Delta t = 0, \tag{3.6}$$

$$Collision\ Operator :: \left[\frac{\partial f_d(c)}{\partial t}\right]_{coll} \Delta t = \frac{\Delta t}{\tau}\left[f^{loc}(c) - f_0(c)\right] - \frac{\Delta t}{\tau} f_d(c). \tag{3.7}$$

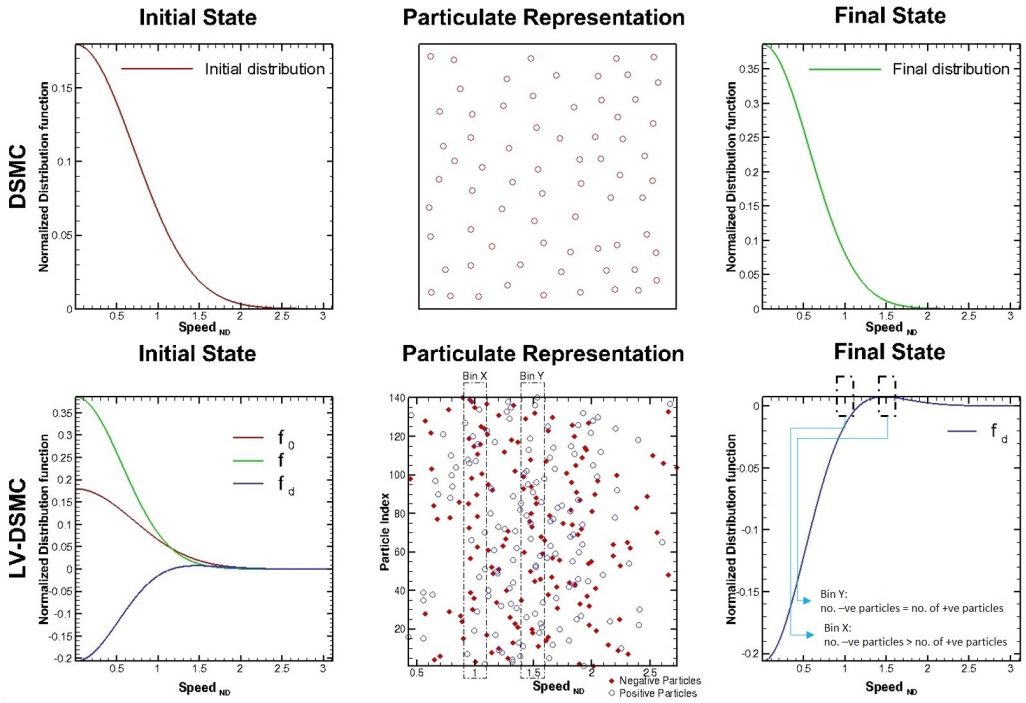


Figure 3.1: Particle generation through sampling of distributions for the standard DSMC(top) and LV-DSMC(bottom)

The choice of $f_{eq}$ can be any generic Maxwell-Boltzmann distribution function although an ill-considered choice might lead to a large $f_d$ resulting in the need for the creation of a large number of particles. This is undesirable and a choice of $f_{eq}$ such that $f_d \sim 0$ is highly recommended.

The method is stochastic in nature and is thus highly reliant on the generation of an adequate number of samples. These samples are generated once the simulation has reached a steady state. The achievement of such a state is determined through the convergence condition. The quality of the sampling procedure can be improved by taking samples across multiple ensembles.

The discussion of the present implementation is done in the context closely relating to the actual structure of the developed solver titled **P**ore-scale **E**nviron **G**as **A**nalyser and **S**olver **U**tilizing **S**tochastic (PEGASUS). PEGASUS is implemented in three individual sub-programs that need to be run sequentially for a given physical domain. These are, the **Preprocessor**, **Processor** and **Post-processor**.

The entire structure of PEGASUS can be visualized as shown in fig.3.2.

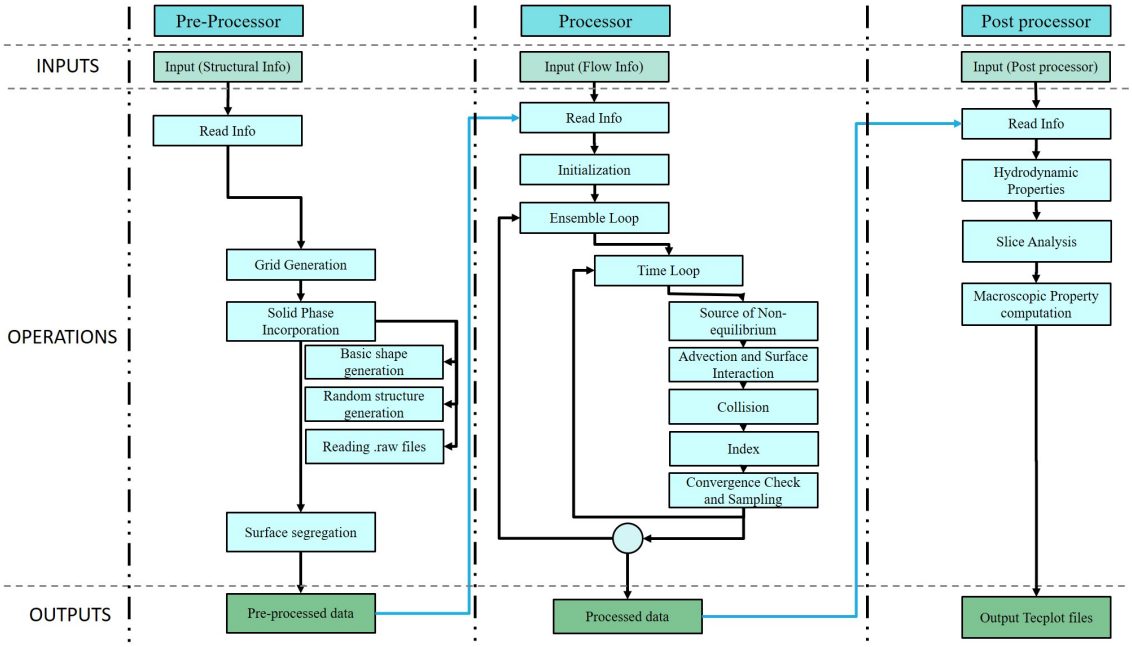


Figure 3.2: Flowchart depicting the various processes of the developed solver (PEGASUS).

## 3.5 PEGASUS : Preprocessor

The Preprocessor concerns itself with the setting up of the physical characteristics of the flow problem. Within its purview are the tasks of

1. Discretizing the domain into a set of Cartesian cells.
2. Distinguishing distribution of the solid and pore phase.
3. Definition of reservoir regions.
4. Transmitting processed data to the Processor.

The information regarding the physical nature of the domain is provided to the Preprocessor through an input file that contains this information in a binary form. Alternatively, provisions have also been developed to directly read in the image file formats commonly encountered in practice such as unprocessed .raw files or processed .jpg, .bmp and .png files. The high resolution of the porous media images makes it viable to adopt the pixel resolution as the cell resolution, although, it is possible to define a finer or coarser cell structure independent of the pixel size if the need arises.

Accordingly, the entire simulation domain $D$ in the physical space is partitioned into $N_{cell}$ spatial cells each with an equal spatial volume $\Delta V_{cell}$. The total number of pore space cells are identified as $N_{ps} \leq N_{cell}$. This information is crucial in the execution of localized collision process. Surface elements are identified as those that are in contact with a pore space cell and are extracted from the cellular matrix. Each of the $N_{surf}$ surface elements have an area denoted by $\Delta A_{surf}$ and unit surface normal

$\overrightarrow{n}_{surf}$ directed into the flow. This information plays a pivotal role in the determination of the reflection characteristics of the particles in addition to the generation of particles at the boundaries.

In addition to this, reservoir regions can also be specified in a connected portion of pore volume. It is possible to identify $N_{reservoir}$ number of reservoirs. These reservoirs act as regions where the equilibrium state differs from the global equilibrium state. Reservoirs can overlap although the overlapping region will exhibit the net result of the two reservoirs.

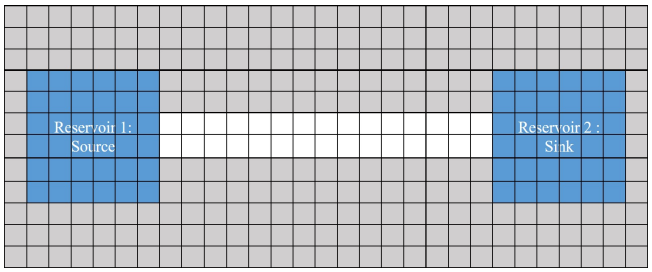


(a) Spatial discretization of the flow domain ($N_{cell} = 29X12X1 = 348$).

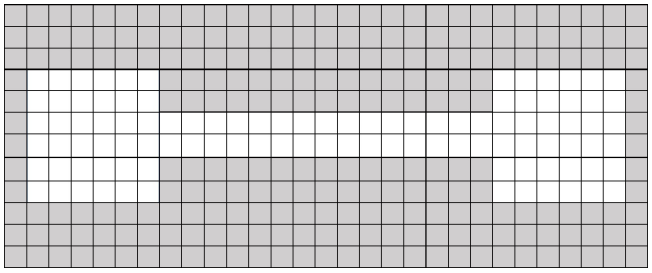

(b) Isolation of pore space ($N_{ps} = 102$).

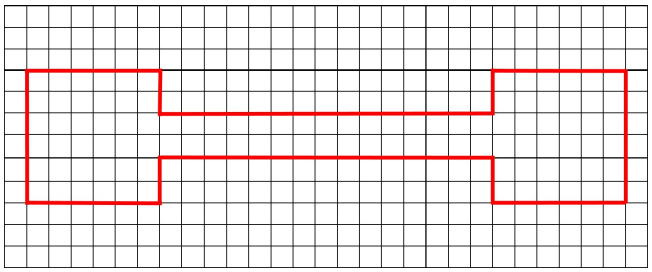

(c) Identification of surface elements ($N_{surf} = 74$).

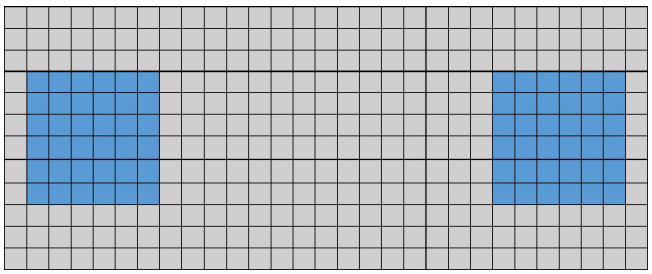

(d) Isolation of reservoir cells ($N_{reservoir} = 72$).

Figure 3.3: Demonstration of Preprocessor activities and capabilities.

Once obtained, the information regarding the pore cells, solid surfaces and reservoirs are compiled into a .bin file and acts as an input for the Processor. In the absence of absorption and surface erosion, these details correspond to the physical aspects of the given input structure that remain invariable under differing flow conditions such as rarefaction, driving mechanism etc. Thus, the preprocessor is typically run once for a given geometry.

## 3.6 PEGASUS : Processor

In addition to information regarding the fluid cells and solid surfaces, details about the flow conditions are provided to the Processor through an input file. This information includes the boundary conditions of the domain, the global rarefaction of the domain and the nature of the solid surfaces and the sources of non-equilibrium and constitute details for a single case. The specification of multiple cases through the variation in any of these properties is possible and doesn't require the rerun of the Pre-processor sub-program. The principal procedures in the processor can be listed as,

1. Domain initialization.
2. Time integration.
3. Output of processed data for post-processing.

### 3.6.1 Domain initialization:

In this process, equilibrium condition specified in the input file is used to set the $(n_0, u_0, c_0)$ in each of the pore cell. The decomposition of the domain into sub-domains to facilitate parallel processing is also carried out in this step. The counters are reset to zero and the bounds for sampling via the Ratio-of-Uniform method (for concept refer Wakefield [178]; for implementation, refer Appendix A of Radtke's thesis [44]) are specified. The time step $\Delta t$ is also determined. In the absence of any source of non-equilibrium, no deviational particles are created and the domain remains in equilibrium.

### 3.6.2 Time integration

During each time step, the advection, the collision and the effect of the non-equilibrium sources on the domain are implemented. The convergence condition is monitored and once it is determined that the convergence is has been achieved, then the sampling operation is incorporated into the process.

The operator splitting, borrowed from DSMC, often leads to a time step error which is reduced here by utilizing Strang's splitting method which has been proven to offer second order convergence with no intrinsic time step error. The current procedure follows the following algorithm during a single time step,

1. Half Sources of NE ($\Delta t_{neq} = 0.5X\Delta t$)
2. Half Advection ($\Delta t_{adv} = 0.5X\Delta t$)
3. Full Collision ($\Delta t_{coll} = \Delta t$)
4. Half Advection ($\Delta t_{adv} = 0.5X\Delta t$)
5. Half Sources of NE ($\Delta t_{neq} = 0.5X\Delta t$)
6. Convergence Check
7. Sample properties

#### 3.6.2.1 Sources of non-equilibrium:

The current implementation allows for a wide range of options for the specification of the source of non-equilibrium enabling the replication of a variety of flow inducing conditions. Although the degree of non-equilibrium can be high, the method's appeal lies in the cases where the non-equilibrium is small and the system is essentially near-equilibrium.

The **first source of non-equilibrium** is the presence of a pressure OR temperature gradient across the domain boundaries. In the context of the present applications of interest these gradients are typically small allowing the representation of these gradients as a constant body force applied over the entire domain. The impetus behind the representation of the gradient as a body force is derived from the seminal work of Cercignani [179] wherein the technique was used to theoretically demonstrate the presence of the Knudsen minimum in pressure driven flows in small capillaries. Thereafter, the technique has been adopted in a number of methods including the present title. As per this formulation, these gradients can be expressed in their appropriately scaled dimensionless form as,

$$\kappa_P = -\frac{L_0}{P_0}\frac{\partial \hat{P}}{\partial \hat{x}}; \quad \kappa_T = \frac{L_0}{T_0}\frac{\partial \hat{T}}{\partial \hat{x}}. \tag{3.8}$$

The effect of such a global force will be to accelerate the particles in the domain thereby causing the local equilibrium to deviate from the global equilibrium necessitating the generation of deviational particles as exhibited by,

$$f = f_{eq} + f_d(body\ force). \tag{3.9}$$

Provided these gradients are small, they are adequately represented by a linearized body force. The change in a unit volume in one time step due to this body force is expressed as shown below,

$$\left[\frac{\partial f_d}{\partial t}\right]_{BF} = c_x \left[\kappa_P + \left(\frac{5}{2} - \frac{\|c - u_0\|^2}{c_0^2}\right)\kappa_T\right] f_0. \tag{3.10}$$

Integrating to include the entire phase space, i.e. the physical space represented by $D$ and the velocity space represented by $R$, over a time step $\Delta t$,

$$\int_D \int_R \left[\frac{\partial f_d}{\partial t}\right]_{BF} \Delta t d^3 r d^3 c = \int_R c_x \left[\kappa_P + \left(\frac{5}{2} - \frac{\|c-u_0\|^2}{c_0^2}\right)\kappa_T\right] f_0 V_{ps} d^3 c \Delta t; \quad (3.11)$$

$$V_{ps} = \int_D d^3 r.$$

Furthermore,

$$\int_D \int_R \left[\frac{\partial f_d}{\partial t}\right]_{BF} d^3 r d^3 c \Delta t = \int_R \frac{\rho_0 c_0}{L} F_{BF} V_{ps} \Delta t d^3 c, \quad (3.12)$$

where,

$$\boxed{F_{BF} = \frac{c_0^2 L}{\rho_0} c_x \left[\kappa_P + \left(\frac{5}{2} - \frac{\|c-u_0\|^2}{c_0^2}\right)\kappa_T\right] f_0.} \quad (3.13)$$

Particles need to be drawn from the distribution $F_{BF}$ in order to reconcile the effect of a body force on the domain. The drawing of the particles must be performed in a mass conservative manner through the creation of an equal number of positive and negative particles. This is achieved through stratified sampling of $F_{BF}$. The total number of particles that need to be created to represent the effect of the body force is determined through the integration of the upper bound of the eq.3.12 determined as,

$$\frac{V_{ps}\Delta t}{m W_{eff}} \int_R \left[\frac{\partial f_d}{\partial t}\right]_{BF} d^3 c \xrightarrow[Bound]{Upper} \frac{\rho_0 c_0 V_{ps} \Delta t}{m W_{eff} L} \int_R \|F_{BF}\| \, d^3 c = N_F^{trial}. \quad (3.14)$$

Ever since the beginning of kinetic theory, the fact that the distribution function is discontinuous at the walls has been a well-established fact. For impermeable wall surfaces, two possible forms of interactions are possible. The first is the reflection of the particles which is discussed later on in the context of the advection step. The second is the imbalance between the state of the wall and the state of the fluid system due to surface features such as a higher surface temperature or a tangential velocity due to a moving wall. This constitutes the **second source of non-equilibrium** which is concerned with the effect of surfaces that are not in equilibrium with the overall domain. The effect of a single surface $k \in N_{surf}$ can be expressed as,

$$f = f_{eq} + f_d(surface\ element\ k). \quad (3.15)$$

The state of the wall surface $k$ can be established by Maxwellian distribution function as,

$$f_k = \frac{\rho_k}{c_k^3 \pi^{\frac{3}{2}}} exp\left(-\frac{\|c-u_k\|^2}{c_k^2}\right). \quad (3.16)$$

The determination of $\rho_k$ depends on the character of the wall. For a permeable wall, influx and out-flux across the wall is a viable. However, for an impermeable wall, the net mass flux across the wall is zero and is enforced by the condition,

$$\int_{inbound} (c \cdot n_k) \frac{\rho_k}{c_k^3 \pi^{\frac{3}{2}}} exp\left(-\frac{\|c-u_k\|^2}{c_k^2}\right) d^3c = \\ -\int_{outbound} (c \cdot n_k) \frac{\rho_0}{c_0^3 \pi^{\frac{3}{2}}} exp\left(-\frac{\|c-u_0\|^2}{c_0^2}\right) d^3c, \tag{3.17}$$

where,

$$\rho_k = \frac{\int_{outbound} (c \cdot n_k) \frac{\rho_0}{c_0^3 \pi^{\frac{3}{2}}} exp\left(-\frac{\|c-u_0\|^2}{c_0^2}\right) d^3c}{\int_{inbound} (c \cdot n_k) \frac{1}{c_k^3 \pi^{\frac{3}{2}}} exp\left(-\frac{\|c-u_k\|^2}{c_k^2}\right) d^3c}. \tag{3.18}$$

Solving the above relation yields,

$$\rho_k = \frac{\rho_0 c_0}{c_k}. \tag{3.19}$$

For surface $k$, the integration of the difference in wall distribution to the global distribution integrated over $\Delta t$ is,

$$\int_{S_k} \int_R F_k \Delta t dA d^3c = \Delta t \Delta A_k \int_R F_k d^3c = \Delta A_k \Delta t \alpha_k (c \cdot n_k) \int_R [f_k - f_0] d^3c, \tag{3.20}$$

where,

$$\boxed{F_k = \alpha_k (c \cdot n_k) [f_k - f_0].} \tag{3.21}$$

Particles need to be drawn from the distribution $F_k$ in order to reconcile the discontinuous nature of distribution function across the wall surface. Mass conservation is enforced once more through the stratified sampling of $F_k$ to ensure the creation of an equal number of positive and negative particles. The total number of particles that need to be created to represent the effect of the surface k is determined through the integration of the upper bound of the eq.3.20 determined as,

$$\frac{\Delta t \Delta A_k}{m W_{eff}} \int_R \left[\frac{\partial f_d}{\partial t}\right]_k d^3c \\ = \frac{\Delta t \Delta A_k}{m W_{eff}} \alpha_k (c \cdot n_k) \int_R [f_k - f_0] d^3c \xrightarrow[Bound]{Upper} \frac{\overline{\rho_k c_k} \Delta t \Delta A_k}{m W_{eff}} \int_R \|F_k\| d^3c = N_k^{trial}, \tag{3.22}$$

where, $\overline{\rho_k} = \frac{\rho_k + \rho_0}{2}$ and $\overline{c_k} = \frac{c_k + c_0}{2}$

The **third source of non-equilibrium** is the presence of a reservoir inside the domain. In the present context, a reservoir is defined as a region that is characterized by a local unvarying equilibrium distribution that is different from the globally defined equilibrium. In a given domain, $N_{RV}$ such reservoirs can co-exist. This results in a deviation in each cell of the reservoir and the effect in cell $i \in reservoir\, r \in N_{RV}$ can

be expressed as,

$$f = f_{eq} + f_d(reservoir\ r; cell\ i). \tag{3.23}$$

Assuming the reservoir has equilibrium state variables as $(n_r, u_r, c_r)$ the reservoir equilibrium distribution function is given by eq.3.24,

$$f_r = \frac{\rho_r}{c_{RV}^3 \pi^{\frac{3}{2}}} exp\left(-\frac{\|c - u_r\|^2}{c_r^2}\right), \tag{3.24}$$

the resulting change in $f_d$ is expressed as eq.3.25,

$$\left[\frac{\partial f_d}{\partial t}\right]_{i \in r} = \left[f_r - f_0(c)\right]. \tag{3.25}$$

Integrating to include the entire phase space over a time step $\Delta t$,

$$\int_{D_r}\int_R \left[f_r - f_0(c)\right] d^3r d^3c = \Delta V_r \int_R \left[f_r - f_0\right] d^3c = \Delta V_r \int_R F_r d^3c. \tag{3.26}$$

The deviation the reservoir from the underlying global distribution function will cause a need to generate particles by sampling,

$$\boxed{F_r = \left[f_r - f_0\right].} \tag{3.27}$$

Particles need to be drawn from the distribution $F_r$ in order to reconcile the discontinuous nature of distribution function in the cells belonging to reservoir $r$. The total number of particles that need to be created to represent the effect of the reservoir is determined through the integration of the upper bound of the eq.3.26 determined as,

$$\frac{\Delta t \Delta V_r}{m W_{eff}} \int_R \left[\frac{\partial f_d}{\partial t}\right]_r d^3c \xrightarrow[Bound]{Upper} \frac{\overline{\rho_r c_r} \Delta t \Delta V_r}{m W_{eff}} \int_R \|F_r\|\, d^3c = N_r^{trial}, \tag{3.28}$$

where, $\overline{\rho_r} = \frac{\rho_r + \rho_0}{2}$ and $\overline{c_r} = \frac{c_r + c_0}{2}$

Particles are distributed randomly in the region delineated by the reservoir definition. Mass conservation is NOT enforced through the creation of an equal number of oppositely signed particles because these reservoirs are essentially a mass source or sink thus, they are expected to cause an imbalance in the number of positive and negative particles.

#### 3.6.2.2 Advection and boundary/surface interaction

The advection subroutine consists of two processes and is one of the computationally intensive operation of the solver. In the first part of the advection routine, the focus is on the movement of particles which is achieved *a la* DSMC. The advection operator is numerically integrated through updates to the particle's position as per the equation

shown below,

$$x_i(t + \Delta t) = x_i(t) + c_i(t)\Delta t_{adv} \quad i \in N_{particles}. \tag{3.29}$$

The second part is the reflection of the particles from the surface which is challenging due to the need for accurate determination of the point of intersection and the fraction of time left post reflection. The process is made even more strenuous by the fact that in microfluidic devices and pore-scale environs, the proximity of the surfaces results in particle reflection from multiple surfaces in a single time step. Thus, the reflection must be treated recursively. This complexity is further increased in 3D structures.

The interaction with surfaces and domain boundaries is characterized by the type of surface interaction. In the present implementation, the following options are implemented,

1. Maxwell wall (Domain boundary and surface)
2. Bounce-back (Domain boundary and surface)
3. Periodic (Domain boundary only)
4. Vacuum (Domain boundary only)

A particle interacting with a Maxwell surface can be subject to a diffusive reflection with a probability of $\alpha$ or a specular reflection with the remaining probability $1 - \alpha$. **Specular reflection** is enforced by reversing the direction of the normal velocity component of the incoming particle. The reflected particle possesses equal angles of incidence and reflection. The specular reflection can physically represent either a smooth, polished wall or a symmetry boundary condition. **Diffuse reflection** is based on the complete accommodation of the particle to the wall and thus, the particle is re-emitted from the intersection point with velocity drawn from the wall distribution and an arbitrarily determined angle. In addition to this, the diffuse surfaces also function as a way of keeping the particle number tractable by deleting oppositely signed particles interacting with the same surface within the time step $\Delta t_{adv}$. This implementation is firmly founded on the basis that since the surfaces are small the oppositely signed particle is essentially colliding at the physical location. The particle's location in velocity space is irrelevant since they are going to be re-sampled from the wall distribution. Thus, the oppositely signed particles are in the same phase space element and their net effect is zero.

**Bounce-back** reflection is commonly employed in the continuum regimes and is implemented by reversing the trajectory of the incoming particle. The implementation can be visualized as a particle impacting perpendicular to the wall. The idea behind such a reflection is that, post reflection, the particle is likely to follow the path of least resistance which in continuum regimes is the same as its incoming trajectory.

**Periodic** boundary conditions are implemented in pairs with opposite sides on the domain. The particle existing through one surface is reinserted through its pair with

no change to its velocity. **Vacuum** conditions are implemented through the removal of the particle from the simulation.

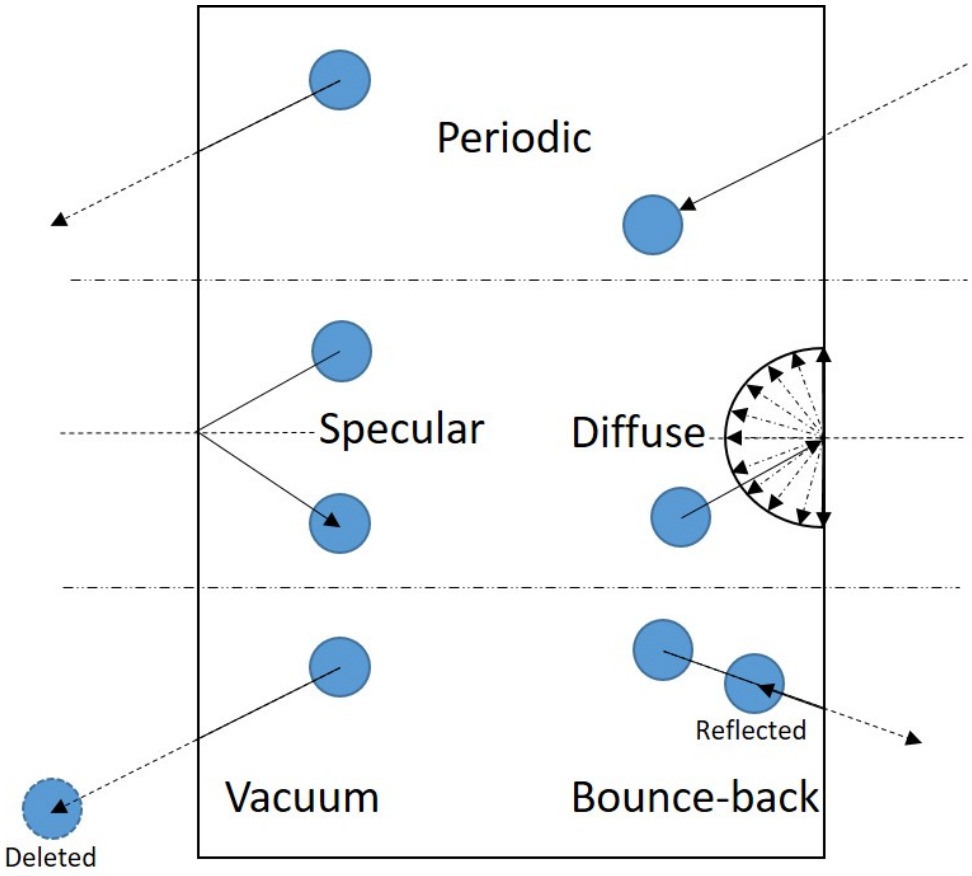


Figure 3.4: Schematic diagram demonstrating the various particle-boundary condition interaction outcomes.

#### 3.6.2.3 BGK collision operator implementation

The BGK collision term can be integrated over time step $\Delta t$ in cell $i$ can be written as,

$$\begin{aligned}
&\int_{D_i}\int_R \left[\frac{\partial f_d(c)}{\partial t}\right]_{coll} \Delta t d^3r d^3c \qquad (3.30)\\
&= \int_{D_i}\int_R \left[\frac{\Delta t}{\tau}\left[f^{loc}(c) - f_0(c)\right]\right] d^3r d^3c - \int_{D_i}\int_R \left[\frac{\Delta t}{\tau} f_d(c)\right] d^3r d^3c \\
&= \int_R \left[\frac{\Delta t \Delta V_i}{\tau}\left[f^{loc}(c) - f_0(c)\right]\right] d^3c - \int_R \left[\frac{\Delta t \Delta V_i}{\tau} f_d(c)\right] d^3c \\
&= \int_R \frac{\Delta t \Delta V_i}{\tau} F_{loc,i} d^3c - \int_R \left[\frac{\Delta t \Delta V_i}{\tau} f_d(c)\right] d^3c
\end{aligned}$$

or

$$= Source + Sink. \qquad (3.31)$$

The structure of the BGK collision operator can be divided in to the source and sink term. The source term can be implemented in cell $i$ by generating particles to resolve the difference between the instantaneous local distribution function $f^{loc}$ and established global equilibrium distribution function $f_0$. The distribution from which the particles are sampled is shown below,

$$\boxed{\left[F_{loc,i} = \frac{c_{loc,i}^3}{\rho_{loc,i}} \left[f^{loc,i}(c) - f_0(c)\right]\right]_{i \in cell}}. \tag{3.32}$$

On the other hand, the sink term is implemented through the removal of deviational particles. The creation or deletion of a particle in cell $i$ during a collision event affects the $(n, u, c)_{cell\ i}$ and thus $f^{loc}$. This impacts the evaluation of sources and sinks in the subsequent collision event in that cell. It is thus, pivotal to maintain an up-to-date value of the hydrodynamic properties in each cell which can be done by tracking the evolution of the departure from equilibrium hydrodynamic properties.

The departure in $n$, $u$ and $c$ in a cell $j$ containing $N_j$ particles is given by,

$$\sum_{i \in N_j} s_i; \quad \sum_{i \in N_j} s_i c_i; \quad \sum_{i \in N_j} s_i c_i^2 \tag{3.33}$$

respectively. Here, $s_i$ indicates that sign of the particle and is either $+1$ or $-1$.

This is performed by first initializing each value at the start of the collision step and adding or subtracting the appropriate value for each particle creation or deletion event. The tracking ensures the accurate computation of $F_{loc,i}$ for each collision event and subsequently the accurate value of $f_d$.

The BGK collision process is formulated in terms of Markov creation and deletion events where each event, termed as a collision event, occurs during a stochastic time step ($tc_j$ with $j = 1, n$). In a given collision step, the number of collision events processed continues up until the sum of the stochastic time steps exceeds the collision time step, i.e. $\sum_{j=1}^{n} tc_j \geq \Delta t_{coll}$

While DSMC processes collisions in every cell, the present instance calls for a more nuanced approach in which an appropriate number of collision events are conducted in a few selected cells that contribute towards the system's return to equilibrium.

The determination of the cell and number of collision events (and ergo, size of the stochastic collision time steps) is dependent on the local properties of the cell defined through $(n, u, c)_{cell\ i}$. These are obtained through the computation of the upper bound on the absolute integral of equation BGK collision term over the entire phase space shown as,

$$\int_D \int_R \left[\frac{\partial f_d(c)}{\partial t}\right]_{coll} d^3r d^3c \xrightarrow[Bound]{Upper} \int_D \int_R \left[\frac{\left|f^{loc}(c) - f_0(c)\right|}{\tau} + \frac{\left|f_d(c)\right|}{\tau}\right] d^3r d^3c \tag{3.34}$$

$$= \sum_{i=1}^{N_{cell}} \frac{\Delta V_i}{\tau_i} \int_R \left[ \left| f^{loc}(c) - f_0(c) \right| + \left| f_d(c) \right| \right] d^3c \tag{3.35}$$

$$= \sum_{i=1}^{N_{cell}} \frac{1}{\tau_i} (B_i^{loc} + N_i^c) = \Lambda, \tag{3.36}$$

where, $B_i^{loc} = \int_R \Delta V_i \left| \left[ f^{loc}(c) - f_0(c) \right] \right| d^3c$, $N_i^c = \int_R \Delta V_i \left| f_d(c) \right| d^3c = \sum_{i=1}^{N_p} |s_i|$ and $\Lambda = \sum_{i=1}^{N_{cell}} \frac{1}{\tau_i} (B_i^{loc} + N_i^c)$.

The parameter $\tau_i$ is the relaxation time-based on the local properties defined for cell $i$ and relates directly to the local rarefaction condition of the cell with a high local $Kn$ corresponding to large relaxation time. In the current process, the sequence of Markov creation and deletion events are carried out with time steps $tc_j$ drawn from the exponential distribution $\Lambda e^{-\Lambda \Delta t_{coll}}$.

The time step parameter $\Lambda$ is indicative of the rate at which trial creation and deletion events are performed and plays a pivotal role in the candidacy determination of cell $i$. The cell is chosen if it passes the acceptance-rejection test which takes into account the local state through the numerator of eq.3.37. Once the cell and stochastic time step have been determined, the particle creation steps are processed with probability $\frac{B_i^{loc}}{B_i^{loc}+N_i^c}$, and random particles are removed (uniformly) from cell $i$ with the remaining probability, i.e.,

$$P_i^{cell} = \frac{B_i^{loc} + N_i^c}{(B_i^{loc} + N_i^c)_{max}} = \frac{B_i^{loc} + N_i^c}{\Lambda \tau_i}. \tag{3.37}$$

The use of instantaneous moments ensures the implementation is devoid of any time step error. Mass conservation is enforced by regenerating the particles created in the collision step with appropriate signs to make the mass deficit approach zero.

#### 3.6.2.4 Monitoring and convergence checking procedure

The strength of any stochastic method is in the sampling which must be done only after the steady state is reached failing which, the entire sample may be polluted. Convergence checks ensure that the steady-state is attained before initiating sampling. In the following solver, three methods of tracking convergence are utilized; one is a generic method whereas the other two are study-specific.

The generic method consists of tracking the number of deviational particles in the domain. In the presence of a constant disturbance like a non-decaying body force, the particles will be generated to represent the effect of the force while, simultaneously, the mechanisms of collision and diffuse reflection will be responsible for the deletion of the particles. The convergence is assumed to occur once the rate of creation equals the rate of deletion thereby making the total number of deviational particles in the domain constant.

In the cases where the flow pathways are not as convoluted as in porous media or reservoirs are , an average velocity can be found at an intermediated time step. This

value is then used to modify the simulation time step dynamically enabling the solver to always step small enough to capture the reflections from surfaces and also long enough to allow a reasonably paced evolution of the system. The simulation time will converge to a constant value indicating that the average velocity of the domain doesn't vary as much as before and thus implying convergence.

The above method is questionable in the case of porous media where the surface interactions along with complex flow paths cause a wide variation in simulation time. The secondary convergence method advocated for these types of flows is centred on the selection of an arbitrary set of fluid cells at which the distribution function's evolution is monitored. At each of the convergence checks, the variation from the previous step is computed and checked against a prescribed tolerance. If more than half the monitored cells feature residues below the tolerance then, convergence is said to have been established. Although the initial selection of the cells is done arbitrarily, the selected cells are reset for every ensemble and it is left to the law of large numbers to provide a good representation of the domain across many ensembles. The strictness of the convergence can be improved by either increasing the number of cells monitored for the residue or increasing the numerical tolerance below which the residue must fall. However, a preliminary understanding of the flow physics is essential to set the appropriate values to yield the fastest possible convergence.

There are cases where all 3 methods seem to state convergence simultaneously or at least in quick succession, although typically employing one of these is sufficient. The sampling may commence once the convergence criteria are met.

#### 3.6.2.5 Instantaneous property computations and sampling

Once a steady-state is established through the convergence, the microscopic properties are accounted for through an aggregate sum of the moments for each cell.

For a cell $j$ containing $N_j$ particles at a time step conducive to sampling, the aggregate sum of mass, momentum, pressure tensor, temperature and heat flux are given by,

$$(Agg\ \Sigma_m)_j = (Agg\ \Sigma_m)_j + \sum_{i \in N_j} s_i; \tag{3.38}$$

$$(Agg\ \Sigma_v)_j = (Agg\ \Sigma_v)_j + \sum_{i \in N_j} s_i c_i; \tag{3.39}$$

$$(Agg\ \Sigma_p)_j = (Agg\ \Sigma_p)_j + \sum_{i \in N_j} s_i c_i c_j; \tag{3.40}$$

$$(Agg\ \Sigma_T)_j = (Agg\ \Sigma_T)_j + \sum_{i \in N_j} s_i c_i^2; \tag{3.41}$$

$$(Agg\ \Sigma_q)_j = (Agg\ \Sigma_q)_j + \sum_{i \in N_j} s_i c_i c_i^2. \tag{3.42}$$

### 3.6.3 Output of processed data

The final deliverables generated from the Processor consist of the aggregate sums in each of the cells along with the total number of interactions each surface element had with a deviational particle and the overall acceptance-rejection ratio of each cell. The information regarding the time taken for each of the processes and the monitoring of the residual for convergence are also part of the final result of the Processor.

The data in this form is not readily understandable and further processing is done in the Post-processor. The data is made available to the post-processor by writing it into a binary .bin file since they are more compact than their ASCII counterparts and, thus, can be easily stored and retrieved for analysis at a future date if the need arises.

### 3.6.4 Sampling of fluxal distributions

Before proceeding to a discussion of the Post-processor operations, it is imperative to address the heretofore undisclosed process of particle generation which, in conjunction with the deletion of deviational particles, form the core operations driving the evolution of the system in the current method.

The sampling of distribution functions to generate particles is a staple of the DSMC method. In it, the procedure is carried out by determining candidates through a Box-Muller sampling and utilizing an acceptance-rejection method to determine their validity. In the current context, the interest is not in the sampling of a distribution function, but rather in the sampling of the difference between two distribution functions denoted by $F$ in this document.

The acceptance-rejection rule can be applied for this *a al* DSMC. The acceptance-rejection is a basic technique for producing samples from a distribution that has a known bound. A trial sample is uniformly distributed in the domain and accepted with a probability $\frac{Fc}{F_{max}}$. If rejected, then a new sample is generated and tested again. The procedure for this is stated below,

Algorithm for sampling $F(c)$

1. Generate uniformly distributed, random velocity vectors $c$ such that $\|c\| < c_c$
2. If $F(c) > R\Delta_{max}$ the particle is generated with velocity $c$, position chosen randomly within region (cell/domain/reservoir) and sign as $sgn(F(c))$.

Here, R is the random number uniformly distributed on $[0, 1]$, $\Delta_{max}$ is the upper bound of $F(c)$ and $c_c$ is the upper bound of $c$.

Another approach is the ratio-of-uniforms method that is proposed by Wakefield [178] and extended to LVDSMC-BGK by Radtke [44]. The estimations for the bounds used for particle creation follows by expanding the function to the first order in the perturbations of the local equilibrium properties with respect to the global equilibrium properties. In the limit of small departure from equilibrium, this expression is sufficient.

The number of trial particles that need to be generated is dependent on the upper bound expressed as,

$$F_{BF} = \frac{c_0^2 L}{\rho_0} c_x \left[ \kappa_P + \left( \frac{5}{2} - \frac{\|c - u_0\|^2}{c_0^2} \right) \kappa_T \right] f_0, \tag{3.43}$$

$$F_{loc,j} \approx F_{loc0,j} = \left[ \frac{\rho_{loc,j} - \rho_0}{\rho_{loc,j}} + 2\frac{u_{loc,j} - u_0}{u_{loc,j}} \cdot c + 2\frac{c_{loc,j} - c_0}{c_{loc,j}} \cdot \left( c^2 - \frac{3}{2} \right) \right] \pi^{\frac{-3}{2}} e^{-c^2}, \tag{3.44}$$

$$F_{RV,j} \approx F_{RV0,j} = \left[ \frac{\rho_{RV,j} - \rho_0}{\rho_{RV,j}} + 2\frac{u_{RV,j} - u_0}{u_{RV,j}} \cdot c + 2\frac{c_{RV,j} - c_0}{c_{RV,j}} \cdot \left( c^2 - \frac{3}{2} \right) \right] \pi^{\frac{-3}{2}} e^{-c^2}, \tag{3.45}$$

and

$$F_{SE,k} \approx F_{SE0,k} = v_n \left[ \frac{\rho_{SE,k} - \rho_0}{\rho_{SE,k}} + 2\frac{u_{SE,k} - u_0}{u_{SE,k}} \cdot c + 2\frac{c_{SE,k} - c_0}{c_{SE,k}} \cdot \left( c^2 - \frac{3}{2} \right) \right] \pi^{\frac{-3}{2}} e^{-c^2}, \tag{3.46}$$

where, $j \in cell$ and $k \in surfaces$.

We simulate the deviation from a global equilibrium distribution with $u_0 = 0$. The normalized characteristic deviation from equilibrium is quantified by $\epsilon$, which is typically related to the characteristic temperature difference or the flow velocity of the problem. As previously observed, in contrast to DSMC, the cost of LVDSMC calculations for a fixed statistical uncertainty does not increase as $\epsilon$ decreases and for this reason, all results are presented here scaled by $\epsilon$. $\epsilon$ can be related to the pressure difference as $\epsilon = \frac{\Delta P}{P}$, or the temperature difference as $\epsilon = \frac{\Delta T}{T}$. In the present context, the velocity contours are most often referred to as $LMNS$ speed where LMNS stands for Local-case Maximum-Normalized Scaled speed.

## 3.7 PEGASUS: Post-Processor

The separate treatment of the post-processing allows for the tailoring in the treatment of the Processor output to the nature and focus of the subject studies in a manner intent on computational savings. For instance, an isothermal flow through a 2D cross-section of a long duct does not require the computation of the temperature or heat flux in each cell and the macroscopic parameters of interest is the reduced mass flux whereas an isothermal flow through a 3D porous media would benefit from a slice by slice analysis with the computation of the permeability as a target.

### 3.7.1 Macroscopic property computations

The evaluation of the hydrodynamic properties is along the similar vein as done in the DSMC method albeit, the summation of the deviational particles corresponds to the difference in between the steady-state values and the equilibrium. The summation terms are obtained from the output generated from the Processor. Accordingly, the hydrodynamic properties of number density, bulk velocity, pressure tensor, temperature and heat flux are computed as shown below,

$$\rho_j = \rho_0 + \frac{nW}{\Delta V_j}(Agg\ \Sigma_m)_j, \tag{3.47}$$

$$\rho_j u_j = \rho_0 u_0 + \frac{nW}{\Delta V_j}(Agg\ \Sigma_v)_j, \tag{3.48}$$

$$P_j + \rho_j u_j u_j = P_0 + \rho_0 u_0 u_0 + \frac{nW}{\Delta V_j}(Agg\ \Sigma_p)_j, \tag{3.49}$$

$$\rho_j \left(3RT_j + u_j^2\right) = \rho_0 \left(3RT_0 + u_0^2\right) + \frac{nW}{\Delta V_j}(Agg\ \Sigma_T)_j, \tag{3.50}$$

$$2\left(q_j + P_j \cdot u_j\right) + \rho_j \left(3RT_j + u_j^2\right) u_j = 2P_0 \cdot u_0 + \rho_0 \left(3RT_0 + u_0^2\right) u_0 + \frac{nW}{\Delta V_j}(Agg\ \Sigma_q)_j. \tag{3.51}$$

### 3.7.2 Properties of interest

The aim of all Boltzmann based equations is the determination of the distribution function through which the hydrodynamics properties can be determined. Under the current consideration of isothermal flows, the crucial hydrodynamic property is the **velocity flow field**. Scrutiny the flow field in the vicinity of the wall makes it possible to discern the effect of rarefaction through **slip velocity**. The effect is simulated through the dynamics of the particles acting under the Boltzmann-BGK system with Maxwell surfaces and are more reliable than Navier-Stokes solution with slip models.

The velocity information, though insightful, are unwieldy and cannot be compared with experimental data and other numerical results directly. Average macroscopic values that reflect the flow behaviour become necessary and consequently, the **mass flow rate**, obtained from the law of conservation of mass, is a function of the average velocity and cross-sectional area. The frictional effects of the surfaces can be obtained through the computation of shear stress at the wall as expressed in the form of **Poiseuille number**. The quantities of utmost importance in the field of porous media such as the **permeability** can be obtained from the mass flow rate and the rarefaction information while the **tortuosity** can de deduced from the velocity flow field.

The newly defined terms of **pore activity** and **surface interactivity** (subsequently elaborated) which are obtained here from microscopic evaluations can be viewed as analogies of **effective porosity** and **specific surface area** respectively.

## 3.8 Features of the developed solver

From an operational perspective, the solver benefits from,

a) A modular implementation of Pre-processor, Processor and Post-processor making it viable for future implementations.

b) A computationally efficient parallel implementation developed through the popular MPI framework.

c) Generation of restart files at the discretion of the user in case of a system reboot.

d) A case specification allowing multiple flow conditions to be simulated on the same preprocessed data avoiding the rerunning of the expensive file reading and storing operations.

e) In each case, the results are generated based on multiple ensembles ensuring reduced uncertainty in the final averaged output of microscopic and macroscopic data.

f) Post-processing based on the user's specification allowing a selection in the output written.

From a conceptual standpoint, the benefits are,

i) Ability to capture the flow characteristics through particle dynamics at pore-level:

The unique pore level description through a system of deviational particles enables the solver to gain some unparalleled insights into the working of the system of interest through two parameters.

In porous media, the size of the pore structures varies in an extremely arbitrary fashion. The effect of these variations on the flow is seen through the presence of multiple regions with various degrees of rarefaction. As explored earlier, collisions are less likely in a region of high rarefaction whereas they are more abundant in low rarefaction regions. In particle methods, this effect is captured through the acceptance probability of collision candidates within a cell. This probability can be used to deduce the parameter termed as **pore activity** which indicates the local degree of rarefaction. Thus for every collision event(either creation or deletion of a particle) in a cell $i \in N_{ps}$, the parameter $AggPA$ is updated as,

$$\begin{aligned} (Agg\ PA)_i &= (Agg\ PA)_i + 1, \\ (Normalized\ PA)_i &= \frac{(Agg\ PA)_i}{(Agg\ PA)_{max}}. \end{aligned} \tag{3.52}$$

Another unique vantage point that is afforded by the particulate nature of the current method is the ability to track the number of particle impacts experienced by a unit elementary surface. The time-averaged version of this value signifies the effect that the surface had in the relaxation to an equilibrium of the system. Termed as **surface interactivity**, this quantity is likely to play a significant role in future studies that consider the effect of adsorption, absorption, etc. If this ratio is high, then the surface is significantly involved in the development of the flow characteristics while a low value signifies that the surface plays a negligible role. Thus for every impact on surface $k \in N_{surf}$, the parameter $AggSI$ is updated as,

$$(Agg\ SI)_k = (Agg\ SI)_k + 1, \tag{3.53}$$
$$(Normalized\ SI)_k = \frac{(Agg\ SI)_k}{(Agg\ SI)_{max}}.$$

ii) The inherent adaptation to multi-scale effects :

The rarefaction is initially specified for the entire domain. However, the collision rules are designed in such a way that they consider the degree of local rarefaction while performing their operations thus, providing a dynamic way to consider the multi-scale effects one comes across in porous media.

This is where the ingenuity of the present implementation and its natural ability to adapt to a multi-scale system is evidenced. During a collision time step, a cell is selected and a collision event, either creation or deletion, is performed. The number of such collision events depends on the collision time step $t_{coll}$ and the time taken during the collision event $t_{c,1}$. If $t_{c,1} < t_{coll}$, then another cell is determined and the collision event with time $t_{c,2}$ is performed. The collision step is concluded when $\sum_{j=1}^{collision\ events} t_{c,j} >= t_{coll}$ The determination of the number of collisions is thus, dependent on $t_{c,j}$ which in turn depends on the local distribution of $(n, u, c)_{cell}$.

To exemplify the adaptation to multi-scale effects, consider that a cell in the region of high Knudsen number is chosen first. Then the time taken for this collision event $t_{c,1}$ will be high and very few other collisions can occur in the remaining portion of the time step $\Delta t_{coll}$. On the other hand, if the cell is chosen from a region of low Knudsen number, then the time taken for this collision event $t_{c,2}$ will be low and very many other collisions can occur in the remaining portion of the time step $\Delta t_{coll}$. This naturally implies that a low Knudsen number region will be collision dominated whereas a high Knudsen number region will be dominated by advection. When the two regions co-exist in a domain, the cell selection favours

the cell where the deviation from equilibrium suggests that the most important collision will occur.

## 3.9 Chapter summary

To summarize, variance reduced particle methods utilize the ability to decompose the distribution function $f$ into equilibrium distribution and a deviational part. $f_{eq}$ is solved analytically and is usually chosen as $f_{mb}$. The deviational part is integrated using particles. The particles are bear some semblance to the DSMC particles such as representing a number of real particles while evolving through decoupled advection and collision operators. In a very generic sense, the method evolves the system by creating particles to represent a deviation from the underlying equilibrium and deletes particles when mechanisms that drive the system towards underlying equilibrium are encountered. Samples are generated once a steady-state has been reached and are consecutively used to determine the deviation of hydrodynamic properties corresponding to the global equilibrium condition.

The work done in the present chapter, namely, the extension of the LVDSMC ideology through the development of a parallel solver for utilization in the field of porous media and MEMS systems is one half of the contribution of this thesis to the scientific community.

The remaining half is achieved through the studies focussing on a wide range of practical applications such as MEMS components and real porous media samples which establish the efficiency, accuracy, and robustness of the developed solver.

# Chapter 4

# Validation and Verification

*"There is nothing more deceptive than an obvious fact."*

*— Sherlock Holmes, The Boscombe Valley Mystery by Sir Arthur Conan Doyle*

## 4.1 Chapter overview

The solver presented in the previous chapter is put to the test by means of solving the classical problems of fluid mechanics. The primary aim of this chapter is to prove the capability of the solver to efficiently and accurately resolve these well-studied problems and thus, provide confidence in studying subsequent problems of greater practical import. The secondary ambition of the chapter is to demonstrate, through simulation of appropriately designed toy problems, the salient features of the solver that were highlighted in the previous chapter. The verification of these features will bolster the confidence when handling complex structures further on in this thesis.

## 4.2 Introduction

Any novelty in the field of academia must be tested so as to ascertain its capabilities, merits and shortcomings. Traditionally, a new method, solver or model is employed to a standard class of problems christened as the benchmarks problems. This class of problems is uniquely suited for assessment with features such as being simple without being trivial involving rich physics that is well understood within the research community. In the field of gas dynamics, some of the long-standing benchmarks have been the Poiseuille flow and Couette flow in between infinitely long parallel plates along with the occasional inclusion of lid driven cavities.

Another objective of this chapter is the demonstration of some of the features salient to this method and solver. Some of the features highlighted here through appropriate toy problems, are the implementation of approximate surfaces, implementation of various domain boundary conditions, reservoir implementation, multi-scale adaptation and measurement of surface interactivity and pore activity.

## 4.3 Validation against classical problems

The plane Poiseuille flow ranks high in the list of boundary value problems studied in the kinetic theory of gases and as such, there is an abundance of literature on this topic. The simplicity has made some researchers attempt to solve the Boltzmann equation by employing analytical approaches whereas other researchers have resorted to numerical simulations using the Boltzmann model equations. The Boltzmann-BGK kinetic model equation is often used since it replaces the integrodifferential Boltzmann equation with a purely integral one which is straightforward to treat numerically and analytically. Among these, the use discrete velocity method to solve the Boltzmann BGK equation for rarefied gas flows were presented by Cercignani [179]. In this work, the foundation of the method for using a body force to represent a small pressure gradient is pioneered. Following this, the concept has been adopted by many consequent researchers including this thesis. In another numerical analysis, based on the Boltzmann equation with the BGK model, Loyalka [180] investigated the effect of the variation of the Maxwell accommodation coefficient on the results of the plane Poiseuille flow.

More intriguing, perhaps, is the Couette flow which is described as the flow induced due to relative motion between the plates. The shear between the plate and the adjacent fluid layer has led to the classification of the flow under shear-driven flows. Another shear-driven flow gaining prominence as a classical problem is the lid-driven cavity. The problem gains it popularity due to the presence of a central re-entrant region (vortex). Most of the studies associated with such flows focus on higher Reynolds numbers where the physics captured by the circulating fluid is richer. Cases, where the lid velocity is low, are of limited practical importance and are, principally, of academic interest. For instance, Li [93] utilized the Couette flow simulation to validate the DSBGK against DSMC results as presented in 2012. Ho [90], further utilized the lid-driven cavity to compare the DSBGK and DVM results for rarefied, low-speed gas flows. Couette and Lid-driven cavities were utilized to establish the accuracy of the DUGKS scheme proposed by Guo in 2013 [85].

### 4.3.1 Problem statement

Poiseuille flows can be described as the flow induced by a force due to a pressure difference between the two ends of the channel. Based on the implementation, the flows are classified as force driven or pressure-driven. In this study, the force-driven method is used to simulate the flow as presented in fig.4.1a. In the Couette flow, the top plate assumed to move from right to left whereas the bottom plate moves from left to right with a non-dimensional X velocity of 1. The flow domain is further clarified in the schematic shown in fig.4.1b. The schematic of the cavity flow is depicted in fig.4.1c wherein the bottom plate moves with a small tangential velocity that is normalized and scaled to unity.

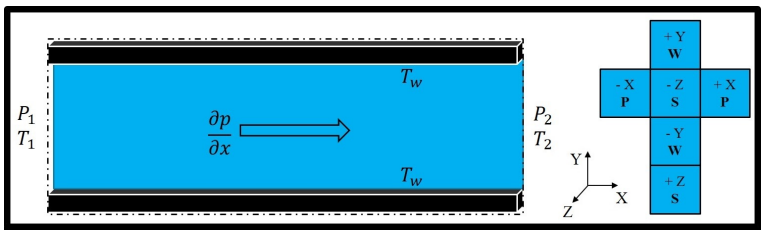


(a) Plane Poiseuille flow

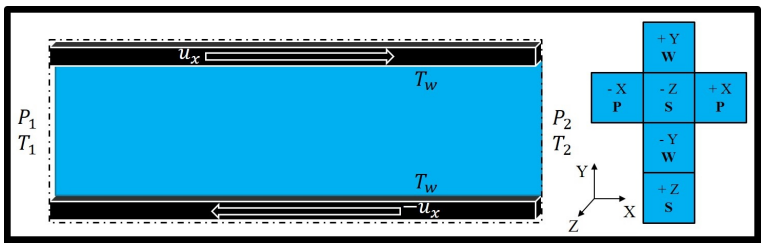


(b) Plane Couette flow

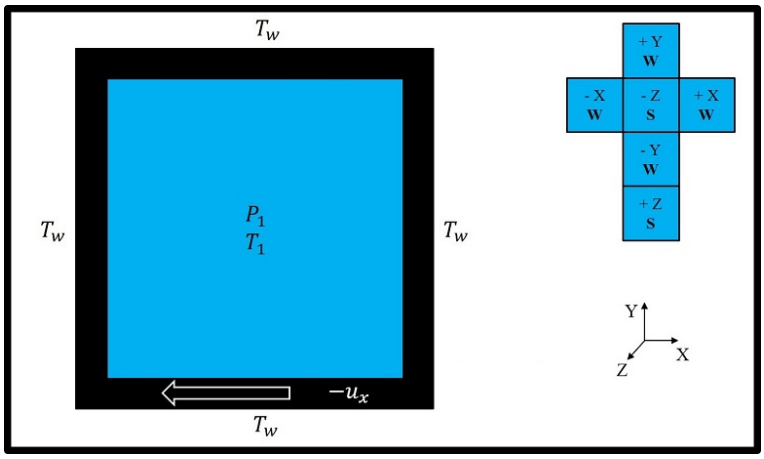


(c) Shear lid driven cavity

Figure 4.1: Schematic diagrams for the various benchmark problems considered for validation.

In order to better validate the results of the present method, the comparison is done against results obtained from popular contemporary methods such as DVM, DSBGK and DUGKS. Each of the benchmark cases studied is presented in the remaining chapter along with the results obtained and their analyses.

### 4.3.2 Simulation results

In the present section, the validation of the solver with respect to each of the benchmark flows is conducted by simulating the flows for the entire range of rarefaction.

Additionally, for the Poiseuille flow, each value of Knudsen number is accompanied by a variation in the accommodation coefficient $\alpha$ between 0.60 to 1.00. The LMNS speed contour for $\alpha = 1.00$ is shown in fig.4.2a. The reduced mass flow rate (computed as discussed in section 2.4.2) with the characteristic length taken as the channel width.

The result is plotted in fig.4.2b. The effect of the various $\alpha$ is shown through fig.4.2c while the velocity profile at the channel center is depicted in fig.4.2d.

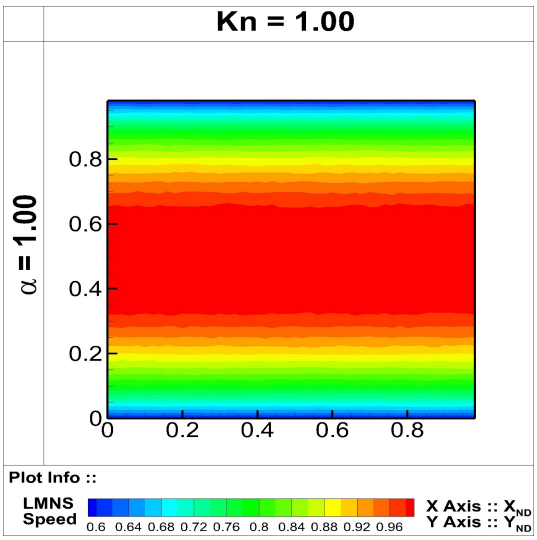


(a) LMNS speed contour plot.

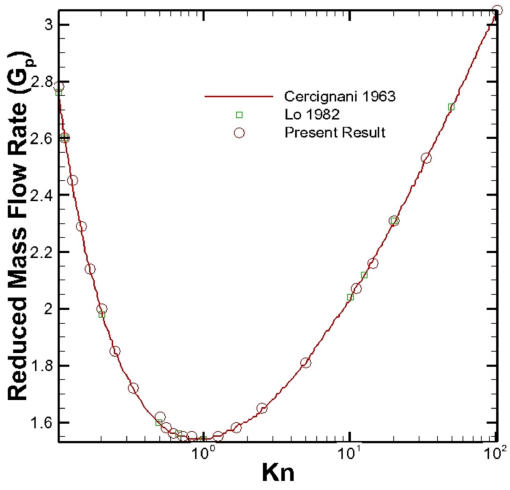


(b) Reduced mass flow rate (Literature: [179], [181]).

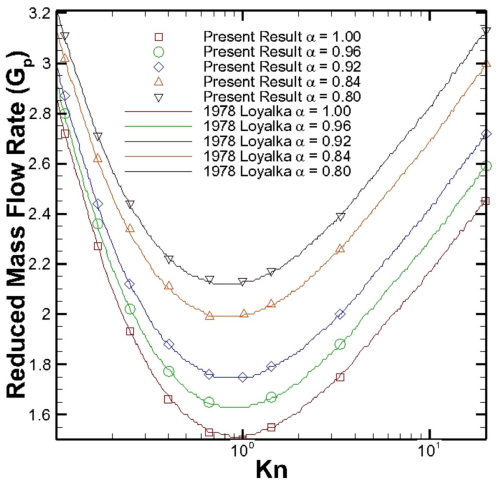


(c) Reduced mass flow rate $\alpha$ variation (Literature: [180]).

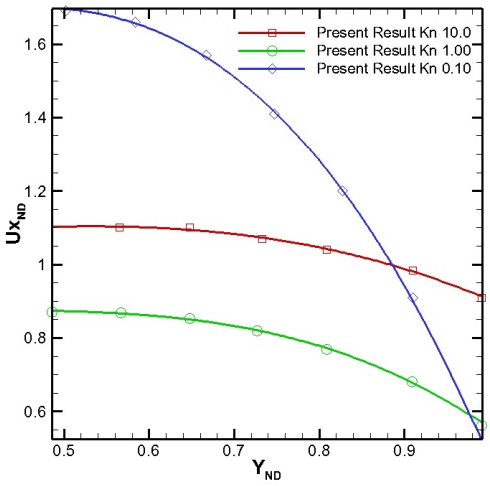


(d) Velocity profile at channel center.

Figure 4.2: Results for the plane Poiseuille flow simulation and comparison with literature.

The results comprising of the LMNS speed contour in addition to the variation of the velocity for a Couette flow is depicted in figs.4.3a and 4.3b respectively. The confined nature of the flow in cavities causes variations in the X and Y velocity components and their profiles along the center of the cavity are shown in fig.4.4c and fig.4.4d along with the LMNS X and Y velocity contour in figs.4.4a and 4.4b respectively.

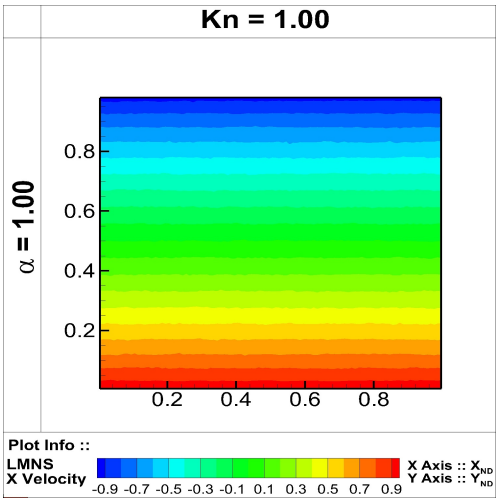


(a) LMNS X velocity contour plot.

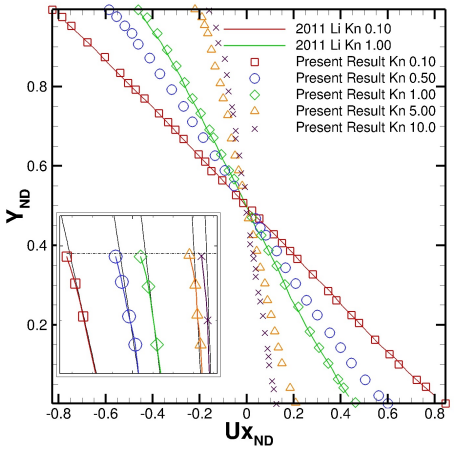


(b) Velocity profile at channel center (Literature: [92]).

Figure 4.3: Results for the plane Couette flow simulation and comparison with literature.

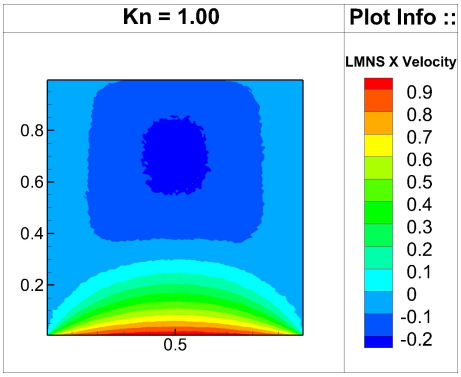


(a) LMNS X velocity contour plot.

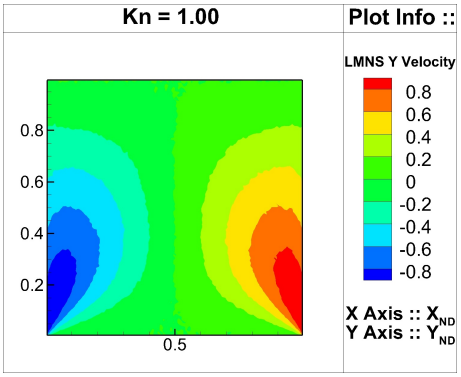


(b) LMNS Y velocity contour plot.

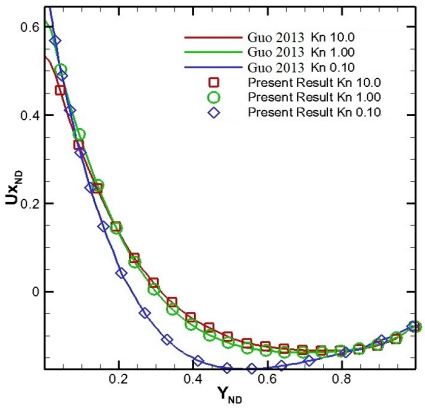


(c) X velocity profile (Literature: [85]).

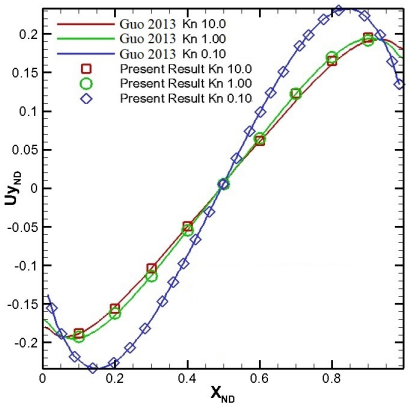


(d) Y velocity profile (Literature: [85]).

Figure 4.4: Results for the shear lid driven cavity flow simulation and comparison with literature.

### 4.3.3 Observations and inferences

One of the great topics of research is the effect of non-equilibrium originating at the walls of the channel/cavity which creates significant differences between the actual flow behaviour and the description provided by the hydrodynamic governing equations such as the Navier-Stokes system. The principal reason behind this discrepancy is explained through the kinetic theory of gases which recognizes the inhomogeneity at the fluid-wall interface where the distribution functions are discontinuous. The consequence is the formation of a region of non-equilibrium adjacent to the wall. The thickness of this (region) layer, called the 'Knudsen layer', is seen to increase with the rarefaction of the gas. For flows with small Knudsen numbers, i.e. continuum flows, it has been observed that the effects are negligible whereas, at higher Knudsen numbers, the thickness of the Knudsen layer is such that the majority of the flow field is influenced by the non-equilibrium effects and the use of continuum methods is no longer applicable without severe reservations with regards to the results obtained.

In Poiseuille flow studies, a peculiarity is observed in the mass flow rate which decreases with a decrease in the degree of rarefaction and attains a minimum in the vicinity of $Kn = 1.00$ (fig.4.2b). Any further decrease in the degree of rarefaction results in an increase in the mass flow rate. Termed as the Knudsen paradox (alternatively, Knudsen minimum), this counter-intuitive phenomenon was first observed by Knudsen in 1909 [182] and explained through the kinetic theory of gases. The influence of a decrease in the accommodation coefficient ($\alpha$) results in an increased mass flow rate at a given Knudsen number (fig.4.2c).

Ever since it was observed, the Knudsen minimum phenomenon has been the subject of intense scrutiny and detailed studies. It is now widely agreed that the phenomenon is an effect of the Knudsen layer. The far reaches of the Knudsen spectrum can be characterized by the most dominant mode of transport. At low Knudsen numbers, the particles are densely packed and thus, the mode of transport of information is mainly through inter-molecular collision mediated bulk transport. Conversely, at high Knudsen numbers, the rarefaction is such that particle collisions are a rare occurrence and thus, the transport of information is through ballistic transport restricted by molecule-wall collisions. The Knudsen minimum occurs in situations where the influence of both the intermolecular collisions and molecule-wall collisions are equally significant. This poses severe opposition to the mass flow and thus, the mass flow rate around $Kn = 1.00$ contains a minimum. On either side of this minimum, the mass flow rate increases as the influence of one form of transport dominates the other.

Another noteworthy effect of the Knudsen layer is the slip velocity at the wall which increases with the Knudsen number.

In Poiseuille flow studies, the LMNS speed field (fig.4.2a) exhibits a region of high value at the channel center whereas, the effect of rarefaction is seen as a slip at the walls. The corresponding velocity profile is parabolic and tends to flatten out as the

gas becomes rarefied (fig.4.2d) which is also indicative of the reduced bulk transport at the channel center and increase transport at the surface.

In the Couette flow studies, the velocity field (fig.4.3a) depicts a stationary central flow region with the velocity at the walls dictated by the wall velocity. The velocity profile at a central X station is traditionally a linear variation with a crossover in sign at the undisturbed fluid layer (fig.4.3b). This conventional result is valid for the continuum regime but, the profile becomes non-linear near the walls as the rarefaction increases(inset of fig.4.3b). Such an effect is attributable to the increased slip at the walls under rarefied conditions.

Lid-driven cavity studies are more compelling than Poiseuille and Couette flows in the context of being the first true 2-D problem handled by the solver with significant velocity variations along two directions. Moreover, the X velocity flow field shows a region of circulation (fig.4.4a). This vortex is close to the vertical line as the velocity profile about $Y$ is symmetric (figs.4.4b and 4.4d) but, exhibits a tendency to move downwards and towards the left, as the rarefaction increases (fig.4.4c). This shift also an outcome of the increased velocity slip at the walls.

Apart from appealing to the physical intuition, these results also show excellent agreement with literature results obtained through contemporary kinetic methods. The agreement, demonstrated in figs. 4.2c, 4.3b, 4.4c, 4.4d, is encouraging and allows the extension of the solver to more complex scenarios.

In summary, the presence of the wall is essentially a source of non-equilibrium and is mitigated through inter-molecular collisions. Rarefaction results in the waning of these collisions consequently strengthening the influence of the wall manifested through a slip velocity. A decrease in the surface accommodation coefficient ($\alpha$) is a decrease in the wall's ability to restrict ballistic transport. Thus, an increase in mass flow rate is effected through increased slip at the walls as $\alpha$ decreases.

## 4.4 Verification of implemented features

In the following section, the various implementations added to the solver are demonstrably verified by qualitative problems. The claims made with regard to the favourable nature of the present method in porous media flows is also verified.

### 4.4.1 Proof of concept - Transient reservoir

A novelty in the current formulation is the implementation of reservoirs that serve as a means of incorporating localized non-equilibrium effects through the introduction of a source or sink of mass or thermal energy. The present purpose is the demonstration of such a transient reservoir. To this end, a system in equilibrium at time $t = 0s$ is considered, an instantaneous source is generated at $t = t_{start}s$ and eliminated at $t = t_{finish}s$. The strength of the source can either be constant or increase/decrease

gradually over the operating time of the reservoir i.e. $(t = t_{finish} - t_{start})$. In the current study, the constant strength reservoir is used and the system is monitored until it re-attains equilibrium.

In concert, the role of surfaces in the relaxation of a disturbed system to equilibrium is also queried. The aforementioned relaxation study is carried out in two possible domains viz.,

1. A fully periodic infinite domain (ID) devoid of walls thereby forcing the relaxation to equilibrium to be driven by collisions only.

2. A confined domain (CD) wherein the relaxation is driven by wall and intermolecular collisions

The reference length is taken to be the $X$ directional length of the unit cell in both cases. The study in both domains is repeated for different degrees of rarefactions. The schematic is shown in fig.4.5. The process is illustrated through a time-lapse contour plot of the LMNS speed in fig.4.6 and the relaxation of deviational mass with time is plotted in fig.4.7.

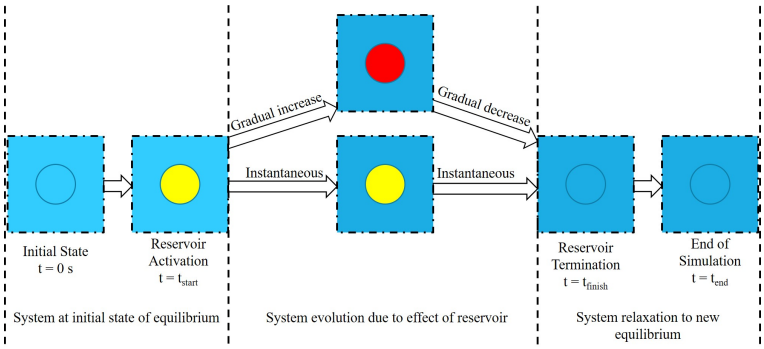


Figure 4.5: Schematic for relaxation study of a transient reservoir.

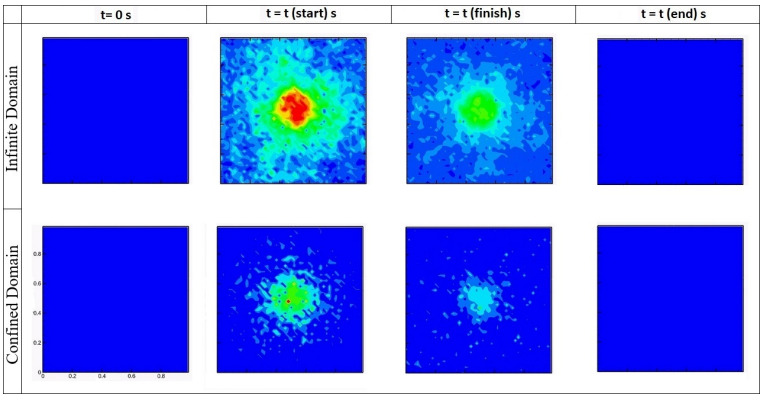


Figure 4.6: Deviational number density plot for relaxation of a transient reservoir (red to blue : highest to lowest).

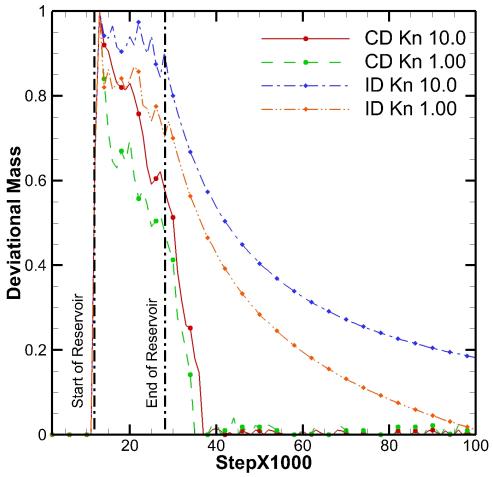


Figure 4.7: Plot depicting the relaxation of deviational number density(mass) for a transient reservoir.

The first noteworthy observation is the difference in the relaxation of the deviational mass for ID and CD systems. It has been previously explained that the diffusive reflection from walls acts as a means of aiding the system attain equilibrium. The efficacy of these surface is seen in the precipitous drop in the deviational mass once the reservoir is eliminated. The lack of walls forces the domain to attain equilibrium through collisions and thus, the relaxation for an ID system is gradual.

The second point of note is the effect of the degree of rarefaction which can be interpreted as a number characterizing the relative importance of inter-molecular collisions and wall interactions. A higher $Kn$ signifies lower inter-molecular collision and is indicated by the slower return to equilibrium of the $Kn = 10.0$ case.

### 4.4.2 Proof of concept - Surface approximation verification

In the present design, of the induction the solid matrix into the computational domain is done through the reading the binary input file that stores the image in pixel maps. The result of the pixel map in conjunction with the Cartesian grid leads to ziggurat-like approximations of slanted and curved surfaces (fig.4.8).

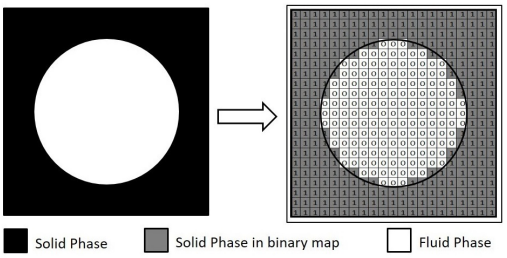


Figure 4.8: Demonstration of pixelated approximation of curved surfaces.

While such approximations are tolerated in porous media studies, principally due to the uncertainty associated with the original nature of the surface, such liberties cannot be extended to studies involving MEMS components that are well-engineered.

In the present implementation, this issue is addressed through the use of approximate surfaces. An approximate surface can take the form of any surface that can be defined by an equation between two points (or 4 points in 3D). The simplest such implementation is a line segment, whereas complicated structures such as sine curves are also possible (though not practical).

When a particle encounters a parent surface, a check is conducted to see if they are associated with an approximate surface. If so, the particle is backtracked until its point of intersection with the approximate surface is determined. The reflection of the particle is then processed from that point, accounting for the angle of the approximate surface. Thus, the reflection is done in a manner that conserves the position and momentum of the particle.

In order to visually appreciate the effect of ziggurat-like approximation of curved surfaces and the implemented corrections, the flow through a coarsely resolved circular long-duct is considered. The results are presented in fig.4.9.

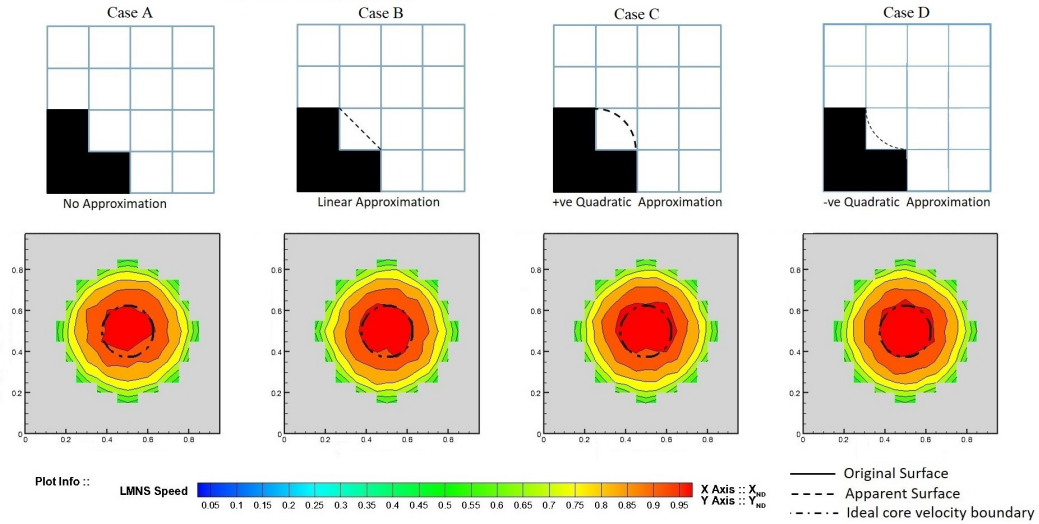


Figure 4.9: Demonstration of surface approximation effect on the LMNS speed contours.

Under the steady, laminar flow condition considered, the velocity contours are expected to take the form of concentric circles with the inner region coinciding with the reference circle represented by dashed lines. It is evident that the conformance is best met for case D followed by cases B, C, and A. The macroscopic effect is better appreciated by comparison of the slip velocity against a highly resolved similar case and the above-observed order is seen to persist.

A mathematical appreciation can be garnered by the percentage difference in slip velocity measured at various points depicted in fig.4.10. Ideally, the slip at these points must be equal owing to the symmetric nature of the flow, but it is seen in table.4.1

Table 4.1: Data for demonstration of surface approximation for a highly resolved circular duct flow.

| Kn | Max. % difference between points. | | | |
|---|---|---|---|---|
| | Case A | Case B | Case C | Case D |
| 10.0 | 0.8100 | 0.0780 | 0.1200 | 0.0281 |
| 1.00 | 1.0200 | 0.0012 | 0.5200 | 0.0010 |
| 0.10 | 0.9800 | 0.0320 | 0.6100 | 0.0130 |
| 0.01 | 1.2200 | 0.0980 | 0.5500 | 0.0240 |

that the closest conformance is met for a surface approximation implemented in Case D.

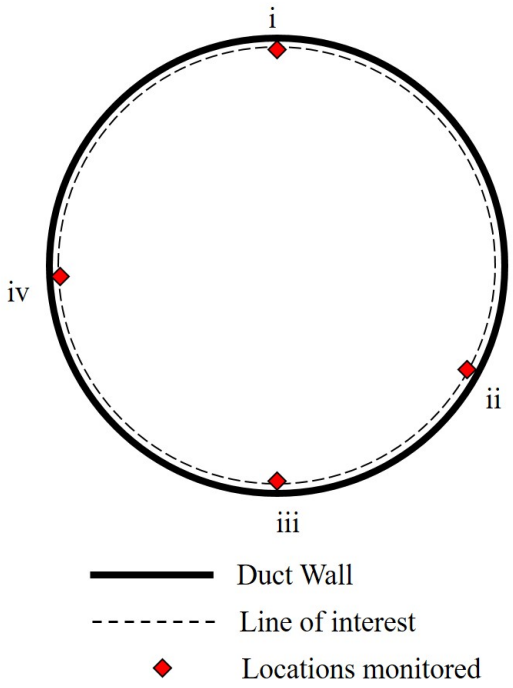


Figure 4.10: Schematic for demonstration of surface approximation for a highly resolved circular duct flow.

### 4.4.3 Proof of concept - Domain boundary condition

The specification of computational domain boundaries is an integral part of the representation of an actual system in a simulated environment. One excellent example is the representation of a large array by a simulated unit cell with periodic boundaries. Other boundary conditions produce various other reproductions of actual cases. The physical interpretation of the various boundary conditions is shown in fig.4.11. The corresponding LMNS speed contours for a $X$ direction pressure gradient is depicted in fig.4.12.

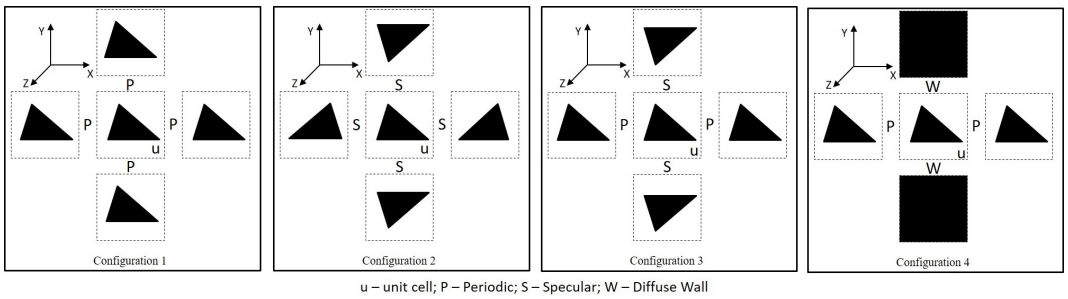


Figure 4.11: Physical interpretation of various boundary conditions.

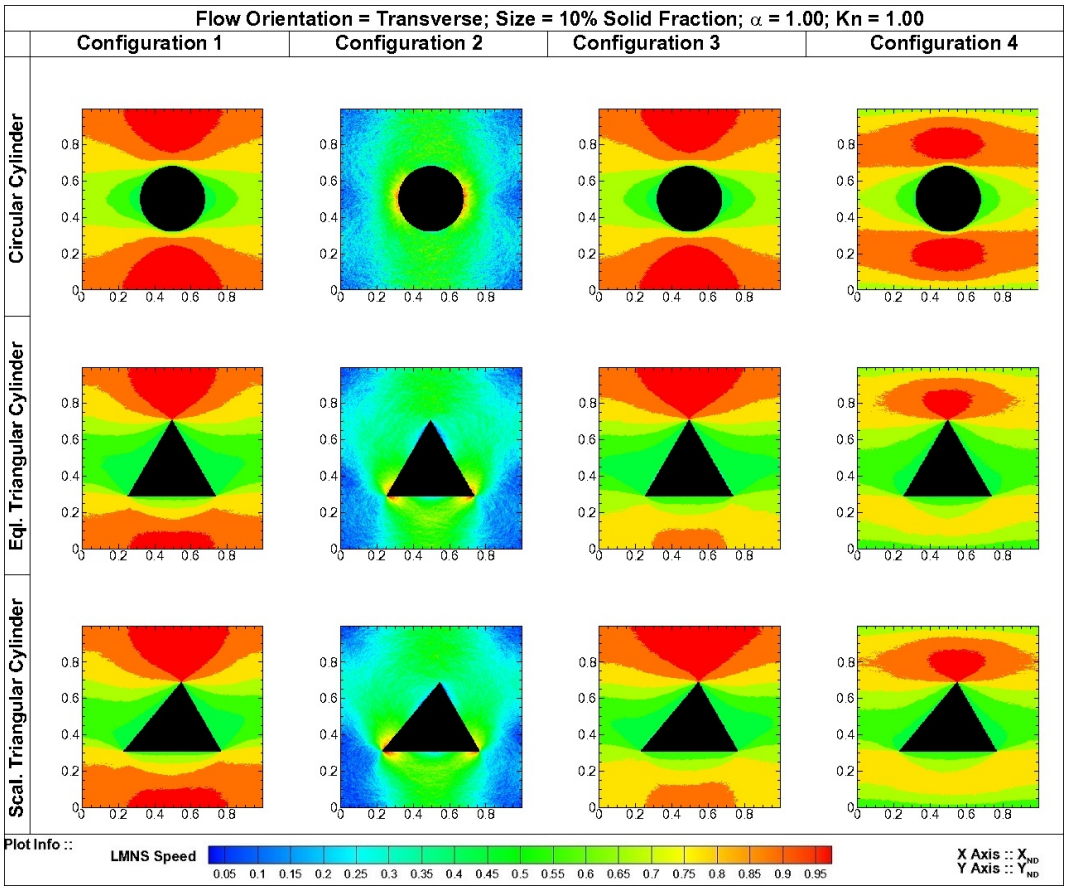


Figure 4.12: LMNS speed contour plot emphasizing the effect of various boundary conditions.

Configuration 1 considers all boundaries as periodic which can be utilized to represent an infinite array of identical, symmetric obstacles. Configuration 2 assumes all boundaries are specular and is indicative of a physical condition where the pressure is equal across the boundary. The lack of a pressure gradient makes the flow inconceivable and the result of a body force is equalized across the boundaries. It is a feature that can be used effectively in conditions where the pressure difference across the boundaries is insignificantly small.

Configuration 3 is a manifestation of a combination of periodic and specular bound-

ary conditions. Periodic boundary conditions are effective in directions where the pressure variation across the boundary is significant whereas the specular boundary condition is more appropriate where the pressure difference across the boundary is insignificant. Such a case is demonstrated by the circular cylinder where the pressure difference across the top and bottom domain boundary conditions is negligible. However, this is untrue for an equilateral triangle which by virtue of its asymmetry along the Y plane, causes a significant pressure difference across the top and bottom domain. This effect is explicitly demonstrated by the velocity profile shown in fig.4.13. For a circular cylinder, Configuration 1 and 3 yield identical profiles whereas the same cannot be said for the equilateral triangle.

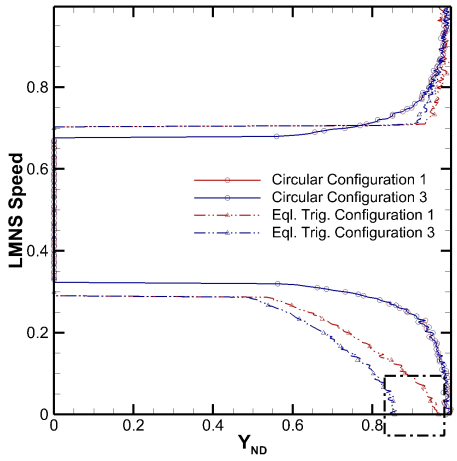


Figure 4.13: Velocity profile at the channel center for the circular and equilateral triangle.

Configuration 4 represents a confined flow of a 1D infinite array through the specification of a periodic boundary condition in the direction of flow and wall surfaces in a direction perpendicular to the flow.

### 4.4.4 Proof of concept - Demonstration of surface interactivity

One of the main reasons for the adoption of the present method is the ability of the method to effectively handle the pore-scale representation of porous media while providing unparalleled insight into the deeper dynamics of the flow. The method achieves this through the determination of the newly defined parameters, such as pore activity and surface interactivity.

The present focus is on the demonstration of surface interactivity. To fully appreciate this, consider the flow problem highlighted in the schematic fig.4.14. The particle nature of the current method makes it possible to monitor and capture every collision between particles and surface elements through eq.3.53.

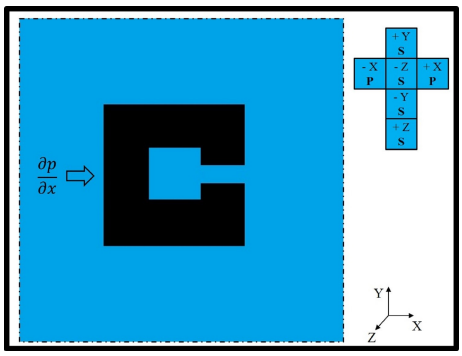


Figure 4.14: Schematic of the flow problem for demonstrating the surface interactivity.

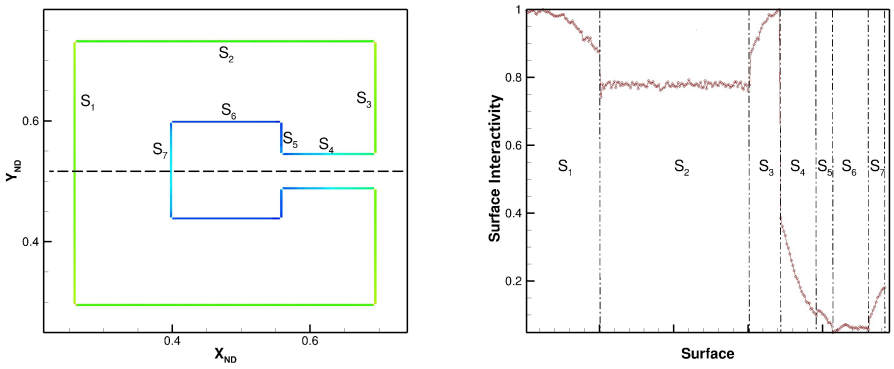


(a) Intensity of reflections at each surface.

(b) Plot for surface interactivity.

Figure 4.15: Results of the flow problem for demonstrating the surface interactivity.

The geometry is a simple approximation of porous media and intuition dictates that the surfaces of the outer square will be subject to more particle interactions than the surfaces of the inner square. True to form, the intensity of particle collision faced by a surface (highlighted in fig.4.15a and graph in fig.4.15b) supports this anticipated outcome.

### 4.4.5 Proof of concept - Demonstration of multi-scale adaptability

The measurement of pore activity (eq.3.52) is essentially the measurement of the collision acceptance in a particular cell and is inherently linked to the demonstration of the automatic adaptation of the present method to multi-scale physics. To demonstrate this, consider the flow problem shown in fig.4.16.

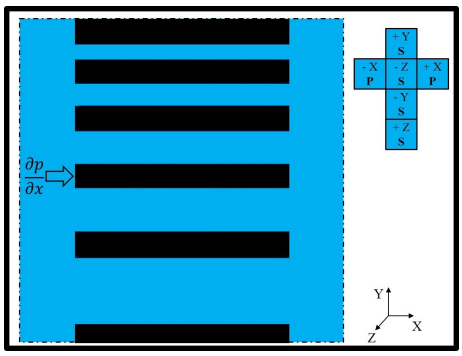


Figure 4.16: Schematic of the flow problem demonstrating the multi-scale adaptability.

The various channel pathways ($R_{1...5}$) have various cross-sectional lengths that essentially imply that their local Knudsen number ($Kn_l$) is different with $R_5$ having the smallest $Kn_l$ and progressively increasing till $R_1$.

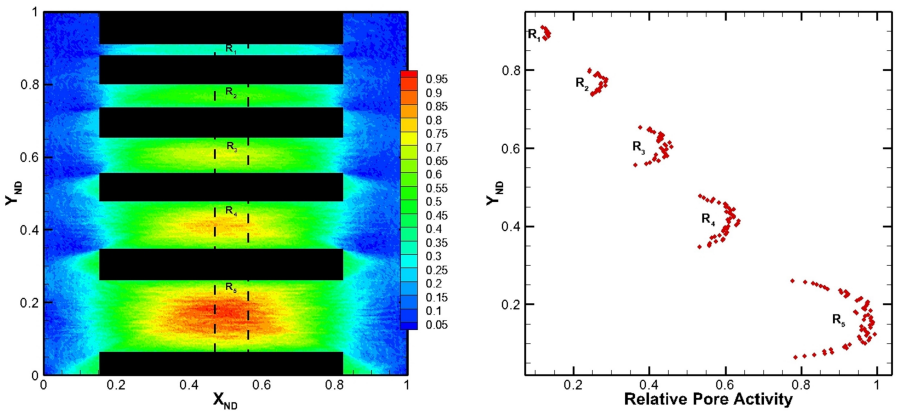


(a) Intensity of pore activity.

(b) Plot for pore activity.

Figure 4.17: Results of the flow problem demonstrating the multi-scale adaptability through pore activity.

A low $Kn_l$ indicates higher intermolecular collisions and thus, higher acceptance of collision candidates (pore activity) as observed in fig.4.17a. It is a fair characterization that the lower the local rarefaction, the higher the pore activity. Furthermore, the intermolecular collisions are expected to be adversely affected in the vicinity of a wall since molecule-wall interactions become likely. This is observed in fig.4.17b where the pore activity plots are parabolic, becoming flatter as higher $Kn_l$ are reached (i.e. $R_1$ ).

Thus, the effect of local rarefaction is automatically captured with no extraneous treatment making this method uniquely suited for the multi-scale porous media problems.

## 4.5 Numerical parameters and computational expenditure

All computations were performed on a workstation comprising of 32 CPU of Intel(R) Xeon(R) CPU $E5-2630\ v3\ @\ 2.40GHz\ architecture\ x86-64$. The simplicity of the cases included in this section facilitates the utilization of a coarse $20X20$ grid to obtain reasonable results, despite which, a finer $100X100$ grid was employed to obtain a better match with literature. The use of 10 particles per cell was found to be sufficient to obtain excellent results. Additionally, optimal computational effort for such simple cases was acquired if 4 processors were employed.

Under these conditions, the computational time for a specific case across 10 Knudsen numbers ranging from rarefied to continuum was obtained in less than an hour. Furthermore, the simplicity of the cases made it possible for a quick convergence, typically around the $500^{th}$ step and 10000 samples were deemed sufficient to obtain hydrodynamic properties through averaging.

## 4.6 Analysis and conclusions

In the present chapter, the focus was on establishing the capabilities of the developed solver. In accordance with this objective, the first part of the chapter is dedicated to validation through the simulation of three canonical micro-flow problems. The latter part of the chapter seeks to provide verification of the features that the solver possess through the simulation of appropriately designed flow problems.

The simulation of the 3 classical flows is seen to reproduce the atypical phenomena that are unique to micro-scales and noticeably absent in their macroscopic counterparts. Foremost among these is the formation and subsequent growth of the Knudsen layer. The manifestation of this layer in the form of the Knudsen minimum in pressure-driven flows and gas slip in shear-driven flows is adequately captured by the current simulation. The veracity is further strengthened by the excellent agreement with literature results that are obtained through well-established methods.

Aside from the benefit of validation, the clandestine motive behind the effort dedicated to the study of plane Poiseuille flow is revealed by a direct quote from Cercignani and Daneri [179] which reads as,

*"The difficulties one is faced with in solving problems by the Boltzmann equations when the geometry is not plane unidimensional one suggest investigating the Poiseuille flow between two parallel plates before treating channels with finite sections..."*

Since the treatment of channels with finite sections is the prospect investigated further on by this thesis (Chapter 5), the advice is greatly relevant.

The myriad of issues plaguing the porous media flow scenarios are seen to be mitigated or adequately managed by the present implementation. For instance, the number of exposed surfaces, which are deemed as a deterrent for most numerical methods due to the associated computational expense are actually a means of keeping the particle num-

ber tractable in the present simulations. Moreover, the multi-scale effects associated with the myriad of pore-sizes is naturally considered through the stochastic approach to the collision operator.

Additional insights are provided by tracking of the particle interactions with the surfaces (quantified by surface interactivity parameter) and collision frequency in each pore (quantified by pore activity). Surface interactivity can play a pivotal role in the modelling of surface phenomena specific to geological porous media structures such as desorption, adsorption, and erosion. For example, the selective application of the adsorption model to surfaces that possess high interactivity and desorption models to surface with low interactivity is a viable strategy to adopt.

In conclusion, it has been decisively proven that the current ideology and its implementation are not only capable of capturing established micro-scale effect but also, endowed with features that make it an ideal candidate for the study of complex micro-scale structures such as MEMS application and porous media. This has been veritably accomplished by the numerous studies presented in this chapter

## 4.7 Chapter summary

The primary function of this chapter was to establish the method's validity and verify the implementation of its features. The validity is established by simulation of a force-driven Poiseuille flow, shear driven Couette flow and shear-Lid driven cavity flow under isothermal, near-equilibrium conditions. The results reproduce the effects observed in literature and agree well with reported results. The features of the associated solver are highlighted by appropriately chosen toy problems. The extension of the investigation to more challenging systems such as MEMS components is addressed in the next chapter.

# Chapter 5

# Applications in MEMS Devices

*"Scientists are actually preoccupied with accomplishment. So they are focused on whether they can do something. They never stop to ask if they should do something."*

*— Dr. Ian Malcolm, Jurassic Park by Michael Crichton*

## 5.1 Chapter overview

The first application of the PEGASUS solver is to the low-speed rarefied gas flows encountered in various microfluidic-MEMS devices which can be broadly classified as either internal flows through ducts, networks etc. or external flows around a large array of obstacles. This chapter also aspires to be a pivotal link that enables the narrative of this thesis to seamlessly transfer its attention from MEMS systems to porous media, whose liberal definitions entitles infinite ordered arrays of obstacles in the flow path to be considered as a rudimentary facsimile.

## 5.2 Introduction

Recognizing that an actual microfluidic-MEMS device is a complex system consisting of a wide range of subsystems; it is impractical to expect to gain meaningful insights as to the efficacy of the solver through simulation of an actual device. Instead, a simpler, fictional device is constructed such that it incorporates the major recurring constituents of an actual microfluidic-MEMS device making it possible to isolate, study and understand the characteristics of these constituents individually.

In the fictional microfluidic-MEMS device shown in fig.5.1, reservoir $R_1$ and $R_3$ are connected through constituent "a" and a path passing through constituent "b". Under the assumption that the reservoirs contain the same species of gas and are at a state where, $T_1 = T_3$ and $P_1 > P_3$, a pressure-driven flow is induced between these reservoirs.

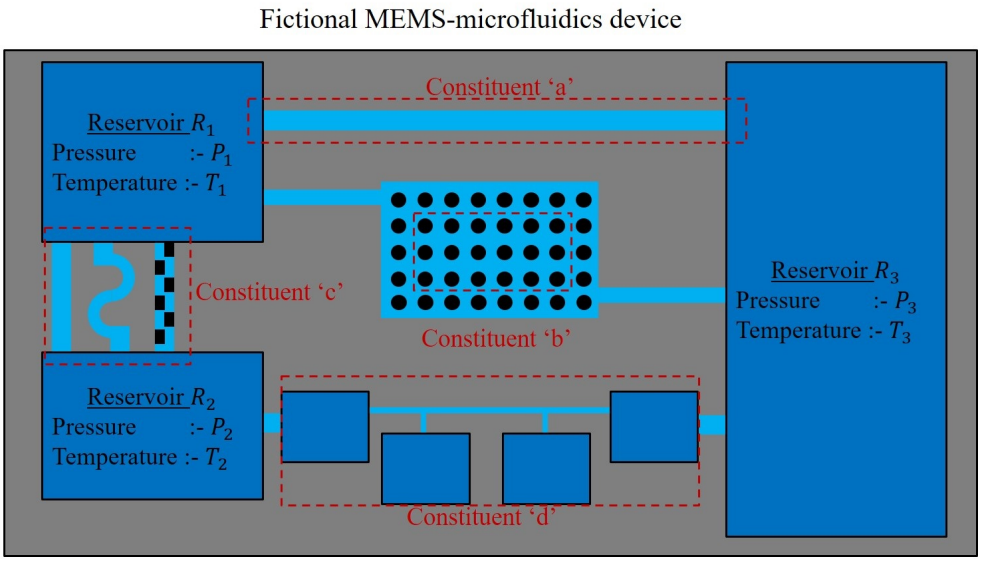


Figure 5.1: Schematic of a fictional microfluidic system with key MEMS components.

Constituent "a" is a duct whose length is much greater than its dimensions in the other directions and is referred to in literature as a "long-duct", often accompanied by a number of assumptions based on sound physical reasoning.

The flow between reservoir $R_1$ and $R_3$ can also occur through constituent "b". Obstacles are often placed in the path of a flow as a means to monitor the flow and provide passive control. These obstacles are usually designed to be ordered arrays extending over a large region; the interior of which is labelled as constituent "b".

Reconsidering fig.5.1 shown above, reservoir $R_1$ and $R_2$ are connected through constituent "c" which is a duct whose length is comparable with its other dimensions, implying that the assumption made in long-ducts are no longer applicable. Furthermore, reservoir $R_2$ and $R_3$ are connected through constituent "d" which is a duct network where the flow can be augmented or deprived of mass due to the presence of intermediate reservoirs. The end effects are active and play a vital role in the evolution of the flow characteristics. Once more assuming that the reservoirs contain the same species of gas, various thermodynamic states such as pressure-driven flows ($T_1 = T_2$ and $P_1 < P_2$), temperature-driven flows ($T_1 < T_2$ and $P_1 = P_2$) or a combination of both ($T_1 < T_2$ and $P_1 > P_2$) are possible.

Based on the above descriptions, the following constituents can be defined and isolated for further studies,

1. Isothermal flow through long-ducts.
2. Isothermal flow past infinite array of obstacles.
3. Isothermal flow through short-ducts.
4. Isothermal flow through networks.

At present, the focus is directed onto the first two constituents (a and b), while the remaining two are considered as subjects for future studies. This restriction in the scope does not diminish the quality of the present study as these constituents find a plethora of applications in the industry such as microelectronic cooling [183], MEMS [184], fuel cell technology [185], medical and biomedical devices [186] and many more.

## 5.3 Studies with regards to MEMS-microfluidics:: Isothermal long-ducts

Either by functionality or necessity (such as lubrication, cooling, etc.), MEMS devices are largely dedicated to the low-speed transport of mass, momentum and energy through structures that are classified as long-ducts. Though this fact lends credence to a number of simplifying assumptions, the flow still warrants scrutiny owing to a significant difference in the behaviour at micro-scales compared to their macroscopic counterparts. This has encouraged a large number of researchers to invest their resources to the investigation of these flows.

### 5.3.1 Literature review

Experimental investigation [187–189] has established that the continuum assumption and associated numerical methods are ill-suited to resolve flows of current interest. Arkilic's [187] investigation of Helium flow through a long rectangular channel of dimensions 52.25 X 1.33 X 7500 $\mu m$ exhibited a reduced pressure drop and friction coefficient compared to the theoretical values based on the continuum hydrodynamics, while, Araki's [188] consideration of Helium and Nitrogen flows through three different trapezoidal cross-sections with hydraulic diameter varying in between 3 to 10 $\mu m$ obtained friction factors that were in deficit compared to the conventional theory.

The above research concludes that the flows through these microchannels are rarefied and the Navier Stokes system needs to be augmented by the slip conditions [190]. Flow in such regimes are of immense practical implication in the microfluidic industries and thus, many researchers have focussed on the slip flow regime through microchannels with various cross-section shapes [138, 191, 192].

Concomitantly, studies of slip flow through channels and circular tubes by Kennard [193], annular and rectangular shapes by Ebert [194] and elliptical cross sections by Duan [195,196] added to the understanding of the cross section's effect. 2D rectangular cross-sections transporting steady, hydrodynamic, developed laminar slip flows were investigated by Morini [197, 198] while, Renksizbulut [199], examined developing flows in 3D rectangular micro ducts. Bahrami [200,201] studied the pressure drop of fully developed, laminar, incompressible flows, validating their results for cross-sections such as rectangular, trapezoidal and elliptical shapes with experimental, analytical and numerical data. Wang [202] conducted analytical studies of slip flows through triangular ducts

and provided the variation of the mass flow rate and friction factor as a function of slip. The solution presented in their work is an exact solution. Low-Pressure Boundary Slip model within the framework of Fluent [203] was developed by Pitakarnnop [204] and applied to triangular and trapezoidal cross-sections. Tamayol [205] obtained closed-form solutions for fully developed slip flows through polygonal, rectangular and rhombic cross-section by assuming the Poisson's equation and applying least squares matching of the boundary values at the wall. The results are found to match with existing literature.

Compendiums of slip flow studies through various cross-sections comprising of analytical, experimental and numerical results are a rich source of information and a number of these exists for laminar flow and forced convection for a Newtonian fluid with constant properties passing through stationary, straight, non-porous ducts of constant cross-section [206–208].

Through experiments, Colin [209] found that the first-order slip boundary condition is deficient in predicting the mass flow rate and proposed a second-order slip boundary condition valid for Knudsen numbers up to 0.25. Other attempts have also been made to extend the studies to the transition regime by extending the slip boundary condition to higher orders such as those by Sreekanth [210] based on experimental data and Colin [211] employing Deissler's [212] implementation. Although a lot of research has been done in extending the slip boundary model to the second-order, they have been met with limited success largely due to the community's inability to reach a consensus regarding the second-order slip coefficient [213]. This, along with the rise of applications that involve micro-ducts with flows that could range from hydrodynamic to free molecular flows, has necessitated methods that are capable of solving the entire rarefaction spectrum.

Much work has been devoted to numerical solutions of the Boltzmann equation with kinetic models for single gas flows through various cross section such as rectangular [214], [215], [216], [217], [218], [219], elliptical [214], [220], [221], triangular [222], [223], trapezoidal [219], [223] or concentric annular [224] cross sections.

Sharipov [225] reviewed and compiled a vast number of studies conducted on the rarefied internal gas flows through ducts listing numerical and analytical results for the major parameters of interest such as mass flow rate and heat flux due to the pressure and temperature drops across the duct. In previous works, Sharipov analysed the flow through a circular duct at any pressure ratio using the Boltzmann-BGK model [226] and any temperature ratio using the Boltzmann-S model [227]. Later works have focussed on the flow through rectangular ducts (where the effect of lateral walls are instrumental) under thermal [216] and isothermal conditions [215] for the whole range of Knudsen numbers. Isothermal [220] and thermal [221] gas flows through the elliptical cross-section was carried out by Graur with extensions to rectangular cross-sections in a subsequent article [217] for the whole range of rarefaction with various aspect ratios using the Boltzmann-BGK and Boltzmann – S model for isothermal and non-isothermal

flows respectively. Rykov [214] obtained results for a fully developed rarefied gas flow under a pressure gradient through rectangular and elliptical cross sections by utilizing a high order method to solve the Boltzmann-BGK equation.

Naris [222] addressed the potential errors of using a Cartesian grid to resolve cross-section shapes that did not conform to such a grid. The research focussed on studying the fully developed rarefied flow through triangular ducts using the Boltzmann equation with the BGK kinetic model equation. The method employed a boundary fitted lattice in place of the Cartesian grid and reported results regarding the velocity profiles and the flow rates for the full range of Knudsen numbers. The results show a good agreement with the analytical results at the free molecular and hydrodynamic limits.

Varoutis [223] conducted experimental and computational studies of fully developed rarefied flows through a number of arbitrary cross-sections such as circular, orthogonal triangular and trapezoidal shapes. The computational and experimental studies cover the whole range of Knudsen numbers and a good agreement is found between them. The computational method is based on the Boltzmann equation with the BGK kinetic model solved using the Discrete Velocity Method and employing Maxwell diffuse specular boundary condition. In another article [219], the authors expand on the work done by Valougeogris [170] and study the variation of the Poiseuille number for a fully developed rarefied gas flow through a rectangular cross-section for the whole range of Knudsen number.

Ritos [228] studied the pressure- and temperature-driven flow through triangular and trapezoidal long-ducts solving the linearized Boltzmann equation with the Shakov kinetic model through DVM. The focus of the research is on the calculation of the mass flow rates and the pressure distribution along the duct in addition to investigating the peculiar phenomenon of thermomolecular pressure difference.

Breyiannis [224] conducted one of the few studies that investigate the fully developed rarefied gas flow through a concentric circular annulus. The flow occurs due to an imposed pressure gradient. The study is interested in the flow rates and the friction factor represented by the Poiseuille number which shows a rapid increase at high degrees of rarefaction but a shallower increase in the transition and slip regime.

Based on this extensive literature review, certain noteworthy details can be discerned.

1. Experimental studies have established the presence of rarefaction effects and analytical solutions of first-order or higher-order slip models are insufficient. Numerical methods capable of solving for the whole range of Knudsen number are desired.

2. The method commonly employed is the Discrete Velocity Method which is a deterministic method. Very few studies are based on stochastic methods such as DSMC [229] owing to reasons discussed previously (refer Section. 2.2.2).

3. Among the various cross-sections employed in the past studies, the common ones are circular, elliptical, square, rectangular, triangular, trapezoidal and annular.

4. In most studies, the paramount parameters are identified as the mass flow rate and the Poiseuille number which characterizes the transport and friction respectively. Observations with regards to microscopic information such as velocity field and slip velocities are lacking.

5. Effect of variation in surface roughness (through $\alpha$) is rarely discussed despite its vital importance. Studies assuming full accommodation are misleading as the experimental study by Ewart [230] demonstrates that $\alpha$ is never really unity.

### 5.3.2 Problem statement

The statement of the problem can be concisely conveyed through fig.5.2.

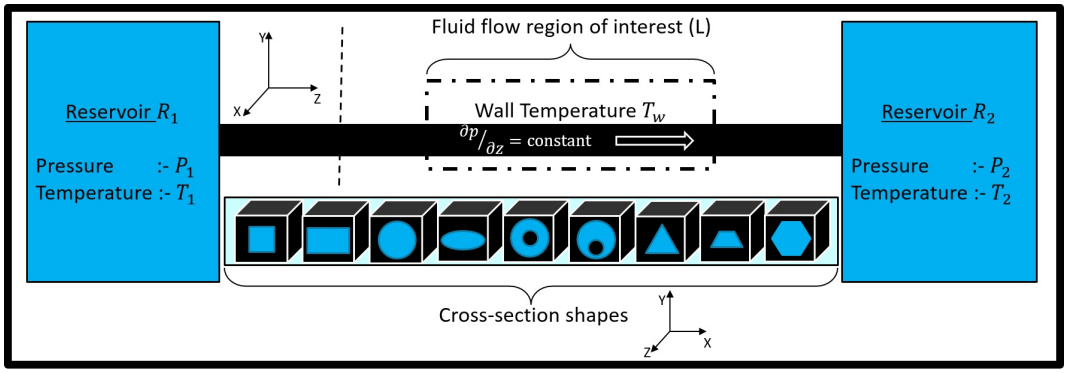


Figure 5.2: Schematic depicting the long-duct geometries.

Consider two reservoirs, $R_1$ and $R_2$ containing the same species of gas at states $P_1$, $T_1$ and $P_2$, $T_2$ respectively. The reservoirs are connected by a micro-duct of length $L$ and wall temperature $T_w$ such that $T_1 = T_2 = T_w = T = constant$ and $P_1 > P_2$.

The gas chosen as the working fluid in these studies is assumed to be monoatomic and pure, i.e. consisting of a single species. The length of the interconnecting micro-duct is such that it can be considered as a long-duct and the associated assumptions are in effect. Importantly, the length of the long-duct isolates the end effects to a small region in the immediate vicinity of the reservoirs and the vast portion of the duct exhibits nearly constant pressure gradients irrespective of the pressure difference $(P_1 - P_3)$. In addition to this, the pressure at a given cross-section of the long-duct is constant and a substantial gradient exists only in the flow direction (z-direction, in this case). The pressure gradient is small and constant allowing the representation of the pressure gradient as a constant body force [179] affecting all the particles in the flow domain.

The main parameters varied in these studies are the cross-section shape, degree of rarefaction and gas-surface interaction.

The interest in various cross-sections is appreciated by recognizing that MEMS came into being as a part of the semiconductor industry and employed the manufacturing techniques associated with the industry such as bulk micro-machining, surface micro-machining, plasma etching, electroplating, laser machining, stereolithography, micro-milling, micro-moulding and ink-jet printing of silicon leading to orthogonal, polar or annular cross-sections. Today, most of the manufacturing techniques used in the creation of MEMS devices is borrowed from the integrated circuit industry where the common practice is chemical etching due to the reliable and uniform surface finish offered. A simple $KOH$ etch on a silicon $\langle 1\,0\,0 \rangle$ wafer is highlighted here specifically because the behaviour of $KOH$ is such that the etch forms an angle of $54°\ 45'$ (alternatively $54.74°$) with the silicon wafer surface [231]. This is the primary motivation behind the studies of triangular and trapezoidal cross-sections with base angles of $54.74°$.

Primitive MEMS devices were manufactured in silicon but today, the use of materials such as glass, ceramics and polymers are commonplace. The use of such diverse materials has led to the need to better understand the gas-surface interaction between various pairs mainly because the inertial effects tend to be insignificant compared to the surface effects at the conditions considered in this study. In this research, the gas-surface interaction is modelled by the Maxwell diffuse-specular kinetic boundary condition where the surface accommodation is characterized by $\alpha$.

The quantities of interest such as mass flow rate, Poiseuille number and velocity fields are scrutinized and compared with literature where available. The non-dimensional formulation is implemented as discussed in a previous section (refer to 2.4.2). The reference length is chosen as the hydraulic diameter $D_h$, although other choices exist. Research work by Graur [220] and Rykov [214] have selected the length of the minor axis of an elliptical duct as the reference length while Duan [196] have used the square root of the flow area as the characteristic length. Appropriate comparison with these results can only be made if the literature results are interpreted under the present formulation.

The research can be divided into 3 separate research prospects, each directed at a specific objective and considering the whole range of rarefaction and surface roughness $\alpha$.

The first prospect is aimed at determining the effect of the cross section's aspect ratio on the flow. In order to achieve this, the aspect ratio of the orthogonal (fig.5.3b) and polar (fig.5.3a) ducts are varied and the resulting cross section are scrutinized. Two pairs of walls, $H$ consisting of $AB$ and $CD$; $V$ consisting of $AD$ and $BC$, are identified. Although a wide range of aspect ratios have been simulated, results are presented only for the 4 cross sections mentioned in table.5.1 as these are sufficiently indicative.

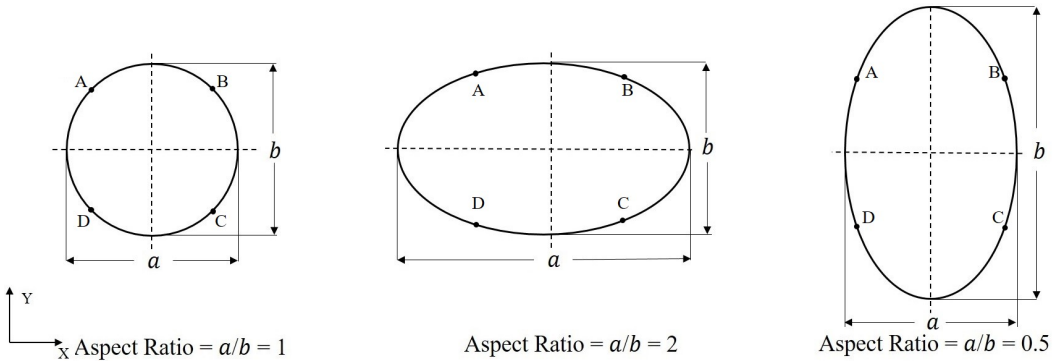


(a) Polar cross sections

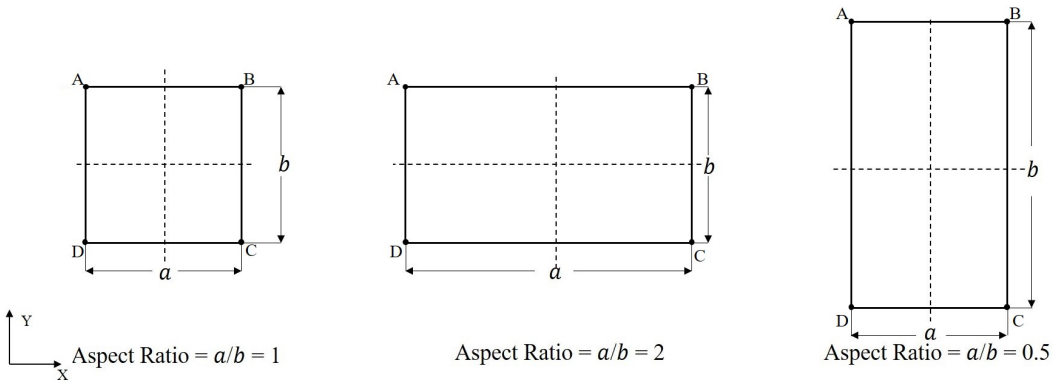


(b) Orthogonal cross sections

Figure 5.3: Schematic diagrams for the various orthogonal and polar long-duct cross sections considered.

Table 5.1: Orthogonal and polar cross sections considered with their tag.

| Tag | Feature |
|---|---|
| Ortho A | Aspect Ratio = 1.00 |
| Ortho B | Aspect Ratio = 2.00 |
| Polar A | Aspect Ratio = 1.00 |
| Polar B | Aspect Ratio = 2.00 |

The present method possess the ability to use approximate surfaces as exposited in section 4.4.2. Utilizing this, the effect of corners on the flow is characterized through the investigation of various triangular (fig.5.4a), trapezoidal and hexagonal (5.4b) cross-sections. Selected results are provided for the geometries listed in table.5.2.

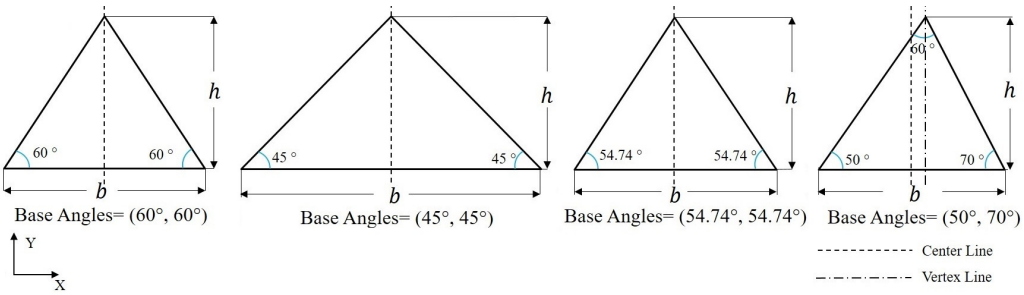


(a) Triangular cross sections

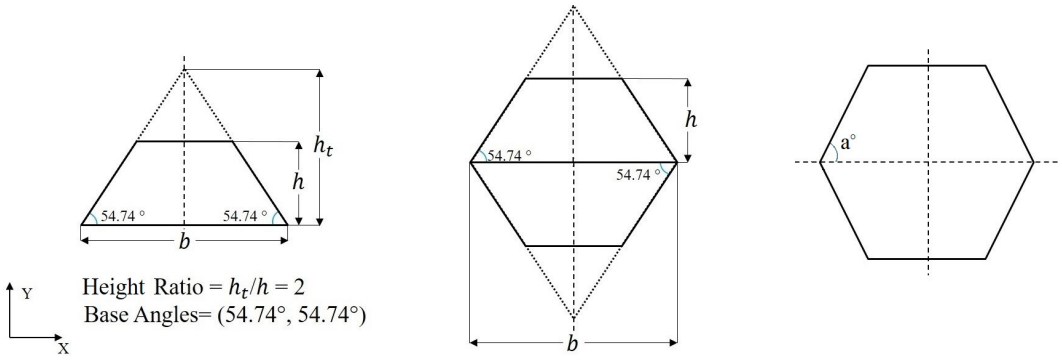


(b) Trapezoidal and Hexagonal cross sections

Figure 5.4: Schematic diagrams for the various triangular and trapezoidal long-duct cross sections considered.

Table 5.2: Triangular and trapezoidal cross sections considered with their tag.

| Tag | Feature |
|---|---|
| Triangle A | Base Angles = (60°, 60°) |
| Triangle B | Base Angles = (57.74°, 57.74°) |
| Triangle C | Base Angles = (45°, 45°) |
| Triangle D | Base Angles = (50°, 70°) |
| Trapezoid A | Height Ratio = 2.00; Base Angles = (60°, 60°) |
| Trapezoid B | Height Ratio = 2.00; Base Angles = (57.74° , 57.74°) |
| Trapezoid C | Height Ratio = 2.00; Base Angles = (45°, 45°) |
| Hexagon A | Interior Angle a = 2 X 60° |
| Hexagon B | Interior Angle a = 2 X 57.74° |

The third and final prospect is directed at the annular cross sections (fig.5.5a) wherein, the effect of increased inner cylinder radius ($r_i$) and eccentricity ($e$) are discerned. In addition to this, further inspection of the surface roughness is done through the differential variation of the inner and outer cylinder's accommodation coefficients (denoted by $\alpha_i$ and $\alpha_o$ respectively). Important cases presented here are identified in table.5.3.

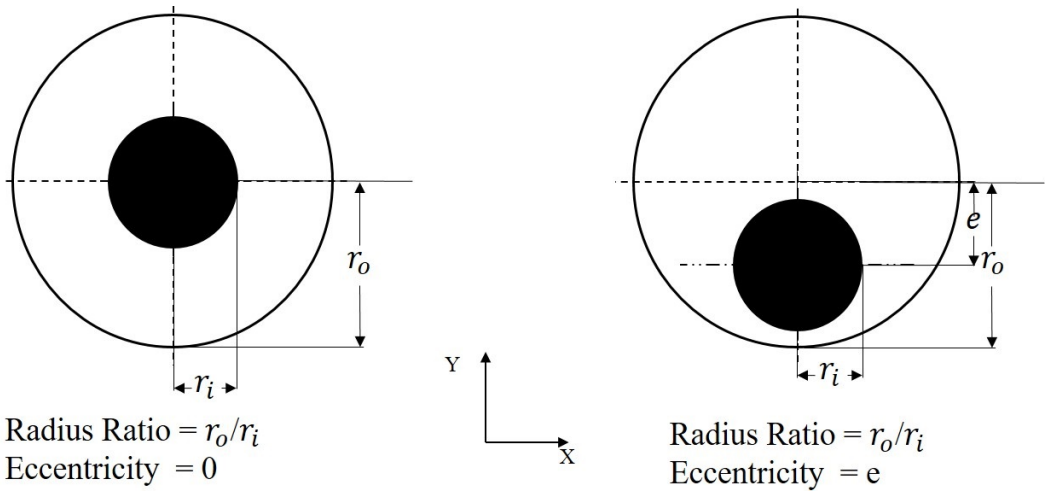


Figure 5.5: Schematic diagrams for the various annular cross sections long-duct.

Table 5.3: Annular cross sections considered with their tag.

| Tag | Feature |
|---|---|
| Concentric Annulus A | Radius ratio (inner/outer) = 0.2000; Eccentricity = 0.00 |
| Concentric Annulus B | Radius ratio (inner/outer) = 0.3651; Eccentricity = 0.00 |
| Concentric Annulus C | Radius ratio (inner/outer) = 0.5000; Eccentricity = 0.00 |
| Concentric Annulus D | Radius ratio (inner/outer) = 0.5773; Eccentricity = 0.00 |
| Concentric Annulus E | Radius ratio (inner/outer) = 0.8165; Eccentricity = 0.00 |
| Eccentric Annulus A | Radius ratio (inner/outer) = 0.3651; Eccentricity = 0.30 |
| Eccentric Annulus B | Radius ratio (inner/outer) = 0.3651; Eccentricity = 0.25 |
| Eccentric Annulus C | Radius ratio (inner/outer) = 0.3651; Eccentricity = 0.20 |
| Eccentric Annulus D | Radius ratio (inner/outer) = 0.3651; Eccentricity = 0.15 |
| Eccentric Annulus E | Radius ratio (inner/outer) = 0.3651; Eccentricity = 0.10 |
| Eccentric Annulus F | Radius ratio (inner/outer) = 0.3651; Eccentricity = 0.05 |

### 5.3.3 Simulation results

The simulation results relating to the first study are presented here through the velocity contours fig.5.6a where, in each of the contour, the left half denotes the results for $\alpha = 1.00$, while the right half denotes the results for $\alpha = 0.70$. The reduced mass flow rate and Poiseuille number are presented in fig.5.6.

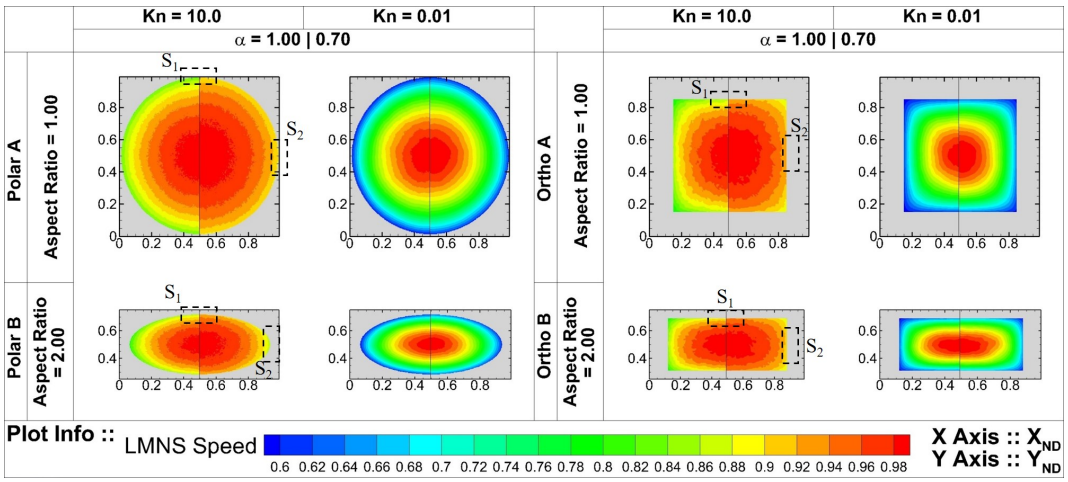


(a) LMNS speed contours

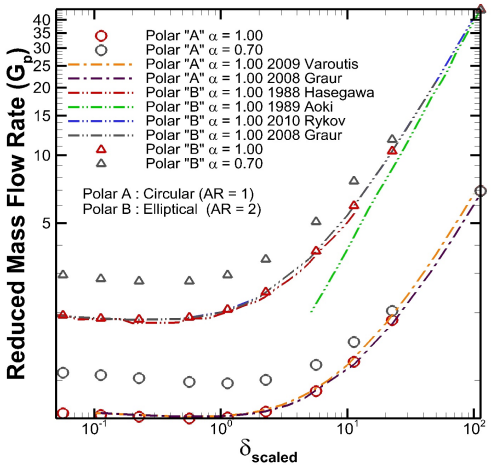


(b) Reduced mass flow rate for polar cross sections (Literature: [223], [220], [214]).

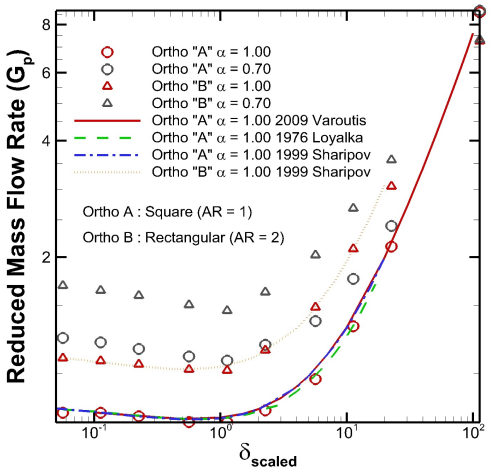


(c) Reduced mass flow rate for orthogonal cross sections (Literature: [223], [180], [215]).

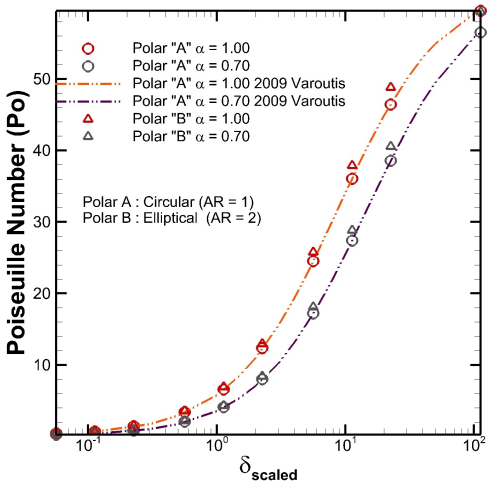


(d) Poiseuille number for polar cross sections (Literature: [219]).

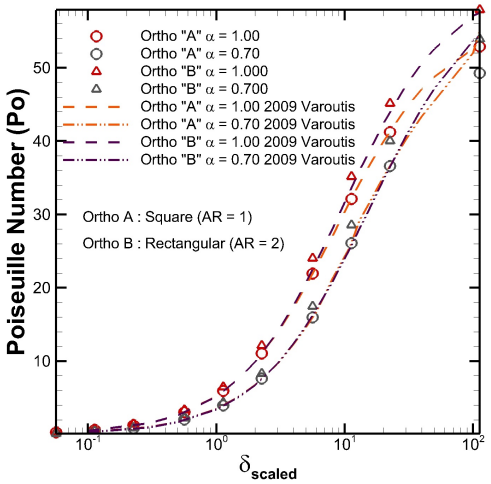


(e) Poiseuille number orthogonal cross sections(Literature: [219].

Figure 5.6: Results for the various orthogonal and polar long micro-duct cross sections considered.

Following this, velocity contours for triangular and trapezoidal sections are shown in fig.5.7a, while the results for the reduced mass flow are compared with those available in literature and depicted in figs.5.7b and 5.7c respectively. Tabulated results in table.5.4 for triangular sections and table.5.5 for the trapezoidal sections are presented. The variation of the slip velocity at the corner as a function of the angle for triangular cross section is plotted in fig.5.8.

Table 5.4: Poiseuille number for triangular long micro-duct cross sections.

| $\delta_{mod}$ | Triangular cross sections | | | | | | | |
|---|---|---|---|---|---|---|---|---|
| | Triangle A | | Triangle B | | Triangle C | | Triangle D | |
| | Po. no. | | | | | | | |
| | $\alpha = 1.00$ | $\alpha = 0.70$ | $\alpha = 1.00$ | $\alpha = 0.70$ | $\alpha = 1.00$ | $\alpha = 0.70$ | $\alpha = 1.00$ | $\alpha = 0.70$ |
| 0.1 | 0.5290 | 0.3176 | 0.5287 | 0.3174 | 0.5220 | 0.3134 | 0.5263 | 0.3160 |
| 0.25 | 1.3922 | 0.8841 | 1.3916 | 0.8959 | 1.3738 | 0.8955 | 1.3854 | 0.8916 |
| 0.5 | 2.6576 | 1.7193 | 2.6564 | 1.7423 | 2.6225 | 1.7416 | 2.6446 | 1.7338 |
| 1.0 | 5.0908 | 3.4016 | 5.0884 | 3.4001 | 5.0236 | 3.3567 | 5.0658 | 3.3849 |
| 2.5 | 11.5193 | 8.0108 | 11.5140 | 8.0071 | 11.3673 | 7.9051 | 11.4627 | 7.9715 |
| 5.0 | 19.2309 | 13.9502 | 19.2220 | 13.9436 | 18.9771 | 13.7659 | 19.1364 | 13.8816 |
| 10.0 | 28.4750 | 22.8332 | 28.4617 | 22.8227 | 28.0991 | 22.5318 | 28.3351 | 22.7211 |
| 25.0 | 39.3707 | 35.0715 | 39.3524 | 35.0551 | 38.8509 | 34.6084 | 39.1773 | 34.8991 |
| 50.0 | 44.0909 | 40.1921 | 44.0704 | 40.1733 | 43.5087 | 39.6614 | 43.8742 | 39.9945 |
| 100.0 | 49.6341 | 45.3126 | 49.6104 | 45.2915 | 48.9786 | 44.7143 | 49.3902 | 45.0899 |

Table 5.5: Poiseuille number for trapezoidal long micro-duct cross sections.

| $\delta_{mod}$ | Trapezoidal cross sections | | | | | |
|---|---|---|---|---|---|---|
| | Trapezoid A | | Trapezoid B | | Trapezoid C | |
| | Po. no. | | | | | |
| | $\alpha = 1.00$ | $\alpha = 0.70$ | $\alpha = 1.00$ | $\alpha = 0.70$ | $\alpha = 1.00$ | $\alpha = 0.70$ |
| 0.1 | 0.5635 | 0.3383 | 0.5952 | 0.3573 | 0.6151 | 0.3692 |
| 0.25 | 1.4831 | 0.9544 | 1.5667 | 1.0081 | 1.6189 | 1.0418 |
| 0.5 | 2.8311 | 1.8561 | 2.9906 | 1.9606 | 3.0903 | 2.0260 |
| 1.0 | 5.4231 | 3.6236 | 5.7286 | 3.8278 | 5.9196 | 3.9554 |
| 2.5 | 12.2712 | 8.5337 | 12.9625 | 9.0145 | 13.3946 | 9.3150 |
| 5.0 | 20.4861 | 14.8606 | 21.6403 | 15.6978 | 22.3616 | 16.2211 |
| 10.0 | 30.3335 | 24.3235 | 32.0424 | 25.6938 | 33.1105 | 26.5503 |
| 25.0 | 41.9403 | 37.3604 | 44.3032 | 39.4652 | 45.7799 | 40.7808 |
| 50.0 | 46.9685 | 42.8152 | 49.6146 | 45.2273 | 51.2684 | 46.7349 |
| 100.0 | 52.8735 | 48.2700 | 57.7131 | 50.9894 | 55.8529 | 52.6891 |

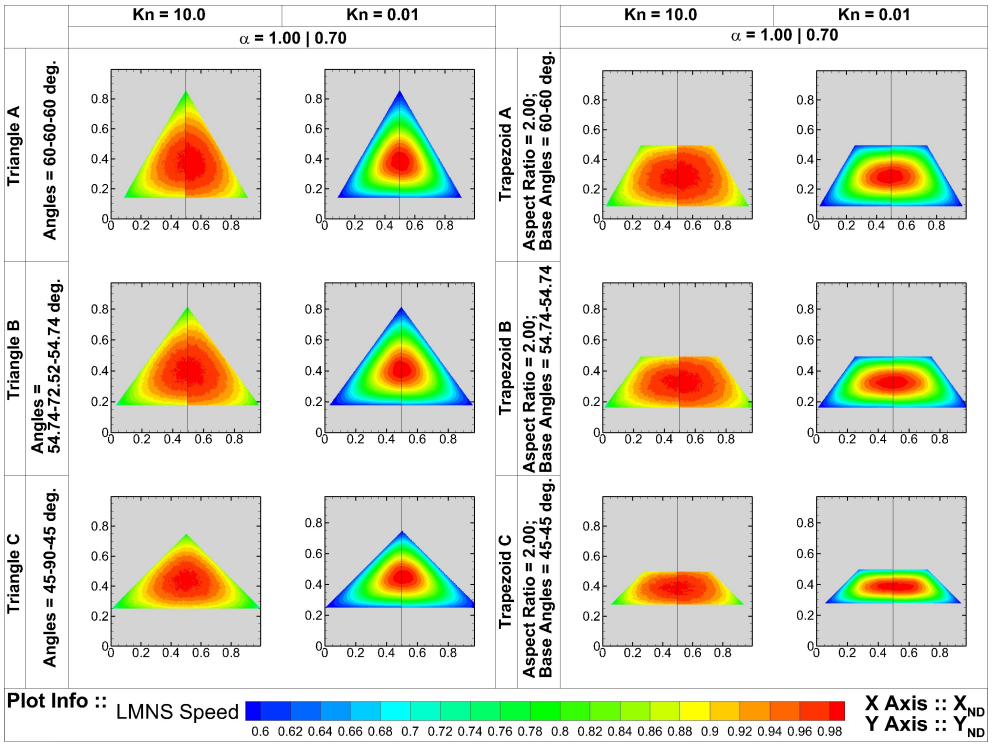


(a) LMNS speed contours

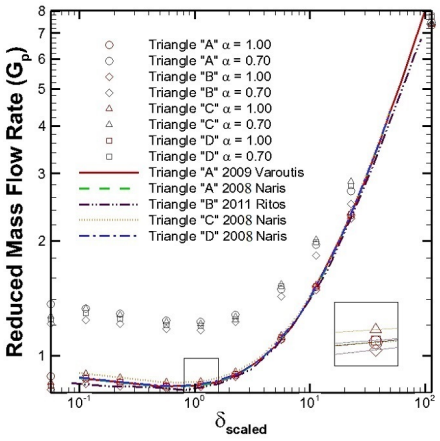


(b) Reduced mass flow rate for triangular cross sections (Literature: [223], [222], [228]).

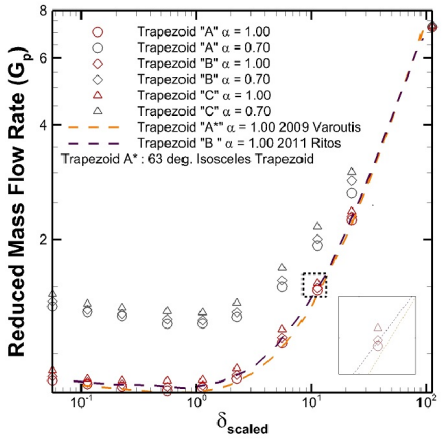


(c) Reduced mass flow rate for trapezoidal cross sections (Literature: [223], [228]).

Figure 5.7: Results for the various triangular and trapezoidal long micro-duct cross sections considered.

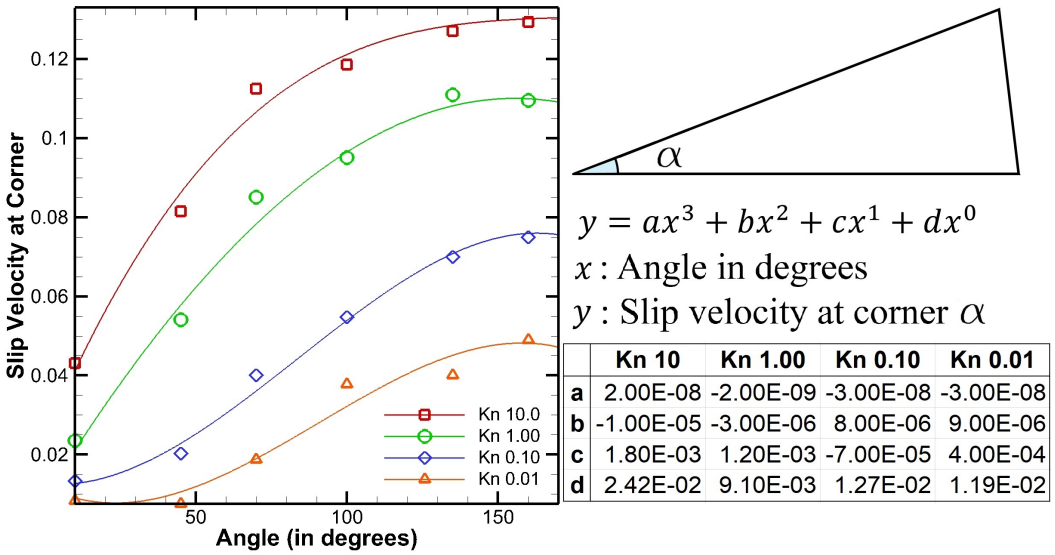


| | Kn 10 | Kn 1.00 | Kn 0.10 | Kn 0.01 |
|---|---|---|---|---|
| a | 2.00E-08 | -2.00E-09 | -3.00E-08 | -3.00E-08 |
| b | -1.00E-05 | -3.00E-06 | 8.00E-06 | 9.00E-06 |
| c | 1.80E-03 | 1.20E-03 | -7.00E-05 | 4.00E-04 |
| d | 2.42E-02 | 9.10E-03 | 1.27E-02 | 1.19E-02 |

Figure 5.8: Plot for the variation of corner slip with angle for triangular long micro-duct cross sections.

Special attention is drawn to the velocity contours of the hexagons considered in these studies as portrayed in fig.5.9.

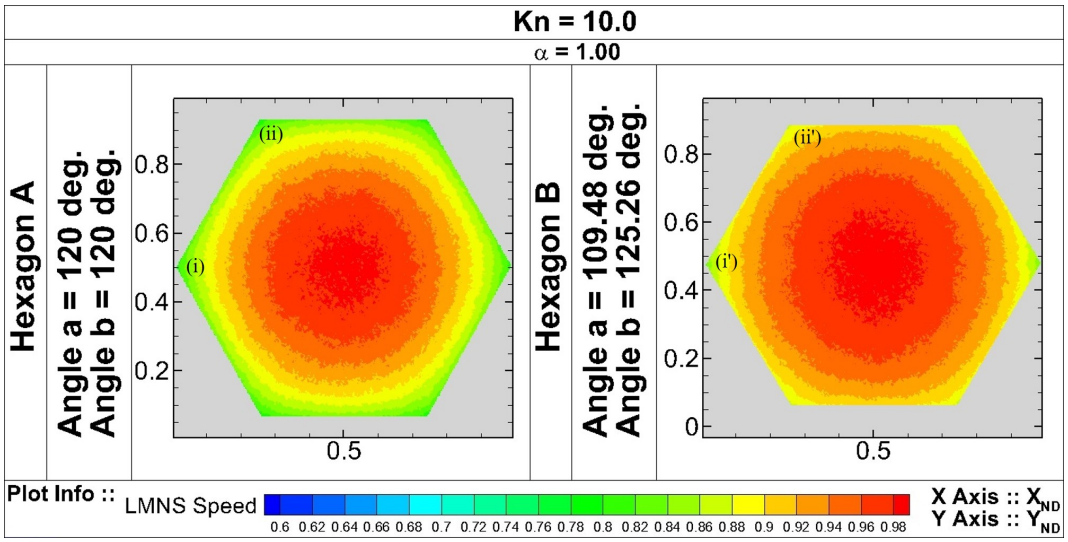


Figure 5.9: LMNS speed contour for Hexagonal long micro-ducts.

The velocity contours for annular ducts as the radius ratio, relative surface roughness and eccentricity varies are shown in figs.5.10a, 5.10b and 5.10c respectively. The corresponding plots for reduced mass flow and Poiseuille number for these variations are presented in figs.5.11, 5.13 and 5.12 respectively.

The variation of the surface interactivity (refer Section. 4.4.4) along the surface of the inner cylinder for an eccentric and concentric annulus is provided in fig.5.14

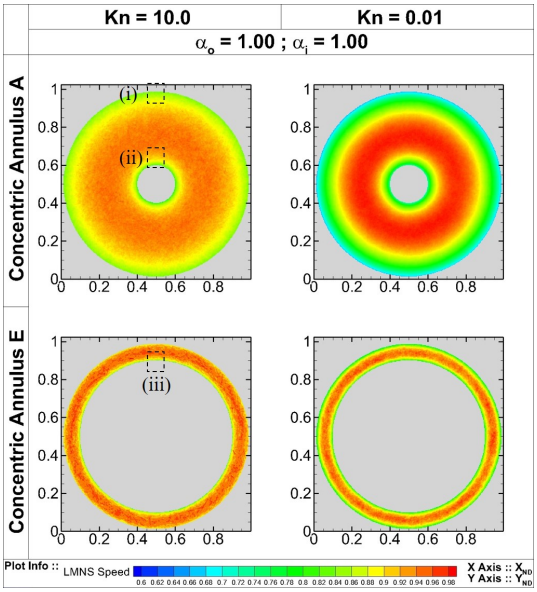


(a) Radius ratio variation.

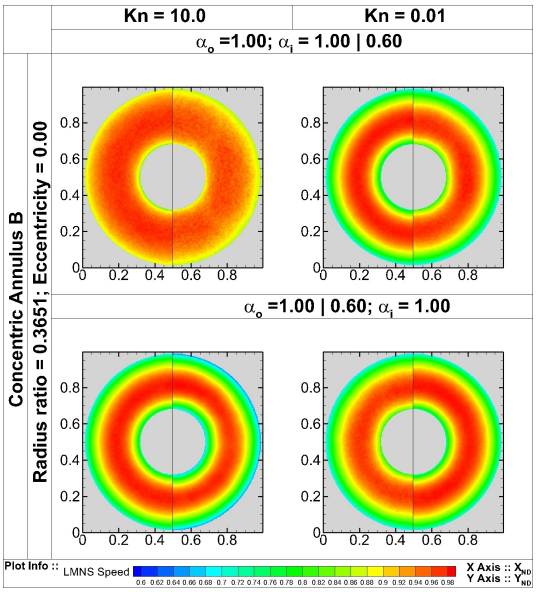


(b) Surface roughness variation.

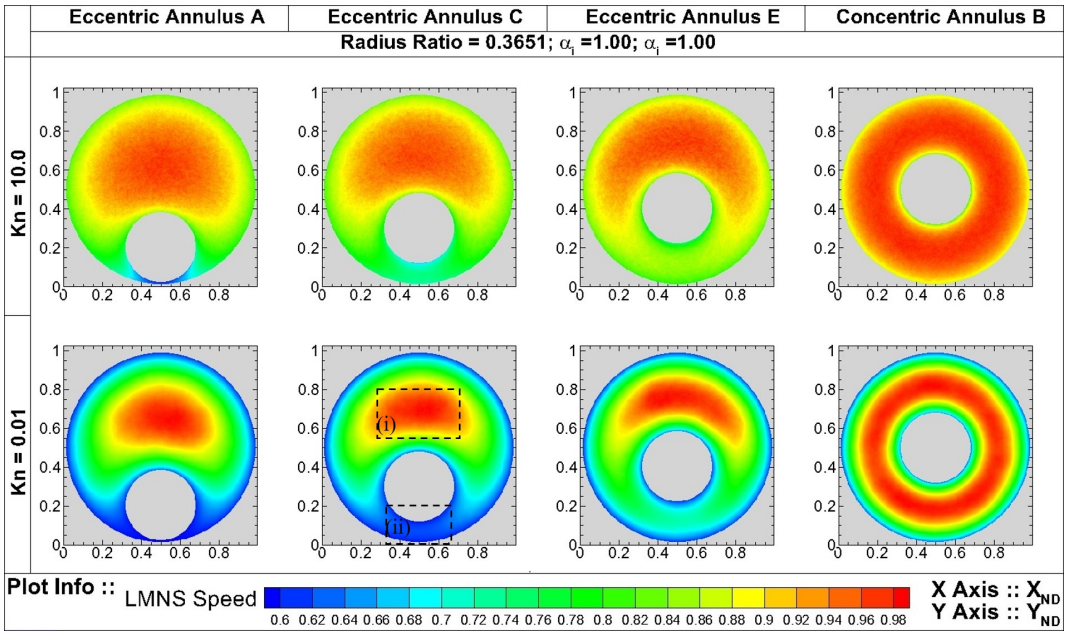


(c) Eccentricity variation.

Figure 5.10: LMNS speed contour plots for the annular cross section long micro-duct.

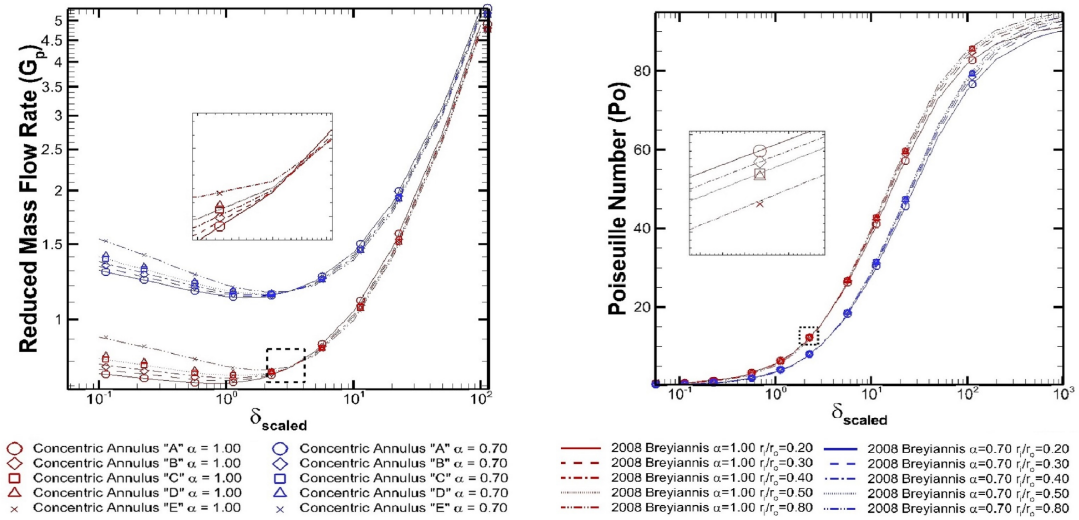


(a) Reduced mass flow rate (Literature: [224]).

(b) Poiseuille Number (Literature: [224]).

Figure 5.11: Macroscopic property variation for annular long micro-duct with variations in radius ratio.

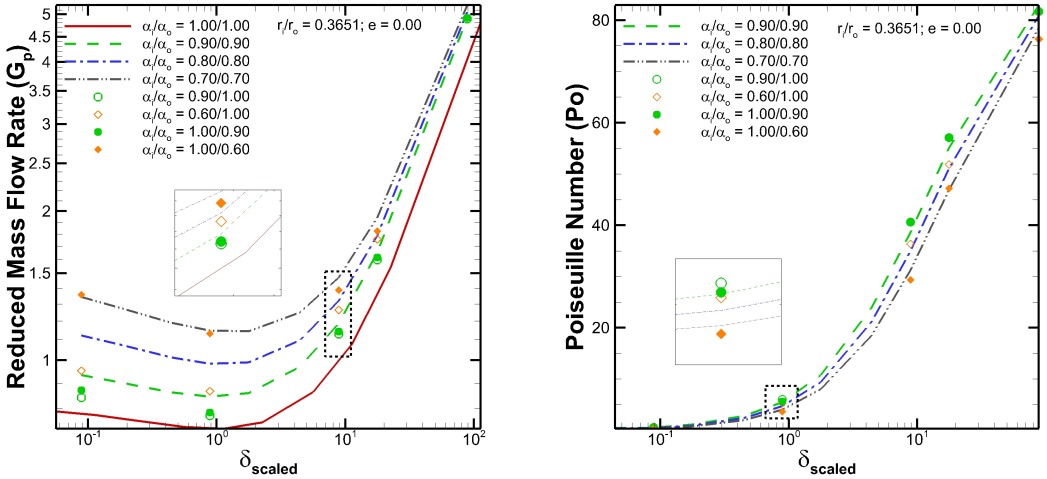


(a) Reduced mass flow rate

(b) Poiseuille number

Figure 5.12: Macroscopic property variation for annular long micro-duct with variations in relative surface roughness.

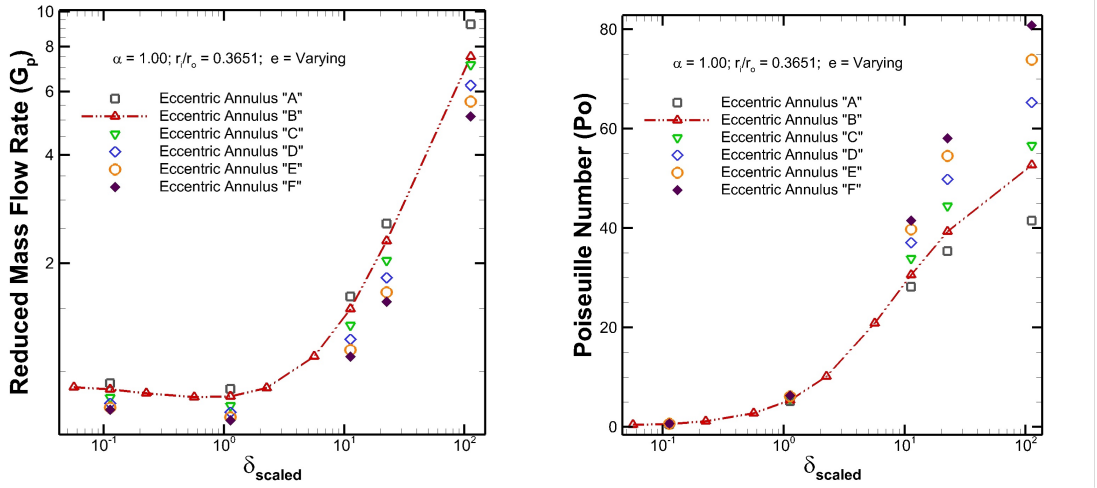


(a) Reduced mass flow rate (b) Poiseuille number

Figure 5.13: Macroscopic property variation for annular long micro-duct with variations in eccentricity.

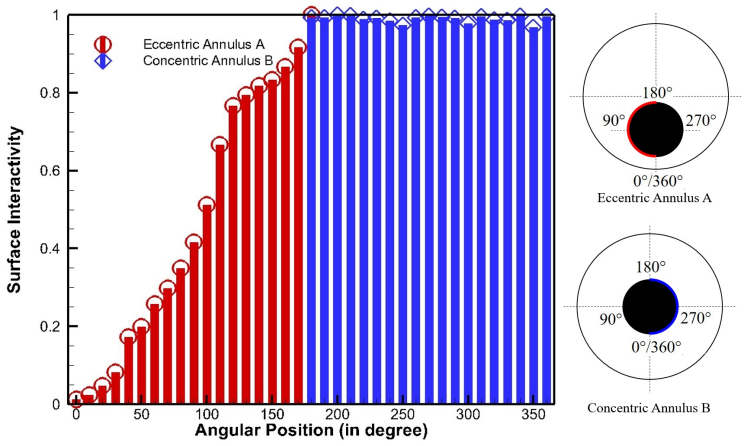


Figure 5.14: Surface interactivity comparison for an eccentric and concentric annular long micro-duct cross section.

The velocity profiles at the channel center for the Orthogonal and Polar sections are presented in fig.5.15a whereas, the velocity profile for a concentric annulus ($e = 0.00$) with radius ratio 0.3651 is shown in fig.5.15b.

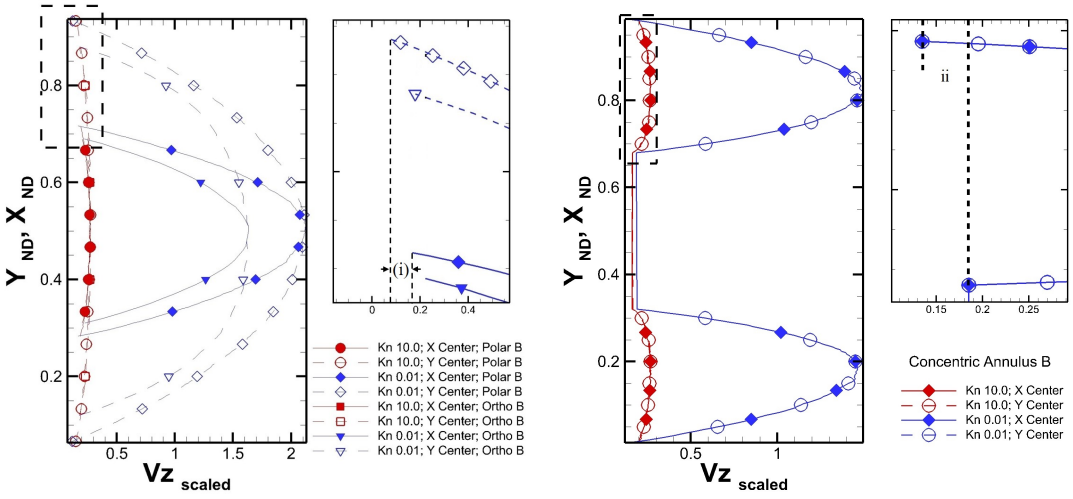


(a) Orthogonal and Polar

(b) Concentric Annulus

Figure 5.15: Velocity profile for selected long micro-duct cross section of importance.

Finally, the Poiseuille number obtained through the simulations at the lowest degree of rarefaction ($Kn = 0.01$) for all the cross sections discussed in the present research are compared with analytical results presented in literature obtained at the continuum hydrodynamic limit ($Kn \sim 0.00$) and are exhibited in table.5.6.

Table 5.6: Poiseuille number comparison at $Kn = 0.01$ versus continuum results reported in literature.

| Cross section Tag | Poiseuille No. | | |
|---|---|---|---|
| | Kn = 0.01 | Shah and London [208] X 4 | Percentage Difference |
| Polar A | 59.518 | 64.000 | 7.257 |
| Polar B | 62.580 | 67.292 | 7.256 |
| Ortho A | 52.910 | 56.908 | 7.281 |
| Ortho B | 57.899 | 62.192 | 7.149 |
| Triangle A | 49.634 | 53.332 | 7.182 |
| Triangle B | 49.610 | 52.328 | 5.332 |
| Triangle C | 48.978 | 52.616 | 7.161 |
| Triangle D | 49.390 | 52.840 | 6.749 |
| Trapezoid A | 52.873 | 56.804 | 7.168 |
| Trapezoid B | 57.713 | 57.920 | 0.358 |
| Trapezoid C | 55.852 | 58.080 | 3.911 |
| Hexagon A | 60.052 | 60.200 | 0.246 |
| Hexagon B | 56.053 | 63.716* [232] | 12.796 |
| Concentric Annulus A | 82.229 | 92.040 | 11.259 |
| Concentric Annulus B | 84.162 | 94.400 | 11.467 |
| Concentric Annulus C | 85.021 | 95.320 | 11.421 |
| Concentric Annulus D | 85.085 | 95.640 | 11.680 |
| Concentric Annulus E | 85.653 | 96.212 | 11.611 |
| Eccentric Annulus A | 41.455 | 45.754 | 9.859 |
| Eccentric Annulus B | 52.525 | 53.020 | 0.937 |
| Eccentric Annulus C | 56.500 | 61.766 | 8.905 |
| Eccentric Annulus D | 65.133 | 71.480 | 9.291 |
| Eccentric Annulus E | 73.626 | 84.438 | 13.680 |
| Eccentric Annulus F | 80.511 | 91.395 | 12.662 |

### 5.3.4 Long-duct data interpretation

Throughout the following study, the hydraulic diameter expressed as, $D_h = \frac{4\,Area}{Perimeter}$, is maintained as the reference length $L_0$. A prescribed reference state defined as $(n_0, T_0, P_0)$ is used to non-dimensionalize the state variables.

Additionally, for flows under a small and constant pressure or temperature gradient along a direction (say, $z$), the non-dimensional form of the gradient can be expressed as,

$$\xi_p = \frac{D_h}{P_0}\frac{\mathrm{d}P}{\mathrm{d}z}; \left|\xi_p\right| << 1. \tag{5.1}$$

The smallness of the pressure gradient is used to scale the velocities to higher values to avoid computational errors arising from rounding up of the small velocities. Thus,

$$u_{ND} = \frac{u}{\xi_p c_0}. \tag{5.2}$$

The results are expressed either through contour plots of the LMNS speed defined as, $LMNS\,Speed = \frac{|V|}{|V|_{Max}}$, or through plots of the variation in the mass flux and friction characteristics with the degree of gaseous rarefaction. The rarefaction is characterized through the rarefaction parameter, $\delta_{mod} = \frac{2}{\sqrt{\pi}}\frac{1}{Kn}$, while the mass flux is expressed as the reduced mass flow rate computed as, $G_p = 2\int\int n_{ND}u_{ND}dA_{ND}$.

The friction characteristics are represented by the Poiseuille number which can be expressed in a special form for long-ducts by kinetic considerations as [170], $Po = \frac{\delta_{scaled}}{u_{\bar{N}D}}$

Prior to continuing this discussion, it is necessary to highlight two key points. Firstly, in most studies of this nature, the reference length is chosen to be the hydraulic diameter, but there are cases in which alternate choices are made. One such example is the elliptical cross section where, the most common choice is the half-length of the minor axis (we will use Graur's 2009 paper for example). For an ellipse, the hydraulic diameter is given by the relation,

$$D_h = \frac{4ab(64-16e^2)}{(a+b)(64-3e^4)}; e = \frac{(a-b)}{(a+b)}. \tag{5.3}$$

Here,

$$AR = \frac{a}{b} = 2; e = \frac{1}{3}, \tag{5.4}$$

This alternate choice can be reconciled with the present choice by transformations in the reference length, rarefaction parameter, and reduced mass flow rate (due to the pressure gradient) as demonstrated by eqs. 5.5, 5.6, and 5.7 (5.8) respectively.

$$D_h = 2.6 * b; L_{0\,Present} = 2.6 * L_{0Graur}, \tag{5.5}$$

thus,

$$\delta_{Graur} = \frac{bp}{\mu V_{mp}} = \frac{b}{D_h}\frac{D_h p}{\mu V_{mp}} = \delta_{mod}/2.6. \tag{5.6}$$

Table 5.7: Demonstration of transformation required to present results to compare with literature for elliptical cross section.

| Polar cross section AR = 2.00 | | | | | |
|---|---|---|---|---|---|
| Original Result | | Transformed Result | | Literature [221] | |
| $\delta_{mod}$ | $G_p$ | $\delta_{Graur} = \delta_{mod}/2.6$ | $G_{p_{Graur}} = 2.6 * G_p$ | $\delta_{Graur}$ | $G_{p_{Graur}}$ |
| 0.1 | 0.7297 | 0.0385 | 1.8973 | 0 | 2.0655 |
| 0.25 | 0.7185 | 0.0962 | 1.8680 | 0.01 | 2.0160 |
| 0.5 | 0.7299 | 0.1923 | 1.8977 | 0.02 | 1.9880 |
| 0.75 | 0.7568 | 0.2885 | 1.9677 | 0.05 | 1.9404 |
| 1 | 0.7829 | 0.3846 | 2.0355 | 0.1 | 1.9015 |
| 2.5 | 0.7274 | 0.9615 | 1.8912 | 0.2 | 1.8740 |
| 5 | 0.8038 | 1.9231 | 2.0900 | 0.5 | 1.9010 |
| 7.5 | 0.9525 | 2.8846 | 2.4765 | 0.8 | 1.9741 |
| 10 | 1.1779 | 3.8462 | 3.0625 | 1 | 2.0323 |
| 25 | 2.2031 | 9.6154 | 5.7281 | 2 | 2.3695 |
| 50 | 3.8819 | 19.2308 | 10.0930 | 5 | 3.4901 |
| 75 | 5.9378 | 28.8462 | 15.4383 | 10 | 5.4423 |
| 100 | 7.6981 | 38.4615 | 20.0150 | 20 | 9.4100 |

The reduced mass flow rate is modified as,

$$G_{p_{Graur}} = \frac{2}{\pi abp\xi_{p_{Graur}}} V_{mp}\dot{m}_{ND} = 2.6 * \frac{2}{\pi abp\xi_{p_{Present}}} V_{mp}\dot{m}_{ND} = 2.6 * G_{p_{Present}}, \tag{5.7}$$

where,

$$\xi_{p_{Graur}} = \frac{b}{P_0}\frac{\mathrm{d}P}{\mathrm{d}z} = \frac{b}{D_h}\frac{D_h}{P_0}\frac{\mathrm{d}P}{\mathrm{d}z} = \xi_{p_{Present}}/2.6. \tag{5.8}$$

The above transformations leads to the interpretations of the present results as shown in table. 5.7.

Secondly, although results of these studies are expressed in non-dimensional terms, it is instructional and illuminating to interpret the result in dimensional form. For the particular case of flow of Argon gas at a reference pressure and temperature of $P_0 = 10^5 Pa$ and $T_0 = 293K$, the corresponding values of the most probable velocity and gas viscosity are $V_{mp} = 349.02m/s$ and $\mu = 22.3X10^{-6}Pas$ respectively. For a circular channel of hydraulic diameter $D_h = 0.07\mu m$, the rarefaction parameter is computed to be $\delta_{mod} = 1.00$. Referring to the results table, the reduced mass flow rate is $G_p = 0.7829$ which is interpreted as a dimensional mass flow of $1.726X10^{-15}kg/s$.

### 5.3.5 Observations and inferences

In the present study, the geometric profile of a long micro-duct, conducting flow axially, is varied to study the: influence of lateral walls through the variation in the aspect ratio on Orthogonal and Polar cross-sections, influence of corners through the variations of the base angles and profiles in Triangular and Trapezoidal cross-sections and effect of multiple independent surfaces through the investigation of annular cross-

sections. The flow condition under the entire Knudsen spectrum is considered along with the surface roughness effect through the accommodation coefficient $\alpha$.

Prior to considering the effect of these parameters, a few noteworthy observations irrespective of the cross-sectional shape can be made.

The effect of forcing the gas through a cross-section, as opposed to an infinite channel, is the added restriction due to the confinement of the flow to the cross-section profile. The influence of these confining walls, as established through the Poiseuille flow studies, is to detract the flow velocity in their vicinity. This effect is seen to weaken as the rarefaction increases or the $\alpha$ decreases (figs. 5.6a, 5.7a, 5.9, 5.10), both of which entice surface transport through slip flow. The outcome is the division of the flow field into an unrestricted inertial core region encouraging bulk transport and a slip afflicted region enveloping this inertial core region conducive to surface transport.

The resemblance of long-ducts to Poiseuille flow through channels (presented in section 4.3) in terms of the presence of a Knudsen minimum in the vicinity of $Kn = 1.00$ for the reduced mass flow rate (figs. 5.6b, 5.6c, 5.7b, 5.7c, 5.11a) is an anticipated outcome especially considering that the channel flow is retrieved as the limiting case for all cross-sections considered.

The trend exhibited by the Poiseuille number plots (figs.5.6d, 5.6e, 5.11b) can be described as inversely related to the gaseous rarefaction with a steep decrease in the continuum to slip regime, moderate drop in the transition regime and a nearly constant value in the high rarefaction regimes. The effect of increasing $\alpha$ is observed to be more pronounced at higher degrees of rarefaction and is seen to converge as the continuum regime is approached, highlighting the insignificant role in mass transport played by the surfaces in continuum. Moreover, at any specified rarefaction, the mass flow rate is higher for a lower $\alpha$ intuitively implying that the surface's effort to inhibit the flow is weakened as the roughness decreases. This is conclusively verified by the $Po$ plots where the smaller $\alpha$ corresponds to a lower $Po$.

The ability of the solver to obtain accurate macroscopic results for the cross-section considered has been established by comparison of the reduced mass flow rate and Poiseuille number data with literature data. The cases considered here are simple since they are quasi-unidirectional and thus, an excellent match with literature for the macroscopic properties is expected.

In addition to this, the lowest $Kn$ simulated here is $Kn = 0.01$ and can be cautiously viewed as a continuum regime solution. The comparison of Poiseuille number at $Kn = 0.01$ with analytical ( [208]) and experimental ( [232]) solutions shown in table 5.6 demonstrates the strength of this claim. The multiplicative factor of 4 is applied to the results presented by Shah [208] since the literature reports Fanning friction factor instead of the Darcy friction factor reported here.

Attention is now directed to the specific prospects identified in the problem statement.

Firstly, the effect of aspect ratio can be sufficiently established by considering the

Polar and Orthogonal cross-sections. It is worthwhile to note that a large $AR \to \infty$ or small $AR \to 0$ tend to resemble an infinite channel and the confinement imposed by the lateral walls is more prominent in the vicinity of unity aspect ratio. For an aspect ratio of unity, the similarity of the velocity contours (fig.5.6a) in the region around surface element $S1$ of $H$ and $S2$ of $V$ indicates that these surfaces exert equal influence on the flow field. However, as the aspect ratio varies, the similarity is lost implying that one pair ($V$ for $AR = 2.00$) has lower influence than the other ($H$ for $AR = 2.00$). Furthermore, the proximity of $H$ to the unrestricted core region compared to $V$ results in the velocity gradient being steeper for $S1$ than for $S2$ causing a higher slip velocity at $S1$ compared to $S2$ as highlighted by $i$ in fig.5.15a, where the percentage difference is $\sim 80\%$ for Polar B at $Kn = 0.01$, $AR = 2.00$ and $\alpha = 1.00$.

The effect of the equal significance of both pairs of walls is manifested at a macroscopic level by the high Poiseuille number and low mass flow rate at $AR = 1.00$ while, $AR = 2.00$ indicates a weakening of the pair of walls through increase in mass flow rate and reduced Poiseuille number. At continuum regimes, the effect of the lateral walls is still potent, as noted in the Poiseuille plots (figs.5.6d, 5.6e); but, not prominent as the bulk transport dominates the reduced mass flow rate noted in figs.5.6b, 5.6c.

In conclusion, the aspect ratio presents itself as a number that characterizes the relative influence of one pair of walls to the other.

A second by-product of confining flows to a cross-section is the introduction of corners that experience the combined inhibitive effects of two walls causing them to exhibit the lowest slip velocity in a given flow field. This is sufficiently highlighted through the observation of flows through the triangular and trapezoidal duct as depicted in fig.5.7a.

A discussion of the microscopic details, such as velocity at the corner region, requires a great deal of confidence in the ability of the solver to accurately replicate the effect. In order to do so, the surface approximation described in section 4.4.2 is utilized. An appreciation for the sensitivity of the solver to variations in corner angles can be gained by recognizing that the hexagon A considered in fig.5.9 has an interior angles $i = ii = 120^\circ$ while, hexagon B features an interior angle $i' \sim 110^\circ$ which differs from angle $ii' \sim 125^\circ$. The variation between these angles is small despite which, the velocity contours are markedly different exhibiting a lower slip velocity at smaller angles. Quantitatively, the angular difference between ($i$, $ii'$) and ($i$, $i'$) is $\sim 5^\circ$ and $\sim 10^\circ$ respectively; the corresponding difference in slip velocity at $Kn = 10.0$ and $\alpha = 1.00$ is $\sim 40\%$ and $\sim 20\%$ respectively.

While it is well established that a wall has a deleterious effect on flows, a corner is even more unfavourable. The unfavourable nature at a sufficiently high Kn is strongly dependent on the angle suspended by the corner. The more obtuse the angle, higher is the velocity at the corner as is evidenced for a triangular cross section by fig.5.8.

The third class considers annular sections which merit an independent examination principally because they comprise of two independent surfaces, the inner surface of the

outer cylinder (hereafter denoted by $S_o$; associated properties are marked with $_o$) and the outer surface of the inner cylinder (hereafter denoted by $S_i$; associated properties are marked with or $_i$).

The first geometric variation is in the flow area which is restricted through an increase in the size of the inner cylinder. It is intuitive that a decrease in the flow area will result in a decreased mass flow. This is observed in fig.5.11a where, in the continuum regimes, the duct with a larger area conducts a higher mass transport. However, as the rarefaction increase, a reversal is observed in the vicinity of $Kn = 1.00$ subsequently leading to the duct with the smaller area demonstrating a higher flow rate than a larger area duct. This effect is attributed to the decrease in the significance of the bulk transport in the unrestricted flow core and increased transport at the walls as rarefaction increases. As the rarefaction increase, the surface transport rises (locations $i$ and $ii$ in fig.5.10a). Furthermore, as the two surfaces draw closer, the slip at the surfaces decreases (locations $i$ and $iii$ in fig.5.10a) contributing to the observed effect.

In the second consideration, the flow area is preserved through the specification of a fixed radius ratio ($\frac{r_i}{r_o} = 0.3651$) and eccentricity ($e = 0.00$). The relative roughness of the inner and outer surfaces are varied through the variation of $\alpha_i$ and $\alpha_o$ respectively. The prime motivation behind this novel study is the realization that, in spite of the symmetry of the cross-section, the peak velocity is not located at the center of the region between $S_i$ and $S_o$ but rather is skewed towards $S_i$. This causes a differential gradient in velocity profile similar to the effect observed in the case of Orthogonal and Polar cross-section with non-unity aspect ratios. The gradient translates to slip velocity and accordingly, slip at the inner surface is higher than the slip at the outer surface. This observation has been reported previously for Stokes flow conditions by Ebert [194].

As indicated from previous studies regarding $\alpha$ variation, smoother surfaces are expected to favour mass transfer through increased slip velocity as is evidenced by the lines in fig.5.12a and locations $i$ and $ii$ in the velocity contours featured in fig.5.10b. However, of particular note is the fact that smoothing the outer surface is more conducive to flow rate than the inner surface as is shown clearly by $\frac{\alpha_i}{\alpha_o} = \frac{0.60}{1.00}$ and $\frac{\alpha_i}{\alpha_o} = \frac{1.00}{0.60}$ data points in fig.5.12a. Thus, an improvement in flow rate is better achieved by a smoother outer surface and practical applications would benefit if efforts were focussed on the polishing of $S_o$ rather than $S_i$. The effect is seen to disappear in the continuum regime but is dominant at higher rarefactions.

In the final consideration of annular ducts, a constant radius ratio i.e. $\frac{r_i}{r_o} = 0.3651$ and complete accommodation at surfaces ($\alpha = 1.00$) are assumed. The structural variation through the eccentricity, $e$, does not affect the flow area geometrically although the physical characteristics of the flow field are affected through the creation of an unrestricted flow region (location $i$ in fig.5.10c) and a severely restricted flow region (location $ii$ in fig.5.10c) above and below the inner cylinder. Mass transport is primarily attributed to unrestricted flow regime and thus, is maximum for the largest eccentricity ($e = 0.30$), at all degrees of rarefaction, including very high and very low degrees of

rarefaction as depicted in fig.5.13a. The Poiseuille number is depicted in fig.5.13b and is seen to be minimum for $e = 0.30$. This is because, at high eccentricities, the surfaces involved in the severely restricted flow region *ii* are effectively inactive and do not contribute towards the frictional effects of the flow. As the eccentricity decreases, the flow envelopes the inner cylinder making more of the inner cylinder surface active. This observation is further bolstered by the use of the newly defined Surface interactivity as depicted in fig.5.14.

## 5.4 Studies with regards to MEMS-microfluidics :: Isothermal infinite arrays

The study of flow around obstacles placed in the path of a flow driven by small gradients in pressure or temperature is of immense practical significance most notably fulfilling the function of a heat sink or part of an active or passive flow controller in various MEMS microfluidics devices. These obstacles are seldom singular and usually deployed as a bank or array leading to their consideration as infinite arrays. The physical characteristics can be modified to better suit the application on hand through either obstacles definition which can be identical or similar in size and shape or through an arrangement in a specific manner.

While these studies are cases where the flow is through ordered 2 phase systems, which according to the nomenclature used in this thesis makes it a feature of MEMS components, there is also a scope to treat these as porous media, admittedly an elementary one. Most porous media are granular although there are examples in which porous media particles are long and the flow direction is such that it is more appropriate to consider them as fibrous porous media instead of granular porous media. Practical examples of these are steel wool, cotton batting although some researchers have credibly extended the definition to banks of heat exchanger tubes often encountered in MEMS applications.

We refrain from doing so and treat porous media as 2 phase disordered systems featuring either inhomogeneity in arrangement or size or shape in this thesis.

### 5.4.1 Literature review

The engineering importance of the flow through arrays has led to it being in the research spotlight from a very early stage as exemplified by the study dating back to 1925 when Emersleben [233] analytically examined the parallel flow through circular cylinders arranged in a square array at low densities. Such configurations have frequently been investigated under the paradigm of fibrous porous media which have been the focus of scientific studies since the 1940s. The versatility of such an approximation is emphasized by studies such as those by Sullivan in 1942 [234], wherein the experimental investigation of flow through a compact bundle of parallel fibres was conducted

with the intent of determining the specific surface area. The fibres used varied from cotton fibres to goat wool to blond and Chinese hair among other materials. A valuable, detailed compendium of these experimental studies and comparison of results is provided by Jackson in 1986 [235].

The analytical studies for longitudinal flow past circular cylinders arranged in a square and triangular array through Eigenfunction expansion and collocation were carried out by Sparrow in 1959 [236]. In this work, the results for the pressure drop and the friction factor are evaluated for various obstacle sizes, effectuated by varying the spacing-to-diameter ratio. Furthermore, the fundamental solution of Stokes flow past a cubic array of spherical objects through the Fourier series and square array of circular cylinders through elliptical functions was obtained by Hasimoto in 1958 [237]. In a short communication, Banerjee in 1973 [238] presented their results for the fully developed laminar flow around circular cylinders arranged in a triangular array. They employed a variational technique to investigate the pressure drop and friction factor for various porosities, finding that their results matched well with those of Sparrow [236]. A comprehensive enquiry was led by Drummond in 1984, wherein the longitudinal and transverse flow through circular cylinders arranged in square, triangular, hexagonal and rectangular array was studied. The nature of the flow was assumed to be fully developed viscous laminar flow. The importance of transverse flows encouraged many consequent research ventures such as those by Wang in 1997 [239] who used Eigenfunction expansion and collocation method to study the Stokes flow through a channel with inline or staggered vertical fins. The focus was on the determination of the resistance encountered due to the presence and configuration of the fins. In another later publication, the same method was employed to analyse flow through a rectangular array of circular cylinders in 2001 by Wang [240]. The flow in both the longitudinal and transverse direction is treated by solving the Poisson equation and bi-harmonic equation respectively. Various cylinder sizes were considered and the calculated permeability is presented in this work.

Solutions incorporating slip models in conjunction with the Stokes equation for axial [241] and transverse flow [242] in various arrangement of circular and elliptical cylinders under the assumption of a 2D porous media with an emphasis on the surface flow were obtained by Larson. Further studies into the effect of slip using the method of Eigenfunction expansion and collocation were conducted by Wang in 2003 [243] for circular cylinders arranged in a triangular array.

Permeability studies utilizing numerical methods for circular cylinders arranged in an inline arrangement were conducted by Tamayol [244] in 2008. Tamayol [244, 245], further extended their integral model to include square, triangular, hexagonal and octagonal formations of circular cylinders. Permeability in the transverse and longitudinal direction was computed along with the role porosity plays on the permeability. This included cases of increasing cylinder sizes up to touching cylinders. The results are compared to the analytical solution obtained from the Poisson equation in addition to

the experimental results presented in the literature.

Through first-order slip models, the effect of gas slippage at rarefaction as high as $Kn = 0.1$ for circular cylinders in a square array has been theoretically investigated by Chai in 2011 [246]. They calculated the permeability for high and low solid fractions using the lubrication theory and cell model, respectively, proceeding to then put forth a hybrid model for intermediate solid fractions. At a given value of the solid fraction, they discovered an increase in permeability as rarefaction increases. The same case along with its extension to a 3D sphere was numerically modelled at the macroscopic scales and results with regards to the permeability and slip correction as a result of gas slippage were discussed by Lasseux as recently as 2014 [247]. Their consideration also extends to van der Waal's gases where the molecules occupy volume.

The above literature sheds light onto some of the physical aspects of the flows around obstacle arrays although, a keener observation reveals that these studies are highly restricted and the potential avenues for further investigation are plentiful. Consider the following facts,

1. There is a marked dearth of studies that consider the flow of rarefied gases through ordered arrays such as those indigenous to MEMS applications. Even instances where such studies are conducted, the degree of rarefaction extends into the slip regime at best.

2. Baring a few rare instances, the shape of the obstacle is considered to be a circular cylinder. While its practical viability is undeniable, modern applications may require a different shape for which, results are lacking.

3. While the approximation as fibrous porous media justifies the use of complete wall accommodation (i.e. $\alpha = 1.00$), the widespread usage of such arrays in MEMS devices necessitates the establishment of the surface effect of the flow.

4. Efforts have been primarily focussed on the solution of continuum-based governing equations with a heavy emphasis on the fundamental Stokes flow. An investigation employing higher-order governing equations with modern computational methods are noticeable only by their absence.

5. The close resemblance of these infinite arrays to fibrous porous media has resulted in the majority of the results being communicated through porous media terminologies such as porosity, permeability and specific surface area.

### 5.4.2 Problem statement

The implication of isolating the consideration to the interior of an infinite array from a fluid dynamic point of view is that it enables the computations to neglect the flow disturbances caused by the initial encounter of the flow and first rank of obstacles. Consequently, the flow in the interior can be treated as a steady, fully developed flow.

In the present study, the investigative spotlight is directed on the physical response of isothermal flows driven by a small pressure gradient past/through obstacles arrays exhibiting variation in a number of physical features and flow conditions.

The variation in the **flow orientation** can be pictorially depicted as shown in fig. 5.16a.The pressure gradient can be oriented in the direction of the axis of the obstacles. Such a flow, with its principal flow direction parallel to the obstacle axis, is called a parallel or axial or longitudinal flow. On the other hand, the pressure gradient can be oriented in a direction perpendicular to the axis of the obstacles. Such a flow, with its principal flow direction normal to the obstacle axis, is called a transverse or cross or lateral flow. It is worthwhile to note that the variation in flow orientation can also be interpreted as the **grain orientation** in porous media lexicon with longitudinal and transverse flow corresponding to fibrous and granular porous media respectively.

In an infinite array, the **shape** can be arbitrary as long as every obstacle forming the infinite array are identical. The present study utilizes standard shapes such as circular, square, equilateral triangular and a 50°-60°-70° scalene triangular cylinder as depicted in fig.5.16b.

The **size** of the obstacle is an important parameter to study and once a size is defined, it is retained for every obstacle in the array. In the present context, the size of the obstacles is expressed in terms of the solid fraction ($SF$) of a unit cell. The effect of the solid fraction on the geometry for an in-line arrangement of circular cylinders is shown in fig.5.16c. Another noteworthy point is that in terms of porous media quantities, the solid fraction and porosity ($\phi$) are the complement of each other (i.e. $SF\% = 100 - \phi\%$) and can be used interchangeably.

Practical demands often result in the use of various **arrangements** of the obstacle forming the arrays. At present, arrangements usually represented in literature have been adapted for this study as well. Accordingly, the arrangements considered are the in-line or rectangular array, staggered or triangular array and the honeycomb or hexagonal array. These are illustrated in fig.5.16d.

Flows in infinite arrays interact frequently with the obstacles of the array and are very sensitive to the characteristics of the obstacle surfaces. The isothermal nature of the present study imposes the temperature of the surface. However, the **surface roughness** can be modified by varying the value of the accommodation coefficient.

**Rarefaction** plays a pivotal role in the characterization of flows through obstacle arrays. The principal effect of rarefaction is to govern the degree of gas-surface interaction and consequently gaseous slippage.

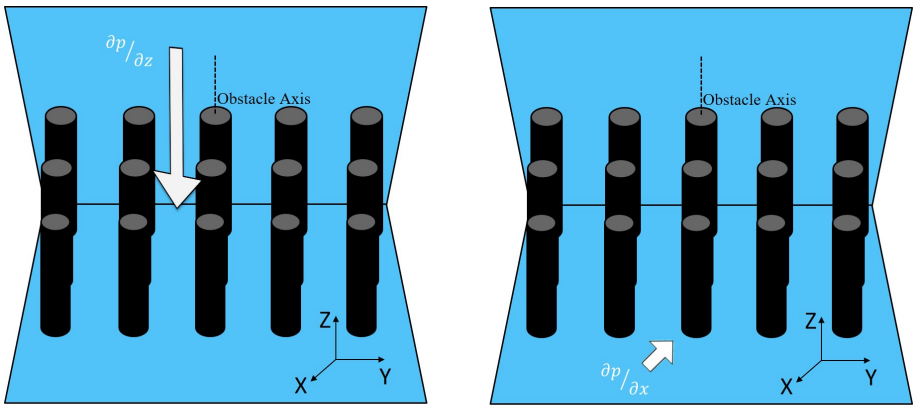


Longitudinal flow orientation | Transverse flow orientation

(a) Flow orientation variation

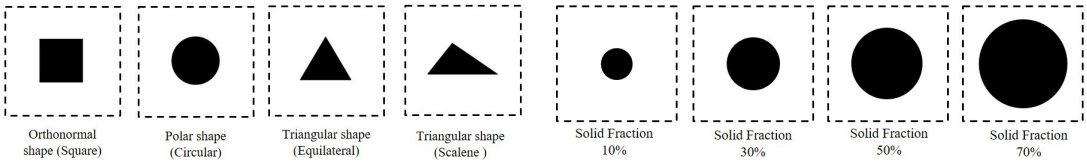


(b) Shape variation (c) Size variation

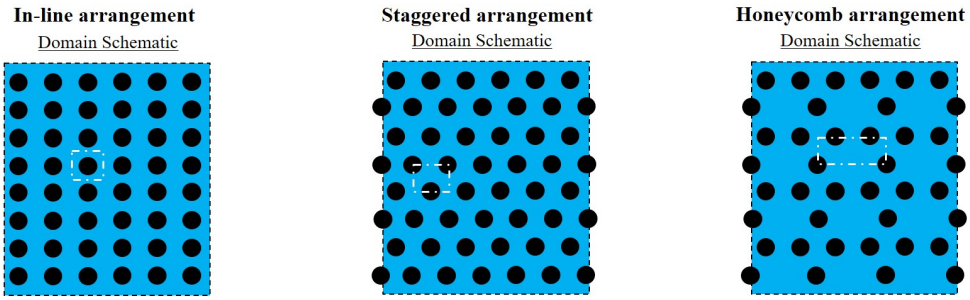


(d) Arrangement variation

Figure 5.16: Schematic diagrams for the variable parameters associated with the definition of an infinite array.

Such a large number of alterable parameters results in the definition of a cornucopia of cases apt for simulation and analysis. Although a large number of these simulations were performed, selective results that are capable of representing the key insights are illustrated here in order to avoid superfluity. Thus, the variation of obstacle shapes is limited to either a circular (C) or square (S) cylinder. Moreover, special cases of square arrangement for an in-line array (henceforth, SQRA), equilateral triangular arrangement for a staggered array (henceforth, TRIA) and a regular hexagonal arrangement for a honeycomb array (henceforth, HEXA) are selected. Longitudinal flows are denoted by $L$ while, transverse flows are denoted by $T$.

To retain clarity during these studies, a case is defined by the set termed as Array Feature (AF), whose nomenclature is,

$$AF = \{Orientation, Shape, Size, Arrangement, \alpha, Kn\} \tag{5.9}$$

As an illustration, $AF = \{L, C, 10, HEXA, 1.00, All\}$, indicates the data pertaining to the Longitudinal flow around Circular cylinders of size 10% of the domain (unit cell) arranged in a Hexagonal array with accommodation coefficient 1.00 over the entire range of rarefaction.

The study of an infinite array of cylinders is largely predicated on the definition of the array structure and the identification of a unit cell that adequately replicates the effect of the entire array. The onus of both these tasks in borne by a large degree on the proper specification of the unit cell's boundary condition. The commonly employed boundary conditions and their physical interpretation have been demonstrated previously in section 4.4.3.

Based on the knowledge of the different effects produced by the boundary condition, the unit cell for each of the cases to be studied is chosen judiciously. Fig.5.17 depicts the three arrangements considered here along with the unit cell and boundary conditions considered.

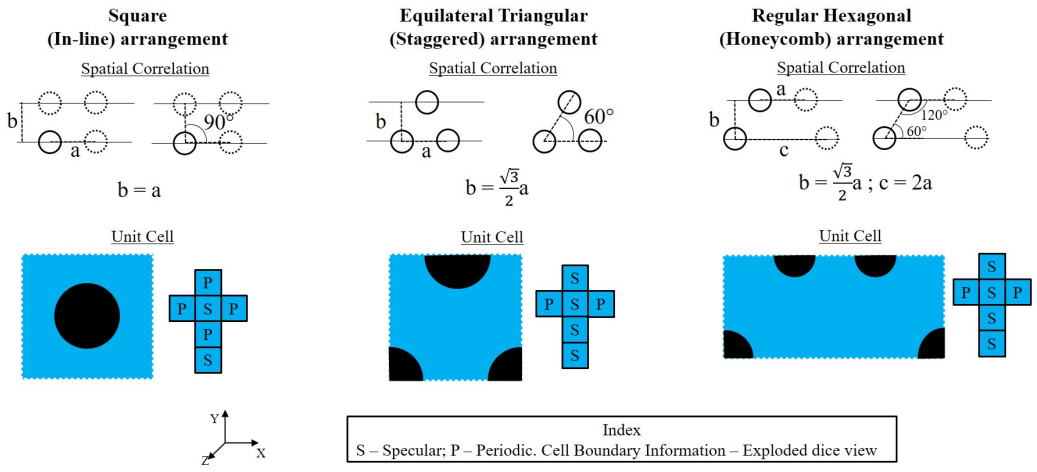


Figure 5.17: Schematic depicting the arrangements considered in this study and the definition of their appropriate unit cells.

In these simulations, the priority is on the procurement of the velocity flow field while the determination of porous media quantities such as permeability and tortuosity with gaseous rarefaction are also entertained.

### 5.4.3 Simulation results

The first consideration is the effect $\alpha$ has on the resulting flow field. The case presented here can be described as $AF = \{T, C, 10, SQRA, All, All\}$. The LMNS speed contours are presented in fig.5.18a with variation of rarefaction exhibited along a row and variation in $\alpha$ along a column. Additionally, the variation of macroscopic property of permeability is depicted in fig.5.18b.

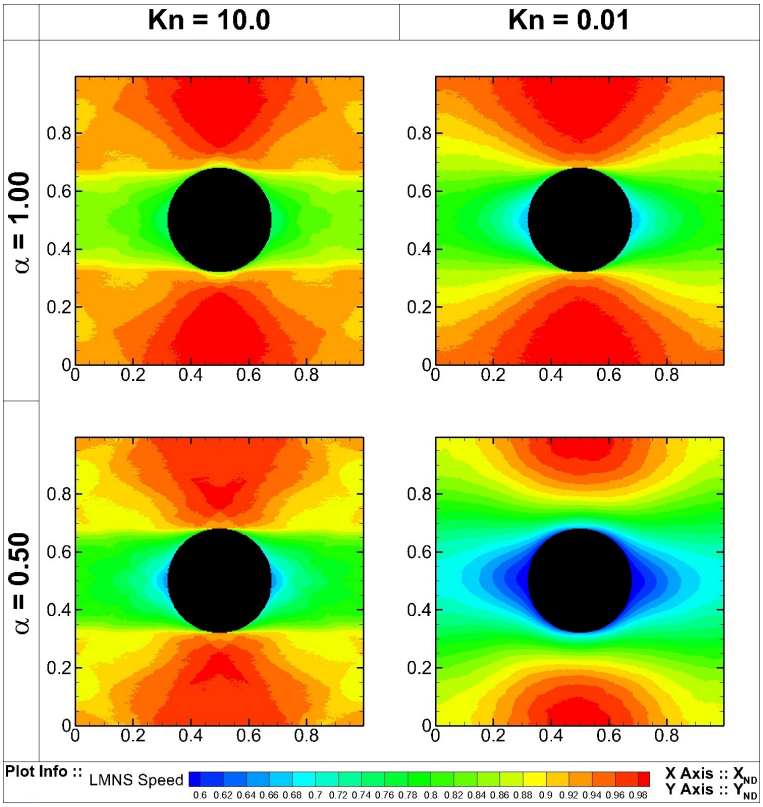


(a) LMNS speed contour.

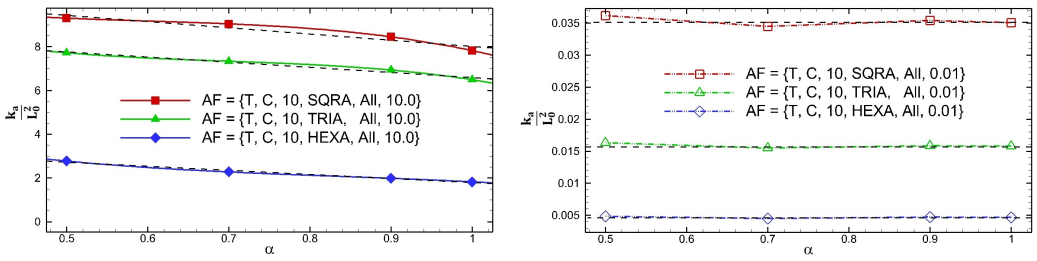


(b) Permeability at $Kn = 10.0$ and $Kn = 0.01$.

Figure 5.18: Results for transverse flow in square arrangement of circular cylinders in infinite arrays with variation in $\alpha$.

The second consideration presented is a simultaneous effect of the variation in flow orientation, size, arrangement and rarefaction. In the LMNS speed contour plots shown in fig.5.19, the left half represents longitudinal flow whereas, the right half depicts transverse flow. The Knudsen number variation in each flow orientation case is presented along a row while the variation in the arrangement is presented along a column. Moreover, the size of 10% is presented for SQRA, size of 50% is presented for TRIA and size of 50% is presented for HEXA.

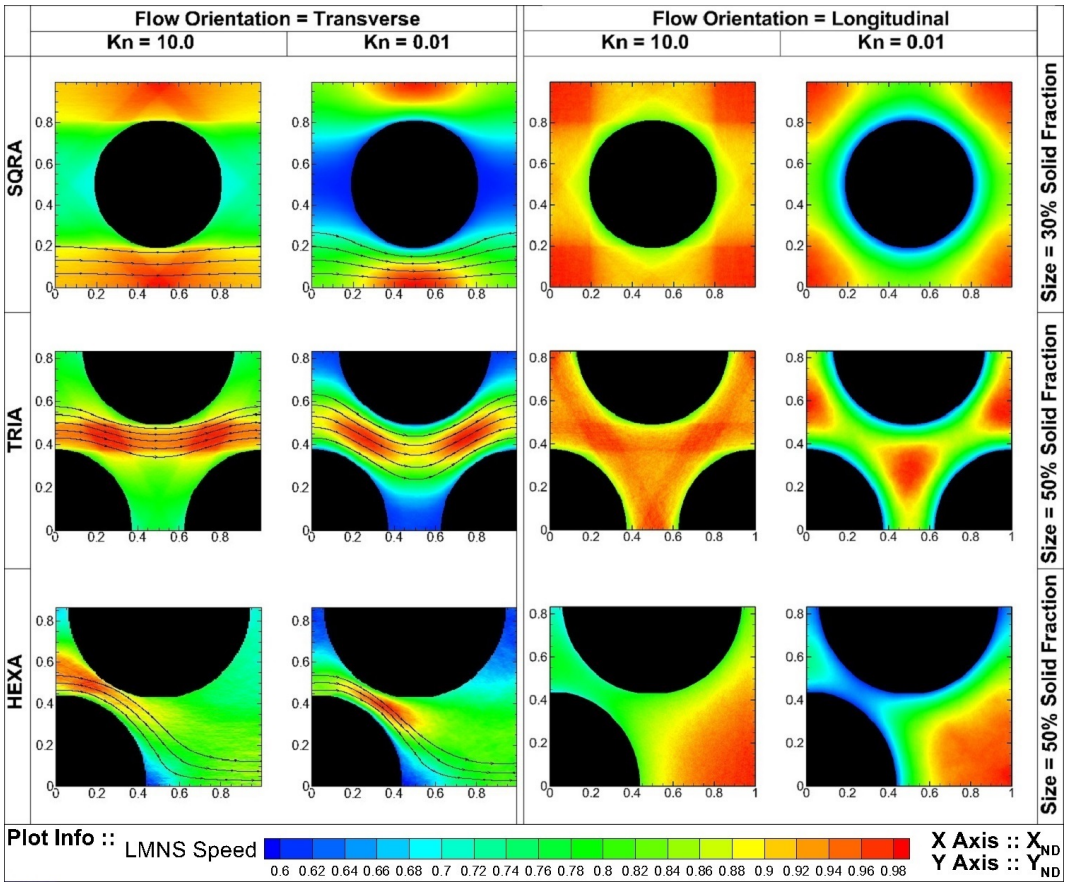


Figure 5.19: LMNS speed contours for both orientations, all arrangements and sizes at differing degrees of rarefaction.

The third consideration is the effect of shape of the obstacles and is illustrated here by LMNS speed contours for cases, $AF = \{All, C, 10, All, 1.00, 10.0\}$ and $AF = \{All, S, 10, All, 1.00, 10.0\}$. Accordingly, in fig.5.20, the left half is devoted to transverse flows while the right half is devoted to longitudinal flows. Within each flow orientation, the left and right halves represent the circular and the square cylinder respectively. The degree of rarefaction corresponds to $Kn = 10.0$ and the maximum surface accommodation is assumed ($\alpha = 1.00$).

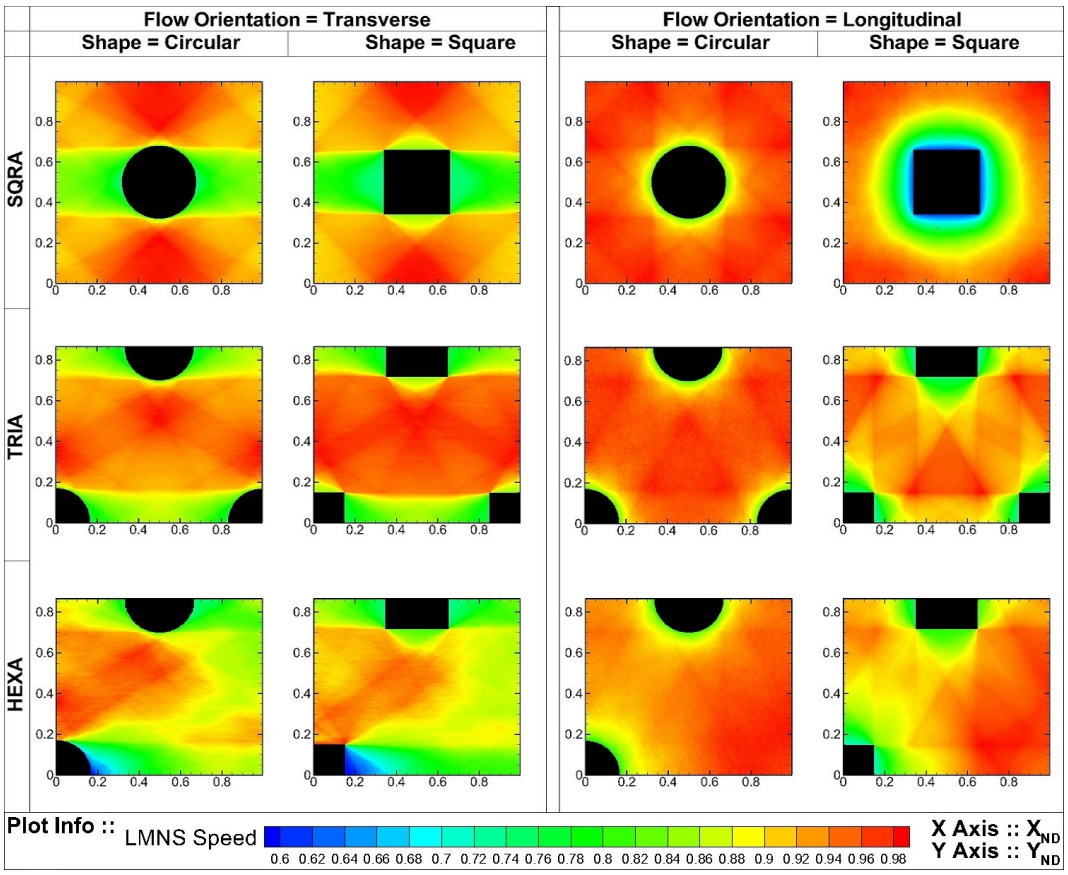


Figure 5.20: LMNS speed contours for all arrangements and orientation of infinite arrays with variation in obstacle shape (obstacle size: 10%).

The variation in permeability for all arrangements, shapes, sizes and entire range of rarefaction for transverse (fig.5.21a) and longitudinal (fig.5.21b) flows are presented. The tortuosity is more insightful for transverse flows and is presented in fig.5.21c.

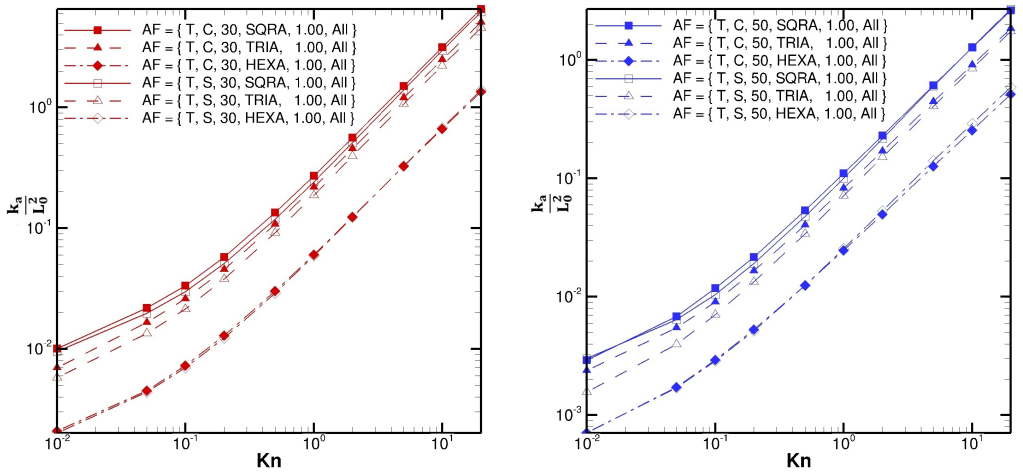


(a) Permeability for Transverse flows.

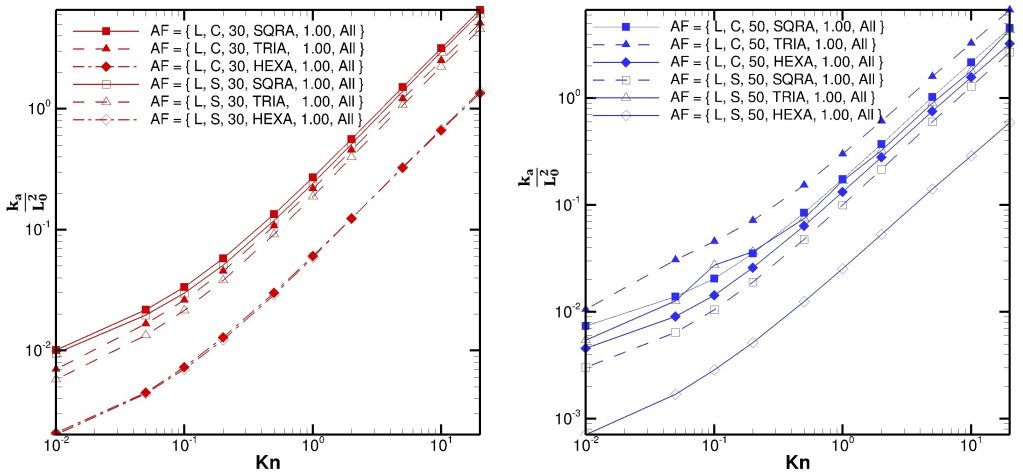


(b) Permeability for Longitudinal flows.

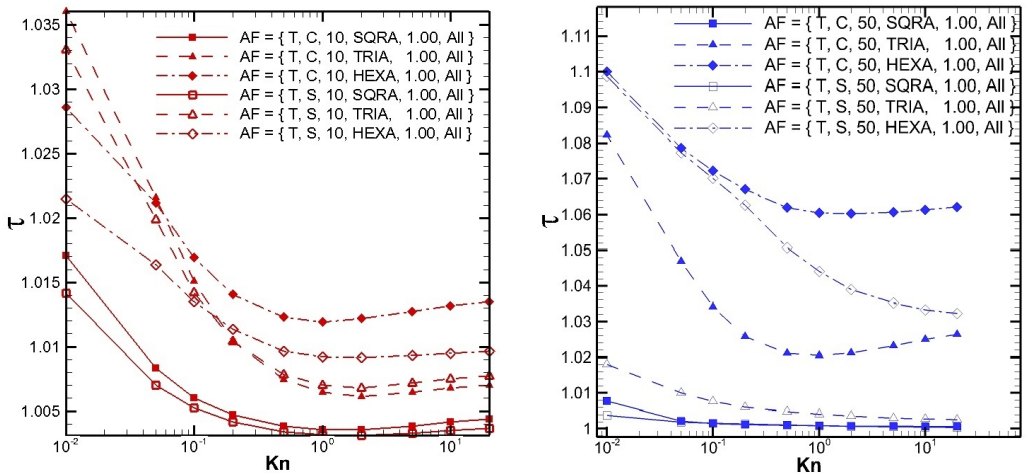


(c) Tortuosity for Transverse flows.

Figure 5.21: Variation of permeability and tortuosity versus rarefaction for both orientations, all arrangements shapes and sizes.

The rarefaction case of $Kn = 0.01$ is the lowest degree of rarefaction considered here and is compared with permeability results obtained for the continuum regime in figs.5.22a and 5.22b.

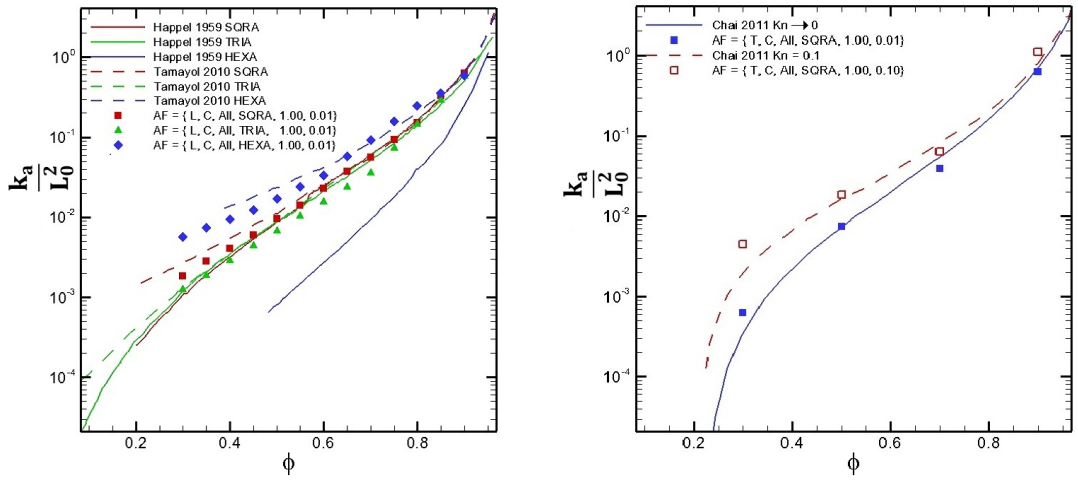


(a) Permeability for Longitudinal flows.

(b) Permeability for Transverse flows.

Figure 5.22: Comparison of permeability for both flow orientations with available literature data at low degrees of rarefaction.

### 5.4.4 Infinite array data interpretation

As per the precedent set by long-duct studies, the reference state variables $(n_0, T_0, P_0)$ are used to non-dimensionalize the quantities. The flow is driven by a small pressure gradient in the $X$ or $Z$ direction as appropriate. The gradient for a $Z$ direction flow is given by , $\xi_p = \frac{L_0}{P_0}\frac{dP}{dz}$, where, the small gradient $(|\xi_p| << 1)$ is used to scale the velocity $(u_{ND} = \frac{u}{\xi_p c_0})$. Similar treatment is employed for a flow in the $X$ direction.

The flow field is described in terms of the LMNS speed, $LMNS\ Speed = \frac{|V|}{|V|_{Max}}$, whereas, the rarefaction is characterized through the Knudsen number $(Kn)$ defined with a reference length as the longest side of the unit cell, i.e., $L_0 = L_x = a$.

These definitions are also utilized to compute the non-dimensional permeability as, $\frac{\hat{k_a}}{L_0^2} = KnG_p$, where the definition of the mass flux remains unchanged i.e., $G_p = 2\int\int n_{ND}u_{ND}dA_{ND}$. Tortuosity for a pressure gradient in the $X$ direction is computed as, $\tau = \frac{\Sigma u_{mag}}{\Sigma u_x} = \frac{\langle u_{mag}\rangle}{\langle u_x\rangle}$.

In the present computation of non-dimensional permeability, the characteristic length is chosen as the X dimension of the unit cell. The reason for this choice is principally the convenience since this length is maintained at unity for all the arrangements considered. However, literature indicates that the non-dimensionalization length utilized is typically the diameter of the obstacle. The value of this diameter and the corresponding radius for all the cases considered here is presented in the table.5.8.

$$A_{UC} = \frac{L_x}{L_0}\frac{L_y}{L_0} = \frac{L_y}{L_x} \tag{5.10}$$

$$A_S = \frac{SF}{100} A_{UC} \tag{5.11}$$

$$(A_S)_{SQRA} = \pi r_p^2 = \frac{\pi D_p^2}{4} \tag{5.12}$$

$$(A_S)_{TRIA} = \pi r_p^2 = \frac{\pi D_p^2}{4} \tag{5.13}$$

$$(A_S)_{HEXA} = \frac{3}{4}\pi r_p^2 = \frac{3}{4}\frac{\pi D_p^2}{4} \tag{5.14}$$

Table 5.8: Determination of the obstacle's non-dimensional diameter and radius in the various arrangements considered.

| Arrangement | Solid Fraction | Unit Cell Area | Solid Area | $D_p^2$ | $D_p$ | $r_p$ |
|---|---|---|---|---|---|---|
| SQRA | 10% | 1.000 | 0.1000 | 0.1273 | 0.3568 | 0.1784 |
| | 30% | 1.000 | 0.3000 | 0.3820 | 0.6180 | 0.3090 |
| | 50% | 1.000 | 0.5000 | 0.6366 | 0.7979 | 0.3989 |
| | 70% | 1.000 | 0.7000 | 0.8913 | 0.9441 | 0.4720 |
| TRIA | 10% | 0.8660 | 0.0866 | 0.1103 | 0.3321 | 0.1660 |
| | 30% | 0.8660 | 0.2598 | 0.3308 | 0.5751 | 0.2876 |
| | 50% | 0.8660 | 0.4330 | 0.5513 | 0.7425 | 0.3713 |
| | 70% | 0.8660 | 0.6062 | 0.7718 | 0.8785 | 0.4393 |
| HEXA | 10% | 0.8660 | 0.0866 | 0.1470 | 0.3834 | 0.1917 |
| | 30% | 0.8660 | 0.2598 | 0.4411 | 0.6641 | 0.3321 |
| | 50% | 0.8660 | 0.4330 | 0.7351 | 0.8574 | 0.4287 |
| | 70%* | 0.8660 | 0.6062 | 1.0291 | 1.0145 | 0.5072 |

The appropriate comparison with literature requires a modification of the presented permeability according to the computed diameter of the cylinders. The modified results for transverse flows at $Kn = 0.1$ corresponding to results of Chai [246] require the simulation at Knudsen numbers modified as demonstrated by eqs.5.15 These are presented in table.5.9 and a reasonable agreement is seen.

$$Kn_{Present} = \frac{\lambda}{L_0} \tag{5.15}$$

$$Kn_{Chai} = \frac{\lambda}{r_p}$$

$$Kn_{Present} = \frac{r_p}{L_0} Kn_{Chai}$$

Corresponding modification and the comparison to longitudinal flows at $Kn = 0.01$ presented by Tamayol [245] is showcased in table.5.10. A good agreement is seen

Table 5.9: Demonstration simulation results with conditions modified as per the paradigm set in literature for transverse flows at $Kn = 0.1$.

| Transverse Flow | | | | |
|---|---|---|---|---|
| | | Present Result | | Literature [246] |
| Arrangement | Solid Fraction | $\frac{ka}{L_0^2}$ ($Kn = 0.1$) | $\frac{ka}{D_p^2}$ ($Kn = r_p$*0.1) | ka ($Kn_{Chai} = 0.1$) |
| SQRA | 10% | 0.0411 | 0.3226 | 0.8053 |
| | 30% | 0.0146 | 0.0382 | 0.0800 |
| | 50% | 0.0116 | 0.0183 | 0.0163 |
| | 70% | 0.0041 | 0.0046 | 0.0020 |
| TRIA | 10% | 0.0075 | 0.0682 | – |
| | 30% | 0.0030 | 0.0092 | – |
| | 50% | 0.0028 | 0.0052 | – |
| | 70% | 0.0017 | 0.0022 | – |
| HEXA | 10% | 0.0254 | 0.1731 | – |
| | 30% | 0.0101 | 0.0229 | – |
| | 50% | 0.0040 | 0.0039 | – |
| | 70%* | 0.0004 | 0.0006 | – |

further adding to the assumption that simulations at $Kn = 0.01$ can be considered as continuum solutions.

The asterisk attached to the 70% solid fraction case of the HEXA structures is indicative of the overlap of the solid structures present in this configuration. The result of this overlap is the complete obstruction of the flow path that leads to a near-zero mass flow (and permeability) in the transverse flow case (refer table.5.9).

Numerical appreciation of these results is obtained by considering circular cylinders in the three arrangements, namely SQRA, TRIA and HEXA, at 30% solid fraction. The reference hydrodynamic state is assumed to be Argon gas at a pressure and temperature of $10^5 Pa$ and $273K$ respectively. The resulting values of most probable speed, gas viscosity and mean free path is $V_{mp} = 349.02m/s$, $\mu = 22.3X10^{-6}Pas$, and $\lambda = 5.2X10^{-8}m$ respectively.

The horizontal length of the unit cell is designed to be $L_x = L_0 = 5.2X10^{-8}m$ leading to the dimensional diameter ($D_P * L_0$) for the three arrangements computed as $3.213X10^{-8}m$ , $2.990X10^{-8}m$ and $3.453X10^{-8}m$ respectively. The degree of rarefaction characterized by the Knudsen number corresponds to $Kn = \frac{\lambda}{L_0} = \frac{5.2X10^{-8}}{5.2X10^{-8}} = 1.00$.

The non-dimensional permeability for transverse flows in the SQRA, TRIA and HEXA arrays at $Kn = 1.00$ as obtained by the simulation are 0.2708, 0.0603, and 0.2181 while the corresponding dimensional permeability ($k_a \xi_p L_0^2$) are $7.322X10^{-19}m^2$, $1.6305X10^{-19}m^2$, and $5.8974X10^{-19}m^2$ respectively in SI units and $741.84nd$, $165.15nd$, and $597.51nd$ respectively in petroleum industry units ($nd$: nanodarcys).

Table 5.10: Demonstration of the transformations to the present results required to effectuate a comparison with literature for longitudinal flows at continuum.

| Longitudinal Flow | | | | |
|---|---|---|---|---|
| | | Present Result at Kn = 0.01 | | Continuum [245] |
| Arrangement | Solid Fraction | $\frac{ka}{L_0^2}$ | $\frac{ka}{D_p^2}$ | $\frac{ka}{D_p^2}$ |
| SQRA | 10% | 0.0652 | 0.5123 | 0.6447 |
| | 30% | 0.0216 | 0.0565 | 0.0565 |
| | 50% | 0.0060 | 0.0095 | 0.0110 |
| | 70% | 0.0016 | 0.0019 | 0.0027 |
| TRIA | 10% | 0.0610 | 0.5530 | 0.6447 |
| | 30% | 0.0119 | 0.0361 | 0.0599 |
| | 50% | 0.0037 | 0.0068 | 0.0088 |
| | 70% | 0.0010 | 0.0012 | 0.0013 |
| HEXA | 10% | 0.1150 | 0.7820 | 0.6639 |
| | 30% | 0.0400 | 0.0907 | 0.0847 |
| | 50% | 0.0123 | 0.0168 | 0.0236 |
| | 70%* | 0.0058 | 0.0057 | – |

### 5.4.5 Observations and inferences

Much of the study of porous media has now evolved to the point where it is common to adopt geometrically complex structures produced by various algorithms as subjects of study. While these studies provide insight, they are practically unwieldy as a means of validating a new methodology or solver. There is a fundamental disconnect in the research where, the gas slippage effects with increasing rarefaction for ordered, reproducible constructions have been by-passed in favour of such studies through complex geometries.

Although it is an approximation of porous media and admittedly a poor one, the study of infinite arrays is an attempt to fill this void by conducting a thorough analysis of simple, reproducible porous media facsimiles.

The object of this study was to discern the flow features brought about by variations in the obstacle constituting an infinite array. To this end, observations obtained by the simulation are characterized and described systematically in this chapter.

Firstly, the effect of the surface roughness is seen to affect the flow adversely with an increase in the value of $\alpha$ corresponding to the reduced value of permeability. The effect is demonstrated for transverse flow through an in-line arrangement of circular cylinders of 10% solid fraction in fig.5.18a. The decrease in permeability is more significant at higher rarefaction than at lower rarefaction as shown in fig.5.18b. The non-existent variation at $Kn = 0.01$ is indicative of the insignificant role played by surface transport in comparison to the bulk transport mechanisms. Similar trends are seen to persist at all the sizes and shapes considered here.

Secondly, the influence of the flow (or grain) orientation is discussed. It is considered

to be one of the most intuitive effects to appreciate. The presence of obstacles will restrict the flow through the denial of flow area and the creation of narrow gaps. The former is largely seen in the longitudinal flows whereas, the latter effect is more tangible in transverse flows. The understanding is further strengthened by observing the fig.5.19 where the flow avoids the narrow gaps and tends to be concentrated in the unrestricted region for longitudinal flows (indicated by $i$) but is forced to navigate these tight spaces in the case of transverse flows (indicated by $ii$). The immediate outcome is the exhibition of meandering streamlines in transverse flow while the streamlines for longitudinal flow are mostly straight and directed into the page. The implication of this observation is seen in an increase in the tortuosity for a transverse flow (fig.5.21c), while the longitudinal flow tortuosity is nearly constant at 1 (not plotted here). Moreover, the effect of increased tortuosity results in a reduced permeability as is seen in fig.5.21a. This established trend is seen to hold true for any given condition of arrangement, size, shape and $Kn$, indicating that a longitudinal flow is always more permeable and less tortuous than a transverse flow. In short,

$$(k_a)\{L, All, All, All, All, All\} > (k_a)\{T, All, All, All, All, All\} \tag{5.16}$$

$$(\tau)\{L, All, All, All, All, All\} < (\tau)\{T, All, All, All, All, All\} \tag{5.17}$$

The third and fourth parameters subject to change are that of the size and shape of the obstacles. An increase in the obstacle size is associated with a reduction in the area available for the flow and facilitates an increase in the hindrance offered to the flow. Justifiably, a larger size leads to lower permeability in both transverse and longitudinal flows (figs.5.21a and 5.21b). Transverse flows further exhibit an increase in the tortuosity for increased size (fig.5.21c) as the flow is forced to navigate the tighter spaces between the obstacles. Longitudinal flow, on the other hand, exhibits a slight variation in tortuosity owing to the tendency of flows to avoid narrow regions in favour of continuous unobstructed flow spaces such as the central region of a HEXA arrangement. These features are brought into view by the field contours of fig.5.19.

The present discussion is restricted to simple shapes of a circular and square cylinder and is observed that the shape effect becomes significant only at high solid fractions. The inter-obstacle pathway provided by the curvature of the circle proves to be less tortuous than the sharply changing pathways created by the corners of the square cylinder making them more tortuous as is depicted in fig.5.21c. The corresponding permeability data reflects the effect of the tortuosity by showcasing a higher permeability for the circular cylinder in fig.5.21a. Furthermore, the tortuosity for transverse flows is higher as the continuum regime is approached because the surfaces constituting the gap increase their restrictive influence on the flow field and further confine the flow to a narrower pathway. An alternate view is to consider that the effective size of the obstacles increases as the rarefaction decreases.

The fifth and final consideration relates to the arrangement of the obstacles in the

flow domain. For a longitudinal flow orientation, the large region of unobstructed flow in the central region of HEXA is reflected in the high value of permeability succeeded by the SQRA and lastly by the TRIA (fig.5.21b). The variation is poorly reflected in the variation of tortuosity as the flows are parallel to the obstacles and are not a flow hindrance as much as a flow area reduction. Conversely, the obstacles for transverse flow fulfil the role of both a flow hindrance and an area denial. The result is the high tortuosity for the HEXA followed by the TRIA and ending with the SQRA (fig.5.21c). The order is faithfully represented in the permeability as well(fig.5.21a). In short,

$$\begin{aligned} (k_a)_L &: HEXA > SQRA > TRIA \\ (\tau)_L &: HEXA \sim SQRA \sim TRIA \end{aligned} \tag{5.18}$$

$$\begin{aligned} (k_a)_T &: SQRA > TRIA > HEXA \\ (\tau)_T &: HEXA > TRIA > SQRA \end{aligned} \tag{5.19}$$

Apart from these considerations, the permeability for the flows close to continuum is studied. As noted earlier, the vast majority of the literature resources are concerned with continuum or Stokes flows. This regime is also amenable to analysis by analytical model equations as is done in Chai [246]. At present the results for all three arrangements considered are compared for the longitudinal continuum flow conditions in fig.5.22a and are found to agree reasonably well with literature ( [245]). Transverse flow through SQRA arrangements has been investigated at continuum and at $Kn = 0.1$; the results are plotted in fig.5.22b and exhibit an agreeable match.

## 5.5 Numerical parameters and computational expenditure

All computations were performed on a workstation comprising of 32 CPU of Intel(R) Xeon(R) CPU $E5-2630\,v3$ @ $2.40GHz$ *architecture* $x86-64$. Between the two class of problems included in this consideration, the arrays proved to be a more challenging prospect from a physics point of view and thus, necessitating a deployment of a finer $500X500$ grid of instead of the $300X300$ grid used for the long-ducts. No significant difference was observed in the results when the simulation utilized 10 and 20 particles per cell making it prudent to proceed with the former option.

The computational resource deployed depended on the case, specifically the solid fraction. This is because the parallel decomposition is restricted to the pore space only implying that using more processors for a low pore space study spoils the gains due to communication overhead between processors. Hence, 8 processors were found to be economical for the high solid fractions whereas, 16 processors were deemed adequate for low solid fractions.

The convergence was typically attained with in 2000 steps for all cases considered

across all Knudsen number and $\alpha$ conditions, consequently producing results based on 50000 samples. Typical run times for the most challenging cases was clocked at around 6 to 10 hours.

## 5.6 Analysis and conclusions

In the above study, a kinetic particle approach based on the variance reduced form of the Boltzmann-BGK model with Maxwell diffuse-specular reflection model was employed to investigate the steady, isothermal flow under the influence of a small pressure gradient through internal and external structures found in MEMS devices at varying degrees of surface accommodation and rarefaction. The validity of the results is established by comparing them with literature where available.

The following conclusions can be drawn from these studies,

Firstly, the common theme of both branches has been the investigation of the flow features on account of surface roughness alterations. It is seen that this effect is most prominent in the high rarefaction conditions, diminishing as the flow attains continuum. It can thus be inferred that surfaces play an insignificant role in flow transport in the low rarefaction regimes.

Secondly, geometry plays a pivotal role in the determination of the flow behaviour. In long-ducts, the effect of lateral walls, corners and internal surfaces are seen to affect not only the microscopic velocity field but also the macroscopic properties of mass flux and Poiseuille number which are indicators of the mass and momentum transfer. For flows in infinite arrays, longitudinal flow (grains oriented parallel to the flow) are more favourable than the transverse flow (grains oriented perpendicular to the flow) featuring higher permeability and lower tortuosity. The effect of the arrangement is highly influential on the flow orientation. In the longitudinal flow orientation, the hexagonal arrangement is the most permeable whereas, in the transverse flow orientation, the square array seems to be the most permeable. The effect of size is to hinder the flow and both flow orientations suffer from an increase in size. The shape of the obstacle is dormant at small solid fraction and becomes important as the size increases.

In both branches, the lowest degree of rarefaction considered is that of $Kn = 0.01$ which, by convection, falls in the continuum regime. However, the comparison of the present results with analytical solutions do not yield a perfect match and show slight discrepancies. These can be associated with the multi-scale effects prevalent in microflows. To regard the solutions at $Kn = 0.01$ as a pure continuum solution is ill-advised and must be treated with certain degree of scepticism and caution.

To sum up, the present analysis provides an in-depth view into the effects of geometric, surface and fluid rarefaction of the flow and is an insightful characterization.

## 5.7 Chapter summary

The object of this chapter was to pose a simple yet formidable preliminary challenge of practical import for the assessment of PEGASUS' capabilities and the applicability of the variance-reduced ideology principle. To this end, two popular components found in a generic MEMS device, namely a long-duct and infinite arrays, were simulated under isothermal, pressure-driven flow conditions and are observed to be a worthy test for the solver. The well-studied nature of the long-ducts serves to provide an added layer of validation to the current method and implementation while the results around obstacle arrays manages to capture some important features that are associated with real porous media and enables the a confident transition into the next chapter focusing on porous media.

# Chapter 6

# Applications in Porous Media

*"We demand rigidly defined areas of doubt and uncertainty!"*

*— Vroomfondel, The Hitchhiker's Guide to the Galaxy by Douglas Adams*

## 6.1 Chapter overview

It has been one of the principal objectives of this thesis to determine the flow characteristics of rarefied gas flows in porous media structures. To fulfil this ambition, simulations of idealized porous media consisting of geometrically generated realistic approximations and image-based reconstructions of real porous media samples are carried out in this chapter. The solver's ability to efficiently extend to 3D flows is also explored and established in the process.

## 6.2 Introduction

The trivial definition of porous media as a two-phase structure wherein one phase is a solid and the other is a fluid is severely misleading as there is a dearth of information regarding scale and connectivity. A more informative definition would be to describe a porous media as a two-phase structure such that the solid phase is distributed all through the domain in a manner that it forms an interconnected network of multi-scale pore space that facilitates flow while exposing a significant solid surface area to the fluid [248].

The multi-scale aspect of porous media arises from the great degree of variability in the pore-space region, often ranging from $> 100\,nm$ to $< 1\,nm$. **Pore sizes** larger than $50\,nm$ are referred to as macro-pores and the flow in such structures is viscous with bulk diffusion as the dominant mechanism of transport. Pore sizes between $50\,nm$ and $2\,nm$ are classified as mesopores and feature flow dominated by surface transport and Knudsen diffusion. Micro-pores consists of pore sizes less than $2\,nm$ and are subject to molecular effects such as capillary condensation in addition to Knudsen diffusion

and surface effects. This change in the physics of fluid transport is at the heart of the complexity associated with porous media flows.

Apart from pore sizes, the **pore distribution** is another aspect of porous media that influences the flow immensely. Typically, naturally occurring porous media, specifically those of geological origins, are often characterized by diverse pore sizes distributed in an arbitrary fashion. Such porous media typically have low connectivity and high bulk densities. On the other hand, porous media originating from industrial processes, such as metallic foams, exhibit an ordered pore distribution with correlated pore sizes. The connectivity is very high and bulk densities are low making them ideal for low weight heat sink applications.

In addition to the above factors, the **pore orientation** (alternatively, grain orientation) has exhibited great influence in the establishment of the flow field. Based on the grain orientation with respect to the flow direction, porous media can be classified as either granular or fibrous. Granular media are composed of compact grains bound together to form a continuous solid matrix with pore space characterized by large open pores connected by networks of narrow constrictions. Examples of these include rock formations in petroleum reservoirs and packed beds, etc. Reviews of granular media are provided in Larson in 1989 [249] and Chapman in 1994 [250]. Fibrous media may be composed of individual rod-like particles or a complicated mesh of intertwining fibres such as industrial filters. Reviews of fibrous media are provided by Jackson in 1986 [235].

In summary, porous media are complicated structures with a large number of variable geometric parameters resulting in a confluence of flow physics confining computational scientific scrutiny to numerical approaches employing numerous simplifying assumptions applied to approximate representations of porous media. The approach adopting continuum-based methods through the definition of a Representative Elementary Volume or REV is thoroughly presented in literature [248]. Recent advances in computational prowess and kinetic theory-based numerical methods have encouraged the study of porous media at the pore level which is more fundamental. Representations of porous media can be grouped into three principal attempts, namely, statistical geometric creation, geological process-based construction and image-based reconstruction.

In the present chapter, pore-scale simulations are conducted on some of the popularly used statistical geometric idealizations of porous media. This is succeeded by porous media obtained from image-based reconstruction; first on a 2D slice of Berea sandstone and then on 3D volume reconstructions of various samples such as synthetic packs of sand and spherical beads and naturally-occurring core samples of the Gambier, Castlegate and Shale rock. Geological process-based approaches (refer Bryant [251], Bakke [252], Pilotti [253]) requires a mastery of the complex physiochemical process pivotal to the creation process of rocks and is beyond the scope of the current research, whose focus is on gas dynamics rather than geomechanics.

## 6.3 Statistical geometry-based constructions

One of the best approximations for the statistical geometric representation of porous media is the use of geometrically self-similar constructions called fractals first introduced by Mandlebrot in 1982 [254]. Among the various configurations, Sierpinski carpets, which is a plane fractal exhibiting dilational invariance published by Waclaw Sierpinski in 1916 [255], has been a recurring theme of many idealized porous media studies.

Another popular statistical geometric representation of porous media is based on the percolation theory and this approach can lead to the creation of porous media approximations in two ways. The first interpretation of percolation theory is based on the principles introduced by Broadbent and Hammersley in 1957 [256,257] and reviewed and expanded by Essam in 1980 [258]. Under this implementation, the flow domain is populated by a random assortment of solid-phase constructions located without any spatial correlation. The second interpretation identifies points for the creation of the geometries approximated as porous media. One such example is the Voronoi tessellation introduced by Voroni in 1907 [259] which is used to model a porous media with irregular and random pore structures. Further information regarding percolation models for porous media can be obtained from the detailed review provided by Golden in 1997 [260].

### 6.3.1 Literature review

Prior to the ground-breaking revelation of the fractal nature of pore spaces in many geological porous media established through the experimental studies of several sandstones by Katz in 1985 [261], all studies in porous media were concerned with either random geometries which serve as heterogeneous porous media or spatially periodic arrays of identical objects (as in chapter 5, but in a different context) which imitate homogeneous porous media. Their (Katz's) findings laid the foundations for the study of fractal porous media which, owing to their self-similarity and dilational invariance features, are globally homogeneous while being microscopically heterogeneous.

A large volume of the initial numerical studies through these structures is due to the efforts by Adler *et. al.* In their first set of six publications, the focus was on the transport processes in fractal porous media. The first paper [262] is concerned with the hydrodynamic flow characterization through the simplest fractal known as the Leibniz packing which is an ideal candidate due to its theoretical simplicity and resemblance to multi-sized solid grains encountered in porous media. The study determined the equivalent permeability in the lubrication limit finding that the value was controlled by the smallest disk of the packing. Their sixth paper in the series in 1986 [263] considers the longitudinal flow through Sierpinski carpets through the numerical solution of the Stokes flow obtaining permeability results agree well with the Carman equation. The transverse permeability computations for the Sierpinski carpet was presented as the

third article of the second publication series focussed on fractal porous media in 1988 [264] and is compared with random carpet models generated from percolation theory. The results are compared with each other finding that they are in close agreement except in the vicinity of the percolation threshold. Comparisons with classical Carman theory predictions exposed the limitations of the theory to one-dimensional flows.

Following these seminal studies, the fractal geometry, especially Sierpinski carpets, have become a common subject of study in the field of porous media and many efforts to obtain the microscopic velocity field, permeability and tortuosity are present in literature. An analytical study for the determination of the tortuosity dependence on the generation of the Sierpinski carpet was carried out by Hua [265] leading to the presentation of a model equation devoid of any empirical constants and agreeing well with established correlations.

The onset of rarefaction, slip regime specifically, was studied through a finite volume method employing the semi-implicit method for pressure linked equation (SIMPLE) along with local mesh refinement effected in the vicinity of the walls to capture the slip effects modelled through the first-order slip by Zheng in 2016 [266]. The simulation was carried out with a desire to obtain the results for the velocity field, permeability and tortuosity variation with gaseous rarefactions for the Sierpinski carpet and two other derivative structures. Several key insights are noted in this study including the reason for the effect Kn and generation have on apparent permeability. Rarefied gas flows, up till $Kn = 1.00$, through Sierpinski carpets with square and circular initiators was conducted by Rostamzadeh in 2018 [267] utilizing a novel diffuse boundary reflection model within the LBM. This treatment along with varying relaxation time was required in order to extend LBM capabilities to such rarefied flows. They recovered many effects of the carpets such as the velocity field, profile and permeability in the Darcy flow regime in addition to Darcy-Forchheimer regime at high porosities and low rarefaction. They also proposed some correlation models linking Knudsen number, porosity and permeability. A DVM iterative scheme was implemented through a multi-level parallel solver by Ho in 2019 [90]. The BGK equation for various porous media representation including the third generation of the Sierpinski carpet is solved to obtain permeability under gaseous rarefaction as far as $Kn = 1.00$.

In the second series of publications by Adler, the focus was directed onto porous media such as random carpets generated through percolation models. In the first paper of the series in 1987 [268], the Stokes flow through random structures of specified porosity generated by Monte Carlo methods based on site-percolation theory is studied leading to the determination of longitudinal permeability which match qualitatively with the predictions of the Carman. The extension to the computation of transverse permeability is presented later in the series [264].

An example of site percolation is often represented in literature as a random array of objects such as circular cylinders [269] or orthogonal shapes [163]. The viscous flow through such geometries has been scrutinized by Sangani in 1988 [270] where the

variation in the geometries are brought about through area alteration. The study employs numerical method to solve the Stokes equation to ascertain the average transverse and longitudinal permeability for various geometries and these are compared against various approximate theories to establish their validity range. The extension to 3D is realized through a random packing of spheres as was investigated experimentally and through numerical Monte Carlo simulations in 2006 by Socio [271] for rarefied gas flows. A specific configuration of this random array of circular cylinders and packed bed of spheres was also considered by Ho in 2019 [272] in their DVM based numerical simulations precipitating the determination of permeability. A similar configuration along with random arrays of squares was investigated through DVM simulations by Wu in 2017 [149] concluding that the deviation in the permeability of rarefied gas flows through such structures from Klinkenberg law is owing to the tortuous flow path and non-unitary accommodation coefficient at the pore scales.

Site percolation models can also manifest itself as randomized geometries generated by selectively filling up a domain divided into elementary cells. The choice of cells could be arbitrary [273, 274] or based on an algorithm. One such algorithm, namely the Quartet Structure Generation Set (QSGS) [275], was chosen as the subject of DVM based numerical simulation to study the rarefaction effect (restricted to the slip regime) through the computation of the apparent permeability and tortuosity for 400 geometries by Germanou in 2018 [276].

Based on the literature review cited above, a few key statements can be made.

1. Initial research focused on the analysis of gases in continuum regime where the low Reynolds number makes an analytical approach based on Stokes governing equation possible.

2. Recently, there has been a shift towards the kinetic theory-based numerical analysis of rarefied gas through such idealized porous media.

3. Majority of these attempts are based on DVM approaches which inherently require the establishment of discrete velocity space.

4. Characterization has focussed on the attainment of the macroscopic property of permeability and little to no attempt to capture the pore-scale effects has been made.

### 6.3.2 Problem statement

In the present study, the principal interest can be abbreviated to the determination of the effect of rarefaction on porous media approximations as the pore size, pore orientation and pore distribution vary.

The pore size variation is realized through the variation in the generation while the pore distribution effect is considered through the selection of an idealized porous

media approximation. Currently, the study considers the Sierpinski carpets (a fractal-based model) and a random arrangement of circular cylinders (a percolation-based model). The alteration of the pore orientation is achieved by changing the direction of the pressure gradient (flow across the X and Y directions are akin to granular porous media whereas flows in the Z direction are considered as fibrous porous media).

The domain boundary conditions are simulated by symmetry under the assumption that the geometry is placed in-between two reservoirs of nearly identical thermodynamic states. Owing to the large degree of uncertainty associated with the surface knowledge of the porous media, no approximation of surfaces is specified and maximum surface roughness is effected through the specification of accommodation co-efficient as $\alpha = 1.00$.

The object of this exercise is to determine the pore-scale features through velocity field interpretation along with macroscopic features such as permeability and tortuosity variation as the rarefaction, pore orientation, pore distribution and pore size change with each generation.

For the sake of clarity and brevity, the Sierpinski carpets are denoted by SC-* and the Percolation based carpets are denoted by PC-* where the * represents the generation (for eg. SC-III is the Sierpinski carpet of the third generation).

#### 6.3.2.1 For Fractal geometries

The basic concept of the carpet fractal is the establishment of a parent shape and the subsequent generation of smaller copies which are then removed selectively. This process can be continued recursively *ad infinitum* to yield higher generations of carpets. Various ways of generating such geometries are suggested in literature [277–279]. In the present implementation, the parent shape is chosen to be a simple square although it is not restrictive and carpets with triangles and circles have been utilized. The flow domain is assumed to be a perfect square which is divided into 9 identical sub-regions. In the $1^{st}$ generation, the central square is declared as solid. To produce the $2^{nd}$ generation, each of the remaining fluid squares is further subdivided into 9 regions and the central square of each is declared as a solid phase. Successive generations are produced by the repetition of the aforementioned process. At present, we restrict our consideration to the first 5 generations as depicted in figs. 6.1a,6.1b,6.1c,6.1d,6.1e.

The extension of the Sierpinski carpet to $3D$ can be done in one of three ways. The first results in a fractal suspension as depicted in fig.6.1f; the second leads to the creation of a fractal sponge called as the Menger sponge after Karl Menger in 1926 [280] depicted in fig.6.1g whereas, the third results in the generation of a maze (fig.6.1h).

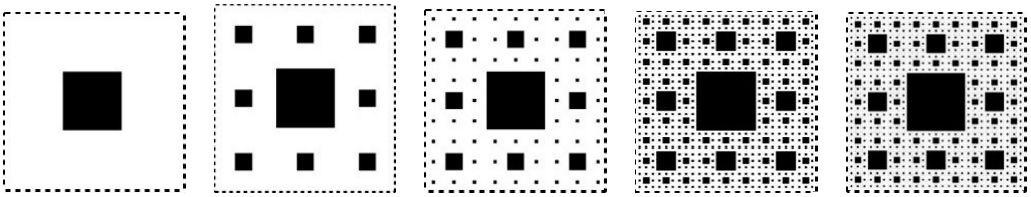

(a) Generation I (b) Generation II (c) Generation III (d) Generation IV (e) Generation V

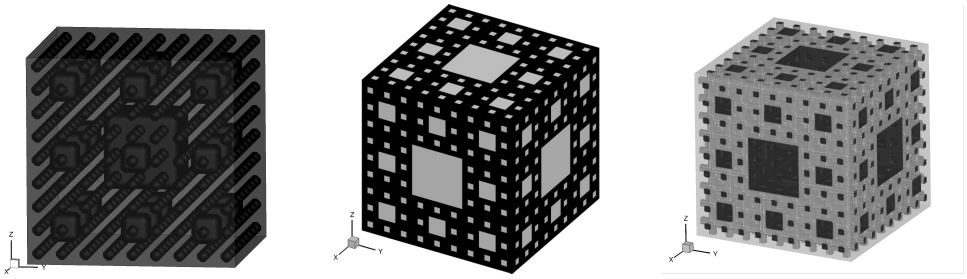

(f) Generation III Sierpinski suspension (g) Generation III Menger sponge (h) Generation III Sierpinski Maze

Figure 6.1: Idealized porous media generated based on statistical geometric approximations using fractal theory (White/Grey : Pore space; Black : Solid phase)

The interest in Sierpinski carpet is due to the large scale variation in obstacle size effectively recreating the multi-scale nature of rarefied gas flow in porous media albeit in a geometry that is easily generated featuring complexity that can be easily and understandably increased.

The popularity of Sierpinski carpets can be attributed to the dilational invariance exhibited by these structures. The global homogeneity is related to the global translational invariance and hence, allows for the application of up-scaled methods such as REV while also including the local (microscopic) heterogeneity which is adequately represented by such fractal carpets.

#### 6.3.2.2 For Percolation-based geometries

Percolation theory is designed to determine whether fluid can traverse the porous media matrix. Presently, studies based on percolation theory generate a random seed map and then construct generation of geometries of increasing complexities till the flow is completely hindered. In the present work, the flow domain is a $2X1$ rectangular domain where 263 points are identified randomly as depicted by fig.6.2a (representing Generation 0 or Seed map).

Once identified, circles are generated at each of the seed points with radii varying in between $r_1$ and $r_2$. The resulting geometry is the first generation of the porous media (fig.6.2b). Each successive generation is created by redrawing the circles with an increase in radius, i.e. $r_{II} = r_I + dr$. The figs.6.2b,6.2c,6.2d,6.2e,6.2f depicts the 5 generations used herein with the red outline indicating the increase in size of the

individual cylinder over the previous generation.

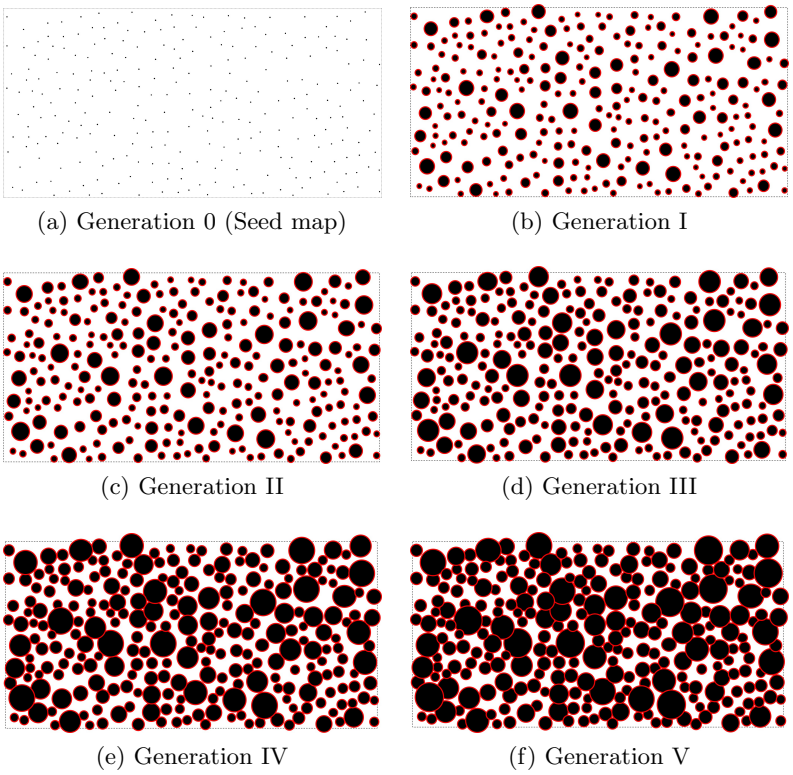

(a) Generation 0 (Seed map) (b) Generation I

(c) Generation II (d) Generation III

(e) Generation IV (f) Generation V

Figure 6.2: Idealized porous media generated based on statistical geometric approximations using Percolation theory

The reference state variables $(n_0, T_0, P_0)$ are used to non-dimensionalize the quantities. The flow is driven by a small pressure gradient in the $X$, $Y$ or $Z$ direction as appropriate. The gradient for a $Z$ direction flow is given by , $\xi_p = \frac{L_0}{P_0}\frac{\mathrm{d}P}{\mathrm{d}z}$, where, the small gradient ($\left|\xi_p\right| << 1$) is used to scale the velocity ($u_{ND} = \frac{u}{\xi_p c_0}$). Similar treatment is extended to the other directions.

The flow field is described in terms of the LMNS speed, $LMNS\ Speed = \frac{|V|}{|V|_{Max}}$, whereas, the rarefaction is characterized through the Knudsen number ($Kn$) defined with a reference length as the side of the unit cell parallel to the flow.

The quantities inherent to porous media such as the the non-dimensional permeability and the tortuosity are computed akin to the infinite array studies with a small caveat for the computation of non-diagonal permeability elements ($k_{ij}; i \neq j$) which are calculated as per equations presented in section 2.3.2. Tortuosity for a pressure gradient in the $X$ direction is computed as, $\tau = \frac{\Sigma u_{mag}}{\Sigma u_x} = \frac{\langle u_{mag} \rangle}{\langle u_x \rangle}$.

### 6.3.3 Simulation results

The variation of the available pore space with generation for the idealized porous media considered in this study is presented in fig.6.3.

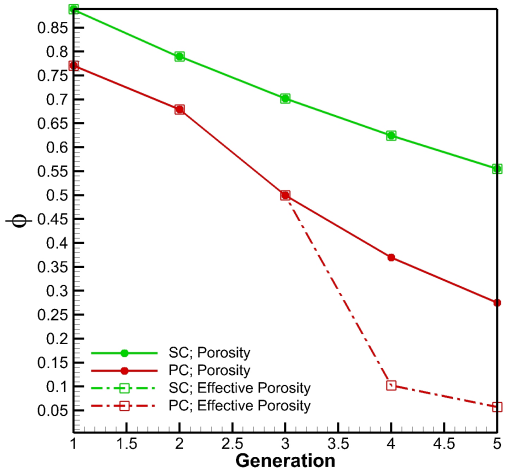


Figure 6.3: Variation of porosity as a function of generation for the fractal-based and percolation-based approximations.

Much information can be gathered regarding the pore scale flow from the velocity field contours that are depicted for the 5 generations of the Sierpinski carpets as shown in fig.6.5 along with rarefaction effect through the permeability and tortuosity plots in figs.6.4a and 6.4b respectively.

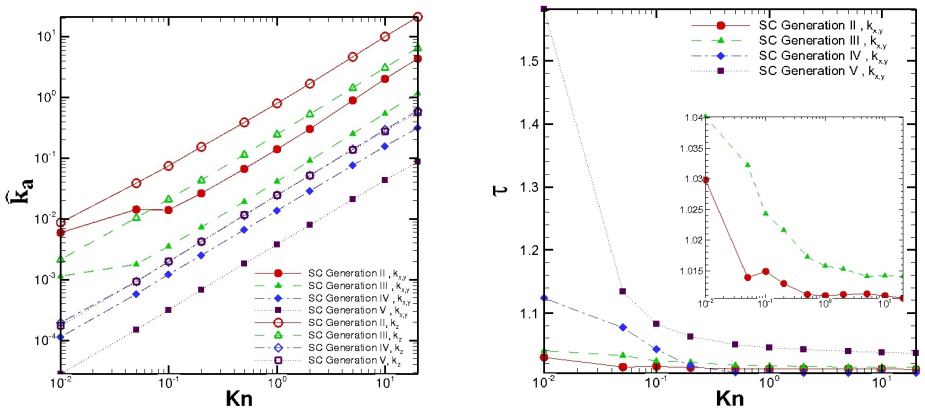


(a) Permeability for Longitudinal and Transverse flows.

(b) Tortuosity for Transverse flows only.

Figure 6.4: Results for 2D manifestation of first 5 generations of 2D Sierpinski carpets.

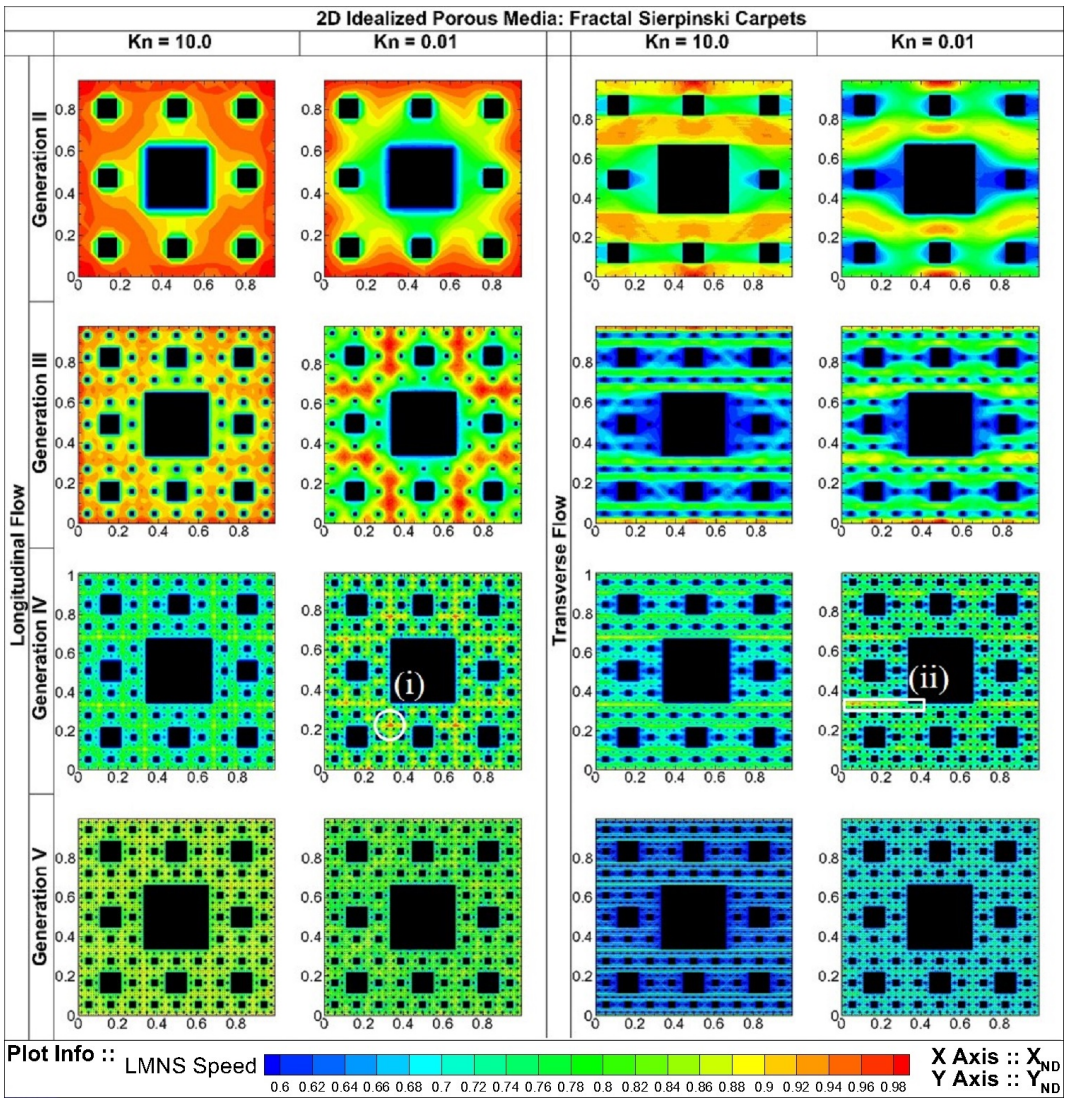


Figure 6.5: LMNS speed contours for 2D manifestation of 5 generations of 2D Sierpinski carpets.

The LMNS speed contours for the 3D extensions are shown for the $3^{rd}$ generation Menger sponge in fig.6.6a, suspensions in fig.6.6b and maze in fig.6.6c. The corresponding permeability variation is presented in plot.6.7a while, the matrix is presented in eq.6.1.

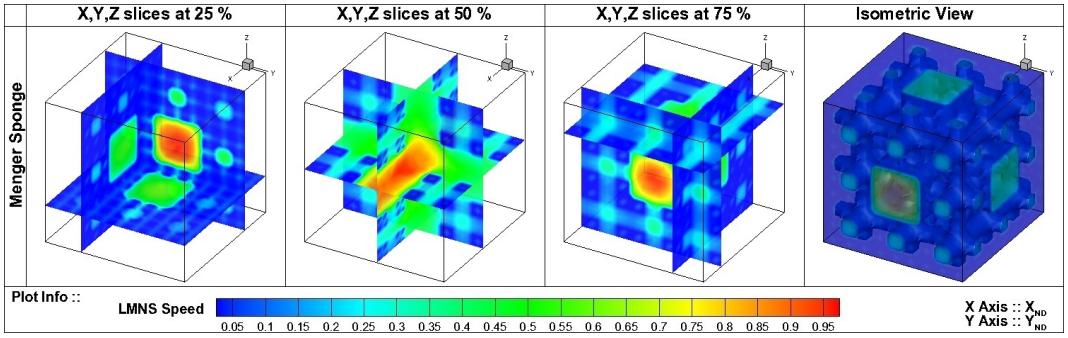


(a) Menger Sponge

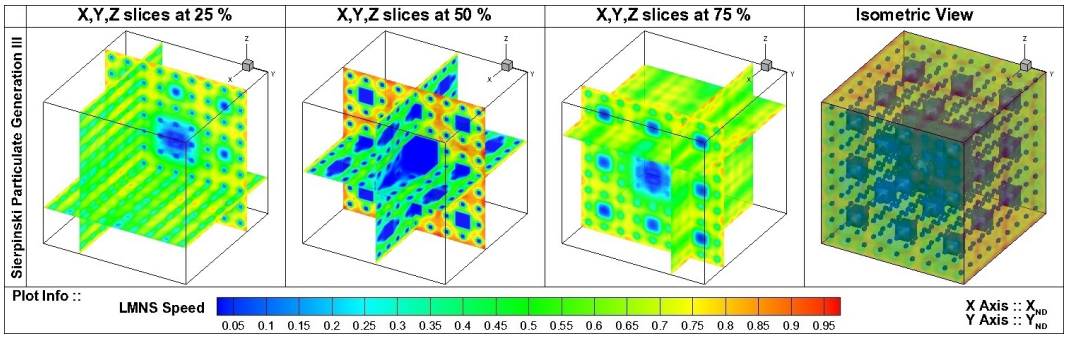


(b) Suspensions

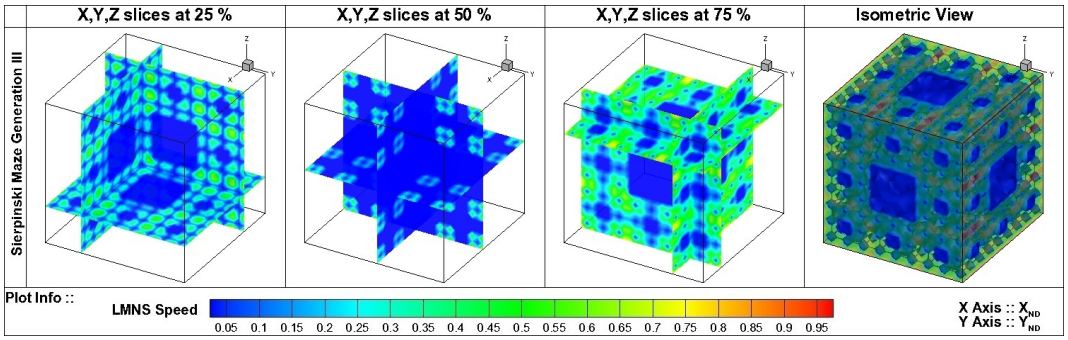


(c) Maze

Figure 6.6: LMNS speed contours plots for 3D manifestation of Sierpinski carpet.

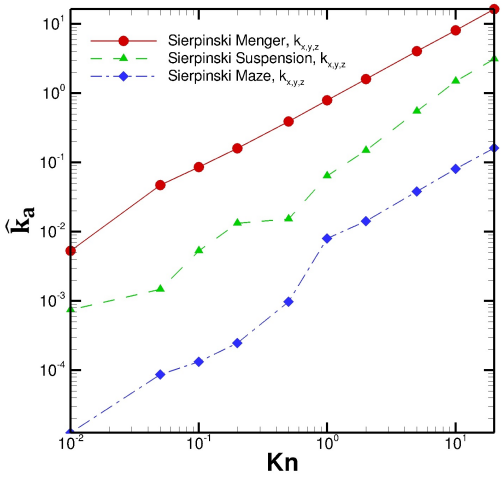


Figure 6.7: Permeability results for 3D manifestation of Sierpinski fractals.

$$\begin{bmatrix} k_{xx} & k_{xy} & k_{xz} \\ k_{yx} & k_{yy} & k_{yz} \\ k_{zx} & k_{zy} & k_{zz} \end{bmatrix} \tag{6.1}$$

$$= \left\{ \begin{bmatrix} 0.7902 & 0.0004 & 0.0004 \\ 0.0004 & 0.7902 & 0.0004 \\ 0.0004 & 0.0004 & 0.7902 \end{bmatrix} \xrightarrow[\%]{Max.Normalized} \begin{bmatrix} 100.00 & 0.05 & 0.05 \\ 0.05 & 100.00 & 0.05 \\ 0.05 & 0.05 & 100.00 \end{bmatrix} \right\}_{Menger\ Sponge}$$

$$= \left\{ \begin{bmatrix} 0.0641 & 0.0005 & 0.0005 \\ 0.0005 & 0.0641 & 0.0005 \\ 0.0005 & 0.0005 & 0.0641 \end{bmatrix} \xrightarrow[\%]{Max.Normalized} \begin{bmatrix} 100.00 & 0.79 & 0.79 \\ 0.79 & 100.00 & 0.79 \\ 0.79 & 0.79 & 100.00 \end{bmatrix} \right\}_{Suspensions}$$

$$= \left\{ \begin{bmatrix} 0.0080 & 0.0001 & 0.0001 \\ 0.0001 & 0.0080 & 0.0001 \\ 0.0001 & 0.0001 & 0.0080 \end{bmatrix} \xrightarrow[\%]{Max.Normalized} \begin{bmatrix} 100.00 & 0.65 & 0.65 \\ 0.65 & 100.00 & 0.65 \\ 0.65 & 0.65 & 100.00 \end{bmatrix} \right\}_{Maze}$$

The velocity contours for the $3^{rd}$ generation of the percolation model are illustrated in fig.6.8a for the pressure gradients in the $X$, $Y$ and $Z$ directions. The associated variation in permeability and tortuosity is plotted in fig.6.8b.Furthermore, the velocity contours for the 5 different generations of the percolation geometries are presented in fig.6.9a and the macroscopic details are provided in fig.6.9b.

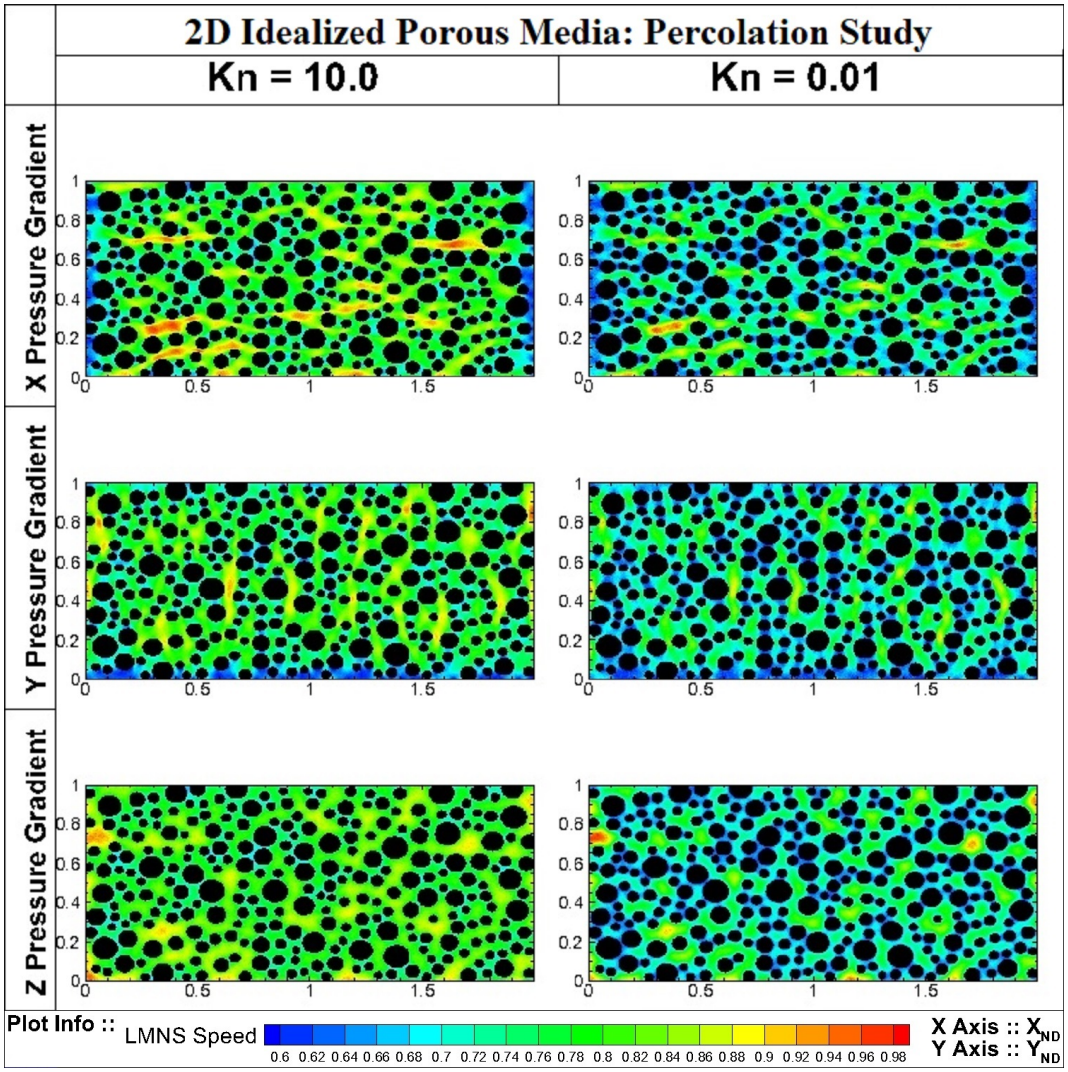


(a) LMNS speed contours.

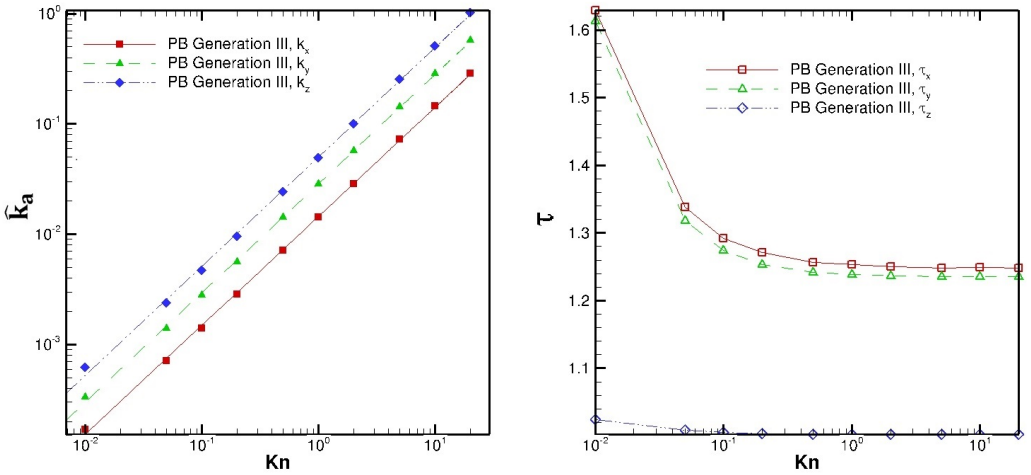


(b) Permeability and Tortuosity.

Figure 6.8: Results for $3^{rd}$ generation PC under 3 pressure gradients.

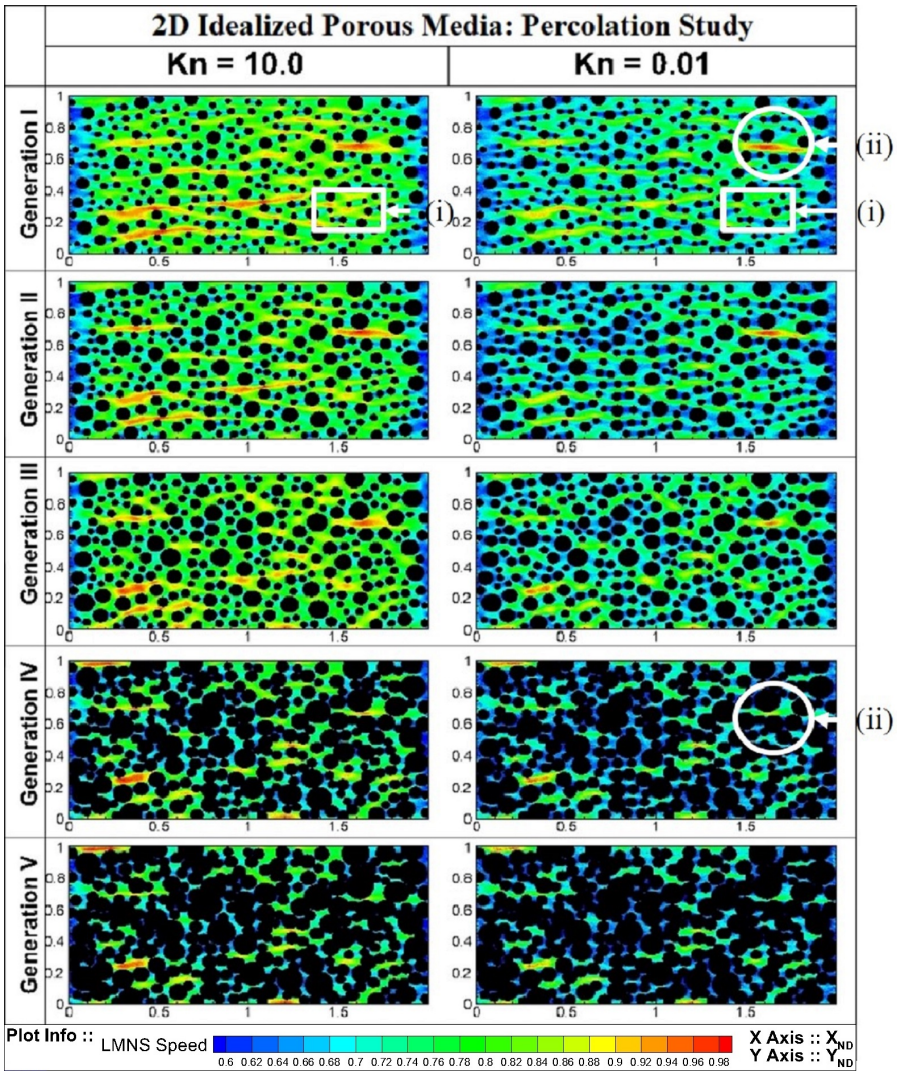


(a) LMNS speed contours.

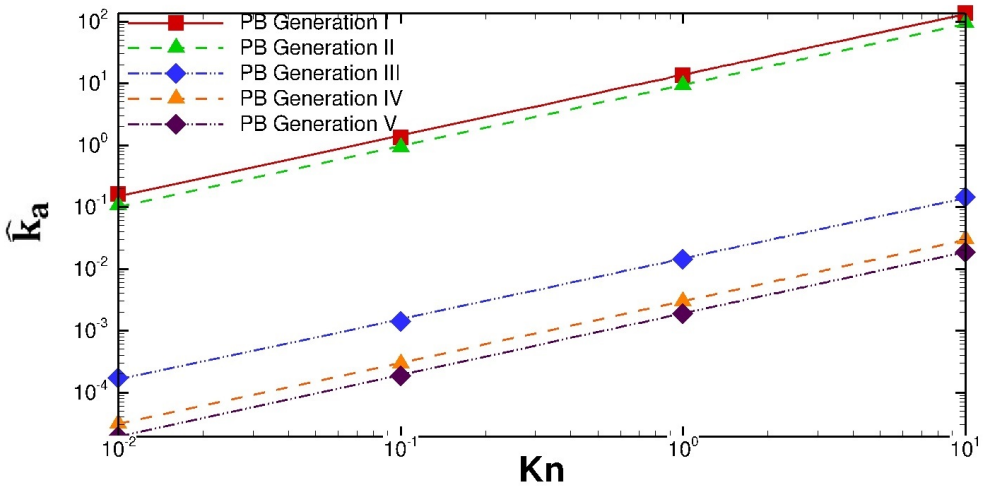


(b) Permeability.

Figure 6.9: Results for 2D manifestation of 5 generations of 2D Percolation carpets.

### 6.3.4 Idealized media data interpretation

The numerical appreciation of the permeability for the longitudinal and transverse flow through SC-III can be obtained by calculating the dimensional value as $k_a \xi_p L_0^2$ where, $L_0$ is considered as the side on the square domain and is assumed to be equal to $\lambda = 10^{-8}m$, thereby making $Kn = 1.00$. The non-dimensional permeability for the longitudinal and transverse flow cases are $k_a = 0.2452$ and $k_a = 0.0415$ respectively which result in a dimensional permeability of $0.2452X10^{-3}X(10^{-8})^2m^2 = 24.84nd$ in the longitudianal direction and $0.0415X10^{-3}X(10^{-8})^2m^2 = 4.20nd$ in the transverse direction($nd$: nanodarcys).

### 6.3.5 Observations and inferences

Based on the simulation results some key insights can be gleaned. However, before continuing on to a discussion of the gas-dynamic aspects through simulation results, it is worth taking into account the structural aspect. A progression in the generation, in both the carpets (SC and PC), implies an increase in the solid fraction and subsequent loss of porosity as is illustrated in fig.6.3. However, the SCs differ from the PCs considered here in the manner of solid fraction growth. Solid grains in SC never overlap and thus, every pore space is accessible to a gaseous flow. This is true irrespective of how high a generation is reached as is indicated by the non-linear variation of the SC plot implying that the percolation threshold can only be reached asymptotically. This nature of the SC results in the equivalence of porosity and effective porosity while the same can't be claimed for PC structures. The overlap in the solid grains significantly alters the resulting flow network by isolating certain pore spaces within the solid matrix thereby, negating their role in gas transport. This is clearly observed in the PC plot where a deficiency (percentage decrease) of approximately 70% and 80% is observed in the porosity for the $4^{th}$ and $5^{th}$ generations respectively.

The gas-dynamic analyses begin by considering the idealization of porous media as 2D Sierpinski carpets of various generations. The SC models exhibit identical structures in the $X$ and $Y$ directions and thus, the flow in the X direction is considered sufficient to characterize the transverse flows while the longitudinal flow features are characterized through the flow in the $Z$ direction.

A cursory observation of the results for the SC simulations reveals the intuitive outcomes such as the adverse effects to the flow field due to the presence of obstacles brought about by an increased generation. Moreover, the effect is more pronounced for the transverse flows as compared to the longitudinal flows as is sufficiently indicated by the fig.6.4a where the longitudinal permeability is always higher than the transverse permeability irrespective of the generation or degree of rarefaction.

The effects achieved by a decrease in rarefaction is more intriguing. As adequately established in the infinite array considerations of Chapter 5, the consequence of rarefaction is exhibited through increased slip at the solid surfaces making surface transport

conducive. In longitudinal flows, this culminates in the confinement of the flow to small regions experiencing the least resistance (marked by $(i)$ in fig.6.5). In the event of transverse flows, the ramification of a generation increase is to restrict the flow pathways thereby, providing an incentive for the gas to seek alternate, possibly longer, pathways (marked by $(ii)$ in fig.6.5). In rarefied regimes, these flow pathways are wide owing to the gas slippage, but as the rarefaction decreases, the width of these pathways becomes narrower due to the increase in the surface influence. This results in an inclination of transverse flows to seek longer paths is illustrated by the tortuosity plot which exhibits higher values for lower $Kn$ at all generations. The effect is weakened at larger $Kn$ indicating that the increase in surface transport empowers the gas to flow in relatively straight pathways (fig.6.4b).

Closer inspection of the contours reveals that the flow in both, longitudinal and transverse, directions have an affinity towards the pore spaces between the youngest members of the generation as brought to light by the markings in fig.6.5. Conversely, the least favourable pore spaces are observed in the vicinity of the central obstacle. This highlights the importance of the heterogeneity in size of the solid grains in porous media.

Moreover, the simulation of $5^{th}$ generation was carried out with an ulterior motive of establishing the fidelity of the solver in recognizing and taking into account the multi-scale aspects of the porous media by accurately representing the effects of all solid grains including the youngest member whose resolution is exactly that of the single simulation cell (essentially a single pixel).

The geometric inability of the Sierpinski carpets to stop the flow encourages another branch of investigation, namely, the flows through carpets based on percolation theory. These models differ from SC in that an increase in the generation affects the pore sizes and distribution significantly leading to well-connected large open pore spaces at lower generations and poorly connected small pore spaces at the higher generations.

The random orientation of the geometries developed under this theory makes tortuosity an important contributing factor that affects the evolution of the velocity flow field and the macroscopic properties especially permeability.

The $3^{rd}$ generation is unique for two reasons; first, the porosity of the structure is 0.50 indicating that the solid and gaseous phases are equally distributed; second, it is the last generation prior to the overlap implying that the entire porosity is accessible to the flow. This makes it an ideal choice for the study of the effect of pore orientation. The resulting LMNS speed field (in fig.6.8a) demonstrates that the flow preference towards larger pore spaces connected by quasi-linear pathways. The profusion of such pathways in the $Y$ direction makes it more permeable than the $X$ direction (nearly a 100 % increase at $Kn = 10.00$). As anticipated, the uncontested nature of the flow along the $Z$ direction makes it the most permeable and least tortuous orientation. The effect is seen to persist at the lowest degree of rarefaction as demonstrated in the inset of fig.6.8b.

Increasing generation results in a reduction in the pore connectivity with the transformation of multiple, parallel flow paths in lower generations into highly contorted serial flow paths at higher generations. Furthermore, a decrease in the rarefaction constricts the available flow paths by reducing gas slippage resulting in the mitigation of flow pathways as is clearly demonstrated by the disappearance of the conducive regions. These characteristics are qualitatively presented in fig.6.9a where, $(i)$ and $(ii)$ demonstrate the effect of rarefaction while $(i)$ and $(iii)$ exhibit the consequence of a generational increase.

Independent of the degree of rarefaction, the rise in generation and the subsequent contortion and elimination of flow pathways is amply appreciable in the permeability and tortuosity plots 6.9b. A precipitous drop of approximately 80 % is present between the generations $III$ and $IV$ while, generation $V$ is considered to have nearly attained the percolation threshold.

For both carpets considered in this study, the most adverse flow conditions encountered corresponds to the transverse flow through the highest generation, namely, the $5^{th}$. However, the permeability at $Kn = 10.0$ for the SC is larger than the PC whose low value is an indicator of the proximity of the structure to attaining the percolation threshold.

The final discussion pertains to the extension of the Sierpinski carpets to $3D$ structures with the view of establishing the tensor nature of the permeability in a coupled manner by applying a unidirectional pressure gradient and obtaining the permeability matrix. For conciseness, the LMNS speed contours for generation $III$ of a suspension (6.6b), a sponge (6.6a) and a maze (6.6c) are chosen as these are an adequate representation of the flow field. The flow is directed in the $X$ direction although it has little bearing on the end result since the structures possess complete symmetry.

The speed contours highlight the structural aspects of these structures. The Menger sponge features straight ducts with branching ducts intersecting at right angles which proves to be discouraging for flows intending to deviate from the direction imposed by the applied pressure gradient. On the other hand, the maze introduces a labyrinth for the flow to navigate and thus, entice the flow to alter their direction. Finally, the flow through the suspension provides a straight pathway for some portion of the flow while hindering the remaining portion with obstacles forcing the gas to seek an alternate route around it.

The structural features also explain the different values in the diagonal elements of the permeability matrix as is plotted in fig.6.7a. The presence of well-connected pathways results in the dominance of the diagonal elements over the off-diagonal elements of eq.6.1. However, the relative significance of the off-diagonal permeability compared to the diagonal element for the different structures considered here is seen to be maximum for the suspensions and minimum for the maze. This can be considered as a measure of the degree to which the flow is forced to deviate from the straight path with the suspensions providing the largest incentive.

Anisotropy of the permeability matrix is not established in these studies as the structures are symmetric about the 3 cardinal axes. 3D extension of the percolation carpets is expected to yield the anisotropic, asymmetric permeability matrix. However, as these structures are obtained through processing of a .raw image file, it more pertinent to address these in the subsequent section.

## 6.4 Image-based reconstructions of porous media

The 3D microstructure of a porous media is obtained through methods such as X-ray computed tomography [281, 282], synchrotron-based micro-tomography [283], focused ion beam – scanning electron microscopy [284–286] and energy-dispersive spectrometry [286,287]. A review of the imaging techniques is provided by Wildenschild and Sheppard [288]. Such methods are expensive and time consuming while also being restricted in terms of image resolution and sample size.

Alternatively, the porous media can be subjected to serial sectioning and the 2D thin section can be imaged through FIB-SEM. The series of 2D slices are then reconstructed using computational algorithms [289] utilizing statistics to establish interconnectivity. This process is relatively convenient and inexpensive while providing high-resolution images. The trade-off is the realization that the reconstructed media is unlikely to perfectly represent the pore size, shape and connectivity of the original 3D sample [290–292]. However, it is expected that the reconstructed media will faithfully represent the averaged macroscopic properties [293, 294]. This expectation has led to a large volume of research dedicated to the development of these algorithms and continues to be an active field of research [295, 296].

### 6.4.1 Literature review

Hampered by computational restraints, many researchers have taken recourse to the simulation and analysis of flows through 2D slices of image-reconstructed porous media. The study of one such media under the effects of gaseous rarefaction was considered by Kalarakis in 2012 [297]. The work featured a tandem simulation utilizing DSMC and LBM to obtain permeability which differed significantly from the intrinsic permeability as the gas slippage effect increases reflecting the Klinkenberg effect. Furthermore, the DSMC method was found to be woefully slow as the flow approached continuum whereas, special consideration of the relaxation time was required for LBM so as to adequately represent the effects of local rarefaction as Kn increased. The relationship between the relaxation time (viscosity) and Knudsen number was described using a Bosanquet approximation and the resulting coefficient, set *a priori*, was found to be a weak function of the pore size and was relatively constant in the transition regime. 2D porous media slice of the Berea sandstone was the topic of many investigations such as the single-phase flow study by Boek in 2010 [298] and the single and multiphase

study by Wu in 2016 [299]. The single and relative permeability calculated based on the LBM simulations have shown excellent agreement with experimental data. Though these studies validate that the LBM is a viable approach to calculate fluid flow in complex porous media, the ability of this method to appropriately capture rarefaction effects is severely questionable without some consideration for the relaxation time.

Recent times has witnessed the advent of pore-scale simulations in 3D reconstructed models such as the laminar single and multiphase flow simulations of Piller in 2014 [300]. They demonstrated the ability of CFD software to reconstruct the complex morphology of porous media from binarized information followed by simulations to determine the apparent and relative permeability. The extension of the research interest to 3D Berea sandstone followed suit with single and multiphase studies [301]. Single-phase 3D flows through the Bentheimer sandstone using LBM was studied by Boek in 2010 [298]. In a direct numerical investigation lead by Muljadi in 2016 [302], OpenFOAM using the PISO (Pressure Implicit with Splitting Operator) for water flow through Beadpack, Bentheimer and Estallides rocks were undertaken with the focus on the effect of transition from the Darcy to the Forchhimer flow regimes. The permeability and tortuosity as a function of the Reynolds number are reported and monotonic fall and rise is observed respectively. The high Reynolds number is conducive to vortex formation which contributes to an increase in tortuosity and decreased permeability. Furthermore, at higher flow rates, the flow appears to be focussed in straight high-speed zones termed as inertial core by Dybbs in 1984 [303]. For rarefied gaseous flows, Klinkenberg effect was verified by comparison of water and gas (Nitrogen) permeability obtained from experimental studies conducted on sedimentary rock samples obtained from the western foothills of Taiwan by Tanikawa in 2006 [304].

The attention commanded by mudrocks such as shale and siltstone is justified; industrially due to their store of unconventional gases in ultra-tight pores and academically due to the complexities arising from their nanoscale structures [305] and adsorption/desorption effects. These effects have been verified through experimental studies such as those by Ju on 2016 [306] on shale rocks in Zhanhua depression and on Marcellus shale by Goral in 2015 [307]. New numerical models intent on accurately modelling these nanopores and nano grooves received attention from the research community with the application of second-order slip boundary condition in Navier Stokes based studies on the Shale rocks by Moghaddam in 2016 [134] and a new model based on the gas molecule-pore wall interaction was proposed by Javadpour in 2009 [308]. A pore network for the simulation of flows in shales was put forth by Ma in 2014 [309] with validations performed against available experimental results. In 2015, Kazemi [310] used the regularized 13-moment method to analytically obtain the permeability for the ultra-tight pores of the Shale rocks where rarefaction effects are most significant. The adsorption effects are modelled using the Langmuir isotherms of different shale samples. The results are compared to the experimental data obtained for the Marcellus Shale sample and reasonable agreement was established. In addition to this, multiple shale

samples such as Barnett, Eagle Ford, Marcellus and Montney were also considered. The consideration of adsorption effect in the case of Shale rock formations is an active research challenge and has encouraged various diverse approaches as exemplified by Yu in 2017 [311] where the effect was addressed by appealing to molecular dynamics. The corrections needed for rarefied gas flows through such tight gas reservoirs is investigated by Ziarani in 2012 [312] in the context of flows through Mesaverde sandstone. The Klinkenberg correction and Knudsen correction with coefficient from Beskok [136] and Civan [150] are compared with experimental data for the whole spectrum of rarefaction. The conclusion of this study is that the Klinkenberg model underestimates the permeability, especially at high Knudsen regimes and recommends the use of the Knudsen permeability correlation for such tight gas reservoirs. The insufficiency of the Klinkenberg correction to model the high gas rarefaction was also recognized in a study conducted by Mohammadmoradi in 2016 [313] where a novel approach employing the CFD and DSMC methods was applied to study gas-water displacement scenarios in Travis Peak Tight Sandstone.

In the most recent addition to the literature, Ho [272] demonstrated DVM's ability to ascertain the macroscopic properties such as apparent permeability for various porous media structures such as the 2D Berea sandstone and 3D reconstructed samples of sand-pack and ultra-tight Fayetteville shale rock. The results are compared and contrasted against LBM and the correlation models reaffirming the issues with LBM and need for higher-order correlations examined previously in this brief. Furthermore, the article states that though theoretically, larger Kn require DVM to employ a larger set of discrete velocities; practically, a smaller velocity set is capable of accurately predicting the permeability in complex porous media due to the rarefied gases' proclivity to gravitate towards the least resistive pathways that correspond to the larger pore spaces.

The above survey makes it possible to make a few definitive statements regarding the status of studies dealing with fluid flows through porous media to-date, namely,

1. The complexity increment from idealized porous media considerations is immediately apparent with a negation of the ability to reliably predict the permeability using simple correlation models, such as the Klinkenberg correction.

2. Numerical approaches have varied greatly with LBM, DVM and moment methods prevalent at present. Though academically viable, these methods are cumbersome to the uninitiated industrial use.

3. DVM and LBM are encumbered by their deterministic nature which demands a certain degree of pre-cognizance regarding the number of important factors, for instance, the number of discrete velocities to be employed. Regularized moment methods are mathematically sound, but are lacking the intuitive quality characteristic of particle methods. DSMC, while possessing this quality, in addi-

tion to being stochastic, is mired by the low signal nature of the flow leading to the computational effort being tethered to the procurement of a large number of samples.

4. As such, there is an absence of an industrially deployable, computationally efficient, fire-and-forget spirited method capable of performing the entire procedure, from core image reading to microscopic flow-field and macroscopic quantity determination. This is the vacuity addressed by the present method.

5. Finally, figure-of-merit in nearly all the literature involved with complex porous media is the macroscopic property of permeability. Characterization at the pore level is usually provided through velocity fields which are unwieldy to comprehend. Novel means of describing insightful pore-level information is needed.

### 6.4.2 Problem statement

The advances in digital imaging are put to use in the following study wherein, the structure of the porous media is directly obtained from the image. The process of reading, digitization, binary representation and solution of real porous media is carried out by the present solver.

#### 6.4.2.1 For 2D - Berea Sandstone

In the 2D consideration, the thin section of a Berea sandstone is utilized as it is one of the main samples used by the petroleum industry for many years as a standard. The reason is due to the special properties of the rock such as homogeneity, availability and well-sorted, well-rounded nature of its grains. The composition is mostly quartz with the presence of feldspar, dolomite and clays [314]. The particular image considered here (fig.6.10) has been engineered from the 3D Berea sandstone rock sample of dimensions 1418 X 1774 $\mu m$ with an etch depth of 24.54 $\mu m$ at the Schlumberger Cambridge Research and the image is a of resolution of $453X457X1$ pixels with a porosity of approximately 30%.

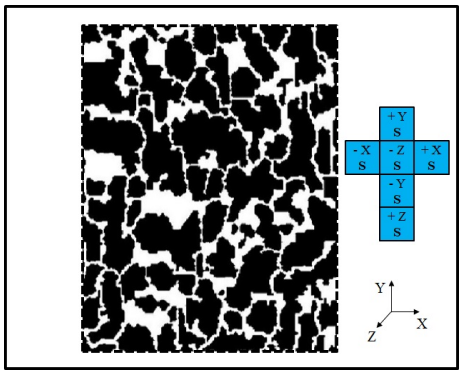


Figure 6.10: 2D Image based reconstruction of a Berea sandstone

#### 6.4.2.2 For Image-based reconstructions 3D - Packs and Rocks

In the 3D consideration, the micro-CT images of porous media data regarding the structure of various synthetic packs and actual rock samples are considered.

Among the synthetic packs, a bead pack made up of glass spheres of diameter $1.59\mu m$ and voxel side length $17.472\mu m$ (fig.6.11a) and LRC32 grade fluvial sand pack of voxel side length of $9.184\mu m$ (fig.6.11b) are considered.

Two of the three samples of rocks considered here are outcrops, namely, a Castlegate sandstone from southeastern Utah in the USA with a voxel length of $5.6\mu m$ (fig.6.11c) and fossiliferous Gambier sandstone obtained from Mt. Gambier in South Australia (fig.6.11d)with a voxel length of $3.024\mu m$ .

The final sample is a shale rock obtained from the underground gas reservoirs which can be identified as clastic sedimentary rock, featuring tightly packed small grains often resulting in low porosities and ultra-low permeability. Extraction of gas reserves within these rocks is uneconomical through conventional means earning them the title of unconventional gas reservoirs. At present, the Fayetteville shale rock sample with a voxel length of $4.6\mu m$ is chosen as the subject of the current study (fig.6.11e).

The pixel data for the above samples are used in the unprocessed .raw format and is digitally reconstructed as depicted in fig.6.11.

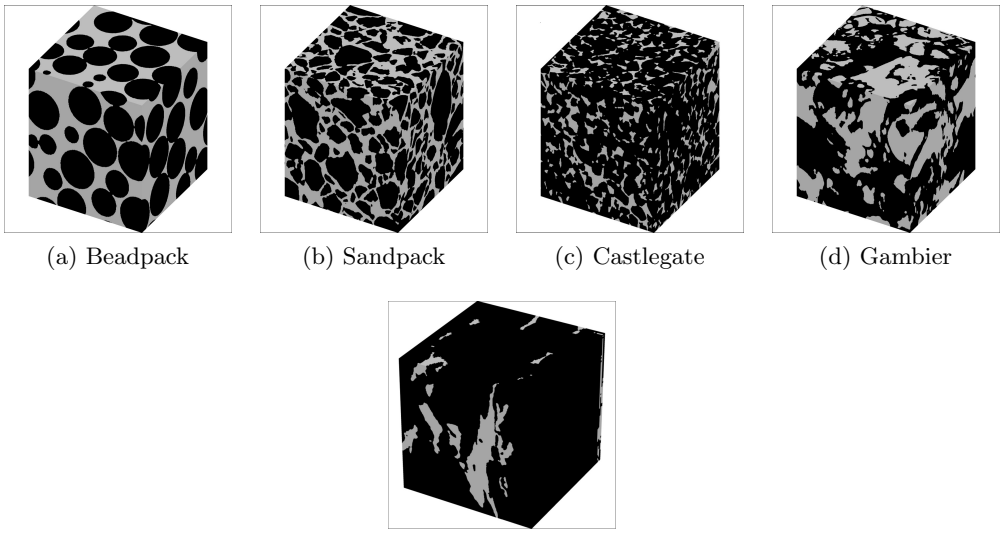

(a) Beadpack (b) Sandpack (c) Castlegate (d) Gambier

(e) Shale

Figure 6.11: 3D Image based reconstruction of a synthetic packs and rock samples

The reference state variables $(n_0, T_0, P_0)$ are used to non-dimensionalize the quantities. The flow is driven by a small pressure gradient in the $X$, $Y$ or $Z$ direction as appropriate. The gradient for a $Z$ direction flow is given by , $\xi_p = \frac{L_0}{P_0}\frac{\mathrm{d}P}{\mathrm{d}z}$, where, the small gradient ($\left|\xi_p\right| << 1$) is used to scale the velocity ($u_{ND} = \frac{u}{\xi_p c_0}$). Similar treatment is extended to the other directions.

The flow field is described in terms of the LMNS speed, $LMNS\ Speed = \frac{|V|}{|V|_{Max}}$,

whereas, the rarefaction is characterized through the Knudsen number ($Kn$) defined with a reference length as the side of the unit cell parallel to the flow. In the case of the 3D cases, the unit cells are cubic enabling the choice of any side as the reference length, i.e., $L_0 = L_x = L_y = L_z$.

The quantities inherent to porous media such as the non-dimensional permeability and the tortuosity are computed akin to the infinite array studies with a small caveat for the computation of non-diagonal permeability elements ($k_{ij}; i \neq j$) which are calculated as per equations presented in section 2.3.2. Tortuosity for a pressure gradient in the $X$ directions is computed as, $\tau = \frac{\Sigma u_{mag}}{\Sigma u_x} = \frac{\langle u_{mag} \rangle}{\langle u_x \rangle}$.

Additionally, the internal structural characteristics are quantified through the pore activity (PA) and surface interactivity (SI) parameters defined in section 4.4.4 and 4.4.5 respectively. In the present work, these novel parameters are interpreted through a binning process to produce a population distribution that is immensely insightful. The bins are defined for pore activity and surface interactivity as shown in tables.6.1 and 6.2 respectively. Here, $i$ is the index for the pores and $j$ is the index for the surface elements. The maximum value of the pore activity $PA_{max}$ and surface interactivity $SI_{max}$ are used to normalize the population.

Table 6.1: Definition of pore activity bins based on normalized population.

| Bin No. | PA Range |
|---|---|
| PA Bin 1 | 1.00 X $PA_{max} > PA_i \geq$ 0.90 X $PA_{max}$ |
| PA Bin 2 | 0.90 X $PA_{max} > PA_i \geq$ 0.80 X $PA_{max}$ |
| PA Bin 3 | 0.80 X $PA_{max} > PA_i \geq$ 0.70 X $PA_{max}$ |
| PA Bin 4 | 0.70 X $PA_{max} > PA_i \geq$ 0.60 X $PA_{max}$ |
| PA Bin 5 | 0.60 X $PA_{max} > PA_i \geq$ 0.50 X $PA_{max}$ |
| PA Bin 6 | 0.50 X $PA_{max} > PA_i \geq$ 0.00 X $PA_{max}$ |

Table 6.2: Definition of surface interactivity bins based on normalized population.

| Bin No. | SI Range |
|---|---|
| SI Bin 1 | 0.00 X $SI_{max} < SI_j \leq$0.10 X $SI_{max}$ |
| SI Bin 2 | 0.10 X $SI_{max} < SI_j \leq$0.20 X $SI_{max}$ |
| SI Bin 3 | 0.20 X $SI_{max} < SI_j \leq$0.30 X $SI_{max}$ |
| SI Bin 4 | 0.30 X $SI_{max} < SI_j \leq$0.40 X $SI_{max}$ |
| SI Bin 5 | 0.40 X $SI_{max} < SI_j \leq$1.00 X $SI_{max}$ |

### 6.4.3 Simulation results

The consideration is that of the section of the Berea sandstone section which is once again subjected to 3 independent studies with applied pressure gradients restricted to a single direction. For each of these studies, the degree of rarefaction is varied. The LMNS speed contours for the 2D slice of a Berea sandstone are illustrated in fig.6.13 which highlights the microscopic features whereas, the permeability and tortuosity are

presented in fig.6.12

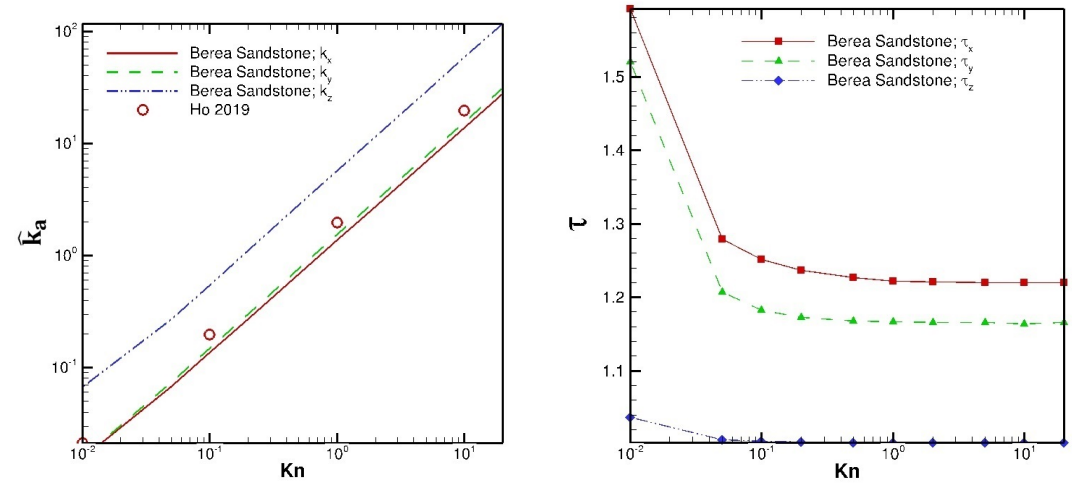


(a) Permeability (Literature: [272]). (b) Tortuosity

Figure 6.12: Macroscopic results for the Berea sandstone slice.

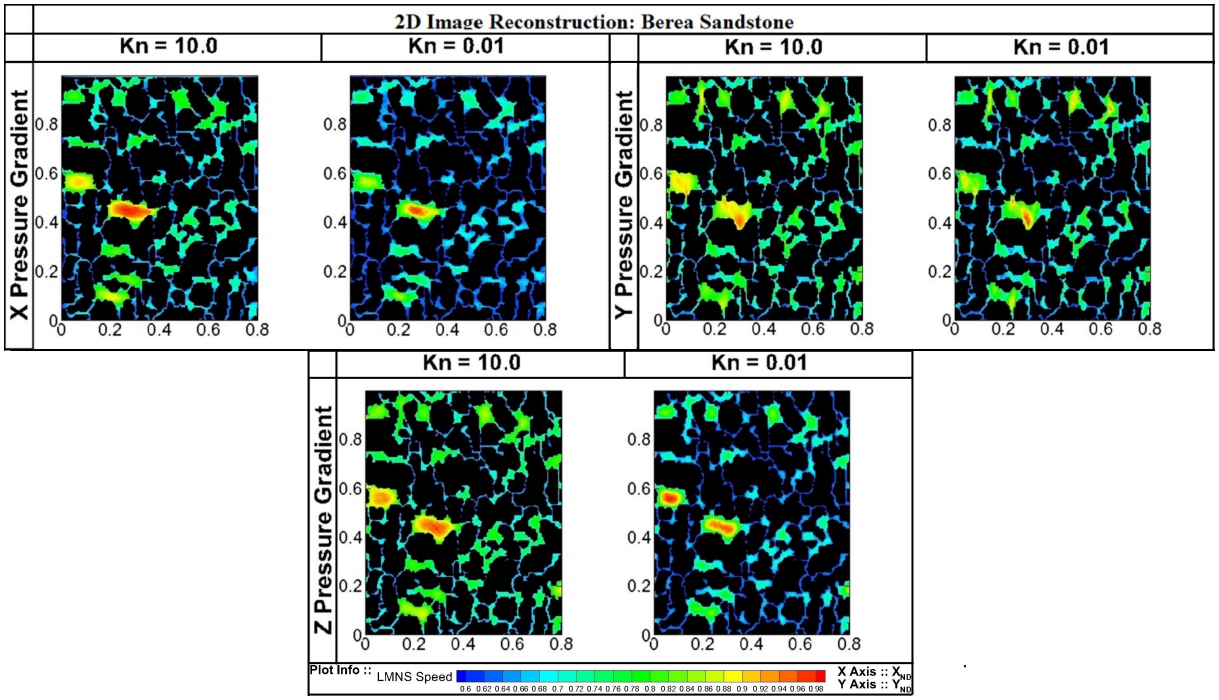


Figure 6.13: LMNS Speed contours for the image-based reconstructed Berea sandstone.

The flow contours for a X directional pressure gradient at $Kn = 1.00$ has been depicted for the Bead pack (fig.6.14a), Sand pack(fig.6.14b), Gambier(fig.6.14c), Castlegate(fig.6.14d) and Shale(fig.6.14e) rocks are presented below. The macroscopic feature is characterized by the permeability presented in fig.6.15.

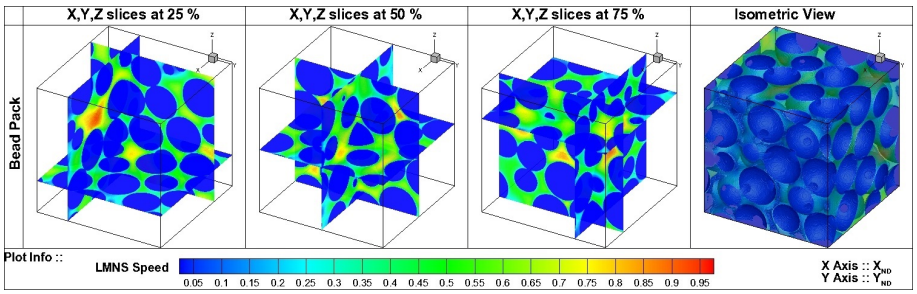


(a) Bead Pack

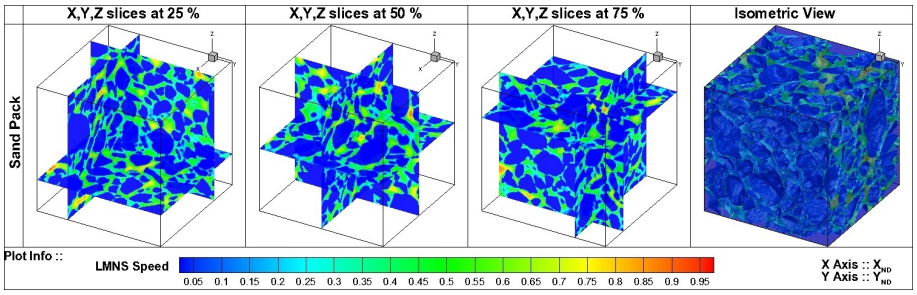


(b) Sand Pack

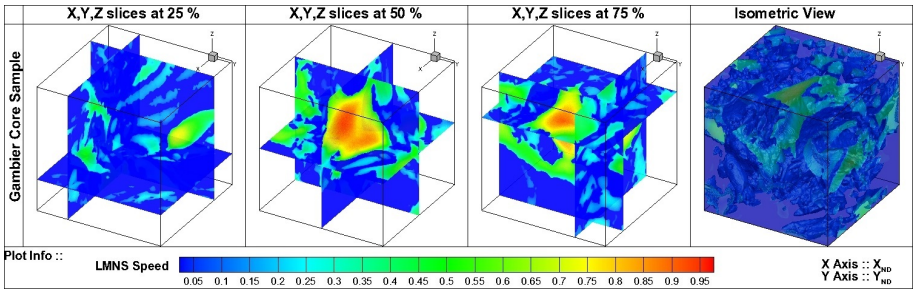


(c) Gambier Rock

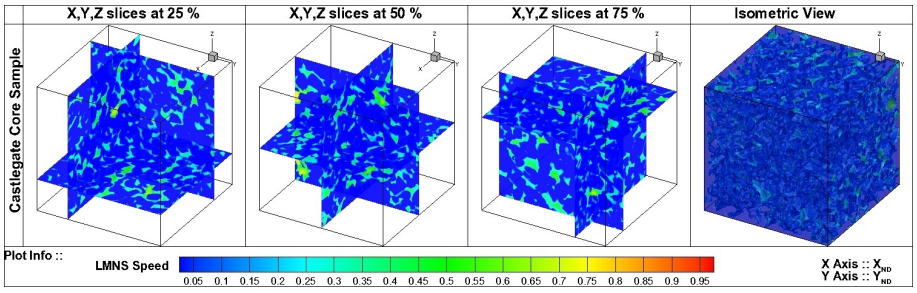


(d) Castlegate Rock

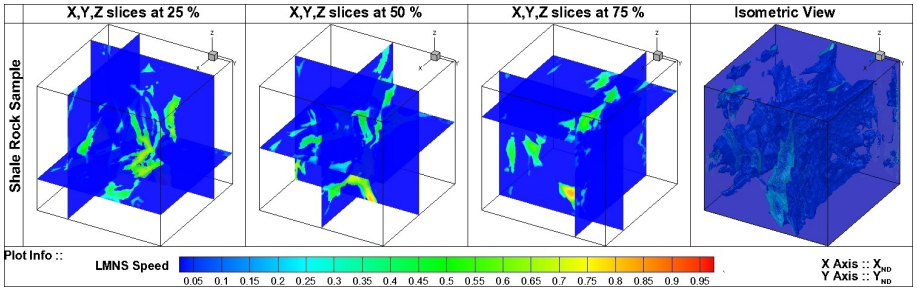


(e) Shale Rock

Figure 6.14: LMNS speed contours for 3D reconstructed porous media .

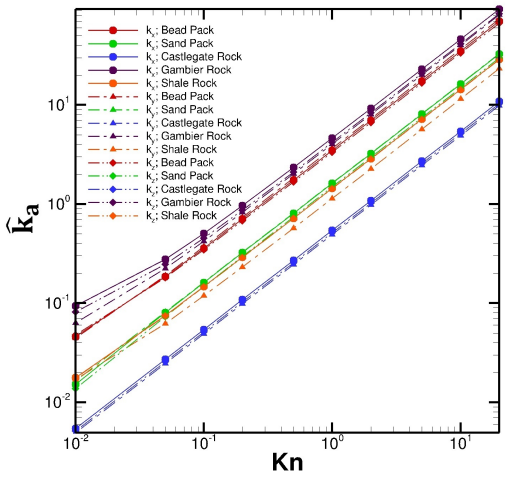


Figure 6.15: Result plots for Reconstructed Porous Media; Permeability

The information regarding the pore-scale flow dynamics that can be obtained from the velocity contour is appreciable and insightful when the 2D images are analysed. However, their effectiveness is severely restricted when 3D structures are considered. A more meaningful approach is to resort to the previously mentioned pore activity(fig.6.17) and surface interactivity(fig.6.16).

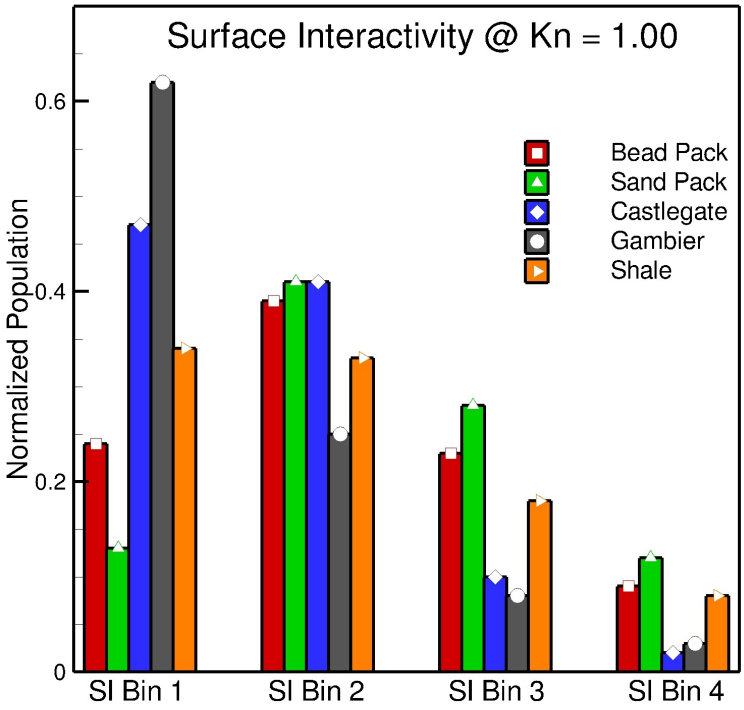


Figure 6.16: Result plots for Reconstructed Porous Media; Surface Interactivity.

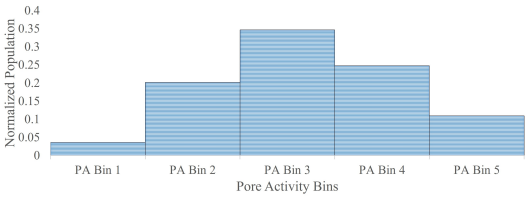


(a) Bead Pack @ $Kn = 10.0$

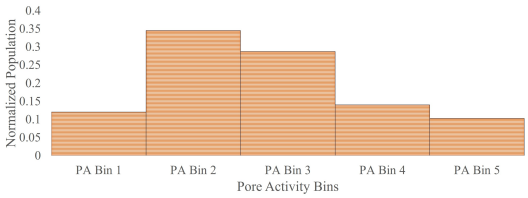


(b) Bead Pack @ $Kn = 0.10$

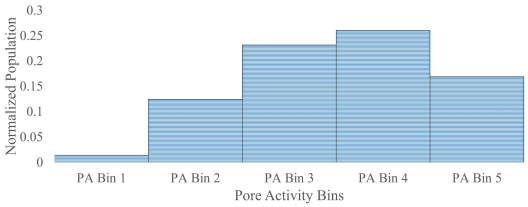


(c) Sand Pack @ $Kn = 10.0$

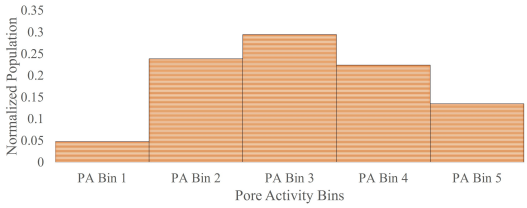


(d) Sand Pack @ $Kn = 0.10$

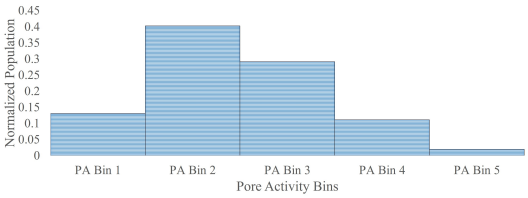


(e) Castlegate Rock @ $Kn = 10.0$

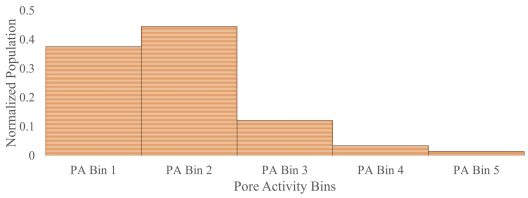


(f) Castlegate Rock @ $Kn = 0.10$

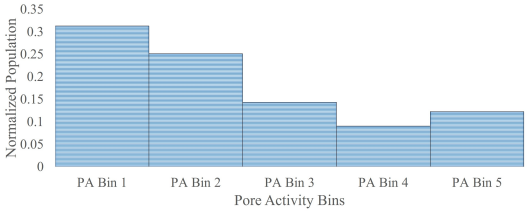


(g) Gambier Rock @ $Kn = 10.0$

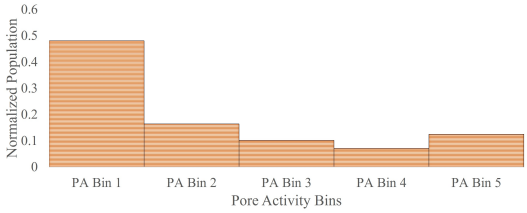


(h) Gambier Rock @ $Kn = 0.10$

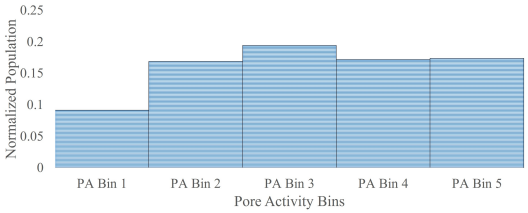


(i) Shale Rock @ $Kn = 10.0$

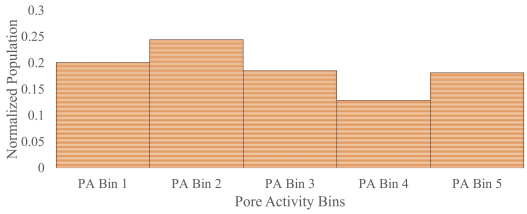


(j) Shale Rock @ $Kn = 0.10$

Figure 6.17: Result plots for Reconstructed Porous Media; Pore Activity vs. Rarefaction.

The pore activity is also used to determine the porosity of every sample considered in this study as displayed in table.6.3

Table 6.3: Porosity determination using pore activity compared to values reported in literature.

| Sample | Porosity (reported) | Porosity (computed) |
|---|---|---|
| Berea Sandstone | 0.32 | 0.321 |
| Bead Pack | 0.379 | 0.371 |
| Sand Pack | 0.363 | 0.377 |
| Castlegate Outcrop | 0.206 | 0.224 |
| Gambier Outcrop | 0.436 | 0.438 |
| Shale Core rock | 0.170 | 0.172 |

The permeability matrix for the various 3D reconstructions at $Kn = 1.00$ is represented in eq.6.2.

$$\begin{bmatrix} k_{xx} & k_{xy} & k_{xz} \\ k_{yx} & k_{yy} & k_{yz} \\ k_{zx} & k_{zy} & k_{zz} \end{bmatrix} \tag{6.2}$$

$$= \left\{ \begin{bmatrix} 3.4876 & 0.0395 & 0.0348 \\ 0.0398 & 3.6464 & 0.0065 \\ 0.0346 & 0.0066 & 3.3412 \end{bmatrix} \xrightarrow[\%]{Max.Normalized} \begin{bmatrix} 95.65 & 1.08 & 0.95 \\ 1.09 & 100.00 & 0.18 \\ 0.95 & 0.18 & 91.63 \end{bmatrix} \right\}_{Bead\ Pack}$$

$$= \left\{ \begin{bmatrix} 1.6214 & 0.0097 & 0.0127 \\ 0.0096 & 1.6350 & 0.0167 \\ 0.0126 & 0.0167 & 1.4859 \end{bmatrix} \xrightarrow[\%]{Max.Normalized} \begin{bmatrix} 99.17 & 0.59 & 0.78 \\ 0.59 & 100.00 & 1.02 \\ 0.77 & 1.02 & 90.88 \end{bmatrix} \right\}_{Sand\ Pack}$$

$$= \left\{ \begin{bmatrix} 0.5430 & 0.0011 & 0.0027 \\ 0.0011 & 0.4915 & 0.0031 \\ 0.0027 & 0.0031 & 0.5132 \end{bmatrix} \xrightarrow[\%]{Max.Normalized} \begin{bmatrix} 100.00 & 0.20 & 0.49 \\ 0.20 & 90.50 & 0.57 \\ 0.50 & 0.58 & 94.51 \end{bmatrix} \right\}_{Castlegate\ Rock}$$

$$= \left\{ \begin{bmatrix} 4.6390 & 0.0049 & 0.0849 \\ 0.0050 & 4.0274 & 0.1401 \\ 0.0846 & 0.1403 & 4.1871 \end{bmatrix} \xrightarrow[\%]{Max.Normalized} \begin{bmatrix} 100.00 & 0.10 & 1.83 \\ 0.11 & 86.82 & 3.02 \\ 1.82 & 3.02 & 90.26 \end{bmatrix} \right\}_{Gambier\ Rock}$$

$$= \left\{ \begin{bmatrix} 1.4427 & 0.0259 & 0.0115 \\ 0.0258 & 1.1414 & 0.0177 \\ 0.0116 & 0.0177 & 1.4315 \end{bmatrix} \xrightarrow[\%]{Max.Normalized} \begin{bmatrix} 100.00 & 1.79 & 0.80 \\ 1.79 & 79.11 & 1.23 \\ 0.80 & 1.23 & 99.22 \end{bmatrix} \right\}_{Shale\ Rock}$$

### 6.4.4 Reconstructed media data interpretation

Although no prior research considers all the 5 samples reconstructed here, the paper by Ho in 2019 [272] presents results for the Sand-pack and Shale rock. A direct comparison is not viable as the definition of the Knudsen number varies for the one used here. This variation originates from the different definition of $\lambda$ and is elaborated in eq.6.3.

$$\begin{aligned} \lambda_{Ho} &= \frac{\mu}{p}\sqrt{\frac{\pi K_B T_0}{2}} \\ &= \tau_0 c_{mp}\frac{\sqrt{\pi}}{2} \\ \lambda_{Present} &= \tau_0 \bar{c} \\ &= \frac{2}{\sqrt{\pi}}\frac{\bar{c}}{c_{mp}}\lambda_{Ho} \\ \lambda_{Present} &= \frac{4}{\pi}\lambda_{Ho} \\ Kn_{Present} &= \frac{4}{\pi}Kn_{Ho} \end{aligned} \tag{6.3}$$

The numerical interpretation of the permeability can be obtained by obtaining the dimensional value as $k_a \xi_p L_0^2$ where, $L_0$ is considered as the side on the cubic voxel and is thus, different for each of the 3D reconstructed media. For the $X$ directional pressure gradient through the Shale rock sample at $Kn_{Present} = 1.00$, the non-dimensional permeability obtained is $k_a = 1.4427$. This translates to a dimensional permeability of $1.4427X10^{-3}X(4.6X10^{-6})^2 m^2 = 30.52md$ ($md$: milidarcys) which is in close agreement with the value of $29.30md$ predicted for the same Shale rock samples under similar rarefaction ($Kn_{Ho} = 1.00(Kn_{Present} = 1.2732)$) conditions presented in Ho in 2019 [272].

### 6.4.5 Observations and inferences

In spite of their immense structural complexity, all the reconstructed porous media considered in this section have a well connected pore space network devoid of any dead-end pores resulting in a every sample possessing equal true and effective porosities. In the present simulation, this conclusion is attained by comparing the population of pores exhibiting non-zero pore activity with the reported values as is shown in table.6.3. An excellent agreement is found between the computed and reported values strengthening the confidence in the manner of calculation of pore activity.

The first consideration is the 2D Berea sandstone slice as it is a highly regarded sample in the annals of porous media studies owing to its intrinsic structural feature of possessing an interconnected pore space with a wide pore size distribution. The flow behaviour through this sandstone slice is observed to be preferential, with some

pathways being more active than others.

The primary interest in the study of Berea sandstone is the recognition and procurement of the interstitial flow patterns and their variation with flow direction (brought about by varying the direction of the pressure gradient) and rarefaction as is shown in fig.6.13. The 2D nature of the sample is clearly presented by the variation in the permeability in the $X$ and $Y$ directional flows which is attributed to the direction-dependent grain structure. The flow in the $Z$ direction is an example of fibrous sandstone, which is a fictitious entity, and is included for the sake of completion. These patterns dictate the macroscopic effects such as the permeability that is plotted in fig.6.12 and indicates a good agreement with those reported in the literature. These flows are the first consideration where interstitial flows have gained prominence and it will be a recurring theme in the study of porous media.

Unlike their 2D counterparts, the speed contours for a 3D reconstructed porous media are obscure in the amount of information revealed due to their complicated internal structure. While the contour plots (fig.6.14) provide a general overview of the nature of the flows, the primary characterization has traditionally been the permeability illustrated in fig.6.15. The appreciable information gleaned from this plot is the difference in permeability of the various reconstructed rocks which establish the Gambier and the Castlegate as the most and least permeable samples respectively. The focus on the permeability matrix for the reconstructed rock samples (eq.6.2), apart from their obvious aim to establish that the matrix is anisotropic, is because of their significance in identifying the flow direction that each of the samples has a proclivity towards. This is indicated by the maximum diagonal element which is seen to be the $k_{xx}$ for the synthetic packs indicating that the X gradient flow is most favourable whereas the Y direction is preferred among the rocks as indicated by the dominance of $k_{yy}$.

Prior to considering these results for the specific rocks, it is beneficial to gain a feel for these numbers and the physics they encapsulate. A high pore activity is synonymous with high intermolecular collisions which typically occur in low rarefaction regimes. Thus, in order to possess a high pore activity, the pore must be part of a pore space that is large enough to sustain locally low rarefied conditions. In addition to this, the pore space must endure limited restriction from the surfaces. If a sample possesses a large population of highly active pores, then it implied that the sample houses large pore spaces.

The surface interactivity population can be best understood as a classification of the surface with regards to their role in flow development. In order to possess low interactivity, the surface must offer limited resistance to the flow which suggests that the surface is parallel to the flow. On the other hand, a surface is expected to have high interactivity if it is located directly in the path of the flow. A high population of low interactivity surfaces indicates that the sample possesses a large number of resistive surfaces ($0.00 \text{ X } SI_{max} < SI_j \leq 0.10 \text{ X } SI_{max}$) but low number of obstructive surfaces ($0.30 \text{ X } SI_{max} < SI_j \leq 0.40 \text{ X } SI_{max}$) and vice versa.

Populations in PA bin 6 (0.50 X $PA_{max} > PA_i \geq 0.00$ X $PA_{max}$) for pore activity and SI bin 5 for surface interactivity (0.40 X $SI_{max} < SI_j \leq 1.00$ X $SI_{max}$ ) are considered irrelevant as their population is very low.

Under this established paradigm, two situations are considered for exploration and analysis. Firstly, the Gambier outcrop is selected on the merit of featuring the single largest pore space among all the samples considered. The region fosters a flow as is indicated by marking ($i$) in the LMNS speed contour (fig.6.14c) and is thus, subject to a high degree of pore activity. This is represented in the high population of PA bin 1 in figs.6.17g and 6.17h.

Moreover, the weak effects of the surfaces are highlighted by the high population resistive surfaces (SI bin 1) as shown in fig.6.16. Under high rarefaction conditions, the inability of the surfaces to detract flow is further exacerbated and the effect is seen in the high populations of PA bin 2 and PA bin 3 in fig.6.17g. However, the decrease in the rarefaction and the subsequent increase in the surface influence are tangible. At $Kn = 0.10$, the pore activities are isolated to a small central region of the large pore space leading to a high population of PA bin 1 and severe curtailment of activities of other pore spaces as is demonstrated through the fall of the population of PA bin 2 and PA bin 3 in fig.6.17h.

Secondly, the Sand Pack and Castlegate rock samples are considered together owing to the similarity in their internal structure. The Castlegate sample is clearly less porous than the Sand pack (table.6.3) which should result in the latter featuring a larger population of high activity pores. This is, however, not the case as at $Kn$ 10.0, PA bin 1 of Castlegate (6.17e) displays a higher population than PA bin 1 of the Sand pack (6.17c). This apparent anomaly is explained through the surface interactivity populations.

Comparison of surface activity population distribution of the Castlegate and the Sand pack sample shows that the Sand pack has

1. A very low population in SI bin 1.
2. Comparable population in SI bin 2
3. Considerably higher populations in SI bin 3
4. High populations in SI bin 4

This essentially means that a large portion of the surface in sand pack fulfils obstructive roles whereas the remaining smaller portion is restrictive surfaces. The inverse is true for the Castlegate sample making it more conducive to support local regions of rarefactions. Thus, though the porosity suggests that the pore spaces are more abundant in the Sand pack, the nature of the surfaces results in the Castlegate sample having larger activity in its pores spaces.

A plethora of other microscopic characterizations can be made based on these population distributions, however, the two discussed above cover the major themes of these results sufficiently.

## 6.5 Numerical parameters and computational expenditure

All computations were performed on a workstation comprising of 32 CPU of Intel(R) Xeon(R) CPU $E5-2630\ v3\ @\ 2.40GHz\ architecture\ x86-64$ . The computational effort in these subjects on this chapter depends on the dimensionality of the cases. For the $2D$ studies, the specifications are similar to the study of arrays reported in chapter 5. $3D$ structures however, prove to be more challenging; requiring the deployment of 20 particles per cell and 16 processors to obtain satisfactory results. The convergence was typically attained around 5000 steps followed by the generation of 80000 samples for hydrodynamic property evaluation. Depending on the complexity of the pore spaces and grid resolution, the most challenging cases in these studies took around 18 to 30 hours to complete.

The reconstructed media studies are the most expensive case considered in this thesis and merits a separate, deep-dive investigation which is provided in chapter 7.

## 6.6 Analysis and conclusions

In the above study, the capability of the developed PEGASUS solver to investigate isothermal, pressure-driven flows through complex, 2D and 3D structures is amply exhibited. The structures considered are either generated based on a logical procedure (such as the Sierpinski and percolation carpets) or through the reading of a binary image file in .dat (Berea) or .raw (Bead pack, Sand pack, etc.) format.

Various aspects encountered in micro-flows in porous media are replicated through the idealized porous media studies. The multi-scale aspect of the gas flow along with the heterogeneity of the solid grains are first examined by the Sierpinski carpet studies. The simulations are successful in identifying that the multi-scale flow features are particularly concentrated between the youngest members of a generation. The inability of these structures to completely stop the flow is considered as an incentive to study 2D carpets generated based on the percolation theory. The effect of allowing the solid grains to isolate pore spaces is seen to decrease the effective porosity and adversely affect the ensuing permeability. The permeability of the higher generations is extremely low leading to the conclusion that these flows are at the percolation threshold. In addition to the in-depth descriptions, these preliminary 2D simulations are suggestive of the flow patterns that is likely to ensue when the gas flows through actual porous media are considered. For example, a high solid fraction (generational increase) and low rarefaction increase the tortuosity of the flow by constriction either through physically occupying the space with a solid (as in PC) or rendering the region adjacent to

a solid unfavourable for flow (as in the SC). The extension of the Sierpinski carpets to 3D structures is carried out with a view of establishing the tensor nature of the permeability.

The solver's ability to reproduce porous media structures from binary image files is then utilized to conduct studies in a 2D Berea sandstone slice and 3D reconstructions of various synthetic packs and real rock samples. Insights are acquired from the interstitial flow field, permeability matrix highlighting significance of the off-diagonal permeability elements and tortuosity. Although the initial aim is to follow the examples in literature and compute the macroscopic properties; the innovative particle nature of the method allows for a more insightful characterization through the pore activity and surface interactivity parameters. As illustrated for the two case studies, it is possible to determine the regions of low and high pore activity that represents the local high and low rarefaction regions. In additions to this, it is possible to characterize the orientation of the internal surfaces depending on the interactivity of the surfaces. A highly interactive surface is obstructive as is the case in the sand pack sample considered here.

In conclusion, it can be stated with the utmost confidence that one of the prime objectives of this thesis, namely, the simulation and characterization of the gas flow through porous media, has been performed successfully. The results have established the solver's credibility as a uniquely viable tool in the pore-scale studies pertaining to porous media.

## 6.7 Chapter summary

It was the ambition of this chapter to deploy the low-variance ideology and the developed parallel solver (PEGASUS) to acquire the microscopic flow features and their macroscopic implications in structurally complex, multi-scale, low-speed environments that are the hallmark of industrial and geological porous media. Therefore, the simulation is performed through idealized (fractal and percolation theory-based generations) and reconstructed porous media with the results being compared with literature where available. The novel parameters procured, solely due to the particle nature of the method, demonstrate an ability to descry the inner workings of the porous media flows at a pore-scale leading to some unprecedented insights. Moreover, this achievement is carried out with an unprecedented computational efficiency as will be expounded upon in the succeeding chapter.

# Chapter 7

# Computational Performance and Accuracy

*"I'm sorry, Frank, I think you missed it. Queen to Bishop 3, Bishop takes Queen, Knight takes Bishop. Mate. Thank you for a very enjoyable game. "*

*— HAL 9000, 2001:A space odyssey by Arthur C. Clarke*

## 7.1 Chapter overview

Any new method and solver is subject to a rigorous check to ascertain its performance parameters that essentially characterize the computational effort needed and the accuracy of the result delivered. The objective of the present chapter is to demonstrably establish the high performance offered by the present methodology and its solver.

## 7.2 Introduction

This thesis is a response to the growing need to understand the microscopic characteristics of low signal micro-flows that occur under a very unique set of conditions which have risen to prominence due to the inclination of modern technological endeavours towards application that harbour such flows. The thesis recognizes the immense amount of work done in the field of low speed rarefied gas dynamics and also recognizes that the models used have some over-simplified assumption or are based on unreliable empirical data.

The attempt here has been to gain an understanding of the flow through the first principles with close relevance to the physics involved. This is achieved through a kinetic particle method that has hitherto not been employed in the low speed rarefied gas dynamics applications.

Particle studies are critically dependent on a number of parameters such as cell size, time step and the particles used per cell. The time step is enforced to be less

than the mean collision time and consequences of not obeying this condition have been extensively studied in literature [315, 316]. Furthermore, the cell size usually advised to be restricted to a fraction of the mean free path. Accordingly, 10% of the mean free path was used by Mohammadzadeh in 2012 [101] and 33% of the mean free path was used by Oran in 1998 [317]. A DSMC study in order to determine the pore-scale permeability of porous media conducted by Mohammadmoradi used 65% of the mean free path [313]. Finally, the number of particles per cell (PPC) are usually found to yield accurate results if they are at 20 as established by Mohammadzadeh [101].

To ascertain the effect of these parameters on the current implementation, the permeability for the image-reconstructed porous media considered in chapter 6 is revisited with varying performance parameters. It is seen that for sensible values of these parameters, the variation in the results is less than 5%. The effect of moving away from the resolution of the image is a little suspect as an upscaling may solidify previously void spaces and the converse can happen in downscaling. The effective geometry is thus, changed.

## 7.3 Performance studies

The method espoused in this thesis has been expounded in Chapter 3. While the accuracy of the method has been bolstered by comparison with literature data, it is pivotal to remember that the very essence of the method is stochastic. The fallout of this is that the results generated must be viewed with a certain degree of warranted scepticism owing to the uncertainty inherent with such approaches. The main sources contributing to this uncertainty are the pure stochastic nature of the simulation and the number of particle per cell (PPC) deployed.

### 7.3.1 Effect of ensemble averaging and PPC on efficiency and accuracy

The stochastic nature is overcome by considering multiple samples and averaging them to produce a time-averaged solution. Unlike DSMC, the current method requires a reasonably small number of samples to produce an acceptable degree of uncertainty. The samples for time-averaging are taken once the convergence criteria are met ensuring that the steady-state is established.

In certain occasions, it is prudent to further reduce the degree of uncertainty by considering multiple ensembles. The averaged result of such an operation is a time- and an ensemble-averaged result which is sure to produce the most minimal degree of uncertainty.

In the present study, such an occasion arises when the PPC is set to a low value. The PPC is a parameter that determines the weight of a particle and as such a reasonable estimate of the PPC is sufficient. While an extremely low value is undesirable due to

the increased uncertainty of the result, so too is a very high value which will increase the associated computational time in exchange for a small reduction in the degree of uncertainty. Thus, in some aspects, the PPC can be regarded as a Goldilocks parameter although the penalty of an inappropriate decision is tangible though not threatening. This is specifically demonstrated by the simulation of a pressure gradient flow through an array with a unit cell consisting of the structure named as "JL+SZ" (after the classical Tetris components used; fig.7.1a) over the entire rarefaction regime. The simulation is conducted using 5, 10, 20 and 100 PPC in PEGASUS along with a DVM simulation employing a $26X26$ discrete velocities. The simplicity of the structure is used to the advantage and only a single ensemble is used, i.e. the evaluation is a time-averaged result. The contours plots are presented for the LMNS speed and are enlightening, demonstrating that, due to the lower number of particles, PPC 5 tends to smudge the microscopic flow features that are prominently captured in PPC 20. Regions where the aforementioned effect are evident are marked in fig.7.1c by $(i), (ii)$. The results for the PPC 100 are considered to be the most accurate and is used as the baseline for the other results. The difference between PPC 100 and the other cases is plotted in fig.7.1b. The simplicity of the structure leads to the difference being small although, the discrepancies between PPC 5 and the others are perceptible.

At present, all the cases considered here produce a time average that is sufficiently precise except when the PPC is set too low. The demonstration of this fact is presented through the data spread of the ensembles generated for the X direction pressure gradient flow through the Shale rock structure at $Kn = 1.00$ (fig.7.2). It is seen that the lower PPC produces a mean value that differs significantly from the higher PPC value owing to the large spread of its data points. The spread can be decreased by considering a larger number of ensembles although the averaged result still varies from the higher PPC case. The spread for all the reconstructed images has been analysed and it is determined that the PPC of 20 is a fairly stable estimate for acquiring acceptable degrees of uncertainty. The degree of uncertainty is characterized by the standard deviation and its value for all the reconstructed images is provided in table.7.1 for $Kn = 1.00$.

Although the above discussion indicates that a PPC 20 is desirable compared to a PPC 5 case, the percentage difference in permeability is only 0.0838%. Such a discrepancy maybe considered tolerable owing to trade-off gained in the form of decreased computational time. An idea of the reduction offered by the reduction of the PPC for 16 processors by table.7.2.

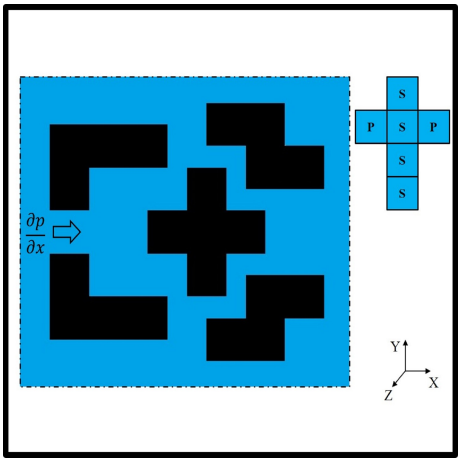


(a) Schematic

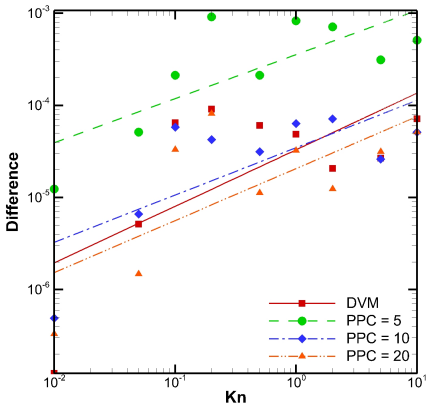


(b) Data scatter

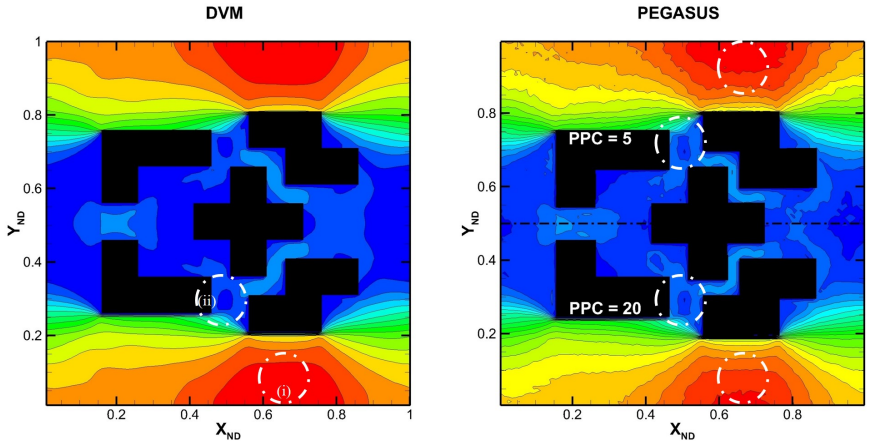


(c) Contour plot at $Kn = 1.00$

Figure 7.1: Results for JL+SZ structures considered in the context of PPC variation.

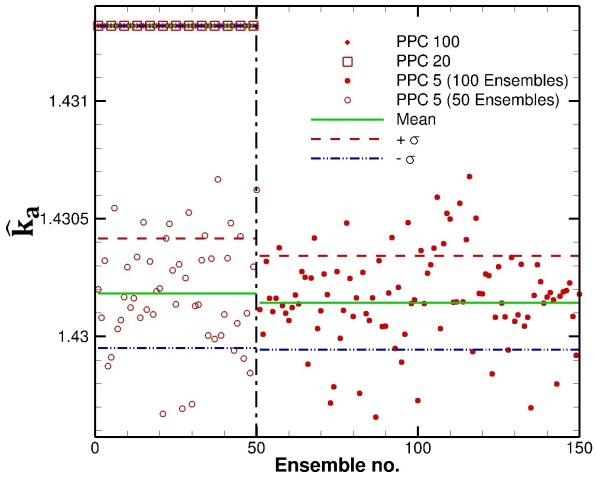


Figure 7.2: Shale data scatter for variation in PPC and ensemble at $Kn = 1.00$

Table 7.1: The standard deviation of the reconstructed media at $Kn = 1.00$ for various PPC and 10 ensembles.

| Kn = 1.00 | | PPC = 100 | PPC = 20 | | PPC = 5 | |
|---|---|---|---|---|---|---|
| | Direction | | Mean | $\sigma$ | Mean | $\sigma$ |
| Bead Pack | X | 3.4877 | 3.4876 | 1.69E-06 | 3.2765 | 3.02E-02 |
| | Y | 3.6461 | 3.6464 | 4.38E-05 | 3.3950 | 4.17E-02 |
| | Z | 3.3411 | 3.3412 | 9.87E-06 | 3.1312 | 3.42E-02 |
| Sand Pack | X | 1.6213 | 1.6214 | 7.95E-06 | 1.4920 | 2.29E-02 |
| | Y | 1.6351 | 1.6350 | 1.14E-05 | 1.4752 | 2.53E-02 |
| | Z | 1.4859 | 1.4859 | 1.53E-06 | 1.3819 | 1.75E-02 |
| Gambier Rock | X | 0.5430 | 0.5430 | 9.19E-07 | 0.4971 | 7.08E-03 |
| | Y | 0.4914 | 0.4915 | 4.28E-06 | 0.4715 | 3.19E-03 |
| | Z | 0.5132 | 0.5132 | 4.48E-07 | 0.5012 | 1.98E-03 |
| Castlegate Rock | X | 4.6390 | 4.6390 | 4.55E-06 | 4.1799 | 6.80E-02 |
| | Y | 4.0275 | 4.0274 | 4.37E-06 | 4.0074 | 3.19E-03 |
| | Z | 4.1871 | 4.1871 | 1.88E-06 | 4.0571 | 2.42E-02 |
| Shale Rock | X | 1.4427 | 1.4427 | 3.97E-06 | 1.3627 | 1.51E-02 |
| | Y | 1.1413 | 1.1414 | 1.38E-05 | 1.1404 | 1.64E-04 |
| | Z | 1.4313 | 1.4313 | 2.06E-08 | 1.4301 | 1.99E-04 |

Table 7.2: The effect of number of particle per cell on computational time (in seconds).

| | | MPI 16 | | |
|---|---|---|---|---|
| | | PPC = 20 | PPC = 10 | PPC = 5 |
| Bead Pack | Kn 10.0 | 29.54 | 9.75 | 7.34 |
| | Kn 0.01 | 456.03 | 196.09 | 123.95 |
| Sand Pack | Kn 10.0 | 48.87 | 27.85 | 14.30 |
| | Kn 0.01 | 631.10 | 399.11 | 313.42 |
| Gambier Rock | Kn 10.0 | 63.10 | 27.31 | 14.12 |
| | Kn 0.01 | 641.48 | 255.76 | 122.25 |
| Castlegate Rock | Kn 10.0 | 21.68 | 11.14 | 5.76 |
| | Kn 0.01 | 337.88 | 207.70 | 105.57 |
| Shale Rock | Kn 10.0 | 52.44 | 26.67 | 12.06 |
| | Kn 0.01 | 487.88 | 352.98 | 266.25 |

### 7.3.2 Effect of parallel implementation on efficiency

The premise of the present technique is the reliance on the particle-based formulation akin to DSMC, etc. and like all modern numerical methods, the solver benefits from a parallel implementation. The implementation of the parallel framework is done through domain decomposition although the domain considered is the pore space. Focus is allocated to ensure proper load balancing by allocating an equal number (or close) of pore spaces per MPI processor. All computations were performed on a workstation comprising of 32 CPU of Intel(R) Xeon(R) CPU $E5-2630v3@2.40GHz architecture x86-64$.

The effect of MPI-based parallel implementation on computational time for the

case presented in fig.7.1a is shown in fig.7.3. The simple $2D$ nature of the flow restricts the possible scaling of the parallel efficiency due to the increase in communication overhead between processors. Eventually an optimal point is attained at 8 processors for all Knudsen numbers. For the depicted case of $Kn = 1.00$, the best efficiency that can be obtained is around 700 seconds for 1000 steps using around $10^6$ particles (maximum of 20 PPC in a $500X500$ grid).

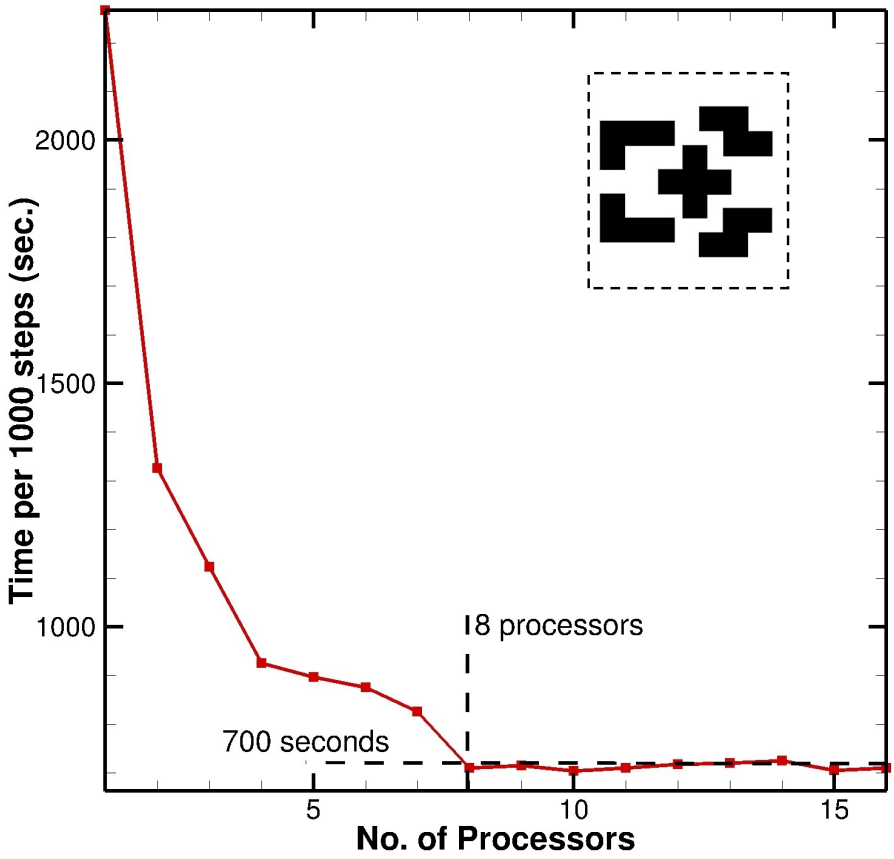


Figure 7.3: Parallel efficiency scaling for the $JL+SZ$ structure considered at $Kn = 1.00$

The effect of MPI-based parallel implementation on computational time for the five 3D image-reconstructed rocks are considered for analysis as these are the most computationally challenging. The results for 1000 time steps considering a PPC of 20 is presented in table.7.3 and depicts certain interesting characteristics.

The asterisk accompanying the MPI 2 case is due to the inability of the workstation to allocate memory for the array. Thus, a workaround in the form of writing and accessing files dynamically has been implemented. These read and write operations lead to an increase in the overall computational time and thus, this reported time must be treated tentatively.

Firstly, the increase in the number of computational power through 16 MPI cores is seen to be faster than employing 2 MPI processors by a factor of X for Kn = 10 and Y for Kn = 0.1. The variation is not linear as would have been ideal.

Table 7.3: The effect of number of parallel processors employed on the computational time (in seconds).

| | | PPC = 20 | | | |
|---|---|---|---|---|---|
| | | MPI 16 | MPI 8 | MPI 4 | MPI 2* |
| Bead Pack | Kn 10.0 | 29.54 | 46.31 | 55.74 | 239.49 |
| | Kn 0.01 | 456.03 | 981.36 | 1429.60 | 9490.24 |
| Sand Pack | Kn 10.0 | 48.87 | 53.01 | 89.21 | 288.75 |
| | Kn 0.01 | 631.10 | 1607.60 | 1758.88 | 14198.80 |
| Gambier Rock | Kn 10.0 | 63.10 | 73.23 | 97.68 | 451.19 |
| | Kn 0.01 | 641.48 | 1536.40 | 2200.47 | 16103.20 |
| Castlegate Rock | Kn 10.0 | 21.68 | 28.23 | 68.15 | 188.97 |
| | Kn 0.01 | 337.88 | 577.65 | 759.96 | 5442.13 |
| Shale Rock | Kn 10.0 | 52.44 | 68.10 | 119.19 | 568.75 |
| | Kn 0.01 | 487.88 | 715.60 | 1144.16 | 10295.91 |

In addition, to the effect of the number of processors employed, it is also noted that the lower degrees of rarefactions are magnitudes more expensive than their rarefied counterparts. The reason for this is appreciated when it is recognized that in a given time step, the collision process is the most computationally expensive operation. This is further highlighted for the Gambier and Castlegate outcrops in figs.7.4a and 7.4b respectively, where the time taken by the individual processes are broken down and presented. The processes of indexing, convergence verification, sampling and other housekeeping operations are classified under the miscellaneous (Misc.) piece of the pie. It is evident that as the rarefaction decreases (inner to outer ring) the computational time consumed by the collision processes increases. This effect manifests itself as an increased computational time at lower degrees of rarefactions as noted.

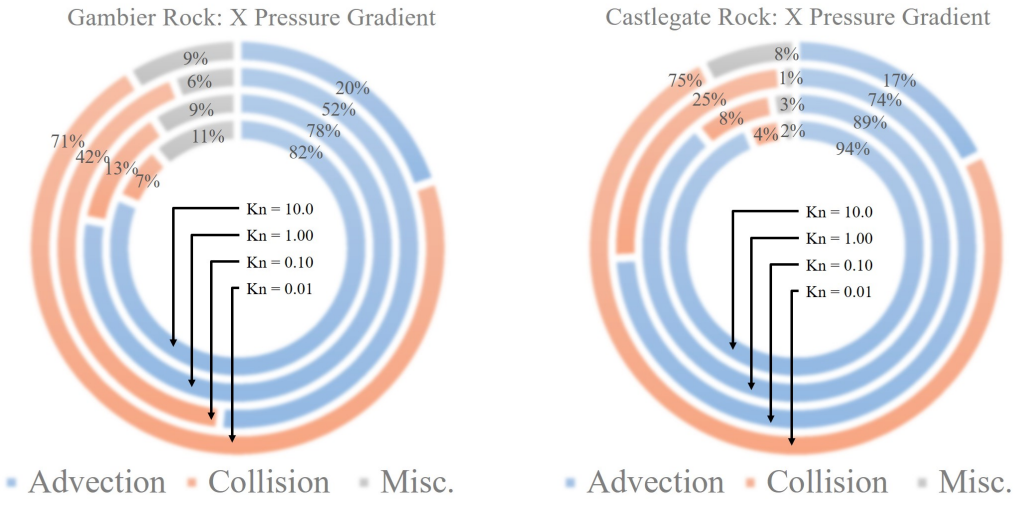


(a) Gambier Rock.

(b) Castlegate Rock.

Figure 7.4: Computational time breakup for the individual process involved.

The breakdown for all the reconstructed media is presented here as table.7.4,

Table 7.4: The percentage of computational time occupied by individual processes.

| | Direction | Kn = 10.0 | | | Kn = 0.1 | | |
|---|---|---|---|---|---|---|---|
| | | Advection % | Collision % | Misc. % | Advection % | Collision % | Misc. % |
| Bead Pack | X | 80.69 | 8.43 | 10.88 | 47.10 | 46.07 | 6.83 |
| | Y | 77.67 | 9.03 | 13.29 | 47.18 | 46.20 | 6.62 |
| | Z | 84.27 | 14.56 | 1.18 | 47.49 | 51.64 | 0.87 |
| Sand Pack | X | 85.00 | 8.96 | 6.04 | 53.20 | 43.88 | 2.92 |
| | Y | 88.32 | 6.88 | 4.81 | 59.32 | 37.96 | 2.72 |
| | Z | 81.84 | 16.93 | 1.22 | 41.47 | 57.70 | 0.83 |
| Gambier Rock | X | 81.47 | 7.32 | 11.21 | 51.63 | 42.50 | 5.87 |
| | Y | 85.09 | 13.74 | 1.17 | 58.74 | 40.41 | 0.85 |
| | Z | 89.81 | 9.18 | 1.01 | 55.09 | 44.03 | 0.88 |
| Castlegate Rock | X | 93.74 | 4.32 | 1.94 | 74.12 | 24.49 | 1.39 |
| | Y | 83.79 | 15.13 | 1.08 | 55.30 | 43.89 | 0.81 |
| | Z | 84.06 | 14.86 | 1.07 | 53.54 | 45.69 | 0.77 |
| Shale Rock | X | 70.43 | 14.06 | 15.51 | 46.73 | 47.15 | 6.13 |
| | Y | 84.27 | 14.49 | 1.25 | 53.41 | 42.09 | 4.50 |
| | Z | 89.57 | 9.36 | 1.07 | 58.71 | 36.96 | 4.33 |

The final point of interest highlighted by table.7.3 is, in fact, further proof to the multi-scale nature of the simulations. For a determined number of MPI processes and rarefaction, the highest computational effort is needed for the Gambier outcrop followed by the Sand pack.

This effect is not so evident and any attempt to explain this through relation to macroscopic properties is misleading. The effect is in fact, microscopic and relates to the presence of larger pore size and the multi-scale nature of porous media. In large pore spaces, the particles are largely independent of the effect of solid surfaces are locally less rarefied meaning that the process of collision is more prevalent and relevant in these regions. As previously noted, collisions are the most expensive part of the operation and thus the computational time is seen to increase.

While it is true that the Gambier rock has the highest porosity and the highest computational time, the linking of these two can be severely misleading. The relationship cannot be generalized as the Bead and Sand pack considered are nearly equal in porosity; the difference in their pore sizes and distribution affects the computational time between them significantly. Furthermore, the correlation would dictate that the lowest porosity would have the lowest computational time which should be the shale rock but is actually the Castlegate rock due to the highly intrusive nature of the solid grains curtailing the number of a localised region of low rarefaction.

## 7.4 Chapter summary

Through this chapter, the exceptional computational performance of the present implementation is underscored through the presentation of the computational expenses for the complicated reconstructed porous media considered in Chapter 6. Furthermore, the discourse on the effect of ensembles and particles per cell, accompanied by an independent example study, is aimed at dispelling the aura of scepticism associated with such stochastic particle approaches. The veracity of the implementation and the conviction of PEGASUS are reinforced in the next and final chapter, whose purpose is to provide a comprehensive review of the features demonstrably revealed in the course of this thesis.

# Chapter 8

# Conclusion

*"If a conclusion is not poetically balanced, it cannot be scientifically true."*

*— Dr. Han Fastolfe, The Robots of Dawn by Isaac Asimov*

## 8.1 Final remarks

The prime directive of this thesis is to provide an alluring, promising, innovative, and viable alternative to the numerical solution of the Boltzmann equation for low-speed rarefied gas flows. To this end, the research conducted here utilizes a stochastic kinetic particle-based approach offering a physical solution to the Boltzmann-BGK equation through the incorporation of variance reduction principles. Prior to the efforts of this thesis, the ideology's viability was restricted to a technical demonstration for various classical problems of fluid mechanics. In the course of this research, substantial additions to the ideology have been made thereby enabling it to handle 3D flows through complex geometries. The realization of this method is achieved through the design and development of a dedicated parallel solver (PEGASUS).

The principal task of this research; as the title suggests; is to, firmly and demonstrably, establish the *ability* of the present ideology and developed solver to resolve low-speed rarefied gas flows at micro- and nanoscales. Owing to the unfamiliarity of the ideology to a large portion of the rarefied gas research community compounded by the aspirations of extending the method to uncharted scenarios, the tone adopted by this thesis is one of cautious advance and thoroughness. This is exemplified by the structure of this thesis along with the manner in which the ability is established, namely, through the establishment of the its constituents as expressed in eq.8.1,

$$Ability = Plausibility + Applicability + Capability + Feasibility + Dependability. \tag{8.1}$$

The question of **Plausibility** is an important one and gains precedence owing to the obscurity of the method which has led to its exclusion from popular kinetic particle

method reviews such as those by Teschner in 2016 [318]. The reluctance of the research community to adopt this method is largely attributable to the suspicion surrounding the use of signed particles, the complex nature when extended to engineering models such as VHS, and the popularity of DVM as an able alternative. Furthermore, the lack of any dedicated attempt to extend the method to practical studies of significant importance thus far has led to the side-lining of the ideology. The existence and failure of a large number of other methods that aspire to emulate DSMC through complicated procedures such as particle weight manipulation, and introduction of new operations such as splitting and combining of particles has contributed to the aura of scepticism surrounding this method. However, the notion of LVDSMC as a caricature of DSMC is a fallacious one and the present thesis is a testament to the method's potential to retain the advantages of a particle treatment while tackling challenges associated with low-signal flows. The theoretical framework, physical laws and equations of each step on the method are elucidated in Chapter 3. It is evident that the procedure lies within the theoretical foundations laid down in Chapter 2. The belief in the method is further bolstered by the solutions of the canonical flow problems and their agreement to solutions provided by an array of contemporary, well-established methods demonstrated in the first half of Chapter 4.

The method specializes in the simulation of low-signal flows that are a feature of MEMS and porous media flows. In order to be deemed applicable (**Applicability**), the present implementation must contend with the unique physics and complexities associated with these applications. The assumption and formulation established in Chapter 3 address these challenges and provide an explanation as to why the method is uniquely suited to dealing with issues such as a large number of exposed surface or multi-scale effects. Tangible evidence is presented through the simulation of appropriately designed flow problems in the latter half of Chapter 4. The utilization of the solver to various applications in the field of MEMS (Chapter 5) and porous media (Chapter 6) flows along with the agreement of the results to literature/underlying physics prove to be irrefutable evidence to the method's applicability.

The **Capability** of the present implementation can only be established through simulations of various flow problems. At first glance, the arrangement of the chapters 4, 5, and 6, may seem application-oriented. However, this is not the case. To an astute observer, the progressive scaling of the complexity in the subject of studies from chapter 4 to 6 will not be remiss. Chapter 4's consideration is dedicated to 1D classical flow through channels, while chapter 5 is a study of quasi-2D flows through long-ducts and infinite arrays. Quasi-2D flows are identified as possessing symmetric geometries that make the flow features along one direction more prominent than the others. This is also true of the Sierpinski carpets considered in chapter 6, although the percolation carpets and Berea sandstone slice contemplations are devoid of such symmetric features and are examples of true 2D flows. Extension of the Sierpinski carpet fractal to 3D structures such as the Menger sponge, maze and suspension is a manifestation of quasi-

3D problems while the final considerations of the image reconstructed rock samples provide a true 3D flow (as is evidenced by the anisotropic nature of the permeability matrix) problem for the solver to resolve. Thus, though the presentation has been done from the point of view of the application, its underlying theme was one of increasing the dimensionality associated with the flow problem. The subjects of the studies are organized to become progressively intriguing and involved with regards to the physics concerned. This manner of establishing capability is in accordance to the slow, cautious and thorough tone of this thesis.

**Feasibility** of the developed solver to evaluate the porous media flow efficiently and in a time-bound manner is essential from an industrial and academic standpoint. The benefits gained through a parallel implementation has been demonstrated in Chapter 7 through a marked decrease in computational time by employing multiple processors. The solver boasts of a previously unachieved computational performance, solving the shale sample in under 12 hours.

**Dependability** remains a pertinent question to address as the results obtained originate from a method that is stochastic in nature which is inherently dependent on the efficiency of the pseudo-random number generators. Moreover, it is demonstrably established in Chapter 7, that the confidence in the results is strongly reliant on the specification of the appropriate performance parameters. Provided these factors are appropriately addressed, the solver exhibits remarkable accuracy as is evidenced by the agreement found with literature in the numerous studies. The robustness of the implementation with regards to resolving porous media structures is amply illustrated by the consideration of generation $V$ of the Sierpinski carpets is Chapter 6, where the youngest members influence on the flow field is reproduced in spite of the fact that the grain is the size of a pixel.

Each of these factors, discussed individually, are suggestive and considered together, are conclusive in establishing the **Ability** of the variance reduced kinetic-particle ideology combined with the PEGASUS solver to resolve micro-scale flows accurately, reliably and efficiently.

## 8.2 Position in the hierarchy

The field has been a subject of intense scrutiny and various methods has been used to study the flows. The discussion of the various governing equations and numerical methods has been discussed in Chapter 2. The flowchart presented is that chapter is redrawn here in fig.8.1. Based on the studies conducted in this thesis, the location of the present method in the family of methods is highlighted and marked as “present work”.

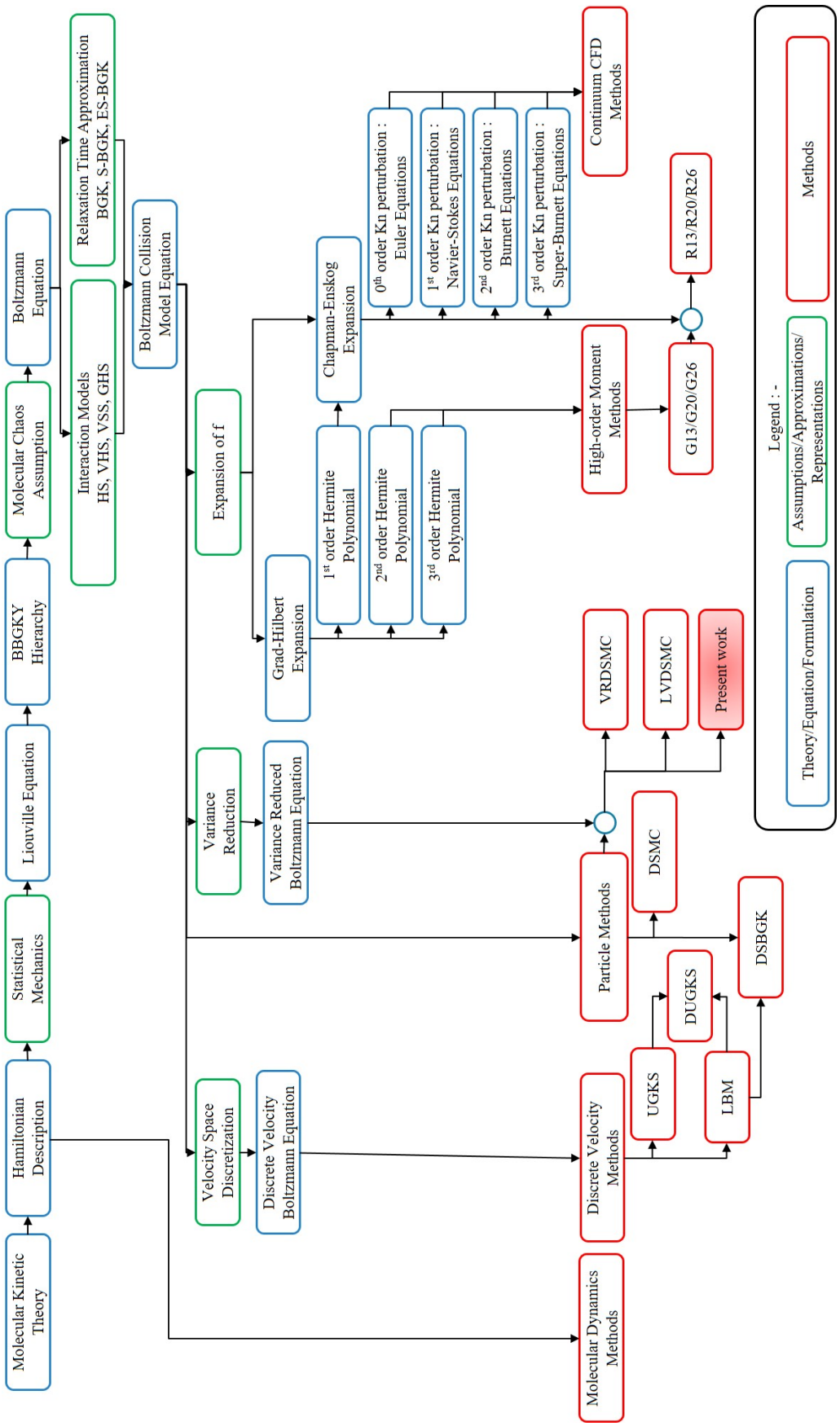


Figure 8.1: Flowchart depicting the position of the present method in the hierarchy methods.

## 8.3 Future potential

The future potential of such a particle-based approach and efficient solver can be divided into two discussions.

The first aspect concerns the immediate future, where work can proceed in the three avenues discussed below. The key idea of the first avenue would be to include the extension of the developed reservoir implementation to act as an inlet and outlet conditions for the short ducts thereby mimicking the end effects of such flows. The critical idea of the second avenue is the replacement of the BGK collision operator by a BGK-S model. This implementation is expected to be relatively straightforward with the confines of the currently developed environment. The idea is not pursued in this work as it has little bearing to the principal subject of interest, namely, natural porous media. The third avenue is with regards to the fracturing mechanism of porous rocks. The research could be directed to monitor the transient response of the gas flow pattern as a fracture propagates. A significant change is expected as the process varies the solid fraction, porosity and flow network.

The second aspect of the future potential pertains to the distant goals of the method, most of which dwell into the deeper characteristics of porous media. The stochastic nature, alongside the particle approach, make the current method an ideal candidate for the pursuance of adsorption/desorption phenomena studies. These can, possibly, be interpreted through an acceptance-rejection check for a particle surface reflection. In the event of acceptance, the surface properties will change which will dictate its interaction with the subsequent particle reflection. The present implementation is for a single species of gas whereas porous media are saturated with multiple species. The extension of the method to such cases requires a change in the fundamental equation, specifically, in the collision process. The use of McCormack collision model in the context of a binary gas has been demonstrated by Szalmas [132]. The extension to the VHS collision model has been performed by Radtke [130] and these approaches are potential candidates to carry out this task. Discussions about chemical interaction between the constituent gases may be unfounded due to the low speeds associated with such flows. Porous media, such as conventional rock reservoirs are stores of liquids such as oils as well as gas and, though the multiphase aspect is a critical one for accurate representation of the reservoirs and their characterization, the realization that such a venture will require the change from the Boltzmann governing equation, which is only applicable for dilute gases, is an area of research in which the author pleads ignorance. The onus of revelation of such extensions if possible and their efficacy are the responsibilities of the future.

# Bibliography


[1] R. Garner, "About the Hubble Space Telescope," *National Aeronautics and Space Administration website*, Jan 2015.

[2] CERN, "The Large Hadron Collider," *European Organization for Nuclear Research website*.

[3] J. Watts, "We have 12 years to limit climate change catastrophe, warns UN," *The Guardian*, 2018.

[4] C. Welch, "How Cape Town is coping with its worst drought on record ?," *National Geographic*, 2018.

[5] L. L. Schramm, *Nano-and Microtechnology from A-Z: From nanosystems to colloids and interfaces*. John Wiley & Sons, 2014.

[6] R. Feynman, "There's plenty of room at the bottom," *Science*, vol. 254, no. 5036, pp. 1300–1301, 1991.

[7] L. Verlaque, "The first Feynman challenge," *Pasadena Museum of History*, 2017.

[8] J. S. Dietrich, "Tiny tale gets grand," *Engineering and Science*, vol. 49, no. 3, pp. 25–26, 1986.

[9] Y. D. Eric Mounier, "The MEMS market is showing a 17.5% CAGR between 2018 and 2023."

[10] J. Lee, S. Newbern, Y.-C. Tai, C.-M. Ho, and P.-H. Adam Huang, "Flight demonstrations of micro-actuator controlled delta wing," *Aircraft Engineering and Aerospace Technology*, vol. 83, no. 5, pp. 324–331, 2011.

[11] G. Rapp, *Archaeomineralogy (Natural Science in Archaeology)*. Springer, 2009.

[12] Y. Deng, *Ancient Chinese Inventions*, vol. 5. 2005.

[13] Anon, "Oil and gas formation," *Blogspot*, 2014.

[14] USEIA, "Natural gas explained,"

[15] M. Q. Morton, "Unlocking the Earth: A short history of hydraulic fracturing," 2013.

[16] G. G. Lash and E. P. Lash, "Early History of the Natural Gas Industry," *AAPG Annual Conventional and Exhibition, Houston, TX, April*, pp. 6–9, 2014.

[17] R. F. King and D. Morehouse, "Drilling sideways— A review of horizontal well technology and its domestic application," *Energy Information Administration*, 1993.

[18] S. S. Zhiltsov, *Shale Gas: Ecology, Politics, Economy*. Springer, 2017.

[19] E. H. Oelkers and D. R. Cole, "Carbon dioxide sequestration a solution to a global problem," *Elements*, vol. 4, no. 5, pp. 305–310, 2008.

[20] K. S. Lackner, "A guide to $CO_2$ sequestration," *Science*, vol. 300, no. 5626, pp. 1677–1678, 2003.

[21] T. A. Torp and J. Gale, "Demonstrating storage of $CO_2$ in geological reservoirs: the Sleipner and SACS projects," in *Greenhouse Gas Control Technologies-6th International Conference*, pp. 311–316, 2003.

[22] H. Boudet, C. Clarke, D. Bugden, E. Maibach, C. Roser-Renouf, and A. Leiserowitz, ""Fracking" controversy and communication: Using national survey data to understand public perceptions of hydraulic fracturing," *Energy Policy*, vol. 65, pp. 57–67, 2014.

[23] G. A. Burton, N. Basu, B. R. Ellis, K. E. Kapo, S. Entrekin, and K. Nadelhoffer, "Hydraulic "fracking": Are surface water impacts an ecological concern?," *Environmental Toxicology and Chemistry*, vol. 33, no. 8, pp. 1679–1689, 2014.

[24] BBC, "Scottish government backs ban on fracking," *BBC News*, October 2017.

[25] J. Fox, *Gasland*. International WOW Company, 2010.

[26] J. Fox, *Gasland 2*. International WOW Company, 2013.

[27] G. Van Sant, *Promised land*. Focus Features, 2013.

[28] B. Warner and J. Shapiro, "Fractured, fragmented federalism: A study in fracking regulatory policy," *Publius: The Journal of Federalism*, vol. 43, no. 3, pp. 474–496, 2013.

[29] BBC, "Judge says fracking not banned in Scotland," *BBC News*, June 2018.

[30] A. D. Boyd, "Risk perceptions of an alleged $CO_2$ leak at a carbon sequestration site," *International Journal of Greenhouse Gas Control*, vol. 50, pp. 231–239, 2016.

[31] A. Pantsios, "Burlington: First U.S. city to run on renewable electricity," *EcoWatch. Certified B Corporation.*, February 2015.

[32] M. Fagan, "Sheikh Yamani predicts price crash as age of oil ends," *The Telegraph*, p. 1, 2000.

[33] V. Y. Alexandrov, O. G. Friedlander, and Y. V. Nikolsky, "Numerical and experimental investigations of thermal stress effect on nonlinear thermomolecular pressure difference," in *AIP Conference Proceedings*, vol. 663, pp. 250–257, 2003.

[34] W. Steckelmacher, "Knudsen flow 75 years on: The current state of the art for flow of rarefied gases in tubes and systems," *Reports on Progress in Physics*, vol. 49, no. 10, p. 1083, 1986.

[35] S. Succi, *The lattice Boltzmann equation: For fluid dynamics and beyond*. Oxford university press, 2001.

[36] J. E. Broadwell, "Study of rarefied shear flow by the discrete velocity method," *Journal of Fluid Mechanics*, vol. 19, no. 3, pp. 401–414, 1964.

[37] G. A. Bird, *Molecular gas dynamics and the direct simulation of gas flows*. Clarendon, 1994.

[38] J. Fan and C. Shen, "Statistical simulation of low-speed rarefied gas flows," *Journal of Computational Physics*, vol. 167, no. 2, pp. 393–412, 2001.

[39] L. L. Baker, *Efficient numerical methods for solving the Boltzmann equation for small scale flows*. PhD thesis, Massachusetts Institute of Technology, 2007.

[40] N. G. Hadjiconstantinou, G. A. Radtke, and L. L. Baker, "Low-variance Monte Carlo solutions of the Boltzmann transport equation," *arXiv preprint arXiv:0905.2218*, 2009.

[41] G. A. Radtke and N. G. Hadjiconstantinou, "Variance-reduced particle simulation of the boltzmann transport equation in the relaxation-time approximation," *Physical Review E*, vol. 79, no. 5, p. 056711, 2009.

[42] D. C. Rapaport, *The art of molecular dynamics simulation*. Cambridge university press, 2004.

[43] T. T. M. M. Homolle, *Efficient particle methods for solving the Boltzmann equation*. PhD thesis, Massachusetts Institute of Technology, 2007.

[44] G. A. Radtke, *Efficient simulation of molecular gas transport for micro-and nanoscale applications*. PhD thesis, Massachusetts Institute of Technology, 2011.

[45] I. Newton, "Philosophiæ naturalis principia mathematica (mathematical principles of natural philosophy)," *London (1687)*, vol. 1687, 1987.

[46] J. Mehra, *The physicist's conception of nature*. Springer, 2012.

[47] J. C. Maxwell, "On the dynamical theory of gases," *Philosophical transactions of the Royal Society of London*, no. 157, pp. 49–88, 1867.

[48] L. Boltzmann, *Lectures on gas theory*. Courier Corporation, 2012.

[49] B. L. Holian, W. G. Hoover, and H. A. Posch, "Resolution of Loschmidt's paradox: The origin of irreversible behavior in reversible atomistic dynamics," *Physical Review Letters*, vol. 59, no. 1, p. 10, 1987.

[50] K. Nanbu, "Variable hard-sphere model for gas mixture," *Journal of the Physical Society of Japan*, vol. 59, no. 12, pp. 4331–4333, 1990.

[51] K. Koura and H. Matsumoto, "Variable soft sphere molecular model for inverse-power-law or Lennard-Jones potential," *Physics of fluids A: fluid dynamics*, vol. 3, no. 10, pp. 2459–2465, 1991.

[52] H. Hassan and D. B. Hash, "A generalized hard-sphere model for Monte Carlo simulation," *Physics of Fluids A: Fluid Dynamics*, vol. 5, no. 3, pp. 738–744, 1993.

[53] J. Fan, "A generalized soft-sphere model for Monte Carlo simulation," *Physics of Fluids*, vol. 14, no. 12, pp. 4399–4405, 2002.

[54] P. L. Bhatnagar, E. P. Gross, and M. Krook, "A model for collision processes in gases. I. Small amplitude processes in charged and neutral one-component systems," *Phys. Rev.*, vol. 94, no. 3, pp. 511–525, 1954.

[55] P. Welander, "On the temperature jump in a rarefied gas," *Arkiv fysik*, vol. 7, 1954.

[56] E. Shakhov, "Generalization of the krook kinetic relaxation equation," *Fluid Dynamics*, vol. 3, no. 5, pp. 95–96, 1968.

[57] L. H. Holway Jr, "New statistical models for kinetic theory: Methods of construction," *The physics of fluids*, vol. 9, no. 9, pp. 1658–1673, 1966.

[58] H. Grad, "On the kinetic theory of rarefied gases," *Communications on pure and applied mathematics*, vol. 2, no. 4, pp. 331–407, 1949.

[59] F. Uribe and A. L. Garcia, "Burnett description for plane Poiseuille flow," *Physical Review E*, vol. 60, no. 4, p. 4063, 1999.

[60] K. Xu, "Super-Burnett solutions for Poiseuille flow," *Physics of Fluids*, vol. 15, no. 7, pp. 2077–2080, 2003.

[61] D. Tong, "Kinetic theory," *Graduate Course, University of Cambridge, Cambridge, UK*, 2012.

[62] L. Saint-Raymond, *Hydrodynamic limits of the Boltzmann equation*. No. 1971, Springer Science & Business Media, 2009.

[63] M. P. Allen and D. J. Tildesley, *Computer simulation of liquids*. Oxford university press, 2017.

[64] H. J. Berendsen and W. F. Van Gunsteren, "Practical algorithms for dynamic simulations," *Molecular-dynamics simulation of statistical-mechanical systems*, pp. 43–65, 1986.

[65] P. H. Hünenberger, "Thermostat algorithms for molecular dynamics simulations," in *Advanced computer simulation*, pp. 105–149, Springer, 2005.

[66] T. Bereau, "Multi-timestep integrator for the modified Andersen barostat," *Physics Procedia*, vol. 68, pp. 7–15, 2015.

[67] N. Metropolis, A. W. Rosenbluth, M. N. Rosenbluth, A. H. Teller, and E. Teller, "Equation of state calculations by fast computing machines," *The Journal of Chemical Physics*, vol. 21, no. 6, pp. 1087–1092, 1953.

[68] B. J. Alder and T. E. Wainwright, "Studies in molecular dynamics. I. General method," *The Journal of Chemical Physics*, vol. 31, no. 2, pp. 459–466, 1959.

[69] W. Smith, T. Forester, and I. Todorov, "The DL POLY Classic user manual," *STFC, STFC Daresbury Laboratory, Daresbury, Warrington, Cheshire, WA4 4AD, United Kingdom, version*, vol. 1, 2012.

[70] M. T. Nelson, W. Humphrey, A. Gursoy, A. Dalke, L. V. Kalé, R. D. Skeel, and K. Schulten, "NAMD: A parallel, object-oriented molecular dynamics program," *The International Journal of Supercomputer Applications and High Performance Computing*, vol. 10, no. 4, pp. 251–268, 1996.

[71] S. Plimpton *et al.*, "LAMMPS user's manual," *Sandia National Laboratory*, 2005.

[72] B. Hess, C. Kutzner, D. Van Der Spoel, and E. Lindahl, "GROMACS 4: Algorithms for highly efficient, load-balanced, and scalable molecular simulation," *Journal of chemical theory and computation*, vol. 4, no. 3, pp. 435–447, 2008.

[73] J. D. Gale and A. L. Rohl, "The General Utility Lattice Program (gulp)," *Molecular Simulation*, vol. 29, no. 5, pp. 291–341, 2003.

[74] B. R. Brooks, R. E. Bruccoleri, B. D. Olafson, D. J. States, S. a. Swaminathan, and M. Karplus, "CHARMM: A program for macromolecular energy, minimization, and dynamics calculations," *Journal of computational chemistry*, vol. 4, no. 2, pp. 187–217, 1983.

[75] D. A. Case, T. E. Cheatham, T. Darden, H. Gohlke, R. Luo, K. M. Merz, A. Onufriev, C. Simmerling, B. Wang, and R. J. Woods, "The Amber biomolecular simulation programs," *Journal of computational chemistry*, vol. 26, no. 16, pp. 1668–1688, 2005.

[76] W. Humphrey, A. Dalke, and K. Schulten, "VMD: Visual Molecular Dynamics," *Journal of molecular graphics*, vol. 14, no. 1, pp. 33–38, 1996.

[77] L. Laaksonen, "GOPENMOL: Program for the display and analysis of molecular structures," *Version*, vol. 1, pp. 1997–1999, 2005.

[78] M. P. Allen *et al.*, "Introduction to molecular dynamics simulation," *Computational soft matter: from synthetic polymers to proteins*, vol. 23, pp. 1–28, 2004.

[79] T. Platkowski and R. Illner, "Discrete velocity models of the Boltzmann equation: A survey on the mathematical aspects of the theory," *SIAM review*, vol. 30, no. 2, pp. 213–255, 1988.

[80] A. Polikarpov, *Numerical simulation of rarefied gas flows based on the kinetic approach.* PhD thesis, Aix-Marseille, 2011.

[81] K. Aoki, P. Degond, L. Mieussens, *et al.*, "Numerical simulations of rarefied gases in curved channels: Thermal creep, circulating flow, and pumping effect," *Communications in Computational Physics*, vol. 6, no. 5, p. 919, 2009.

[82] L. Yang, C. Shu, J. Wu, and Y. Wang, "Numerical simulation of flows from free molecular regime to continuum regime by a dvm with streaming and collision processes," *Journal of Computational Physics*, vol. 306, pp. 291–310, 2016.

[83] K. Xu and J.-C. Huang, "A unified gas-kinetic scheme for continuum and rarefied flows," *Journal of Computational Physics*, vol. 229, no. 20, pp. 7747–7764, 2010.

[84] S. Chen, K. Xu, C. Lee, and Q. Cai, "A unified gas kinetic scheme with moving mesh and velocity space adaptation," *Journal of Computational Physics*, vol. 231, no. 20, pp. 6643–6664, 2012.

[85] Z. Guo, K. Xu, and R. Wang, "Discrete unified gas kinetic scheme for all Knudsen number flows: Low-speed isothermal case," *Physical Review E*, vol. 88, no. 3, p. 033305, 2013.

[86] Z. Guo, R. Wang, and K. Xu, "Discrete unified gas kinetic scheme for all Knudsen number flows. II. Thermal compressible case," *Physical Review E*, vol. 91, no. 3, p. 033313, 2015.

[87] D. A. Wolf-Gladrow, *Lattice-gas cellular automata and lattice Boltzmann models: An introduction.* Springer, 2004.

[88] D. H. Rothman and S. Zaleski, *Lattice-gas cellular automata: Simple models of complex hydrodynamics*, vol. 5. Cambridge University Press, 2004.

[89] X. Shan, X.-F. Yuan, and H. Chen, "Kinetic theory representation of hydrodynamics: A way beyond the Navier–Stokes equation," *Journal of Fluid Mechanics*, vol. 550, pp. 413–441, 2006.

[90] M. T. Ho, L. Zhu, L. Wu, P. Wang, Z. Guo, Z.-H. Li, and Y. Zhang, "A multilevel parallel solver for rarefied gas flows in porous media," *Computer Physics Communications*, vol. 234, pp. 14–25, 2019.

[91] J. Meng and Y. Zhang, "Accuracy analysis of high-order lattice Boltzmann models for rarefied gas flows," *Journal of Computational Physics*, vol. 230, no. 3, pp. 835–849, 2011.

[92] J. Li, "Direct simulation method based on BGK equation," in *AIP Conference Proceedings*, vol. 1333, pp. 283–288, 2011.

[93] J. Li, "Comparison between the DSMC and DSBGK methods," *arXiv preprint arXiv:1207.1040*, 2012.

[94] J. Li, "Efficiency and stability of the DSBGK method," in *AIP Conference Proceedings*, vol. 1501, pp. 849–856, 2012.

[95] M. T. Ho, J. Li, L. Wu, J. M. Reese, and Y. Zhang, "A comparative study of the DSBGK and DVM methods for low-speed rarefied gas flows," *Computers & Fluids*, vol. 181, pp. 143–159, 2019.

[96] J. Li, A. S. Sultan, *et al.*, "Permeability computations of shale gas by the pore-scale Monte Carlo molecular simulations," in *International Petroleum Technology Conference*, 2015.

[97] J. Li and A. S. Sultan, "Klinkenberg slippage effect in the permeability computations of shale gas by the pore-scale simulations," *Journal of Natural Gas Science and Engineering*, vol. 48, pp. 197–202, 2017.

[98] A. Nordsieck and B. L. Hicks, "Monte Carlo evaluation of the Boltzmann collision integral," *Coordinated Science Laboratory Report no. R-307*, 1966.

[99] W. Wagner, "A convergence proof for Bird's direct simulation Monte Carlo method for the Boltzmann equation," *Journal of Statistical Physics*, vol. 66, no. 3-4, pp. 1011–1044, 1992.

[100] J. F. Padilla and I. D. Boyd, "Assessment of gas-surface interaction models for computation of rarefied hypersonic flow," *Journal of Thermophysics and Heat Transfer*, vol. 23, no. 1, pp. 96–105, 2009.

[101] A. Mohammadzadeh, E. Roohi, H. Niazmand, S. Stefanov, and R. S. Myong, "Thermal and second-law analysis of a micro- or nanocavity using direct-simulation Monte Carlo," *Physical review E*, vol. 85, no. 5, p. 056310, 2012.

[102] G. Bird, "Forty years of DSMC, and now?," in *AIP Conference Proceedings*, vol. 585, pp. 372–380, AIP, 2001.

[103] T. Abe, "Generalized scheme of the no-time-counter scheme for the DSMC in rarefied gas flow analysis," *Computers & fluids*, vol. 22, no. 2-3, pp. 253–257, 1993.

[104] C. Cercignani and M. Lampis, "Free molecular flow past a flat plate in the presence of a nontrivial gas-surface interaction," *Zeitschrift für angewandte Mathematik und Physik*, vol. 23, no. 5, pp. 713–728, 1972.

[105] R. Lord, "Some extensions to the Cercignani–Lampis gas–surface scattering kernel," *Physics of Fluids A: Fluid Dynamics*, vol. 3, no. 4, pp. 706–710, 1991.

[106] R. Lord, "Some further extensions of the Cercignani–Lampis gas–surface interaction model," *Physics of Fluids*, vol. 7, no. 5, pp. 1159–1161, 1995.

[107] G. Bird, "The ds2v program user's guide ver. 3.2," *GAB Consulting Pty Ltd., Sydney, Australia*, 2005.

[108] G. Bird, "The DS3V program user's guide ver 1.2.," *GAB Consulting Pty Ltd., Sydney, Australia*, 2005.

[109] T. Scanlon, E. Roohi, C. White, M. Darbandi, and J. Reese, "An open source, parallel DSMC code for rarefied gas flows in arbitrary geometries," *Computers & Fluids*, vol. 39, no. 10, pp. 2078–2089, 2010.

[110] S. Dietrich and I. D. Boyd, "Scalar and parallel optimized implementation of the direct simulation Monte Carlo method," *Journal of Computational Physics*, vol. 126, no. 2, pp. 328–342, 1996.

[111] M. Rose and G. A. Bird, "Open-source interface to Bird's DSMC code for complex interaction," *Progress in Computational Fluid Dynamics, an International Journal*, vol. 11, no. 2, pp. 67–75, 2011.

[112] M. Ivanov, A. Kashkovsky, S. Gimelshein, G. Markelov, A. Alexeenko, Y. A. Bondar, G. Zhukova, S. Nikiforov, and P. Vaschenkov, "SMILE system for 2D/3D DSMC computations," in *Proceedings of 25th International Symposium on Rarefied Gas Dynamics, St. Petersburg, Russia*, pp. 21–28, 2006.

[113] G. LeBeau and F. Lumpkin III, "Application highlights of the DSMC Analysis Code (DAC) software for simulating rarefied flows," *Computer Methods in Applied Mechanics and Engineering*, vol. 191, no. 6-7, pp. 595–609, 2001.

[114] D. Gao, C. Zhang, and T. E. Schwartzentruber, "Particle simulations of planetary probe flows employing automated mesh refinement," *Journal of Spacecraft and Rockets*, vol. 48, no. 3, pp. 397–405, 2011.

[115] M. A. Gallis, J. R. Torczynski, S. J. Plimpton, D. J. Rader, and T. Koehler, "Direct simulation monte carlo: The quest for speed," in *AIP Conference Proceedings*, vol. 1628, pp. 27–36, AIP, 2014.

[116] M. A. Gallis, "About the Hubble Space Telescope," *Sandia National Laboratories*, 2014.

[117] R. Kersevan, *Molflow user's guide*. 1991.

[118] A. K. Chinnappan and R. Kumar, "Modeling of high speed gas-granular flow over a 2D cylinder in the direct simulation Monte-Carlo framework," *Granular Matter*, vol. 18, no. 3, p. 35, 2016.

[119] Q. Sun and I. D. Boyd, "A direct simulation method for subsonic, microscale gas flows," *Journal of Computational Physics*, vol. 179, no. 2, pp. 400–425, 2002.

[120] C. Cai, I. D. Boyd, J. Fan, and G. V. Candler, "Direct simulation methods for low-speed microchannel flows," *Journal of thermophysics and heat transfer*, vol. 14, no. 3, pp. 368–378, 2000.

[121] R. P. Nance, D. B. Hash, and H. Hassan, "Role of boundary conditions in monte carlo simulation of microelectromechanical systems," *Journal of Thermophysics and Heat Transfer*, vol. 12, no. 3, pp. 447–449, 1998.

[122] C. White, M. K. Borg, T. J. Scanlon, and J. M. Reese, "A dsmc investigation of gas flows in micro-channels with bends," *Computers & Fluids*, vol. 71, pp. 261–271, 2013.

[123] J. Chun and D. Koch, "A direct simulation Monte Carlo method for rarefied gas flows in the limit of small Mach number," *Physics of Fluids*, vol. 17, no. 10, p. 107107, 2005.

[124] L. L. Baker and N. G. Hadjiconstantinou, "Variance reduction in particle methods for solving the Boltzmann equation," in *ASME 4th International Conference on Nanochannels, Microchannels, and Minichannels*, pp. 377–383, American Society of Mechanical Engineers, 2006.

[125] T. M. Homolle and N. G. Hadjiconstantinou, "A low-variance deviational simulation Monte Carlo for the Boltzmann equation," *Journal of Computational Physics*, vol. 226, no. 2, pp. 2341–2358, 2007.

[126] T. M. Homolle and N. G. Hadjiconstantinou, "Low-variance deviational simulation Monte Carlo," *Physics of Fluids*, vol. 19, no. 4, p. 041701, 2007.

[127] N. G. Hadjiconstantinou, G. A. Radtke, and L. L. Baker, "On variance-reduced simulations of the boltzmann transport equation for small-scale heat transfer applications," *Journal of Heat Transfer*, vol. 132, no. 11, p. 112401, 2010.

[128] H. A. Al-Mohssen and N. G. Hadjiconstantinou, "Low-variance direct Monte Carlo simulations using importance weights," *ESAIM: Mathematical Modelling and Numerical Analysis*, vol. 44, no. 5, pp. 1069–1083, 2010.

[129] J.-P. M. Péraud and N. G. Hadjiconstantinou, "Efficient simulation of multidimensional phonon transport using energy-based variance-reduced Monte Carlo formulations," *Physical Review B*, vol. 84, no. 20, p. 205331, 2011.

[130] G. A. Radtke, N. G. Hadjiconstantinou, and W. Wagner, "Low-noise Monte Carlo simulation of the variable hard sphere gas," *Physics of fluids*, vol. 23, no. 3, p. 030606, 2011.

[131] G. A. Radtke, J.-P. M. Péraud, and N. G. Hadjiconstantinou, "On efficient simulations of multiscale kinetic transport," *Philosophical Transactions of the Royal Society A: Mathematical, Physical and Engineering Sciences*, vol. 371, no. 1982, p. 20120182, 2013.

[132] L. Szalmas, "Variance-reduced DSMC for binary gas flows as defined by the McCormack kinetic model," *Journal of Computational Physics*, vol. 231, no. 9, pp. 3723–3738, 2012.

[133] S. Schaaf and P. Chambré, "Flow of rarefied gases," *Princeton Aeronautical Paperbacks*, vol. 8, 1961.

[134] R. N. Moghaddam and M. Jamiolahmady, "Slip flow in porous media," *Fuel*, vol. 173, pp. 298–310, 2016.

[135] C. Zhang, T. Thajudeen, C. Larriba, T. E. Schwartzentruber, and C. J. Hogan Jr, "Determination of the scalar friction factor for nonspherical particles and aggregates across the entire Knudsen number range by Direct Simulation Monte Carlo (DSMC)," *Aerosol Science and Technology*, vol. 46, no. 10, pp. 1065–1078, 2012.

[136] A. Beskok and G. E. Karniadakis, "Report: A model for flows in channels, pipes, and ducts at micro and nano scales," *Microscale Thermophysical Engineering*, vol. 3, no. 1, pp. 43–77, 1999.

[137] M. Gad-el Hak, "The fluid mechanics of microdevices—The Freeman scholar lecture," *Journal of Fluids Engineering*, vol. 121, no. 1, pp. 5–33, 1999.

[138] G. Karniadakis, A. Beskok, and N. Aluru, *Microflows and nanoflows: Fundamentals and simulation*, vol. 29. Springer Science & Business Media, 2006.

[139] N. Dongari, A. Sharma, and F. Durst, "Pressure-driven diffusive gas flows in micro-channels: From the Knudsen to the continuum regimes," *Microfluidics and nanofluidics*, vol. 6, no. 5, pp. 679–692, 2009.

[140] N. G. Hadjiconstantinou, "The limits of Navier-Stokes theory and kinetic extensions for describing small-scale gaseous hydrodynamics," *Physics of Fluids*, vol. 18, no. 11, p. 111301, 2006.

[141] G. Karniadakis, A. Beskok, and M. Gad-el Hak, "Micro flows: Fundamentals and simulation," *Applied Mechanics Reviews*, vol. 55, p. B76, 2002.

[142] H. P. G. Darcy, *Les Fontaines publiques de la ville de Dijon. Exposition et application des principes à suivre et des formules à employer dans les questions de distribution d'eau, etc.* V. Dalamont, 1856.

[143] M. Muskat, R. Wyckoff, H. Botset, M. Meres, *et al.*, "Flow of gas-liquid mixtures through sands," *Transactions of the AIME*, vol. 123, no. 1, pp. 69–96, 1937.

[144] B. Ghanbarian and F. Javadpour, "Upscaling pore pressure-dependent gas permeability in shales," *Journal of Geophysical Research: Solid Earth*, vol. 122, no. 4, pp. 2541–2552, 2017.

[145] R. Guibert, M. Nazarova, P. Horgue, G. Hamon, P. Creux, and G. Debenest, "Computational permeability determination from pore-scale imaging: Sample size, mesh and method sensitivities," *Transport in Porous Media*, vol. 107, no. 3, pp. 641–656, 2015.

[146] J. É. J. Dupuit, *Études théoriques et pratiques sur le mouvement des eaux dans les canaux découverts et à travers les terrains perméables: avec des considérations relatives au régime des grandes eaux, au débouché à leur donner, et à la marche des alluvions dans les rivières à fond mobile.* Dunod, 1863.

[147] P. Forchheimer, "Wasserbewegung durch boden," *Z. Ver. Deutsch, Ing.*, vol. 45, pp. 1782–1788, 1901.

[148] L. Klinkenberg *et al.*, "The permeability of porous media to liquids and gases," in *Drilling and production practice*, American Petroleum Institute, 1941.

[149] L. Wu, M. T. Ho, L. Germanou, X.-J. Gu, C. Liu, K. Xu, and Y. Zhang, "On the apparent permeability of porous media in rarefied gas flows," *Journal of Fluid Mechanics*, vol. 822, pp. 398–417, 2017.

[150] F. Civan, "Effective correlation of apparent gas permeability in tight porous media," *Transport in porous media*, vol. 82, no. 2, pp. 375–384, 2010.

[151] G. Tang, W. Tao, and Y. He, "Gas slippage effect on microscale porous flow using the lattice Boltzmann method," *Physical Review E*, vol. 72, no. 5, p. 056301, 2005.

[152] J. Kozeny, "Uber kapillare leitung der wasser in boden," *Royal Academy of Science, Vienna, Proc. Class I*, vol. 136, pp. 271–306, 1927.

[153] A. W. Heijs and C. P. Lowe, "Numerical evaluation of the permeability and the kozeny constant for two types of porous media," *Physical Review E*, vol. 51, no. 5, p. 4346, 1995.

[154] M. B. Clennell, "Tortuosity: A guide through the maze," *Geological Society of London*, vol. 122, no. 1, pp. 299–344, 1997.

[155] J. Bear, *Dynamics of fluids in porous media*. Elsevier, New York., 1972.

[156] F. A. Dullien, *Porous media: Fluid transport and pore structure*. Academic press, 2012.

[157] Y. Bo-Ming and L. Jian-Hua, "A geometry model for tortuosity of flow path in porous media," *Chinese Physics Letters*, vol. 21, no. 8, p. 1569, 2004.

[158] A. Koponen, M. Kataja, and J. Timonen, "Tortuous flow in porous media," *Physical Review E*, vol. 54, no. 1, p. 406, 1996.

[159] A. Koponen, M. Kataja, and J. Timonen, "Permeability and effective porosity of porous media," *Physical Review E*, vol. 56, no. 3, p. 3319, 1997.

[160] M. Matyka, A. Khalili, and Z. Koza, "Tortuosity-porosity relation in porous media flow," *Physical Review E*, vol. 78, no. 2, p. 026306, 2008.

[161] M. Matyka and Z. Koza, "How to calculate tortuosity easily?," in *AIP Conference Proceedings*, vol. 1453, pp. 17–22, AIP, 2012.

[162] A. Duda, Z. Koza, and M. Matyka, "Hydraulic tortuosity in arbitrary porous media flow," *Physical Review E*, vol. 84, no. 3, p. 036319, 2011.

[163] A. Nabovati and A. Sousa, "Fluid flow simulation in random porous media at pore level using lattice Boltzmann method," in *New Trends in Fluid Mechanics Research*, pp. 518–521, Springer, 2007.

[164] J. Comiti and M. Renaud, "A new model for determining mean structure parameters of fixed beds from pressure drop measurements: Application to beds packed with parallelepipedal particles," *Chemical Engineering Science*, vol. 44, no. 7, pp. 1539–1545, 1989.

[165] M. Barrande, R. Bouchet, and R. Denoyel, "Tortuosity of porous particles," *Analytical chemistry*, vol. 79, no. 23, pp. 9115–9121, 2007.

[166] N. Iversen and B. B. Jørgensen, "Diffusion coefficients of sulfate and methane in marine sediments: Influence of porosity," *Geochimica et Cosmochimica Acta*, vol. 57, no. 3, pp. 571–578, 1993.

[167] D. B. Newell, F. Cabiati, J. Fischer, K. Fujii, S. G. Karshenboim, H. Margolis, E. de Mirandés, P. Mohr, F. Nez, K. Pachucki, *et al.*, "The CODATA 2017 values of h, e, k, and NA for the revision of the SI," *Metrologia*, vol. 55, no. 1, p. L13, 2018.

[168] C. Cercignani and M. Lampis, "New scattering kernel for gas-surface interaction," *AIAA journal*, vol. 35, no. 6, pp. 1000–1011, 1997.

[169] NASA, "Mars climate orbiter."

[170] D. Valougeorgis, "The friction factor of a rarefied gas flow in a circular tube," *Physics of Fluids*, vol. 19, no. 9, p. 091702, 2007.

[171] Z. Tan and P. L. Varghese, "The $\delta$-$\varepsilon$ method for the Boltzmann equation," *Journal of Computational Physics*, vol. 110, no. 2, pp. 327–340, 1994.

[172] F. Cheremisin, "Solving the Boltzmann equation in the case of passing to the hydrodynamic flow regime," in *Doklady Physics*, vol. 45, pp. 401–404, Springer, 2000.

[173] L. L. Baker and N. G. Hadjiconstantinou, "Variance reduction for Monte Carlo solutions of the Boltzmann equation," *Physics of Fluids*, vol. 17, no. 5, p. 051703, 2005.

[174] W. Wagner, "Deviational particle Monte Carlo for the Boltzmann equation," *Monte Carlo Methods and Applications*, vol. 14, no. 3, pp. 191–268, 2008.

[175] M. R. Allshouse and N. G. Hadjiconstantinou, "Low-variance deviational monte carlo simulations of pressure-driven flow in micro-and nanoscale channels," in *AIP Conference Proceedings*, vol. 1084, pp. 1015–1020, 2008.

[176] J. Li, C. Shen, and J. Fan, "Improvements to the low-variance deviational Simulation Monte Carlo Method," *Acta Aerodynamica Sinica*, vol. 28, no. 2, pp. 283–243, 2010.

[177] G. A. Radtke, N. G. Hadjiconstantinou, S. Takata, and K. Aoki, "On the second-order temperature jump coefficient of a dilute gas," *Journal of Fluid Mechanics*, vol. 707, pp. 331–341, 2012.

[178] J. Wakefield, A. Gelfand, and A. Smith, "Efficient generation of random variates via the ratio-of-uniforms method," *Statistics and Computing*, vol. 1, no. 2, pp. 129–133, 1991.

[179] C. Cercignani and A. Daneri, "Flow of a rarefied gas between two parallel plates," *Journal of Applied Physics*, vol. 34, no. 12, pp. 3509–3513, 1963.

[180] S. Loyalka, N. Petrellis, and T. Storvick, "Some exact numerical results for the bgk model: Couette, poiseuille and thermal creep flow between parallel plates," *Zeitschrift für angewandte Mathematik und Physik*, vol. 30, no. 3, pp. 514–521, 1979.

[181] S. Lo and S. Loyalka, "An efficient computation of near-continuum rarefied gas flows," *Zeitschrift für angewandte Mathematik und Physik ZAMP*, vol. 33, no. 3, pp. 419–424, 1982.

[182] M. Knudsen, "The law of molecular flow and viscosity of gases moving through tubes," *Ann. Phys.*, vol. 28, p. 75, 1909.

[183] B. Antohe, J. Lage, D. Price, and R. M. Weber, "Numerical characterization of micro heat exchangers using experimentally tested porous aluminum layers," *International Journal of Heat and Fluid Flow*, vol. 17, no. 6, pp. 594–603, 1996.

[184] C.-M. Ho and Y.-C. Tai, "Micro-electro-mechanical-systems (MEMS) and fluid flows," *Annual review of fluid mechanics*, vol. 30, no. 1, pp. 579–612, 1998.

[185] S. W. Cha, R. O'Hayre, and F. B. Prinz, "The influence of size scale on the performance of fuel cells," *Solid State Ionics*, vol. 175, no. 1-4, pp. 789–795, 2004.

[186] A. A. Merrikh and J. L. Lage, "Effect of blood flow on gas transport in a pulmonary capillary," *Journal of biomechanical engineering*, vol. 127, no. 3, pp. 432–439, 2005.

[187] E. B. Arkilic, M. A. Schmidt, and K. S. Breuer, "Gaseous slip flow in long microchannels," *Journal of Microelectromechanical systems*, vol. 6, no. 2, pp. 167–178, 1997.

[188] T. Araki, M. S. Kim, H. Iwai, and K. Suzuki, "An experimental investigation of gaseous flow characteristics in microchannels," *Microscale Thermophysical Engineering*, vol. 6, no. 2, pp. 117–130, 2002.

[189] J. Maurer, P. Tabeling, P. Joseph, and H. Willaime, "Second-order slip laws in microchannels for helium and nitrogen," *Physics of Fluids*, vol. 15, no. 9, pp. 2613–2621, 2003.

[190] J. Liu, Y.-C. Tai, and C.-M. H.-C. Pong, "MEMS for pressure distribution studies of gaseous flows in microchannels," in *Micro Electro Mechanical Systems, 1995. IEEE Proceedings*, p. 209, 1995.

[191] M. Gad-el Hak, *The MEMS handbook*. CRC press, 2001.

[192] J. C. Harley, Y. Huang, H. H. Bau, and J. N. Zemel, "Gas flow in micro-channels," *Journal of Fluid Mechanics*, vol. 284, pp. 257–274, 1995.

[193] E. H. Kennard *et al.*, "Kinetic theory of gases, with an introduction to statistical mechanics," 1938.

[194] W. Ebert and E. M. Sparrow, "Slip flow in rectangular and annular ducts," *Journal of Basic Engineering*, vol. 87, no. 4, pp. 1018–1024, 1965.

[195] Z. Duan and Y. Muzychka, "Slip flow in elliptic microchannels," *International Journal of Thermal Sciences*, vol. 46, no. 11, pp. 1104–1111, 2007.

[196] Z. Duan and Y. Muzychka, "Slip flow in non-circular microchannels," *Microfluidics and Nanofluidics*, vol. 3, no. 4, pp. 473–484, 2007.

[197] G. Morini, M. Spiga, and P. Tartarini, "Laminar viscous dissipation in rectangular ducts," *International communications in heat and mass transfer*, vol. 25, no. 4, pp. 551–560, 1998.

[198] G. L. Morini, M. Lorenzini, and M. Spiga, "A criterion for experimental validation of slip-flow models for incompressible rarefied gases through microchannels," *Microfluidics and Nanofluidics*, vol. 1, no. 2, pp. 190–196, 2005.

[199] M. Renksizbulut, H. Niazmand, and G. Tercan, "Slip-flow and heat transfer in rectangular microchannels with constant wall temperature," *International Journal of Thermal Sciences*, vol. 45, no. 9, pp. 870–881, 2006.

[200] M. Bahrami, M. Yovanovich, and J. Culham, "Pressure drop of fully-developed, laminar flow in microchannels of arbitrary cross-section," *Journal of Fluids Engineering*, vol. 128, no. 5, pp. 1036–1044, 2006.

[201] M. Bahrami, M. M. Yovanovich, and J. R. Culham, "A novel solution for pressure drop in singly connected microchannels of arbitrary cross-section," *International Journal of Heat and Mass Transfer*, vol. 50, no. 13-14, pp. 2492–2502, 2007.

[202] C. Wang, "Slip flow in a triangular duct–an exact solution," *Zeitschrift für Angewandte Mathematik und Mechanik: Applied Mathematics and Mechanics*, vol. 83, no. 9, pp. 629–631, 2003.

[203] Fluent, *Manual and user guide of Fluent Software.* Fluent Inc., 2005.

[204] J. Pitakarnnop, S. Geoffroy, S. Colin, and L. Baldas, "Slip flow in triangular and trapezoidal microchannels," *International Journal of Heat and Technology*, vol. 26, no. 1, pp. 167–174, 2007.

[205] A. Tamayol and K. Hooman, "Slip-flow in microchannels of non-circular cross sections," *Journal of Fluids Engineering*, vol. 133, no. 9, p. 091202, 2011.

[206] S. K. Mitra and S. Chakraborty, *Microfluidics and Nanofluidics Handbook: Chemistry, physics, and life science principles.* CRC Press, 2011.

[207] F. White, *Viscous fluid flow*. New York: McGraw-Hill, 1974.

[208] R. K. Shah and A. L. London, *Laminar flow forced convection in ducts: a source book for compact heat exchanger analytical data*. Academic press, 2014.

[209] S. Colin, P. Lalonde, and R. Caen, "Validation of a second-order slip flow model in rectangular microchannels," *Heat transfer engineering*, vol. 25, no. 3, pp. 23–30, 2004.

[210] A. Sreekanth, "Slip flow through long circular tubes," in *Proceedings of the sixth international symposium in rarefied gas dynamics*, vol. 1, pp. 667–680, 1969.

[211] S. Colin, Cécile Aubert, "High-order boundary conditions for gaseous flows in rectangular microducts," *Microscale Thermophysical Engineering*, vol. 5, no. 1, pp. 41–54, 2001.

[212] R. Deissler, "An analysis of second-order slip flow and temperature-jump boundary conditions for rarefied gases," *International Journal of Heat and Mass Transfer*, vol. 7, no. 6, pp. 681–694, 1964.

[213] R. W. Barber and D. R. Emerson, "Challenges in modeling gas-phase flow in microchannels: From slip to transition," *Heat Transfer Engineering*, vol. 27, no. 4, pp. 3–12, 2006.

[214] V. Rykov, V. Titarev, and E. Shakhov, "Rarefied Poiseuille flow in elliptical and rectangular tubes," *Fluid Dynamics*, vol. 46, no. 3, pp. 456–466, 2011.

[215] F. Sharipov, "Rarefied gas flow through a long rectangular channel," *Journal of Vacuum Science & Technology A: Vacuum, Surfaces, and Films*, vol. 17, no. 5, pp. 3062–3066, 1999.

[216] F. Sharipov, "Non-isothermal gas flow through rectangular microchannels," *Journal of Micromechanics and Microengineering*, vol. 9, no. 4, p. 394, 1999.

[217] I. Graur and M. Ho, "Rarefied gas flow through a long rectangular channel of variable cross section," *Vacuum*, vol. 101, pp. 328–332, 2014.

[218] V. Titarev and E. Shakhov, "Kinetic analysis of the isothermal flow in a long rectangular microchannel," *Computational Mathematics and Mathematical Physics*, vol. 50, no. 7, pp. 1221–1237, 2010.

[219] S. Varoutis and D. Valougeorgis, "Estimation of the Poiseuille number in gas flows through rectangular nano-and micro-channels in the whole range of the Knudsen number," in *IUTAM Symposium on Advances in Micro-and Nanofluidics*, pp. 79–86, 2009.

[220] I. Graur and F. Sharipov, "Gas flow through an elliptical tube over the whole range of the gas rarefaction," *European Journal of Mechanics-B/Fluids*, vol. 27, no. 3, pp. 335–345, 2008.

[221] I. Graur and F. Sharipov, "Non-isothermal flow of rarefied gas through a long pipe with elliptic cross section," *Microfluidics and nanofluidics*, vol. 6, no. 2, pp. 267–275, 2009.

[222] S. Naris, D. Valougeorgis, D. Kalempa, and F. Sharipov, "Flow of gaseous mixtures through rectangular microchannels driven by pressure, temperature, and concentration gradients," *Physics of fluids*, vol. 17, no. 10, p. 100607, 2005.

[223] S. Varoutis, S. Naris, V. Hauer, C. Day, and D. Valougeorgis, "Computational and experimental study of gas flows through long channels of various cross sections in the whole range of the Knudsen number," *Journal of Vacuum Science & Technology A: Vacuum, Surfaces, and Films*, vol. 27, no. 1, pp. 89–100, 2009.

[224] G. Breyiannis, S. Varoutis, and D. Valougeorgis, "Rarefied gas flow in concentric annular tube: Estimation of the Poiseuille number and the exact hydraulic diameter," *European Journal of Mechanics-B/Fluids*, vol. 27, no. 5, pp. 609–622, 2008.

[225] F. Sharipov and V. Seleznev, "Data on internal rarefied gas flows," *Journal of Physical and Chemical Reference Data*, vol. 27, no. 3, pp. 657–706, 1998.

[226] F. Sharipov and V. Seleznev, "Rarefied gas flow through a long tube at any pressure ratio,"

[227] F. Sharipov, "Rarefied gas flow through a long tube at any temperature ratio," *Journal of Vacuum Science and Technology A: Vacuum, Surfaces, and Films*, vol. 14, no. 4, pp. 2627–2635, 1996.

[228] K. Ritos, Y. Lihnaropoulos, S. Naris, and D. Valougeorgis, "Pressure-and temperature-driven flow through triangular and trapezoidal microchannels," *Heat Transfer Engineering*, vol. 32, no. 13-14, pp. 1101–1107, 2011.

[229] Q. He, Q. Wang, X. Wang, and L. Luo, "DSMC simulation of low-speed gas flow and heat transfer in 2D rectangular micro-channel," *Progress in Computational Fluid Dynamics*, vol. 5, no. 3-5, pp. 230–235, 2005.

[230] T. Ewart, P. Perrier, I. A. Graur, and J. G. Méolans, "Mass flow rate measurements in a microchannel, from hydrodynamic to near free molecular regimes," *Journal of fluid mechanics*, vol. 584, pp. 337–356, 2007.

[231] Y. Wang, *KOH etching of Silicon*. PhD thesis, New Jersey Institute of Technology, 2016.

[232] N. Damean and P. P. Regtien, "Poiseuille number for the fully developed laminar flow through hexagonal ducts etched in ¡1 0 0¿ silicon," *Sensors and Actuators A: Physical*, vol. 90, no. 1-2, pp. 96–101, 2001.

[233] O. Emersleben, "The Darcy filter formula," *Phys. Zi*, vol. 26, pp. 601–610, 1925.

[234] R. Sullivan, "Specific surface measurements on compact bundles of parallel fibers," *Journal of Applied Physics*, vol. 13, no. 11, pp. 725–730, 1942.

[235] G. W. Jackson and D. F. James, "The permeability of fibrous porous media," *The Canadian Journal of Chemical Engineering*, vol. 64, no. 3, pp. 364–374, 1986.

[236] E. Sparrow and A. Loeffler Jr, "Longitudinal laminar flow between cylinders arranged in regular array," *AIChE Journal*, vol. 5, no. 3, pp. 325–330, 1959.

[237] H. Hasimoto, "On the flow of a viscous fluid past a thin screen at small reynolds numbers," *Journal of the Physical Society of Japan*, vol. 13, no. 6, pp. 633–639, 1958.

[238] S. Banerjee and G. Hadaller, "Longitudinal laminar flow between cylinders arranged in a triangular array by a variational technique," *Journal of Applied Mechanics*, vol. 40, no. 4, pp. 1136–1138, 1973.

[239] C. Wang, "Stokes flow through a transversely finned channel," *Journal of fluids engineering*, vol. 119, no. 1, pp. 110–114, 1997.

[240] C. Wang, "Stokes flow through a rectangular array of circular cylinders," *Fluid Dynamics Research*, vol. 29, no. 2, p. 65, 2001.

[241] R. Larson and J. Higdon, "Microscopic flow near the surface of two-dimensional porous media. Part 1. Axial flow," *Journal of Fluid Mechanics*, vol. 166, pp. 449–472, 1986.

[242] R. Larson and J. Higdon, "Microscopic flow near the surface of two-dimensional porous media. Part 2. Transverse flow," *Journal of Fluid Mechanics*, vol. 178, pp. 119–136, 1987.

[243] C. Wang, "Stokes slip flow through square and triangular arrays of circular cylinders," *Fluid dynamics research*, vol. 32, no. 5, pp. 233–246, 2003.

[244] A. Tamayol and M. Bahrami, "Analytical determination of viscous permeability of fibrous porous media," *International Journal of Heat and Mass Transfer*, vol. 52, no. 9-10, pp. 2407–2414, 2009.

[245] A. Tamayol and M. Bahrami, "Parallel flow through ordered fibers: An analytical approach," *Journal of Fluids Engineering*, vol. 132, no. 11, p. 114502, 2010.

[246] Z. Chai, J. Lu, B. Shi, and Z. Guo, "Gas slippage effect on the permeability of circular cylinders in a square array," *International Journal of Heat and Mass Transfer*, vol. 54, no. 13-14, pp. 3009–3014, 2011.

[247] D. Lasseux, F. V. Parada, J. O. Tapia, and B. Goyeau, "A macroscopic model for slightly compressible gas slip-flow in homogeneous porous media," *Physics of Fluids*, vol. 26, no. 5, p. 053102, 2014.

[248] J. Bear and Y. Bachmat, *Introduction to modeling of transport phenomena in porous media*, vol. 4. Springer Science & Business Media, 2012.

[249] R. Larson and J. Higdon, "A periodic grain consolidation model of porous media," *Physics of Fluids A: Fluid Dynamics*, vol. 1, no. 1, pp. 38–46, 1989.

[250] A. Chapman and J. Higdon, "Effective elastic properties for a periodic bicontinuous porous medium," *Journal of the Mechanics and Physics of Solids*, vol. 42, no. 2, pp. 283–305, 1994.

[251] S. Bryant and M. Blunt, "Prediction of relative permeability in simple porous media," *Physical review A*, vol. 46, no. 4, p. 2004, 1992.

[252] S. Bakke, P.-E. Øren, *et al.*, "3-D pore-scale modelling of sandstones and flow simulations in the pore networks," *SPE Journal*, vol. 2, no. 2, pp. 136–149, 1997.

[253] M. Pilotti, "Reconstruction of clastic porous media," *Transport in Porous Media*, vol. 41, no. 3, pp. 359–364, 2000.

[254] B. B. Mandelbrot, *The fractal geometry of nature*, vol. 173. WH freeman New York, 1983.

[255] W. Sierpinski, "Sur une courbe cantorienne qui contient une image biunivoque et continue de toute courbe donnée," *CR Acad. Sci. Paris*, vol. 162, pp. 629–632, 1916.

[256] S. R. Broadbent and J. M. Hammersley, "Percolation processes: I. Crystals and mazes," in *Mathematical Proceedings of the Cambridge Philosophical Society*, vol. 53, pp. 629–641, 1957.

[257] J. M. Hammersley, "Percolation processes: Lower bounds for the critical probability," *The Annals of Mathematical Statistics*, vol. 28, no. 3, pp. 790–795, 1957.

[258] J. W. Essam, "Percolation theory," *Reports on progress in physics*, vol. 43, no. 7, p. 833, 1980.

[259] G. Voronoi, "Nouvelles applications des parametres continusa la théorie des formes quadratiques. Premier Mémoire. Sur quelques propriétés des formes quadratiques positives parfaites," *J. reine angew. Math*, vol. 133, no. 97-178, p. 14, 1907.

[260] K. Golden, "Critical behavior of transport in lattice and continuum percolation models," *Physical review letters*, vol. 78, no. 20, p. 3935, 1997.

[261] A. Katz and A. Thompson, "Fractal sandstone pores: Implications for conductivity and pore formation," *Physical Review Letters*, vol. 54, no. 12, p. 1325, 1985.

[262] P. M. Adler, "Transport processes in fractals I. Conductivity and permeability of a Leibniz packing in the lubrication limit," *International journal of multiphase flow*, vol. 11, no. 1, pp. 91–108, 1985.

[263] P. Adler, "Transport processes in fractals. VI. Stokes flow through Sierpinski carpets," *The Physics of fluids*, vol. 29, no. 1, pp. 15–22, 1986.

[264] P. Adler, "Fractal porous media III: Transversal Stokes flow through random and sierpinski carpets," *Transport in Porous Media*, vol. 3, no. 2, pp. 185–198, 1988.

[265] L. Jian-Hua and Y. Bo-Ming, "Tortuosity of flow paths through a Sierpinski carpet," *Chinese Physics Letters*, vol. 28, no. 3, p. 034701, 2011.

[266] J. Zheng, W. Zhang, G. Zhang, Y. Yu, and S. Wang, "Effect of porous structure on rarefied gas flow in porous medium constructed by fractal geometry," *Journal of Natural Gas Science and Engineering*, vol. 34, pp. 1446–1452, 2016.

[267] H. Rostamzadeh, M. Salimi, and M. Taeibi-Rahni, "Permeability correlation with porosity and Knudsen number for rarefied gas flow in Sierpinski carpets," *Journal of Natural Gas Science and Engineering*, vol. 56, pp. 549–567, 2018.

[268] P. Adler and C. G. Jacquin, "Fractal porous media I: Longitudinal Stokes flow in random carpets," *Transport in porous media*, vol. 2, no. 6, pp. 553–569, 1987.

[269] V. Balashov, "Direct Simulation of moderately rarefied gas flows in two-dimensional model porous media," *Mathematical Models and Computer Simulations*, vol. 10, no. 4, pp. 483–493, 2018.

[270] A. S. Sangani and C. Yao, "Transport processes in random arrays of cylinders. II. Viscous flow," *The Physics of fluids*, vol. 31, no. 9, pp. 2435–2444, 1988.

[271] L. De Socio and L. Marino, "Gas flow in a permeable medium," *Journal of Fluid Mechanics*, vol. 557, pp. 119–133, 2006.

[272] M. T. Ho, L. Zhu, L. Wu, P. Wang, Z. Guo, J. Ma, and Y. Zhang, "Pore-scale simulations of rarefied gas flows in ultra-tight porous media," *Fuel*, vol. 249, pp. 341–351, 2019.

[273] V. N. Burganos, "Gas diffusion in random binary media," *The Journal of chemical physics*, vol. 109, no. 16, pp. 6772–6779, 1998.

[274] S. Jain, M. Acharya, S. Gupta, and A. N. Bhaskarwar, "Monte Carlo simulation of flow of fluids through porous media," *Computers & chemical engineering*, vol. 27, no. 3, pp. 385–400, 2003.

[275] M. Wang, J. Wang, N. Pan, and S. Chen, "Mesoscopic predictions of the effective thermal conductivity for microscale random porous media," *Physical Review E*, vol. 75, no. 3, p. 036702, 2007.

[276] L. Germanou, M. T. Ho, Y. Zhang, and L. Wu, "Intrinsic and apparent gas permeability of heterogeneous and anisotropic ultra-tight porous media," *Journal of Natural Gas Science and Engineering*, vol. 60, pp. 271–283, 2018.

[277] Y. Gefen, B. B. Mandelbrot, and A. Aharony, "Critical phenomena on fractal lattices," *Physical Review Letters*, vol. 45, no. 11, p. 855, 1980.

[278] Y. Gefen, A. Aharony, B. B. Mandelbrot, and S. Kirkpatrick, "Solvable fractal family, and its possible relation to the backbone at percolation," *Physical Review Letters*, vol. 47, no. 25, p. 1771, 1981.

[279] Y. Gefen, Y. Meir, B. B. Mandelbrot, and A. Aharony, "Geometric implementation of hypercubic lattices with noninteger dimensionality by use of low lacunarity fractal lattices," *Physical Review Letters*, vol. 50, no. 3, p. 145, 1983.

[280] K. Menger, "Bericht über die Dimensionstheorie.," *Jahresbericht der Deutschen Mathematiker-Vereinigung*, vol. 35, pp. 113–149, 1926.

[281] M. Coles, R. Hazlett, E. Muegge, K. Jones, B. Andrews, B. Dowd, P. Siddons, A. Peskin, P. Spanne, W. Soll, *et al.*, "Developments in synchrotron X-ray microtomography with applications to flow in porous media," *SPE Reservoir Evaluation & Engineering*, vol. 1, no. 4, pp. 288–296, 1998.

[282] M. Coles, R. Hazlett, P. Spanne, W. Soll, E. Muegge, and K. Jones, "Pore level imaging of fluid transport using synchrotron x-ray microtomography," *Journal of Petroleum Science and Engineering*, vol. 19, no. 1-2, pp. 55–63, 1998.

[283] M. A. B. Promentilla, T. Sugiyama, T. Hitomi, and N. Takeda, "Quantification of tortuosity in hardened cement pastes using synchrotron-based X-ray computed microtomography," *Cement and Concrete Research*, vol. 39, no. 6, pp. 548–557, 2009.

[284] B. Inkson, M. Mulvihill, and G. Möbus, "3D determination of grain shape in a FeAl-based nanocomposite by 3D FIB tomography," *Scripta materialia*, vol. 45, no. 7, pp. 753–758, 2001.

[285] M. M. Elgmati, H. Zhang, B. Bai, R. E. Flori, Q. Qu, *et al.*, "Submicron-pore characterization of shale gas plays," in *SPE North American unconventional gas conference and exhibition*, 2011.

[286] M. E. Curtis, C. H. Sondergeld, R. J. Ambrose, and C. S. Rai, "Microstructural investigation of gas shales in two and three dimensions using nanometer-scale resolution imaging : Microstructure of gas shales," *AAPG bulletin*, vol. 96, no. 4, pp. 665–677, 2012.

[287] G. R. Chalmers, R. M. Bustin, and I. M. Power, "Characterization of gas shale pore systems by porosimetry, pycnometry, surface area, and field emission scanning electron microscopy/transmission electron microscopy image analyses: Examples from the Barnett, Woodford, Haynesville, Marcellus, and Doig units," *AAPG bulletin*, vol. 96, no. 6, pp. 1099–1119, 2012.

[288] D. Wildenschild and A. P. Sheppard, "X-ray imaging and analysis techniques for quantifying pore-scale structure and processes in subsurface porous medium systems," *Advances in Water Resources*, vol. 51, pp. 217–246, 2013.

[289] M. Joshi, *A class of stochastic models for porous media*. PhD thesis, Lawrence Kansas University of Kansas, 1974.

[290] B. Biswal, C. Manwart, and R. Hilfer, "Three-dimensional local porosity analysis of porous media," *Physica A: Statistical Mechanics and its Applications*, vol. 255, no. 3-4, pp. 221–241, 1998.

[291] C. Manwart, S. Torquato, and R. Hilfer, "Stochastic reconstruction of sandstones," *Physical Review E*, vol. 62, no. 1, p. 893, 2000.

[292] P.-E. Øren and S. Bakke, "Process based reconstruction of sandstones and prediction of transport properties," *Transport in porous media*, vol. 46, no. 2-3, pp. 311–343, 2002.

[293] C. H. Arns, M. A. Knackstedt, W. V. Pinczewski, and N. S. Martys, "Virtual permeametry on microtomographic images," *Journal of Petroleum Science and Engineering*, vol. 45, no. 1-2, pp. 41–46, 2004.

[294] A. N. Diógenes, L. O. E. dos Santos, C. P. Fernandes, A. Moreira, and C. Apolloni, "Porous media microstructure reconstruction using pixel-based and object-based simulated annealing–comparison with other reconstruction methods," *Revista de Engenharia Térmica*, vol. 8, no. 2, pp. 35–41, 2018.

[295] B. Biswal, R. Held, V. Khanna, J. Wang, and R. Hilfer, "Towards precise prediction of transport properties from synthetic computer tomography of reconstructed porous media," *Physical Review E*, vol. 80, no. 4, p. 041301, 2009.

[296] K. Wu, M. I. Van Dijke, G. D. Couples, Z. Jiang, J. Ma, K. S. Sorbie, J. Crawford, I. Young, and X. Zhang, "3D stochastic modelling of heterogeneous porous media–applications to reservoir rocks," *Transport in Porous Media*, vol. 65, no. 3, pp. 443–467, 2006.

[297] A. Kalarakis, V. Michalis, E. Skouras, and V. Burganos, "Mesoscopic simulation of rarefied flow in narrow channels and porous media," *Transport in porous media*, vol. 94, no. 1, pp. 385–398, 2012.

[298] E. S. Boek and M. Venturoli, "Lattice-Boltzmann studies of fluid flow in porous media with realistic rock geometries," *Computers & Mathematics with Applications*, vol. 59, no. 7, pp. 2305–2314, 2010.

[299] Z.-S. Wu, P.-C. Dong, G. Lei, S. Yang, and N. Cao, "Lattice Boltzmann simulation of fluid flow in complex porous media based on CT image," *Journal of Industrial and Intelligent Information*, vol. 4, no. 1, 2016.

[300] M. Piller, D. Casagrande, G. Schena, and M. Santini, "Pore-scale simulation of laminar flow through porous media," in *Journal of Physics: Conference Series*, vol. 501, p. 012010, 2014.

[301] P.-E. Øren and S. Bakke, "Reconstruction of Berea sandstone and pore-scale modelling of wettability effects," *Journal of Petroleum Science and Engineering*, vol. 39, no. 3-4, pp. 177–199, 2003.

[302] B. P. Muljadi, M. J. Blunt, A. Q. Raeini, and B. Bijeljic, "The impact of porous media heterogeneity on non-Darcy flow behaviour from pore-scale simulation," *Advances in Water Resources*, vol. 95, pp. 329–340, 2016.

[303] A. Dybbs and R. Edwards, "A new look at porous media fluid mechanics—Darcy to turbulent," in *Fundamentals of transport phenomena in porous media*, pp. 199–256, 1984.

[304] W. Tanikawa and T. Shimamoto, "Klinkenberg effect for gas permeability and its comparison to water permeability for porous sedimentary rocks," *Hydrology and Earth System Sciences Discussions*, vol. 3, no. 4, pp. 1315–1338, 2006.

[305] F. Javadpour, D. Fisher, M. Unsworth, *et al.*, "Nanoscale gas flow in shale gas sediments," *Journal of Canadian Petroleum Technology*, vol. 46, no. 10, 2007.

[306] B. Ju and D. Wu, "Experimental study on the pore characteristics of shale rocks in Zhanhua depression," *Journal of Petroleum Science and Engineering*, vol. 146, pp. 121–128, 2016.

[307] J. Goral, I. Miskovic, J. Gelb, J. Kasahara, *et al.*, "Pore network investigation in Marcellus Shale rock matrix," in *SPE Asia Pacific Unconventional Resources Conference and Exhibition*, no. 176988, Society of Petroleum Engineers, 2015.

[308] F. Javadpour *et al.*, "Nanopores and apparent permeability of gas flow in mudrocks (shales and siltstone)," *Journal of Canadian Petroleum Technology*, vol. 48, no. 8, pp. 16–21, 2009.

[309] J. Ma, J. P. Sanchez, K. Wu, G. D. Couples, and Z. Jiang, "A pore network model for simulating non-ideal gas flow in micro-and nano-porous materials," *Fuel*, vol. 116, pp. 498–508, 2014.

[310] M. Kazemi and A. Takbiri-Borujeni, "An analytical model for shale gas permeability," *International Journal of Coal Geology*, vol. 146, pp. 188–197, 2015.

[311] H. Yu, J. Chen, Y. Zhu, F. Wang, and H. Wu, "Multiscale transport mechanism of shale gas in micro/nano-pores," *International Journal of Heat and Mass Transfer*, vol. 111, pp. 1172–1180, 2017.

[312] A. S. Ziarani and R. Aguilera, "Knudsen's permeability correction for tight porous media," *Transport in porous media*, vol. 91, no. 1, pp. 239–260, 2012.

[313] P. Mohammadmoradi and A. Kantzas, "Pore-scale permeability calculation using CFD and DSMC techniques," *Journal of Petroleum Science and Engineering*, vol. 146, pp. 515–525, 2016.

[314] P. Churcher, P. French, J. Shaw, L. Schramm, *et al.*, "Rock properties of Berea sandstone, Baker dolomite, and Indiana limestone," in *SPE International Symposium on Oilfield Chemistry*, no. 21044, pp. 431–446, 1991.

[315] N. G. Hadjiconstantinou, "Analysis of discretization in the direct simulation Monte Carlo," *Physics of Fluids*, vol. 12, no. 10, pp. 2634–2638, 2000.

[316] D. Fedosov, S. Rogasinsky, M. Zeifman, M. Ivanov, A. Alexeenko, and D. Levin, "Analysis of numerical errors in the DSMC method," in *AIP Conference Proceedings*, vol. 762, pp. 589–594, 2005.

[317] E. Oran, C. Oh, and B. Cybyk, "Direct simulation Monte Carlo: recent advances and applications," *Annual Review of Fluid Mechanics*, vol. 30, no. 1, pp. 403–441, 1998.

[318] T.-R. Teschner, L. Könözsy, and K. W. Jenkins, "Progress in particle-based multiscale and hybrid methods for flow applications," *Microfluidics and Nanofluidics*, vol. 20, no. 4, p. 68, 2016.